Investigations of the Growth Mechanism of Metal-Organic Nanotubes

A Dissertation Presented for the
Doctor of Philosophy
Degree
The University of Tennessee, Knoxville

Kristina Marie Vailonis
December 2019

DEDICATION

To my parents, Maria and Joe, and sister, Laura-Ann.

ACKNOWLEDGMENT

First and foremost, acknowledgements go my advisor, Dr. David Jenkins, for his guidance, support, and encouragement during my time at the University of Tennessee. I can truly say that under your advising, I learned something new every day. Your lessons ranged from how to communicate your science, how to be an effective educator, and even how to bake the best brownies and cheesecake. You were always “pumped” to start the day and tackle a new challenge. Thank you for sharing that attitude and excitement of chemistry with me, even if it did usually occur during my morning coffee.

Next, my research would not be possible without the work from my expert collaborators, Dr. Karthikeyan Gnanasekaran and Dr. Nathan Gianneschi from Northwestern University, and Dr. Umesh Strestha and Dr. Mark Dadmun from the University of Tennessee. I have enjoyed our collaborations and cannot wait to see where the research is taken next.

Many thanks to Team MONT, my mentors and friends: Dr. Chris Murdock, Dr. Brianna Solomonson, and Derek Mull. This research would also not be complete without the assistance from the amazing undergraduate students that I had the pleasure to mentor. Thank you, Nick Ross, Rowan Borsari, Gerard Van Trieste, Aleah Schenck, and Alec Vest for all of your hard work. I’d also like to thank past and present Jenkins group members Dr. Gaya Elpitiya, Dr. Xian Carroll, Dr. Joe Dejesus, Kevin Blatchford, Vernon Stafford III, and Isabel Jensen for making the long days in lab better. I will miss our little chemistry family.

Last but sincerely not least, I want to show my appreciation to all of my friends and coworkers in the UT Chemistry department, specifically Brianna Watson, Lindsey Miller, Sara Isbill, Randi Beil, KC Mote, and Michael Orick.

ABSTRACT

Metal-organic nanotubes (MONTs) are the one-dimensional variant of metal-organic frameworks (MOFs), where the nanotubular framework propagates in one-dimension coincident with the pore. Presently, MONTs are studied by conventional solid-state characterization techniques, similar to MOFs. Bulk MONT materials are composed of thousands of nanotubes stacked together and display similar structures to 3D MOFs with tubular pores. Metal-organic nanotubes need to be isolated from this bulk material in order to study their unique one-dimensional properties and truly become a new unique class of materials.

Metal-organic nanotube are synthesized through solvothermal reactions of organic ligands and metal salts, where the design of the ligand plays a large role in the dimensionality of the framework. There were several concurrent goals for improved MONT synthesis described herein. The organic ligand design can be divided in four categories including those ligands that produce (1) large pore MONTs, (2) fluorescent MONTs, (3) reduced aggregation MONTs, and (4) a series of isostructural MONTs. One ligand from each of these categories was incorporated in MONT reactions, but only one new MONT was synthesized. The challenges in predicting the dimensionality of a framework was shown by these MONT syntheses.

To show that MONTs are unique materials, the fundamental chemistry on the nanoscale, the colloidal phase, needs to be understood. This idea revolutionizes the way MONTs are typically studied. Liquid-cell transmission electron microscopy (LCTEM) and small angle neutron scattering (SANS) were used as key nanoscale characterization techniques. LCTEM was able to visualize the formation and growth of nanoscale MONTs in real time for the first time and match the colloidal product to the bulk MONT solid. Small angle neutron scattering provided detail of the initial nanostructures formed within the MONT reactions.

The combination of ligand design and colloidal MONT analysis is vital for future research of these materials. Once the fundamental chemistry of formation is understood, directed syntheses and applications can be applied to MONTs.

TABLE OF CONTENTS

LIST OF TABLES

LIST OF FIGURES

LIST OF SCHEMES

CHAPTER 1

INTRODUCTION TO METAL-ORGANIC NANOTUBES

Metal-Organic Frameworks

Metal-organic frameworks are a class of crystalline porous coordination polymers famously pioneered by Omar Yaghi in the early 1990's.[1-2] As coordination polymers, their infinite lattice is composed of organic ligands bound to metal ions or clusters. Due to their porous nature, MOFs have been utilized for applications in gas storage,[3] separations,[4-5] heterogeneous catalysis,[6] and analyte sensing.[7] A key advantage of metal-organic frameworks is their boundless tunability; the metal center and corresponding organic ligands can be modified to create a desired structure. This designer aspect of MOFs makes this field an ever-evolving area of synthetic chemistry unlike porous materials such as zeolites. In the 25+ years since their creation over 60,000 structures have been reported in the Cambridge Crystallographic Data Centre (CCDC).[8]

Metal-Organic Nanotubes

The topology, connectivity, pore size, pore shape, and even dimensionality of the MOF can be changed as a result of modifying the metal centers and organic ligands.[9] Dimensionality refers to the number of directions the framework propagates. Metal-organic frameworks have been synthesized as one, two, and three-dimensional variants. Three-dimensional MOFs are the most common dimensionality with the framework repeating in all three (x, y, and z) dimensions, creating a structure similar to a traditional tinker-toy set as seen in Figure 1.1.[10] Two-dimensional MOFs form a sheet-like structure where the framework propagates in two dimensions.[11] Lastly, one-dimensional MOFs, which are referred to as metal-organic nanotubes (MONTs), form nanotubular structures where the framework propagates in one-dimension coinciding with the pore. A necessary requirement of MONTs is the presence of covalent bonds connecting each repeating unit within the framework.[12-13] Metal-organic nanotubes are the newest and least common dimensionality of MOFs.

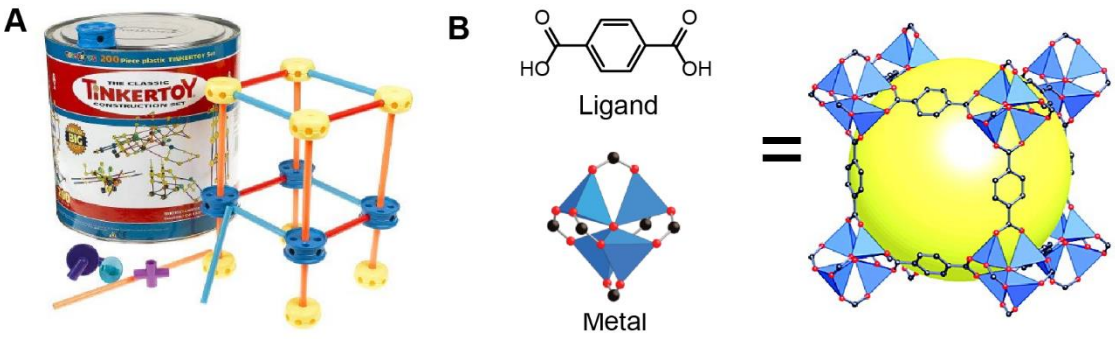

Figure 1. 1. (A) Classic tinker toy (B) 3D metal-organic framework, MOF-5, and its corresponding components. These images are modified from the original references [2, 14-15]

While the comparison of MONTs to 3D MOFs is obvious, there is a distinct 1D material that also offers an important comparison. Single walled carbon nanotubes (SWCNTs) were also developed in the 1990's.[16] The properties of SWCNTs depend on their size and packing structure; however, controlling these properties is quite challenging synthetically. 1D MONTs may be the conceptual combination of both materials: SWCNTs and 3D MOFs (Figure 1.2). The tubular structure is similar to CNTs, but with the hybrid tunability of MOFs allows for MONTs to be a unique new material worth investigating.

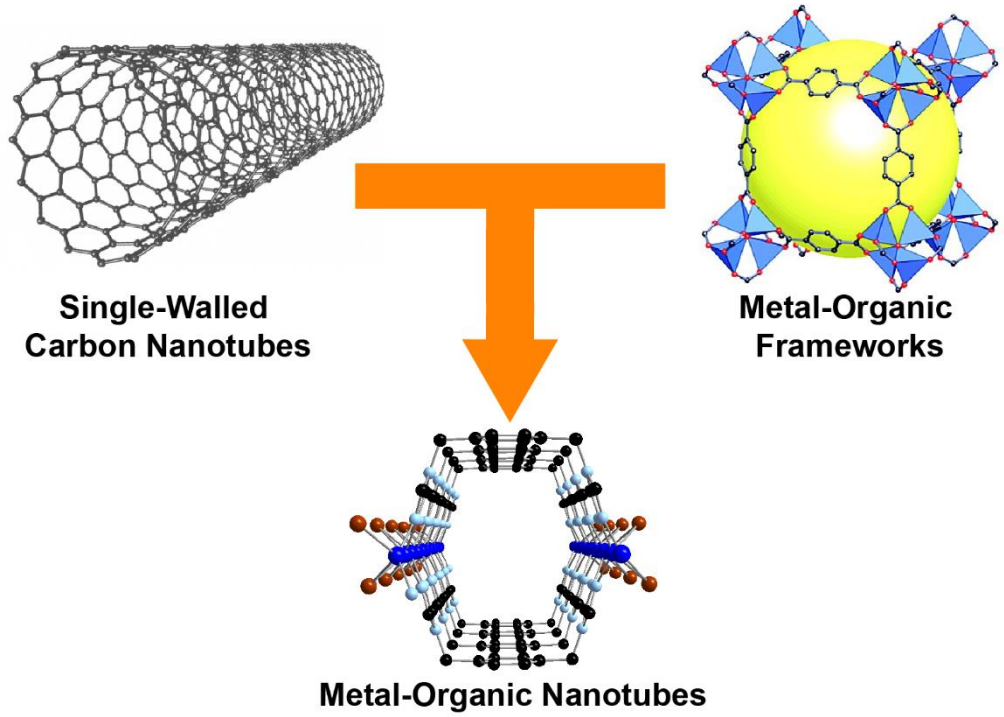

Figure 1. 2. Metal-organic nanotubes are the intellectual product of metal-organic frameworks and single-walled carbon nanotubes. These images are modified from the original references [17]

Hybrid Nature of MONTs

Metal-organic nanotubes are hybrid materials, meaning they are composed of both organic and inorganic pieces. As MONTs are still in their infancy as a material, comparisons to similar materials can give insight and inspiration for possible applications. The completely organic nanotubes for comparison are single-walled carbon nanotubes[18] (SWCNTs) (Figure 1.3A) and the completely inorganic nanotubes are boron-nitride nanotubes (BNTs) (Figure 1.3C).[19-20]

MONTs are structurally analogous to these two materials and can be envisioned to act as nanostraws or nanowires. It is possible to envision MONTs as nanostraws where the tubular architecture is utilized as a transport vehicle that could carry small molecules through their pores. Studies on single-walled carbon nanotubes have shown that this is possible where small molecules have been transported through lipid bilayers[21] (Figure 1.4A). A nanowire type application can allow for the highly anisotropic structure to be used to connect materials through nano-sized junctions. MONTs could even be loaded with conductive small molecules and act as a protective conduit material for the nanowire. SWCNTs have also shown similar style applications and even recently have been incorporated in microprocessors as mini-transistors[22-23] (Figure 1.4B).

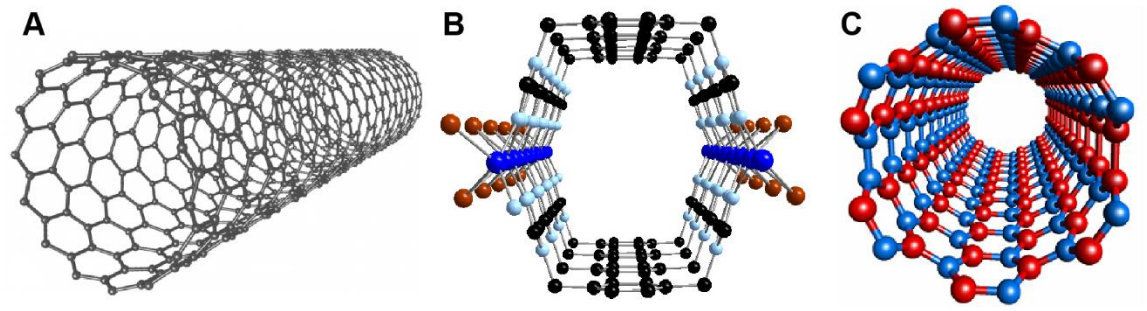

Figure 1. 3. (A) Single-walled carbon nanotubes, (B) metal-organic nanotubes, and (C) boron-nitride nanotubes.

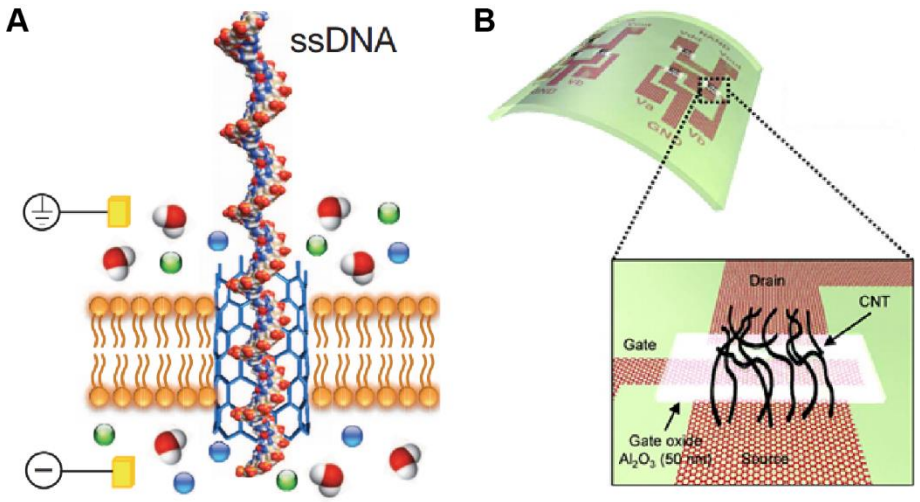

Figure 1. 4. (A) The nanostraw[21] and (B) nanowire[22] applications of SWCNTs. These images are modified from the original references.

Metal-organic nanotubes have beneficial characteristics over these analogous organic and inorganic nanotubes. Metal-organic nanotubes are synthesized through a solvothermal synthetic approach to form nanotubes of identical pore size. CNTs and BNTs may have established synthetic methods; however, all of these methods for synthesis involve high energy techniques such as laser ablation,[24] arc discharge,[25] and chemical vapor deposition.[26-27] These techniques utilize specialized and expensive equipment for their synthesis which typically yields in a distribution of various nanotube pore sizes.

MONTs are also easily and directly modified in comparison to carbon nanotubes and boron-nitride nanotubes. The organic linker can be altered through organic syntheses for a desired structure such as one with an additional tag or functional group.[28] CNTs and BNTs can be modified with external tags; however, the placement of the tag typically depends on defect sites on the nanotube.[29] A direct placement of an external tag cannot be controlled for these nanotubes.

Synthesis of Metal-Organic Nanotubes

Metal-organic nanotubes, like MOFs, utilize combinatorial techniques for their synthesis. By varying the metal center or organic linker, a multitude of possible structures can be made. However, given their tubular structure there is a limit on the types of MONTs that can be formed. To date, four classes of MONTs exist depending of the structural motif that is employed (Figure 1.5).[30] Each class of MONTs has a porous one-dimensional structure with covalent bonds connecting the repeating units within the MONT; however, as the geometric motif or distinct it is not surprising that the ligands employed in the reaction are different between classes. Helical MONTs (Figure 1.5A) employ flexible organic ligands that wrap around each other in a helical fashion to bind with a metal center, forming a MONT.[31] These may be analogous to DNA. A two-column pillared method as shown by Figure 1.5B utilizes an organic ligand in the *syn*-conformation to bind

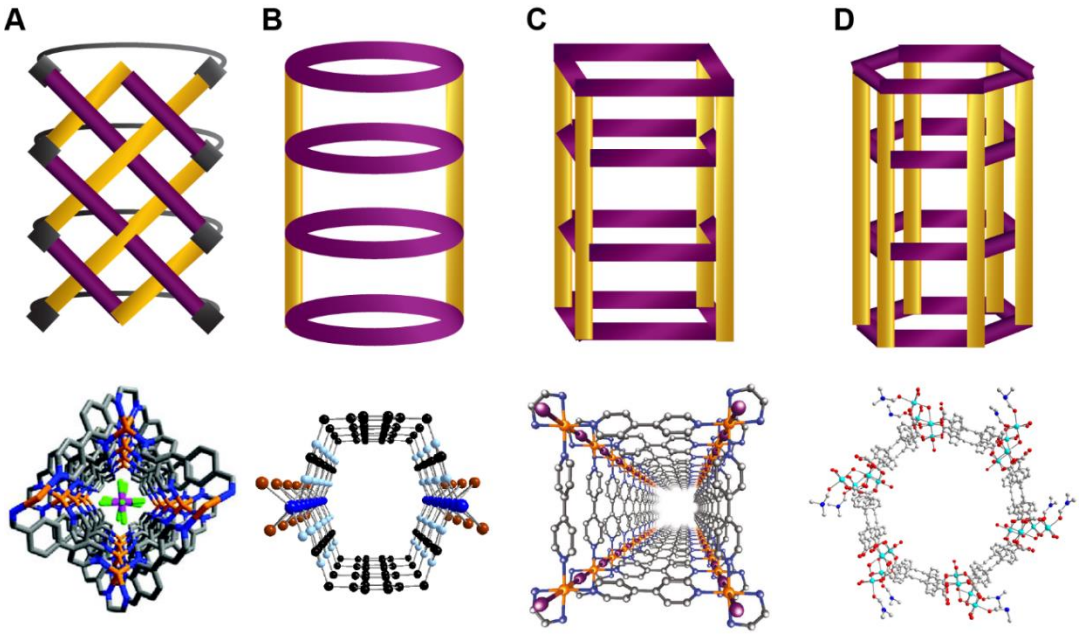

Figure 1.5. Schematic of the four methods to synthesize MONTs, with corresponding literature examples. (A) Helical,[12] (B) 2-column pillar,[32] (C) 4-column pillar,[13] and (D) Greater than 4-column pillar.[33] These images are modified from the original references.

with a metal center, creating the MONT. In this case, two semi-rigid ligands form a pair of “C” shaped to connects the metals. Figure 1.5C illustrates the four-column pillar wherein rigid ligands are connected at 90° angles in a *cis* position on the metals.[32] Greater than four-column pillar approach (Figure 1.5D) either employs a wider angle at a single metal or builds more complex secondary building units to achieve a wider internal angle. The column motifs employ even numbered equivalents of a ligands to react with metal centers to form the MONT. The number of ligands, four, six, and eight, match the edges of the shapes, square, hexagonal, and octagonal, respectively, that are formed.[13, 34]

Jenkins Group Methodology for MONT Synthesis

The Jenkins group has previously shown the successful incorporation of a series of semi-rigid *syn*-confirmation di-1,2,4-triazole ligands in the formation of one-dimensional metal-organic nanotubes (Figure 1.6).[32] The organic ligands vary in width from the smallest, 4,4′-(1,3-(xylene)diyl)bis(1,2,4-triazole) (Figure 1.6, Ligand **1**), to 4,4′-(1,4-(xylene)diyl)bis(1,2,4-triazole) (Figure 1.6, Ligand **2**), and to the widest ligand, 4,4′-[naphthalene-2,6-diylbis(methylene)]bis(1,2,4-triazole) (Figure 1.6, Ligand **3**). Crystal structures were obtained for each framework with single crystal X-ray diffraction. which confirmed that the pore sizes increased with the width of each organic ligand.

Di-1,2,4-triazole ligands are the chosen framework binding moiety for the Jenkins group because they yield the correct geometry for synthesizing a MONT whose 1D channels are created via the metal ion-triazole bonds and capping anions. This chapter will focus on new directions of di-1,2,4-triazole ligands via the 2-column pillar MONT synthetic route in hopes to solve common problems with metal-organic nanotube characterization.

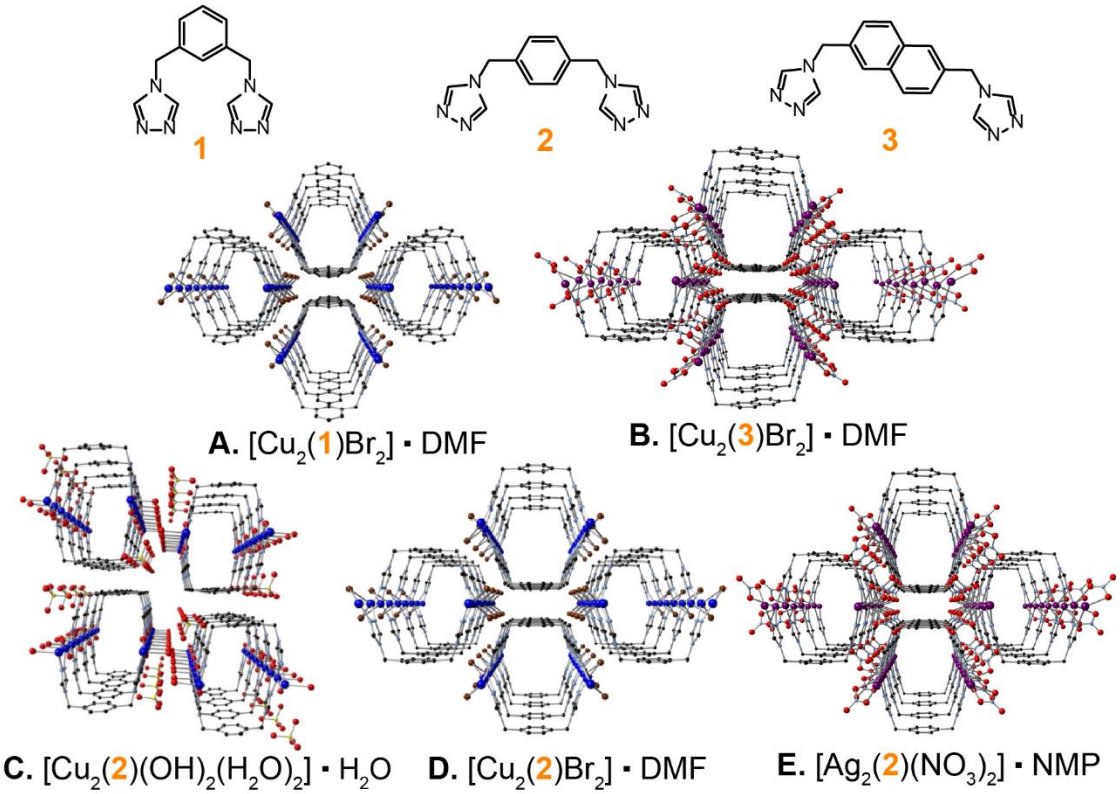

Figure 1.6. The first isostructural series of metal-organic nanotubes previously synthesized by the Jenkins group.[32] These images are modified from the original references.

Importance of Discrete Dimensionality

Currently MONTs have been studied by conventional MOF characterization techniques which include solid-state nuclear magnetic resonance spectroscopy (SSNMR),[35] infrared spectroscopy (IR),[36] powder X-ray diffractometry (PXRD),[37] single-crystal X-ray diffractometry (SCXRD),[38] and gas adsorption measurements.[39] All of these techniques require solid materials on the macro-scale for analysis, typically milligrams of bulk material. This bulk material requirement highlights the main limitation of MONTs. Metal-organic nanotubes need to be isolated from each other in order to exhibit unique properties.

As previously stated, MOFs can be split into three categories based on their dimensionality, similar to the allotropes of carbon. The allotropes of carbon clearly illustrate the relationship between structure and properties of a material. Diamond (3D allotrope) is an extremely hard substance, graphene (2D allotrope) has a unique electronic structure,[40-41] and carbon nanotubes (1D allotrope) have high tensile strength.[18] Each of these allotropes are composed of carbon-carbon covalent bonds, yet exhibit different properties. These differences are especially significant for graphene and carbon nanotubes due to their similar sp^2 hybridization. Similar statements are hypothesized about MOFs. A 3D metal-organic framework with channel-like pores, such as MOF-74,[42] will look structurally similar to a bundle of 1D metal-organic nanotubes (Figure 1.7). Both structures are composed of metal ions linked together via organic ligands creating a structure with tubular pores; the only difference is the connectivity of the framework. Thus, *aggregated MONTs are hypothesized to act similarly to 3D MOFs.*

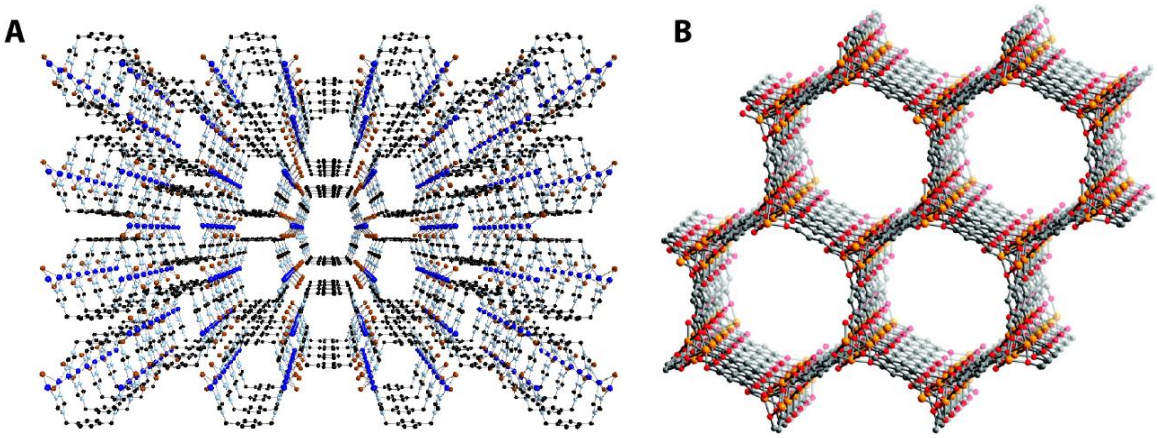

Figure 1. 7. Structural similarities of (A) aggregated MONTs[32] in bulk material and (B) 3D MOFs, such as MOF-74.[42] These images are modified from the original references.

Revolutionary MONT Characterization

In order to characterize MONTs as unique low dimensional materials, new characterization techniques and new methods of analyzing MONTs must be employed. **A discrete or singular MONT will not form large quantities of solid, therefore MONTs must be analyzed in similar methods to nanomaterials or colloidal materials and cannot be treated as bulk porous materials.** This key fact forces a new revolutionary way of thinking towards the preparation and characterization of MONTs. Colloidal nanomaterials have been studied by small-angle X-ray scattering (SAXS),[43-44] transmission electron microscopy (TEM),[45] and fluorescence spectroscopy.[46] These methods should be employed for MONTs.

Initial studies with SAXS by the Jenkins and Dadmun group has allowed for the understanding of the growth mechanism of a previously synthesized metal-organic nanotube.[47] Two preliminary growth mechanisms were proposed as seen in Figure 1.8. The top route in Figure 1.8 (1D Chain Growth) shows initial nanotube growth and then aggregation of the tubes to form bulk crystals, and the bottom route (3D Aggregation) shows aggregation of metal ions and ligands which them grow to form nanotubes and bulk crystals. *Ex situ* SAXS was able to monitor the progression of the solvothermal MONT reaction and analysis of the experiments concluded that the reaction underwent an autocatalytic reaction until all starting materials were consumed. This mechanism can also be described by the bottom 3D aggregation growth route. In addition, the pore size and dimensionality of the structure were able to be correctly modeled and matched to the single-crystal X-ray structure.

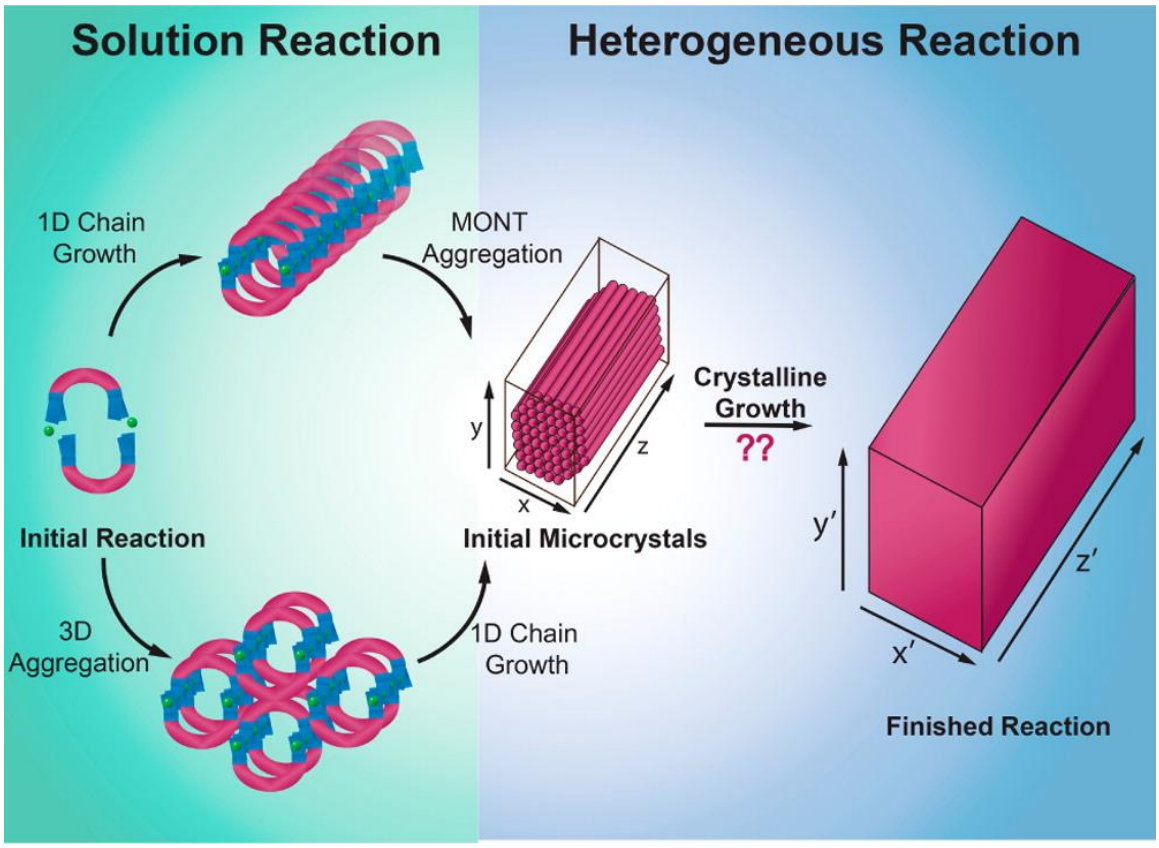

Figure 1. 8. Proposed routes of nucleation and growth of a silver-based MONT by SEM and SAXS analysis. This image is modified from the original reference.[47]

Classically, transmission electron microscopy has been used to image the fine detail of nanomaterials due to their enhanced resolution.[48-49] New techniques have further developed TEM for solution phase imaging by incorporating a liquid-cell into the microscope. This is appropriately known as liquid-cell transmission electron microscopy (LCTEM) and has been shown to successfully monitor the progression of colloidal reactions including those of covalent organic frameworks[45] and metal-organic frameworks[50-52] Figure 1.9 depicts the real-time growth of ZIF-8 over a span of 11 minutes. Important initial structures can be directly imaged with this new technique and can give additional insight towards the reaction mechanisms.

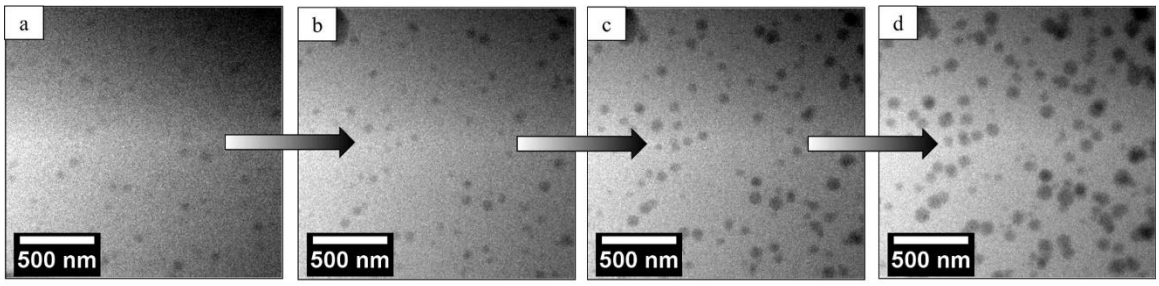

Figure 1. 9. Real time liquid-cell transmission electron microscope images of 3D metal-organic framework, ZIF-8. This image is modified from the original reference.[52]

Additionally, fluorescence spectroscopy can be utilized to study colloidal materials and have been commonly incorporated in the study of single-walled carbon nanotubes.[53] If MONTs were synthesized as colloids, their high aspect ratios could be studied with fluorescence anisotropy measurements to estimate the size and length of the frameworks via their Brownian motion.[54] This would allow for an estimation of particle size or the degree of metal-organic nanotube aggregation. Further studies including confocal fluorescence microscopy could allow for fluorescence imaging of MONTs.[55] The incorporation of a fluorescent substituent within a MONT will open the door to new possible characterization techniques.

For metal-organic nanotubes to truly become a new unique class of materials, it is essential to understand the fundamental chemistry of MONTs at the nanoscale. Only once this is achieved MONTs can be utilized to their full potential. This dissertation takes the first steps towards this goal and will focus on the two specific aspects of metal-organic nanotubes. First, the preparation of new ligands for new metal-organic nanotubes that tackle the challenges regarding the formation of discrete nanotubes, and second, the synthesis of metal-organic nanotubes for colloidal studies with TEM and SAXS.

CHAPTER 2

DESIGN OF DI-1,2,4-TRIAZOLE LIGANDS FOR TOWARDS SYNTHESIS OF METAL-ORGANIC NANOTUBES

Abstract

In synthesizing metal-organic nanotubes, the design of the organic linker is critical. This chapter details the ligand design process for preparing discrete metal-organic nanotubes (MONTs). The general design goal of creating a durable and characterizable MONT was followed by creating ligands that fit in five different categories. A discrete MONT that can be detected by conventional methods needs a ligand that can: (1) form large pores, (2) be fluorescent, (3) mitigate aggregation of formed MONTs, and (4) be a part of an isostructural series of MONTs for comparison. Both complete and partially complete ligand syntheses will be discussed in this chapter.

Introduction

The ability to tailor a structure, and particularly the pore size, to a desired application is a critical feature in MOF chemistry which is what differentiates MOFs from many other materials. The Jenkins group follows the 2-column pillar (Figure 2.1A) approach for MONT synthesis because this style allows for MONTs to be directly and uniformly tailored through two main routes. First, with this method, the height and width of the metal-organic nanotube can be altered independently (Figure 2.1B). Secondly, the organic ligand can also be modified by adding an external tag through conventional organic synthesis (Figure 2.1C). These modifications are clear examples of the superiority of the 2-column pillar approach versus other methods for MONT synthesis previously discussed in Chapter 1 (Figure 1.5).

As previously stated, the *syn* confirmation ligand can be modified in two main locations (Figure 2.1A dark blue, and light blue components). The MONT pore width can be increased or decreased by changing the substituent in the center of the ligand. This central substituent is denoted by the dark blue piece of the ligand in Figure 2.1A. Next, the MONT pore height can be altered by adding a substituent beneath the ‘hinge’ of the ligand. The ‘hinge’ and the modifiable substituent are

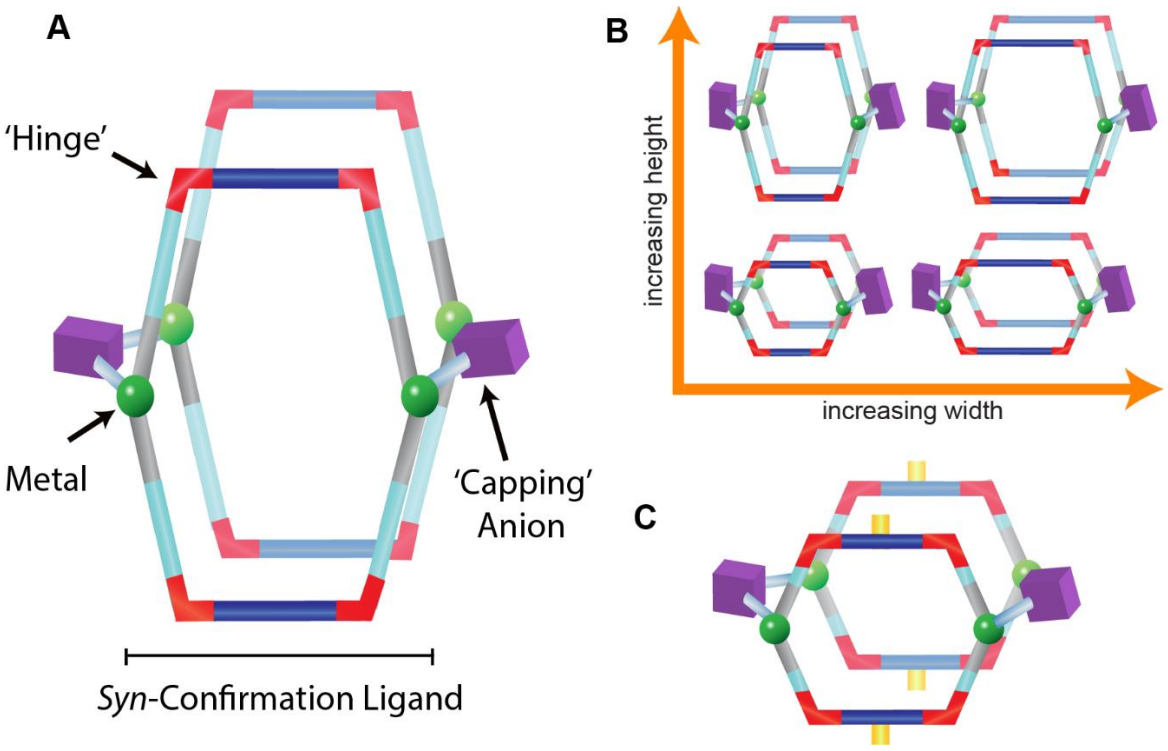

Figure 2. 1. (A) Schematic of a generic 2-column pillar MONT with beneficial features including; (B) independent height and width tuning, and (C) the addition of external tags, such as an alkyne.

denoted by the red and light blue piece respectively, in the organic ligand of Figure 2.1A. To date, a CH_2 moiety is used as the 'hinge' in all of the Jenkins group MONT ligands.

In addition to altering the height and width of the MONT, the organic ligand can be further modified by the incorporation of an external tag or reactive substituent (Figure 2.1C). This modification can take place on the central moiety of the ligand (Figure 2.1A, dark blue location). The addition of an external tag gives opportunities for functionalizing or post-synthetically modifying the metal-organic nanotubes. External tags can participate in a range of chemistries from peptide coupling reactions[56] to click reactions.[57] This expanded scope of available chemistries opens the door to future applications or different characterization methods.

Synthesis of New Di-1,2,4-triazole Ligands

The lack of volume of metal-organic nanotubes in literature is evident. As of 2019, a literature search would yield approximately ~50 structures. This result is in high contrast to the hundreds of two-dimensional and thousands of three-dimensional metal-organic frameworks. As of 2019, there are upwards to 60,000 MOF structures in the CCDC database. The reason there are so few one-dimensional frameworks is partly due to their difficult synthesis. It is commonly understood that MOFs have been shown have labile metal ions within the materials and studies where the metal nodes have been post-synthetically exchanged have proven this. Furthermore, there have also been studies that have shown the production of 2D or 3D MOFs even through MONTs could be formed. For example, if the organic ligand used in the 2-Column Pillar approach does not stay in the *syn* confirmation, a 2D sheet can be formed instead.

This chapter will discuss the rationale and synthetic methods for designing ligands for the formation of MONTs, and in particular, discrete MONTs. It is

hypothesized that the discrete MONTs will exhibit unique properties as compared to bulk, aggregated MONTs; therefore, creating solutions for the pitfalls within MONT synthesis is a vital task.

First, in order to study discrete MONTs with established tools similar to 3D MOF characterization techniques, MONTs need to be of a minimum size for detection. Transmission electron microscopy Has a detection limit of typically around 1 nm, or 10 Å. To study a single, discrete MONT, the structure needs to be larger than the limit of detection. This problem is not a concern for 3D MOFs since their frameworks propagate in three dimensions. However, the framework of MONTs propagate in one dimension yielding highly anisotropic structures with high aspect ratios; therefore, the ability to detect MONTs with most characterization techniques is dependent on the smallest dimension, i.e. the width, or pore size. Previously published MONTs in the Jenkins group range in size from 7.6 Å to 10.3 Å. Other MONTs in the literature range from approximately 2 Å up to 33 Å. A survey of metal-organic nanotube pore diameters is shown in Table 2.1. The MONTs are divided by synthetic design, either column or helical, and by pore size, i.e. extra small, small, medium, and large. Within these categories each MONT is described as anionic, cationic, or neutral, and whether there is intertube hydrogen bonding or π-π stacking. As of now, the majority of MONTs are just below or just above the TEM detection limit. Future MONTs need to be synthesized in a way that produces large pore MONTs that can be easily characterized.

While wider MONTs will allow for direct measurement of the structures, additional approaches can also circumvent this problem. Inspiration from the 2014 Nobel Prize in Chemistry won by Betzig, Hell, and Moerner,[58] shows that single molecule detection can be achieved via fluorescence. We can exploit this by adding a fluorescent substituent into the organic ligand or through an external tag as seen in Figure 2.2. The fluorescence measurement can indicate the degree of MONT bundling.

Table 2. 1. Survey of MONTs with reported pore size in literature. Green represents neutral MONTs, blue represents anionic MONTs, red represents cationic MONTs. ▲ represents intertube π-π stacking while * represents intertube hydrogen bonding. □ represents a MONT with structural amorphism.

Pore Size	Column Design	Ref	Helical Design	Ref
Extra Small (< 5 Å)	3.6 Å 4 Å▲ 4 Å* 5.7 Å	59 60 61 62	2-3 Å*	63
Small (5-10 Å)	5 Å 6-8 Å 7 Å 7.3 Å 7.6 Å 8.2 Å 8.6 Å▲ 8.7 Å 9.1 Å 9.2 Å 9.3 Å 9.9 Å▲ 10 Å* □ 10 Å* 10 Å* 10.3 Å	13 64 65 66 32 67 68 32 32 69 32 70 71 72 73 32	10 Å* □	71
Medium (11-20 Å)	11 Å 13.3 Å 14 Å 14 Å	74 75 76 77	11 Å 12 Å* 14 Å* 15 Å 20 Å*	12 78 79 80 81
Large (>20 Å)	21 Å 23 Å	82 83	33 Å*	84

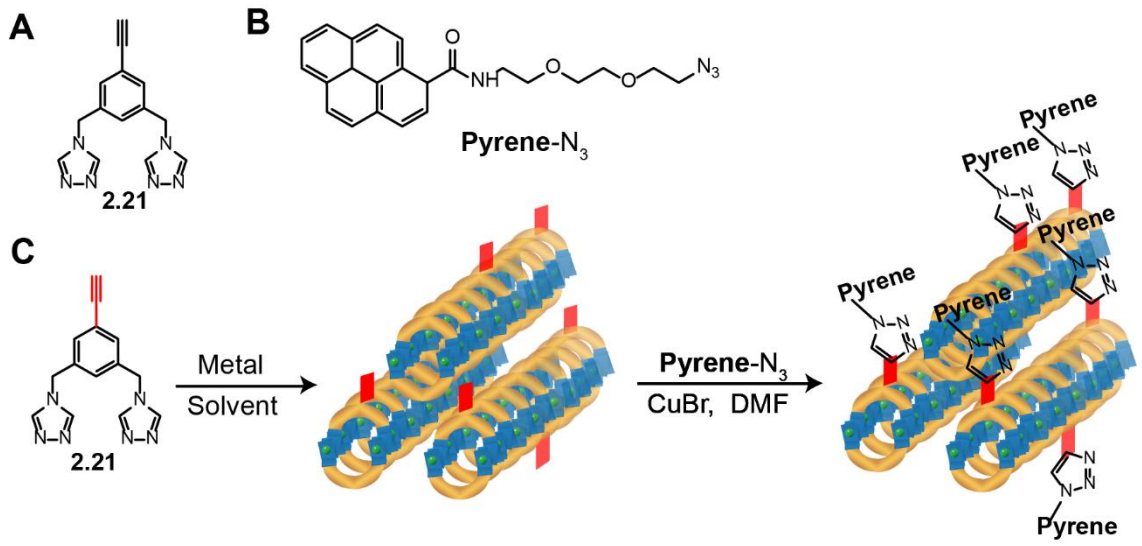

Figure 2. 2. (A) Alkyne functionalized ditriazole ligand, 2.21. (B) Azide functionalized pyrene tag. (C) Schematic of MONT reaction with alkyne functionalized ligand and addition of a fluorescent pyrene tag via Click chemistry.

The goal to synthesize a discrete MONT is immediately hindered by the aggregation of metal-organic nanotubes which was previously discussed in Chapter 1 (Figure 1.7). The aggregation of the nanotubes will hide the unique properties that the discrete material holds. As shown in Figure 2.3, the aggregation of nanotubes is caused by the π-π interactions from vertically adjacent tubes. To obtain a discrete MONT, this aggregation needs to be stopped or controlled. A method to stop this aggregation is with the addition of bulk groups to the organic ligand so that π-π interactions cannot occur.

While there are disadvantages to MONTS, these problems can be solved as long as research continues in this field. For MONTs to be truly understood there must be more examples of structures in the literature. More structures will give a clear understanding of the capabilities of this class of materials. Therefore, the last ligand design category will be centered on expanding the ligand library for MONT synthesis in the Jenkins group. Synthesizing additional *syn* conformation ligands will yield a larger set of isostructural MONTs for direct comparison.

The ligands described in this chapter (Table 2.2) will follow the main design goal; *to create a ligand that would favor the formation of a discrete MONT.* This general design goal has been divided further into subsequent synthetic categories: (1) large pore ligands, (2) fluorescent ligands, (3) aggregation blocking ligands, (4) ligands to build a larger library of isostructural MONTs (Figure 2.4). These four categories are used as guides for ligand design, with most ligands synthesized in this chapter falling under multiple categories.

Results and Discussion

The following discussion will explain the rationale for each proposed ligand. While each ligand has been placed into one of the four previously listed categories, some may have traits from multiple categories. For this reason, the ligand will be placed into the main classification category and any bonus traits will be described.

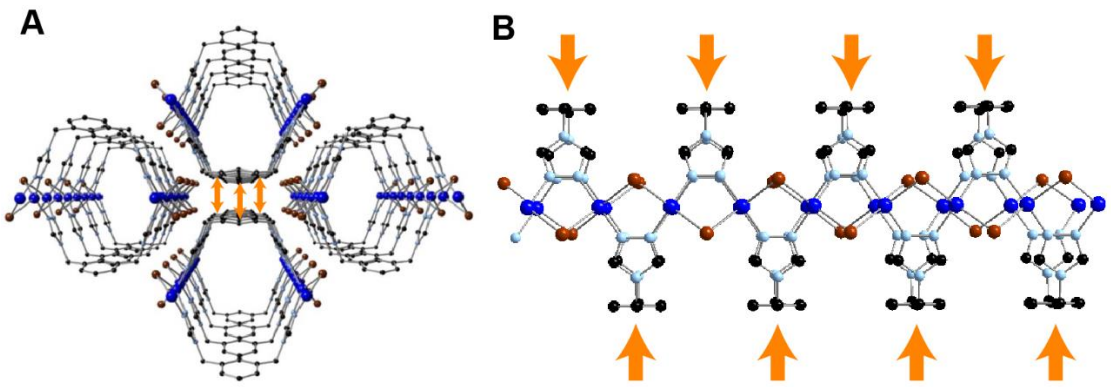

Figure 2. 3. (A) Single crystal X-ray structure illustrating the inter-tube π-π interactions, and (B) locations for functionalization to block inter-tube π-π interactions.

Table 2. 2. Di-triazole ligands synthesized in this chapter.

#	Ligand	Structure	Design Category
2.5	2,7-bis((4H-1,2,4-triazol-4-yl)methyl)anthracene	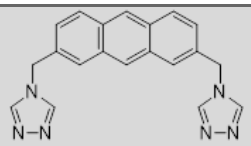	(1) Large Pore MONTs
2.8	9,10-bis((4H-1,2,4-triazol-4-yl)methyl)anthracene	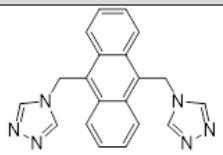	(2) Fluorescent MONTs
2.16	1,4-bis((4H-1,2,4-triazol-4-yl)methyl)anthracene	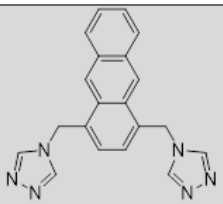	(2) Fluorescent MONTs
2.21	4,4'-((5-ethynyl-1,3-phenylene)bis(methylene)) bis(4H-1,2,4-triazole)	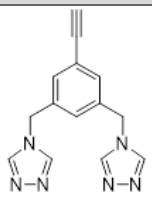	(2) Fluorescent MONTs
2.30	4,4'-((5-(tert-butyl)-1,3-phenylene)bis(methylene)) bis(4H-1,2,4-triazole)	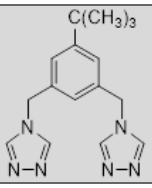	(3) Aggregation Blocking MONTs
2.33	potassium 1,1'-(1,4-phenylene)bis(4-((4H-1,2,4-triazol-4-yl)methyl)-2,6,7-trioxa-1-borabicyclo[2.2.2]octan-1-uide)	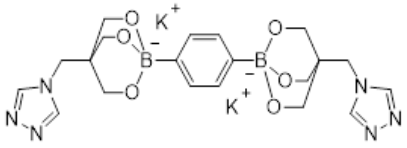	(4) Isostructural MONTs
2.35	1,8-bis((4H-1,2,4-triazol-4-yl)methyl)naphthalene	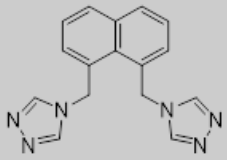	(4) Isostructural MONTs
2.37	2,7-bis((4H-1,2,4-triazol-4-yl)methyl)naphthalene	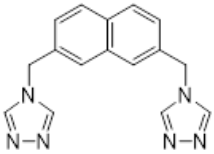	(4) Isostructural MONTs

Category 1. Ligands to Create Large Pore MONTs

The first category involves increasing the pore size of MONTs. The 2-Column pillar synthetic method dictates the width of the organic ligand must be increased to create a wider MONT. Large pore MONTs are a requirement for the analysis of new materials. Direct measurements with electron microscopy give confirmation of the morphology of a material.

The synthesis of large pore MONTs includes the synthesis of ligand **2.5**. From previous success with increasing the pore width by adding additional aryl groups, as seen from the para-xylyl and naphthyl di-1,2,4-triazole ligands, the next step was to create an anthracene based di-1,2,4-triazole ligand. This would allow for an elegant isostructural comparison of one, two, and three aromatic rings along similar designs of isoreticular MOF synthesis by Yaghi.[85] The use of anthracene may also allow for fluorescence measurements.

Ligand **2.5** is synthesized through previously published procedures with two new syntheses in the last two steps, as seen in Scheme **2.1**. This reaction started with a Friedel Crafts alkylation with benzyl alcohol in toluene to form the 2,7-dimethylanthracene, **2.1**. To synthesize the dibromide species, **2.3**, elemental bromine was refluxed in chloroform. This particular species was a challenge to isolate and reproduce. On a small scale, the dibromide species (**2.3**) can be synthesized; however, upon scaling up, the methyl groups on 2.1 are not brominated, but the carbons on the 9 and 10 positions are. DEPT (Distortions Enhancement by Polarization Transfer) NMR which differentiates the type of carbon atoms (C, CH, CH_2, or CH_3) in a molecule confirmed this result. Research by Plunkett also showed the synthesis of a partially hydrogenated pentacene analogue in Scheme 2.2 by similar synthetic means, therefore due to the scalability concerns, the synthesis of ligand **2.5** was not pursued further.

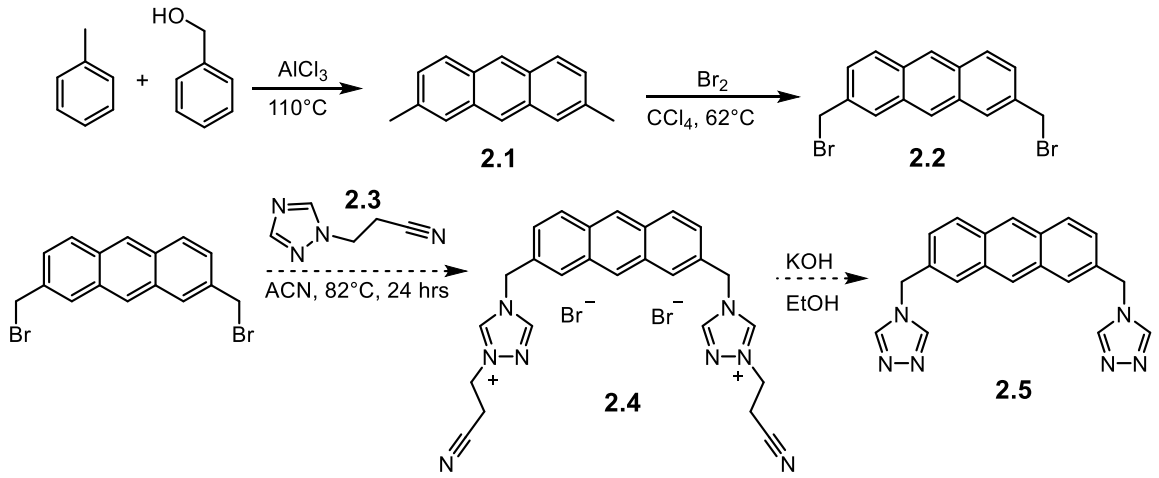

Scheme 2.1. Synthesis of 2,7-bis((4H-1,2,4-triazol-4-yl)methyl)anthracene, 2.5.

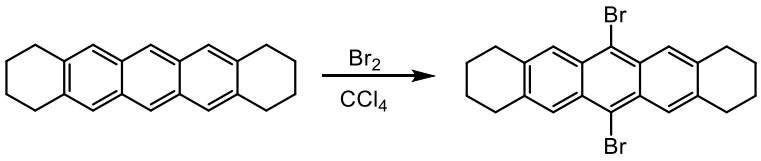

Scheme 2.2. Synthesis of 6,13-dibromo-1,2,3,4,8,9,10,11-octahydropentacene by Plunkett and coworkers.[86]

Category 2. Spectroscopically Active Ligands

The next category for ligand design is the incorporation of spectroscopically active substituents within a ligand. This opens the door to new characterization techniques such as fluorescence spectroscopy. By using fluorescence, single molecule detection can be achieved.

The first set of ligands that fall under this design category are 9,10-bis((4H-1,2,4-triazol-4-yl)methyl)anthracene (**2.8**) and 1,4-bis((4H-1,2,4-triazol-4-yl)methyl)anthracene (**2.16**). Both of these ligands utilize the anthracene moiety as the spectroscopically active ligand component. In addition to the ability to bypass the need for a wider MONT, the additional aromatic rings within the anthracene moiety are hypothesized to act as external 'flags'. If the anthracene moiety is tilted 90° as compared to the xylyl group on the MONT shown in Figure 2.4A, the interactions within the bulk MONT will change. Figure 2.4A depicts the inter-tube π-π interactions from adjacent tubes. These interactions are believed to be the driving force for the MONT aggregation. Figure 2.4B depicts the intra-tube π-π interactions within the MONTs. It is hoped that this orientation will stabilize the MONT and limit greater aggregation.

Taking the knowledge gained from the synthesis of **2.5**, the next ligands were designed by rotating the anthracene moiety 90°, creating a symmetric (**2.8**, Scheme 2.3) and an asymmetric (**2.16**, Scheme 2.4) fluorescent ligand. The protons on the central aromatic ring in anthracene (position 9 and 10) are highly acidic and prone to participating in chemical reactions, anthracene was reacted with paraformaldehyde with hydrobromic acid and acetic acid to produce **2.6**, 9,10-bis(bromomethyl)anthracene by methods of Sun and coworkers.[87] This dibromide was then used in the Horváth method for synthesizing di-1,2,4-triazole ligands. This is the established method used by the Jenkins group where the propane-nitrile triazole reagent (**2.3**) was dissolved in acetonitrile with the dibromide and participated in an S_N2 reaction which formed the intermediate, **2.7**. The final di-1,2,4-triazole ligand (**2.8**) was then made by deprotecting **2.7** with potassium hydroxide.

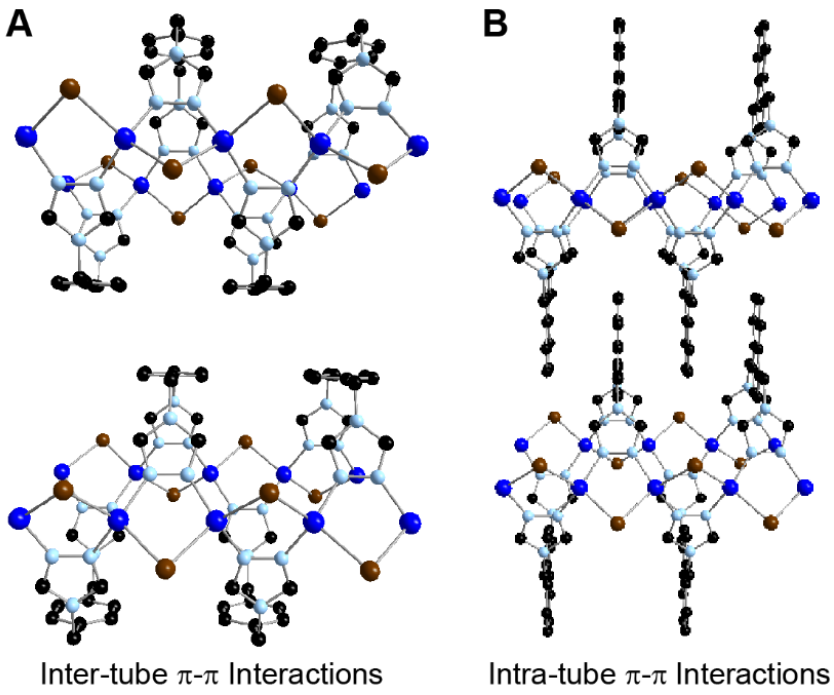

Figure 2. 4. (A) Inter-tube interactions between adjacent MONTs, and (B) intra-tube interactions within a MONT.

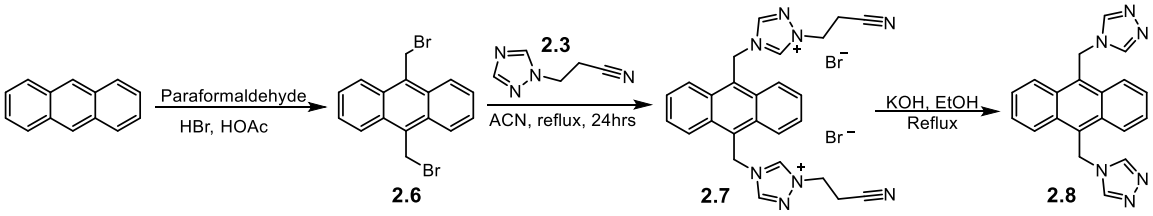

Scheme 2. 3. Synthesis of 9,10-bis((4H-1,2,4-triazol-4-yl)methyl)anthracene, 2.8.

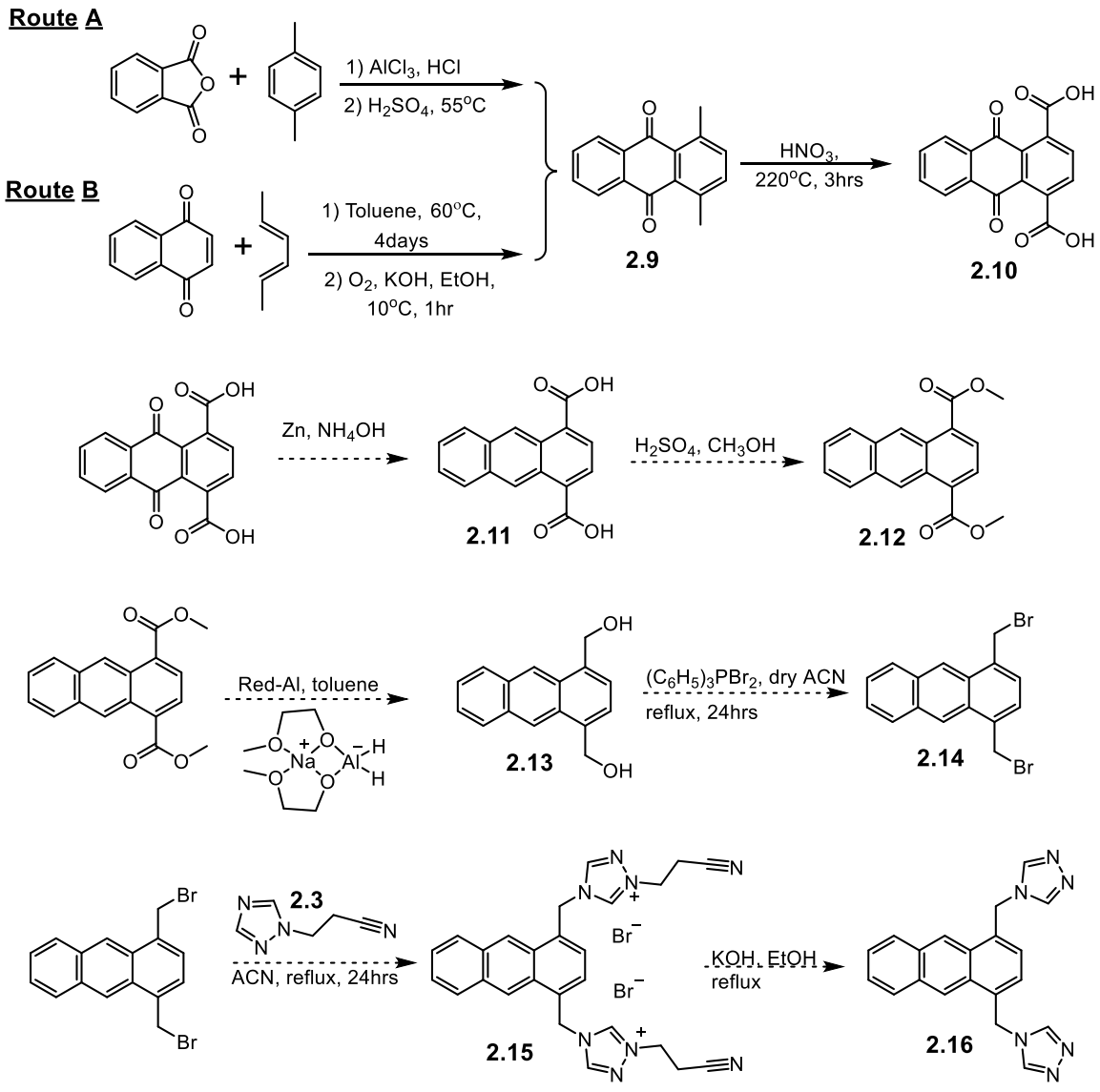

Scheme 2. 4. Synthesis of 1,4-bis((4H-1,2,4-triazol-4-yl)methyl)anthracene, 2.16.

The synthesis of the asymmetric anthracene di-1,2,4-triazole ligand, **2.16**, is much more challenging because the acidic protons on the 9 and 10 position of the anthracene moiety need to be protected. An eight-step synthesis has been proposed, as shown in Scheme 2.3. This synthesis utilizes previously published reactions to synthesize the dibromide compound **2.14** which can then be reacted through new methods to form the di-1,2,4-triazole ligand (**2.16**). First, the 1,4-dimethylanthraquinone, **2.9**, is synthesized. Two possible routes to synthesize this product were attempted and denoted as Routes A and B. Route A uses phthalic anhydride and *para*-xylene through a Friedel Crafts reaction to form **2.9**.[88] This reaction resulted in a thick dark green mixture that was difficult to purify and formed only 3% of the product. Route B was chosen because it utilized a Diels Alder reaction with naphthoquinone and 2,4-hexadiene to form the desired 1,4-dimethylanthraquinone product (**2.9**).[89] This reaction yielded 50% product and while this is still a moderate yield, there was little purification needed, making it the favored route. Next, the 1,4-dimethylanthraquinone was oxidized to form the 1,4-dicarboxylic acid anthraquinone product, **2.10**.[89] This reaction was performed in 25% nitric acid in a metal Parr bomb reactor at 190°C for 24. The next steps proposed are to reduce the quinone (**2.10**) with zinc powder and ammonium hydroxide to yield the 1,4-anthracene dicarboxylic acid (**2.11**).[90] This carboxylic acid substituent will then undergo an esterification process to form **2.12**[91] which will then be reduced to form the diol (**2.13**).[88] This 1,4-anthracene diol will then be brominated[88] to form the 1,4-bis(bromomethyl) anthracene reagent (**2.14**) needed to undergo the addition of the triazole via the Horváth method.

The next ligand that falls in the fluorescence design category is **2.21**. This ligand has the same *meta*-xylene architecture as previous ligands in the Jenkins group; however, **2.21** incorporates an alkyne functional group on the center moiety of the ligand . The alkyne functional group is an important addition because it can participate in Click chemistry which would drastically increase the capabilities of the MONT. Through click chemistry any molecule functionalized with an azide (N_3) can be added to the exterior of the nanotube. This alkyne functionalized ligand

would allow for fluorescent tags such as the pyrene tag in Scheme 2.5 to be easily added to the MONT for fluorescence analysis (Figure 2.2). This final alkyne functionalized ligand can also be blended in with a non-functionalized ligand to statistically control the amount of tags present which

The synthesis of this ligand was proposed through two routes. The first route (Scheme 2.6, Route A) synthesized the necessary dibromide reagent via previous methods of Stoddardt.[92] Initially, the starting material, 2,5-dimethylbenzaldehyde, from Stoddardt's methods was used; however, it was soon changed to 3,5-dimethylbenzaldehyde in efforts to create a symmetrical ligand. An asymmetrical ligand would create a non-uniform nanotube with alkyne functional groups protruding from the right or left side to the tube in an uncontrollable fashion. This could cause difficulty in solving the single crystal structure. 3,5-dimethylbenzaldehyde underwent a Corey Fuches reaction with carbon tetrabromide with triphenylphoshine in methylene chloride to form **2.17**, 1-(2,2-dibromovinyl)-3,5-dimethylbenzene. Compound **2.17** was then reacted with *n*-butyl lithium and trimethylsilylchloride to produce **2.18**, ((3,5-dimethylphenyl)ethynyl)trimethylsilane. At this step, the radical bromination with *n*-bromosuccinimide and aizobisisobutyronitrile in carbon tetrachloride produced a variety of products. This reaction needed to brominate both methyl groups only once; however, it is very difficult to control the degree in which bromines are added to the molecule. Two methyl groups doubled the difficulty of this synthesis. For this reason, Route B was proposed.

Route B was proposed in efforts to circumvent the need for a radical bromination of the two methyl groups. While this route (Scheme 2.7) is seven steps as opposed to the five steps in Route A, most of the reactions follow classic chemistry techniques that have been established and reproduced. Route B starts with 5-aminoisophthalic acid that undergoes a Sandmeyer reaction with concentrated hydrochloric acid, sodium nitrite and potassium iodide to produce the 5-iodoisophthalic acid (**2.22**). This compound will then be transformed into **2.23** via a Fischer esterification process with concentrated sulfuric acid and methanol.

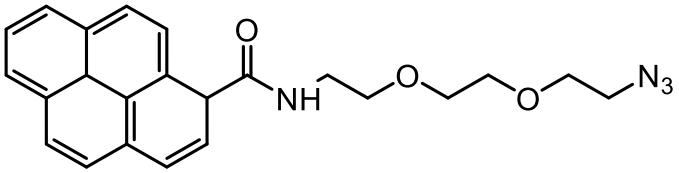

Scheme 2. 5. Azide functionalized pyrene tag for Click chemistry.

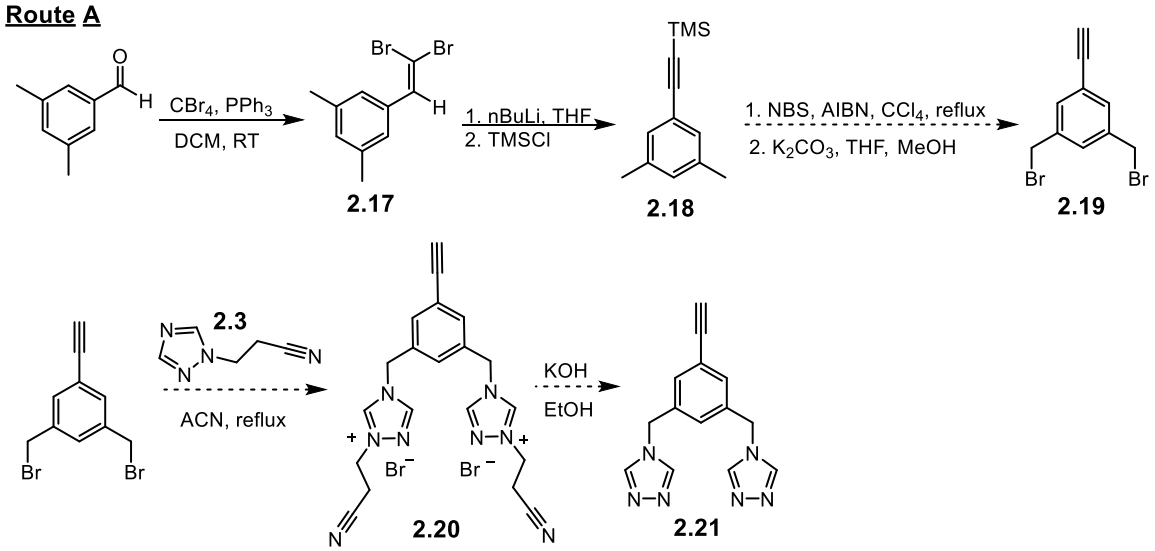

Scheme 2. 6. Synthetic route A for 4,4'-((5-ethynyl-1,3-phenylene)bis (methylene))bis(4H-1,2,4-triazole), 2.21.

Route B

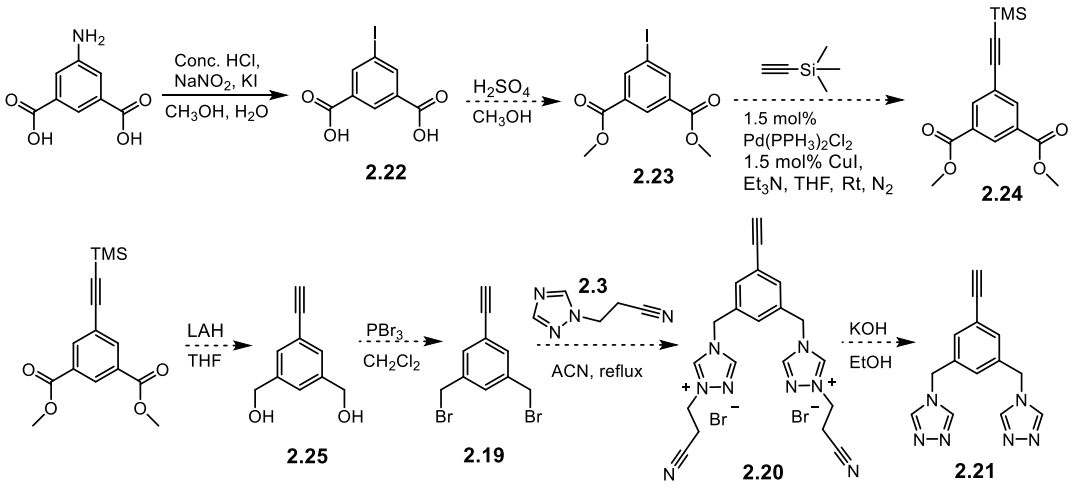

Scheme 2. 7. Synthetic route B for 4,4'-((5-ethynyl-1,3-phenylene)bis (methylene))bis(4H-1,2,4-triazole), 2.21.

Once the ester has been formed, a Sonogashira coupling reaction with trimethylsilylacetylene and **2.23** can be utilized to form **2.24**, dimethyl 5-((trimethylsilyl)ethynyl)isophthalate. The next step is to use lithium aluminum hydride to reduce the ester and deprotect the alkyne functional group to form **2.25**. The diol (**2.25**) is then brominated with phosphorus tribromide to create **2.19**. Finally, the dibromide compound undergoes an S_N2 reaction and deprotection to add the final di-1,2,4-triazole to the ligand.

Category 3. Ligands for Reduced MONT Aggregation

The third ligand design category is aimed towards inhibiting the aggregation of metal-organic nanotubes. As discussed in Chapter 1, a silver-based metal-organic nanotube, $[Ag_2$(4,4′-(1,4-(xylene)diyl)bis(1,2,4-triazole) $(NO_3)_2]\cdot$NMP, was previously studied through small-angle X-ray scattering (SAXS) and the growth mechanism was evaluated (Figure 1.3). The MONT was determined to form through an initial aggregation of preliminary metal and ligand structures, then after this aggregation, anisotropic nanotubes grew. The desired MONT growth mechanism would be the reverse of this observed mechanism where the nanotube growth occurs first, and then aggregates to form bulk crystals. This would infer that it would be possible to stop the MONT reaction prior to the nanotube aggregation so that a discrete MONT could be isolated.

With the goal of synthesizing a discrete MONT in mind, the conclusions from the SAXS analysis were used to design a new ligand. The MONT grew as initial aggregates of the metal salt and organic ligand aggregated together, indicating that ligand **2.30** which incorporates a large bulky group on the center of the ligand may be able to mitigate the aggregation and favor the formation of nanotubes. The synthesis of ligand **2.30** follows a similar path as the previously detailed ligands (Scheme 2.8).[93] The 5-tertbutylisophthalic acid first underwent a Fischer esterification process to form **2.26** which was then reduced with lithium aluminum hydride to form the diol, **2.27**. This diol was brominated with phosphorus tribromide

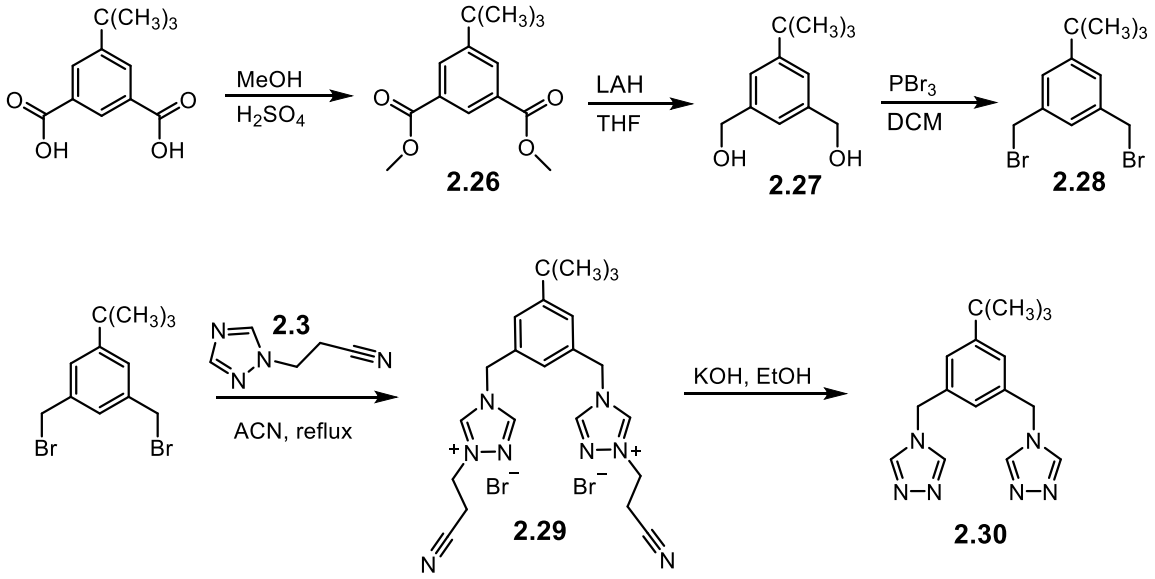

Scheme 2. 8. Synthesis of 4,4'-((5-(tert-butyl)-1,3-phenylene)bis(methylene)) bis(4H-1,2,4-triazole), **2.30**.

to form **2.28**. The last two steps follow the method of Horváth where the di-1,2,4-triazole was added through an S_N2 and deprotection reactions to form the final ligand **2.30**.

Category 4. Ligands for a Set of Isostructural MONTs

Lastly, creating a large library of isostructural MONTs is important because this gives more information about the material as a whole. Not all MOFs have the same characteristics, so it is not a surprise that that is the same for MONTs. A larger MONT library will enable researchers to study more than pore size. Trends in the material as a whole can be made which can further help develop MONTs as a useful material.

An important problem that needs to be addressed is the robustness of metal-organic nanotubes. As synthesized, MONTs can be stored in ambient conditions; however, when characterized, especially with high energy sources such as electron microscopes, MONTs have shown to decompose before full characterization is obtained. Therefore, by synthesizing isostructural MONTs, MONTs can be tuned for additional stability.

As previously discussed in this chapter, Figure 2.1 A illustrates the schematic of a 2-Column Pillar MONT. The ‘capping anion’ (Figure 2.1A, purple cube) on both sides of the metal-organic nanotube is essential to the formation of a one-dimensional structure. This anion allows for charge neutrality within the MONT as well as blocks the framework from propagating in a second dimension to form a two-dimensional MOF with a structure similar to fused nanotubes. This effect has been shown in previous Jenkins group papers.[94] However, the capping anion bonds are weak metal-ligand coordination bonds. To make a MONT that is stable, the general schematic for a 2-Column Pillar MONT can be changed slightly so that there is no need for a capping anion. To do so, an anionic ligand must be synthesized so that when reacted with a divalent metal, a neutral MONT is formed.

Neutral MONTs are hypothesized to be more stable under high energy characterization methods.

From this requirement, ligand **2.33** was proposed. This ligand incorporates charged borate species that are ideal for an anionic ligand. In addition to the benefit of creating charge neutrality, this ligand will also increase the width of the MONT for even greater ability of direct measurements. Scheme 2.9 depicts the four-step process to synthesize the diborate ligand.[95] The propane-nitrile triazole reagent is first reacted with 2-(bromomethyl)-2-(hydroxymethyl)propane-1,3-diol to form **2.31**. The triazole was then deprotected with potassium hydroxide to form **2.32**. Future steps would include the condensation reaction of **2.32** with 1,4-benzenediboronic acid to form the anionic diborate ligand **2.33**.

Another set of similar ligands that can be synthesized following the ligands that have been previously synthesized in the Jenkins group from Figure 1.6 can be seen in Schemes 2.10 and 2.11. The location of the triazole off the central substituent was changed to the 1, 8 and the 2, 7 positions in an effort to synthesize **2.35**, and **2.37** respectively. The starting dibromide materials for both of these ligands was commercially available, therefore, the previously described two-step procedure for adding the triazole by Horváth was followed.

Conclusion

In conclusion, a variety of *syn*-confirmation di-triazole ligands have been proposed and synthesized for the future utilization in MONT synthesis. Each ligand was designed to achieve the overall goal of synthesizing a singular discrete metal-organic nanotube. For this to be achieved, multiple synthetic routes were taken including; the synthesis of ligands that will form large pore MONTs, the synthesis of fluorescent ligands, aggregation blocking ligands, ligands that will form strong MONTs, and ligands to build an expanded library of isostructural MONTs. The completed ligands synthesized in this chapter will be discussed in the MONT syntheses in Chapter 3.

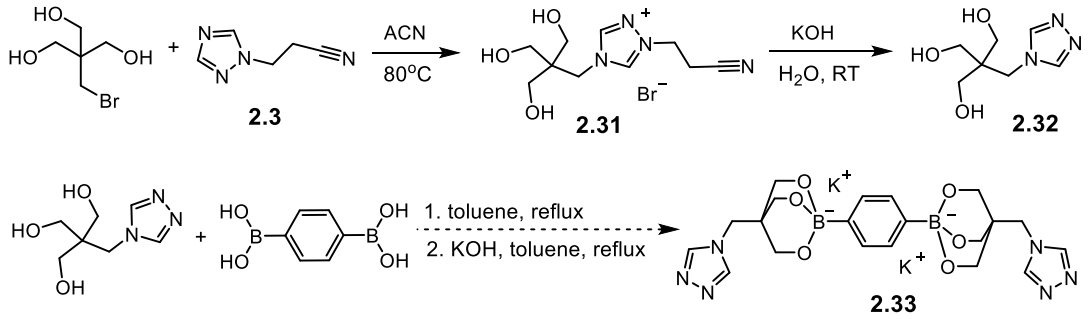

Scheme 2. 9. Synthesis of potassium 1,1'-(1,4-phenylene)bis(4-((4H-1,2,4-triazol-4-yl)methyl)-2,6,7-trioxa-1-borabicyclo[2.2.2]octan-1-uide), 2.33.

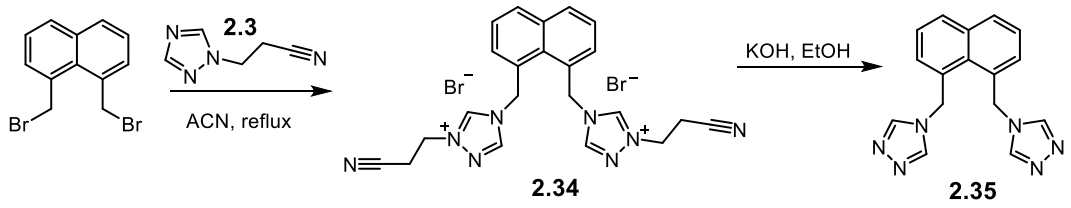

Scheme 2. 10. Synthesis of 1,8-bis((4H-1,2,4-triazol-4-yl)methyl)naphthalene, 2.35.

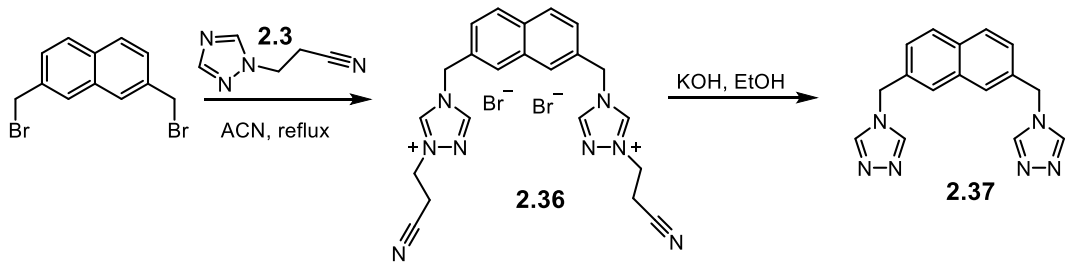

Scheme 2. 11. Synthesis of 2,7-bis((4H-1,2,4-triazol-4-yl)methyl)naphthalene, 2.37.

Experimental

I. General Considerations for Synthesis

Starting material benzyl alcohol was purchased from Fischer Scientific. Starting materials 5-aminoisophthalic acid, anthracene, *p*-xylene, and 5-(*tert-butyl*)isophthalic acid were purchased from Sigma Aldrich. Phthalic anhydride and 3,5-dimethylbenzalhehyde were purchased from Acros, and 1,4-naphthoquinone, and 2,4-hexadiene were purchased from Alfa Aesar. All purchased chemicals were used with no additional purification.

Compounds **2.1,**[96] **2.2,**[87] **2.3,**[97] **2.6**,[87] **2.9**,[88-89] **2.10**,[89] **2.22**,[98] **2.26**- **2.27**,[93] and **2.28**[99] were synthesized according to previous literature procedures. Future experiments will include synthesizing compounds **2.11**,[90] **2.12**,[91] **2.13**-**2.14,**[88] **2.19** and **2.23**-**2.25**[92, 98, 100] by previous literature procedures.

Tetrahydrofuran and methylene chloride were dried on an Innovative Technologies (Newburyport, MA) Pure Solv MD-7 solvent purification system and degassed by three freeze-pump-thaw cycles, on a Schlenk line, to remove O_2 prior.

Synthesis of 2,7-dimethylanthracene, 2.1:

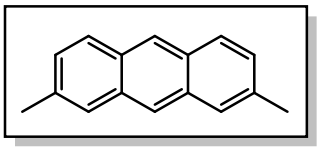

The synthesis of **2.1** was achieved by following the literature procedure by Gong and coworkers.[96] Additional purification was achieved to separate the *syn* and *anti*-dimethylanthracene products. The crude solid was dissolved in minimal chloroform and layered with acetonitrile to crystallize the *syn* product (2,7-dimethylanthracene). Spectra matches literature.

Synthesis of 4,4'-(anthracene-9,10-diylbis(methylene))bis(1-(2-cyanoethyl)-1H-1,2,4-triazol-4-ium) bromide, 2.7:

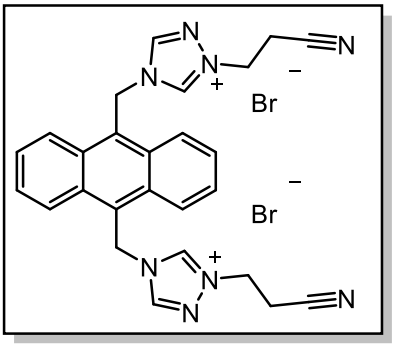

1,4-bis(bromomethyl)naphthalene (0.1014 g, $2.785*10^{-4}$ mol), **2.6**, was dissolved in 10 mL of acetonitrile with 3-(1H-1,2,4-triazol-1-yl)propanenitrile (0.1335 g, $1.0931*10^{-3}$ mmol), **5**, in a 25 mL round bottom flask and refluxed for 3 days. The reaction mixture was cooled to room temperature. Diethyl ether was added to precipitate product, which was then filtered through a fine frit, yielding a pale yellow solid (0.1064 g, 85.2 %).

^{1}H NMR (DMSO-d_6, 499.74 MHz): 10.03 (s, 2H), 9.14 (s, 2H), 8.61 (d, 4H), 7.78 (d, 4H), 6.69 (s, 4H), 4.64 (t, 4H), 3.16 (t, 4H). ^{13}C NMR (DMSO-d_6, 125.66 MHz): 144.73, 143.14, 130.70, 127.87, 125.85, 124.60, 117.58, 47.11, 44.14, 17.30. IR: 3086, 3025, 2919, 2254, 1942, 1704, 1675, 1604, 1508, 1495, 1459, 1419, 1379, 1350, 1275, 1178, 1138, 1041, 1003, 957, 921, 882, 727, 694, 660, 647 cm^{-1}.

Synthesis of 9,10-bis((4H-1,2,4-triazol-4-yl)methyl)anthracene, 2.8:

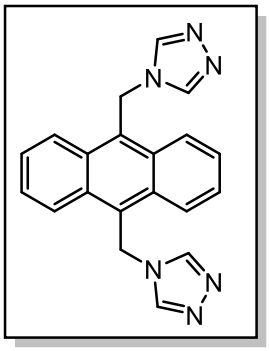

A slurry of **2.8** (0.2690 g, $5.9974*10^{-4}$ mol) and potassium hydroxide (0.1238 g, $2.206*10^{-3}$ mol) was refluxed overnight in 55 mL of ethanol.

This yielded a yellow solid that was collected on a fine frit and washed with THF (0.0159 g, 7.79 %).

^{1}H NMR (DMSO-d_6, 499.74 MHz): 8.60 (d, 4H), 7.70 (s, 4H), 6.38 (d, 4H), 4.34 (d, 2H). ^{13}C NMR (DMSO-d_6, 125.66 MHz): 206.42, 142.75, 130.11, 124.66, 30.69. IR: 3289, 2962, 2924, 2854, 2246, 1954, 1723, 1665, 1599, 1555, 1528, 1447, 1376, 1352, 1318, 1258, 1172, 1159, 1057, 1019, 931, 842, 797, ,767, 723, 694, 676, 637 cm^{-1}.

Synthesis of 9,10-dioxo-9,10-dihydroanthracene-1,4-dicarboxylic acid, 2.10:

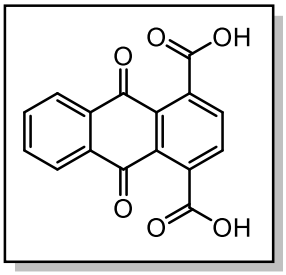

The synthesis of **2.10** was achieved through a modified procedure of Morris and coworkers.[89] A slurry of the dimethyl quinone (**2.9**) (0.8717 g, 3.689*10^{-3} mol) in 12 mL of 25 % nitric acid was placed into a 45 mL PTFE lined autoclave vessel. This vessel was placed into an oven at room temperature. The oven was then heated to 190 °C for 24 hours. After 24 hours, the oven was turned off and allowed to cool to room temperature for an additional 24 hours. The autoclave was then opened, and the resulting slurry was washed with copious amounts of water to produce a bright yellow solid (0.5908 g, 54 %) The spectra matches literature values.

Translated Synthesis of anthracene-1,4-dicarboxylic acid, 2.11:

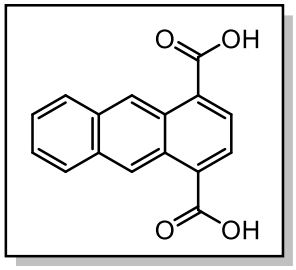

The original synthesis was translated to English from German for future use.[90] An aqueous ammonia solution (1:1), 5g quinone, and 30g zinc dust were mixed together at room temperature. Solution was boiled until the red color turned green/yellow. Reaction mixture was filtered over a hot frit. Residue was washed with hot ammonia solution. Concentrated HCl was added to the liquid resulting in a brown precipitate (crude product). The brown solid was purified by recrystallization with acetic acid.

Translated Synthesis of dimethyl anthracene-1,4-dicarboxylate, 2.12:

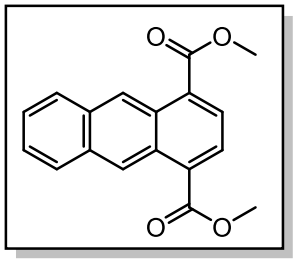

The original synthesis was translated to English from German for future use.[91] Anthracene-1,4-dicarboxylic acid (**2.11**) (25g), 25mL of methanol, and 50 mL of H_2SO_4 were mixed together and refluxed for 4 hours. Reaction was then cooled, and potassium carbonate was added. Solvent was removed. 51% yield.

Synthesis of 1-(2,2-dibromovinyl)-3,5-dimethylbenzene, 2.17:

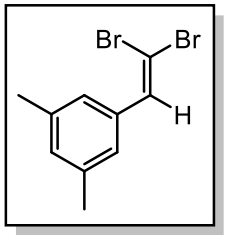

Compound **2.17** was synthesized by a modified procedure of Stoddart and coworkers[92] with the 3,5-dimethylbenzaldehyde starting material. In the glovebox, carbon tetrabromide (0.7739 g, $2.3336*10^{-3}$ mol) and triphenylphosphine (1.1750 g, $4.4798*10^{-3}$ mol) were each dissolved in 5 mL of methylene chloride and mixed together and stirred for 30 minutes. 3,5-dimethylbenzaldehyde was added dropwise to the reaction mixture and allowed to stir at room temperature for 6 hours. Reaction mixture was filtered with a fine frit to afford pure product **2.17**. Spectra matches literature.[101]

Synthesis of ((3,5-dimethylphenyl)ethynyl)trimethylsilane, 2.18:

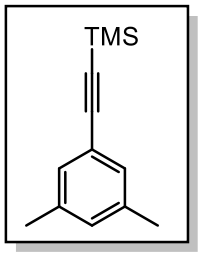

Compound **2.18** was synthesized by a modified procedure of Stoddart and coworkers[92] with the 1-(2,2-dibromovinyl)-3,5-dimethylbenzene (**2.17**) starting material. Spectra matches literature.[102]

Synthesis of 1-(2-cyanoethyl)-4-(3-hydroxy-2,2-bis(hydroxymethyl)propyl)-4H-1,2,4-triazol-1-ium bromide, 2.31:

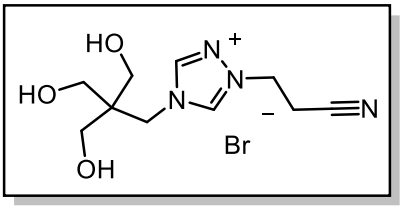

In a glovebox under nitrogen atmosphere, 2-(bromomethyl)-2-(hydroxymethyl)propane-1,3-diol (1.0942 g, 5.497 mmol) was measured into a round bottom flask and dissolved into 15 mL of acetonitrile. This round bottom flask was taken out of the glovebox and attached to a reflux condenser with nitrogen flowing. Compound **2.3** (1.3314 g, 10.90 mmol) was dissolved in an additional 15 mL of acetonitrile and added to the reaction flask. The reaction was refluxed under nitrogen atmosphere overnight to produce a pale-yellow oil.

^{1}H NMR (CD_3CN, 499.74 MHz): 8.28 (s, 1H), 7.94 (s, 1H), 4.43 (t, 3H), 3.54 (s, 2H), 3.53 (s, 4H), 3.13 (s, 2H), 2.98 (t, 2H).^{13}C NMR (CD_3CN, 125.66 MHz): 153.46, 145.07, 118.46, 63.26, 45.88, 45.67, 36.74, 19.47.

Synthesis of 4,4'-((5-(tert-butyl)-1,3-phenylene)bis(methylene))bis(1-(2-cyanoethyl)-4H-1,2,4-triazol-1-ium) bromide, 2.29:

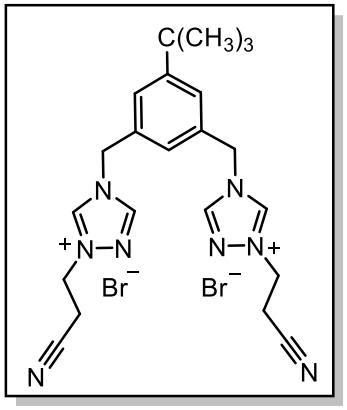

Compound (**2.28**) (0.0643 g, $2.009*10^{-4}$ mol), was dissolved in 6 mL of acetonitrile with 3-(1H-1,2,4-triazol-1-yl)propanenitrile (0.0590 g, $4.831*10^{-4}$ mmol), in a 25 mL round bottom flask and refluxed for 3 days. The

reaction mixture was cooled to room temperature. Diethyl ether was added to precipitate product, which was then filtered through a fine frit, yielding a white solid (0.0218 g, 26.8%).

^{1}H NMR (DMSO-d_6, 499.74 MHz): 10.33 (s, 2H), 9.41 (s, 2H), 7.60 (s, 2H), 7.42 (s, 1H), 5.56 (s, 4H), 4,74 (t, 4H), 1.29 (s, 9H). ^{13}C NMR (DMSO-d_6, 125.66 MHz): 152.81, 144.97, 143.35, 133.92, 126.92, 126.52, 117.68, 50.52, 47.28, 34.76, 30.96, 17.39.

Synthesis of 4,4'-((5-(tert-butyl)-1,3-phenylene)bis(methylene))bis(4H-1,2,4-triazole), 2.30:

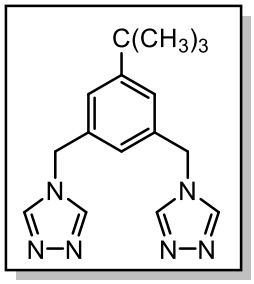

A slurry of **2.29** (0.0301 g, $7.441*10^{-4}$ mol) and potassium hydroxide (0.0129 g, $2.299*10^{-4}$ mol) was stirred at room temperature overnight in 6 mL of DI H_2O. This yielded a white solid that was collected on a fine frit.

^{1}H NMR (DMSO-d_6, 499.74 MHz): 8.62 (s, 4H), 7.33 (s, 2H), 7.07 (s, 1H), 5.25 (s, 4H), 4.43 (t, 4H), 1.23 (s, 9H). ^{13}C NMR (DMSO-d_6, 125.66 MHz): 151.16, 142.29, 136.12, 123.59, 55.01, 46.62, 33.56, 30.02, 17.61.

Synthesis of 4,4'-(naphthalene-1,8-diylbis(methylene))bis(1-(2-cyanoethyl)-4H-1,2,4-triazol-1-ium) bromide, 2.34:

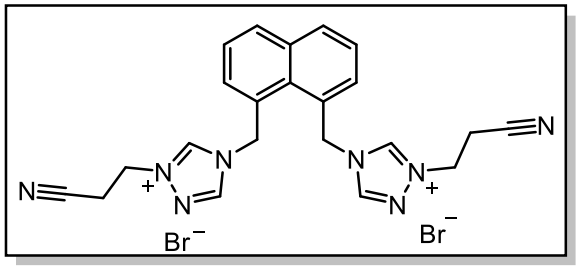

Compound **2.3** (0.1162 g, 0.9514 mmol) was dissolved in 4 mL of acetonitrile with 1,8-bis(bromomethyl)naphthalene (0.1213 g, 0.3863 mmol) and refluxed for 24 hours. Reaction mixture was cooled to room temperature. Ether was added to the flask to help precipitate the product which was then filtered through a fine frit to produce a white solid product (0.1491 g, 69.1 %).

^{1}H NMR (DMSO-d_6, 499.74 MHz): 10.36 (s, 2H), 9.47 (s, 2H), 8.07 (s, 2H), 8.05 (d, 2H), 7.68 (d, 2H), 5.78 (s, 4H), 4.47 (t, 4H), 3.24 (t, 4H)**.** ^{13}C NMR (DMSO-d_6, 125.66 MHz): 145.20, 143.69, 135.44, 131.50, 130.42, 129.15, 128.30, 125.93, 117.77, 51.56, 47.35, 30.70, 17.35, 1.18

Synthesis of 1,8-bis((4H-1,2,4-triazol-4-yl)methyl)naphthalene, 2.35:

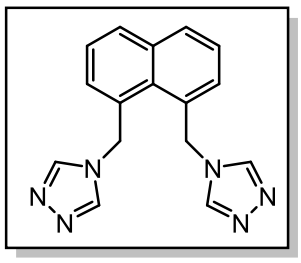

A slurry of **2.34** (0.1043 g, 0.1868 mmol) and potassium hydroxide (27 mg, 0.4812 mmol) was refluxed overnight in 5 mL of ethanol. This yielded a white solid that was collected on a fine frit.

^{1}H NMR (DMSO-d_6, 499.74 MHz): 8.56 (s, 4H), 7.99 (d, 2H), 7.49 (t, 2H), 6.81 (d, 2H), 6.00 (s, 4H).

Synthesis of 4,4'-(naphthalene-2,7-diylbis(methylene))bis(1-(2-cyanoethyl)-4H-1,2,4-triazol-1-ium) bromide, 2.36:

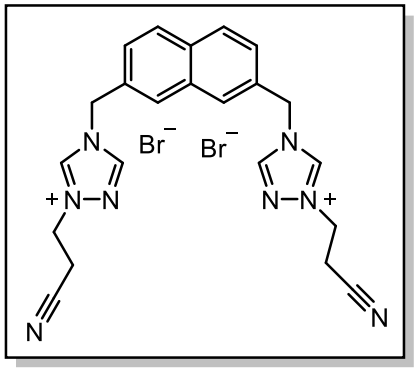

Compound **2.3** (0.7025 g, 5.752 mmol) was dissolved in 70 mL of acetonitrile with 2,7-bis(bromomethyl)naphthalene (0.4100 g, 1.3056 mmol) and refluxed for 48 hours. Reaction mixture was cooled to room temperature. Ether was added to the flask to help precipitate the product which was then filtered through a fine frit to produce a white solid product (0.7205 g, 98 %).

^{1}H NMR (DMSO-d_6, 499.74 MHz): 10.36 (s, 2H), 9.47 (s, 2H), 8.07 (s, 4H), 7.66 (d, 2H), 5.78 (s, 4H), 4.74 (t, 4H), 3.24 (t, 4H)

II. X-ray Structure Determinations

Crystals of **2.6** were recrystallized in warm toluene overnight. A yellow needle crystal was mounted in the 100 K cold stream provided by an Oxford Cryostream low-temperature apparatus on the head of a Bruker D8 diffractometer equipped with a PHOTON 2 CMOS detector, at beamline 12.2.1 of the Advanced Light Source (Lawrence Berkeley National Laboratory, Berkeley, CA). Data were collected with the use of synchrotron radiation (λ = 0.7288 Å).

Crystals of **2.34** were recrystallized in warm toluene overnight. A colorless plate crystal was mounted in the 100 K cold stream provided by an Oxford Cryostream low-temperature apparatus on the head of a Bruker D8 Venture diffractometer equipped with an APEXIII CCD detector, employing the use of Mo K*α* radiation (λ = 0.71073 Å).

All data sets were reduced with Bruker SAINT and were corrected for absorption using SADABS. Structures were solved and refined using SHELXT and SHELXL-2015, respectively.

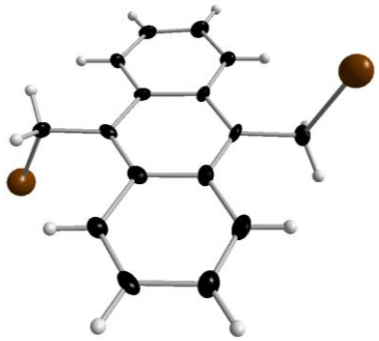

Figure 2. 5. Single Crystal X-ray structure of 2.6 collected on the ALS by Dr. Xian Powers. Black, white, and brown ellipsoids (50% probability) represent carbon, hydrogen, and bromine atoms respectively.

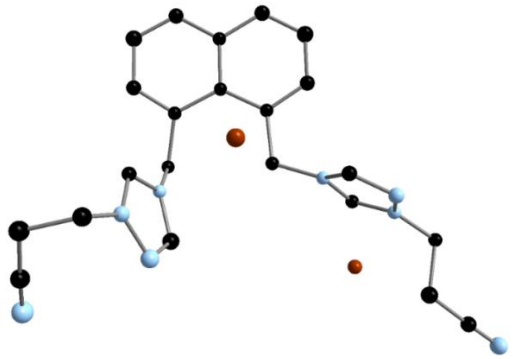

Figure 2. 6. Single Crystal X-ray structure of 2.34. Black, light blue, and brown ellipsoids (50% probability) represent carbon, nitrogen, and bromine atoms respectively. Hydrogen atoms have been omitted for clarity.

III. Selected Spectra and Analytical Data for 2.7-2.36

The corresponding spectra and analytical data for compounds **2.7**, **2.8**, **2.29**, **2.30**, **2.31**, **2.34**, **2.35**, and **2.36** are presented in this section.

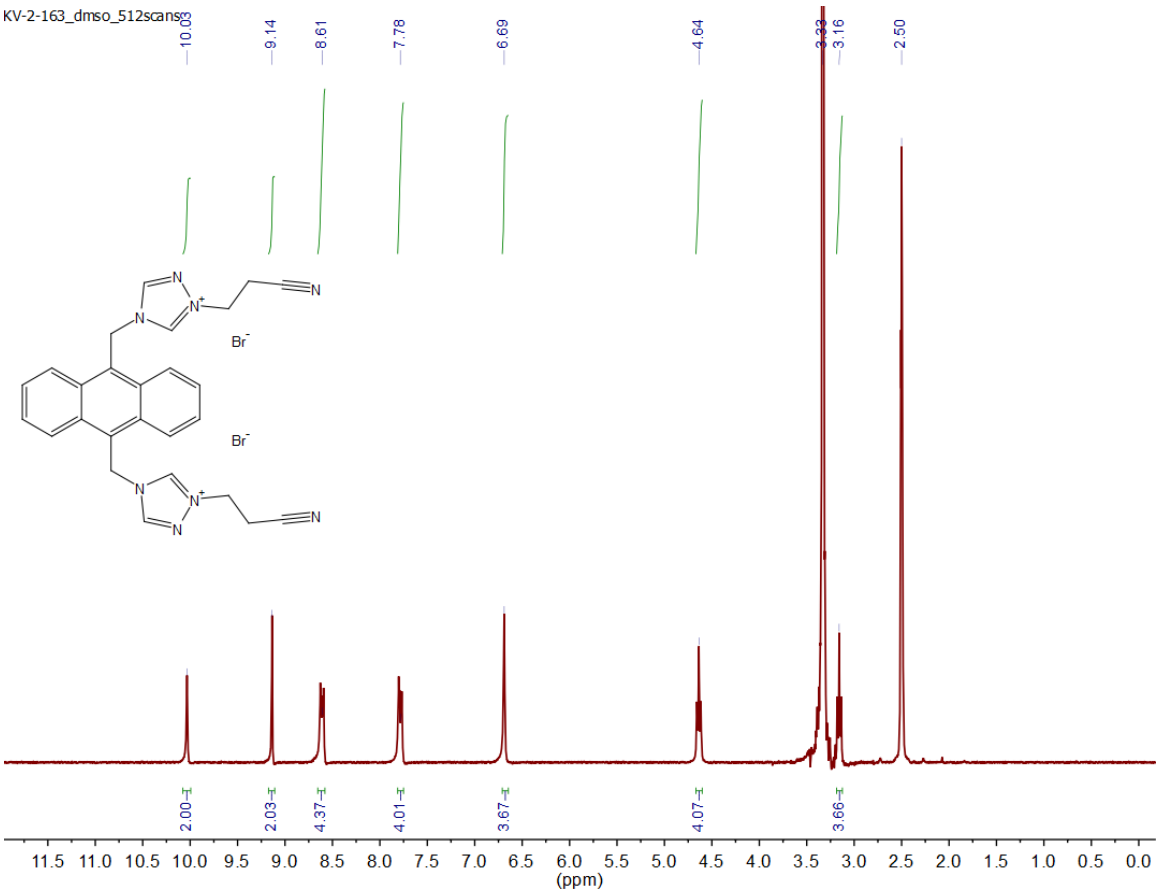

Spectra 2. 1. ^{1}H-NMR of 2.7 in DMSO-d_6.

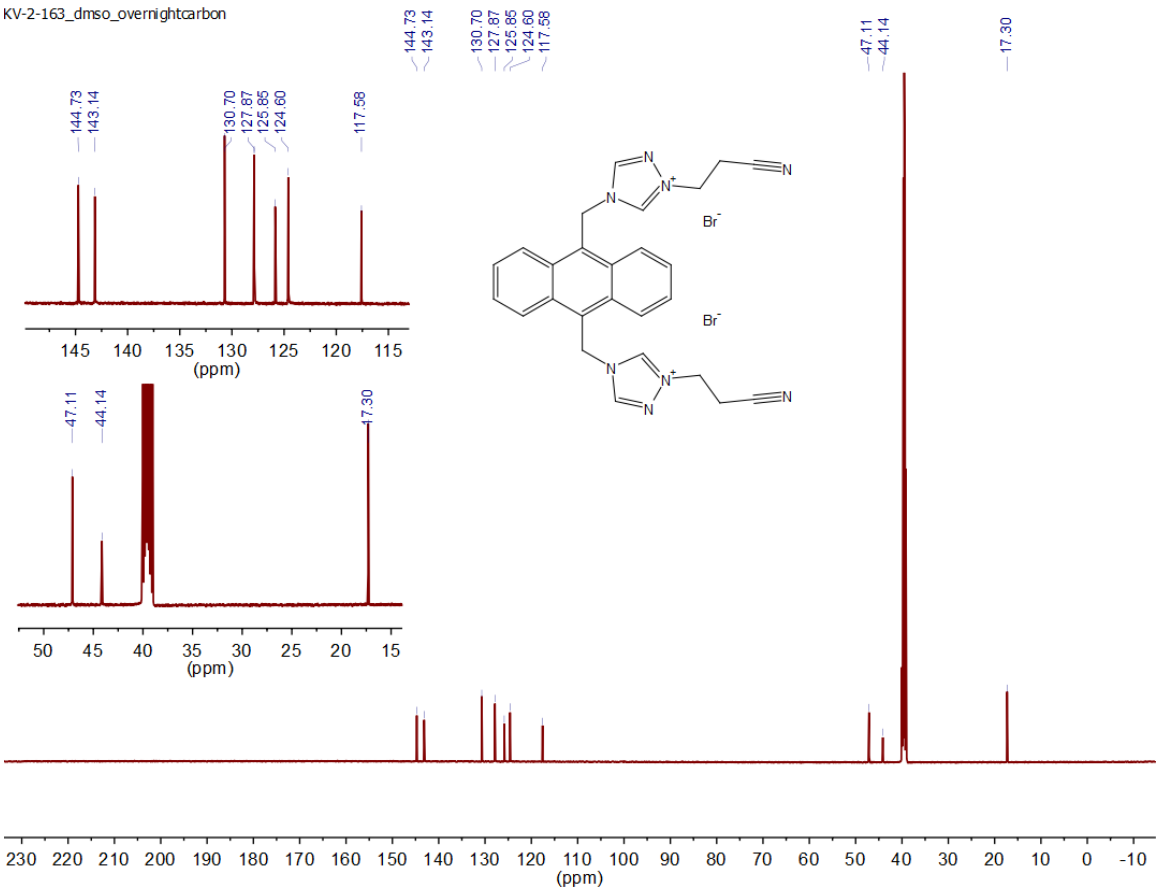

Spectra 2. 2. ^{13}C-NMR of 2.7 in DMSO-d$_6$.

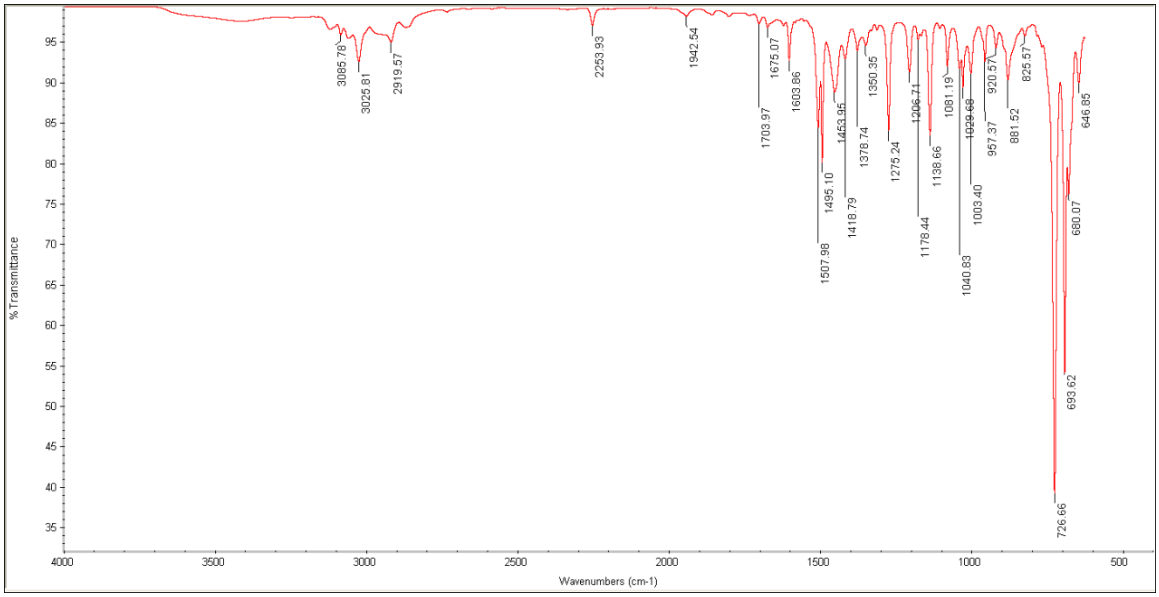

Spectra 2. 3. ATR-IR of 2.7.

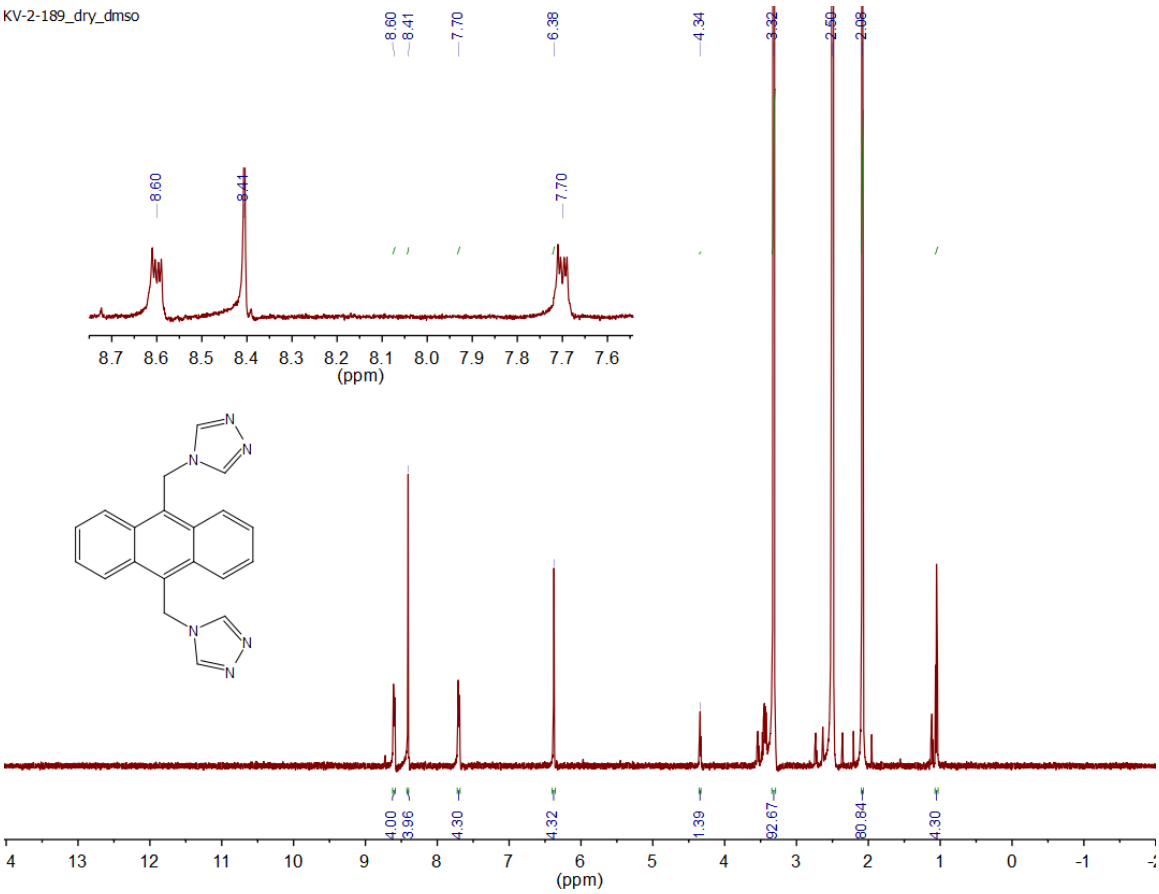

Spectra 2. 4. ^{1}H-NMR of 2.8 in DMSO-d_6.

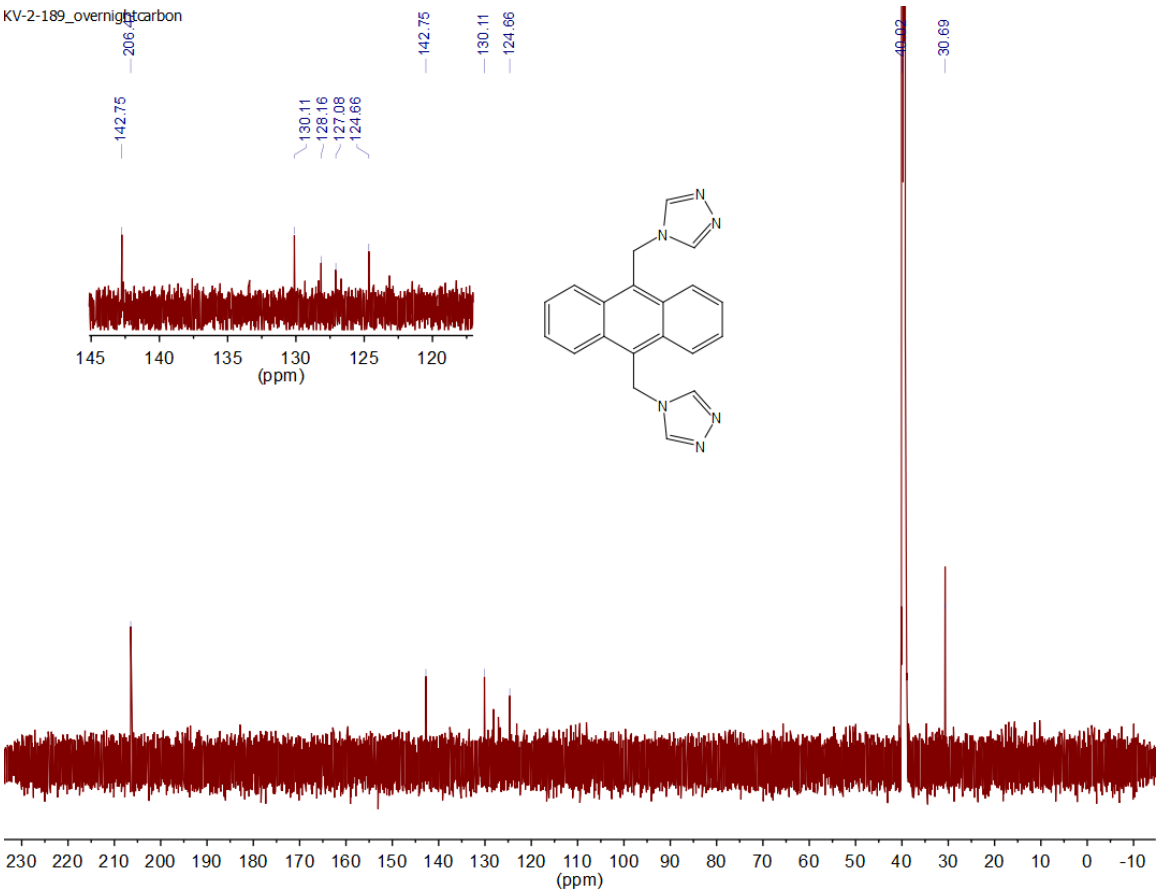

Spectra 2. 5. ^{13}C-NMR of 2.8 in DMSO-d_6.

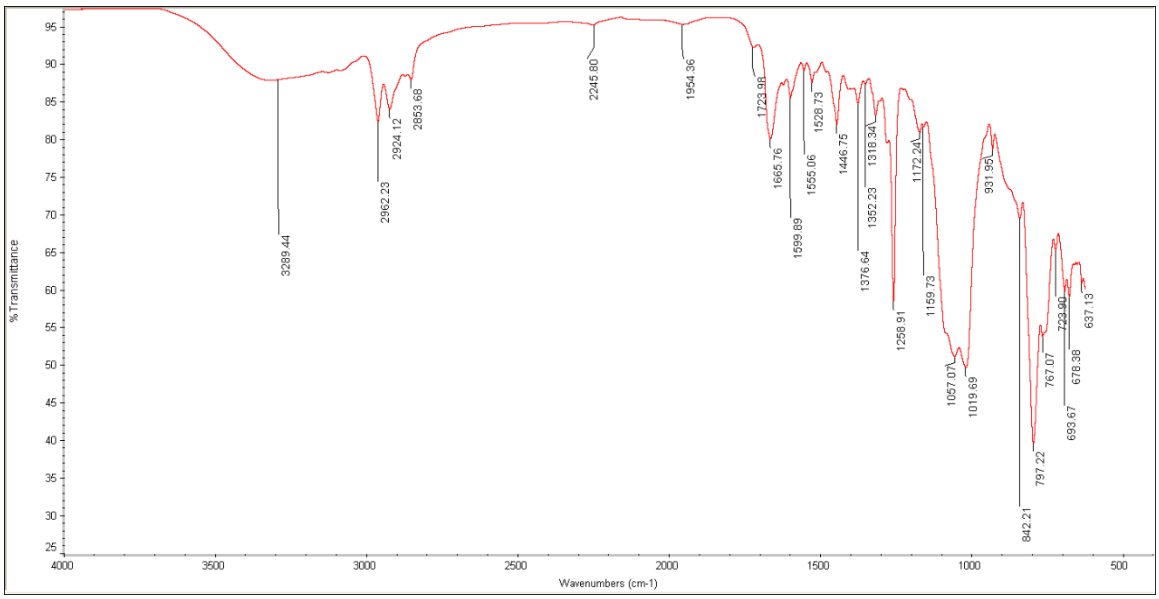

Spectra 2. 6. ATR-IR of 2.8.

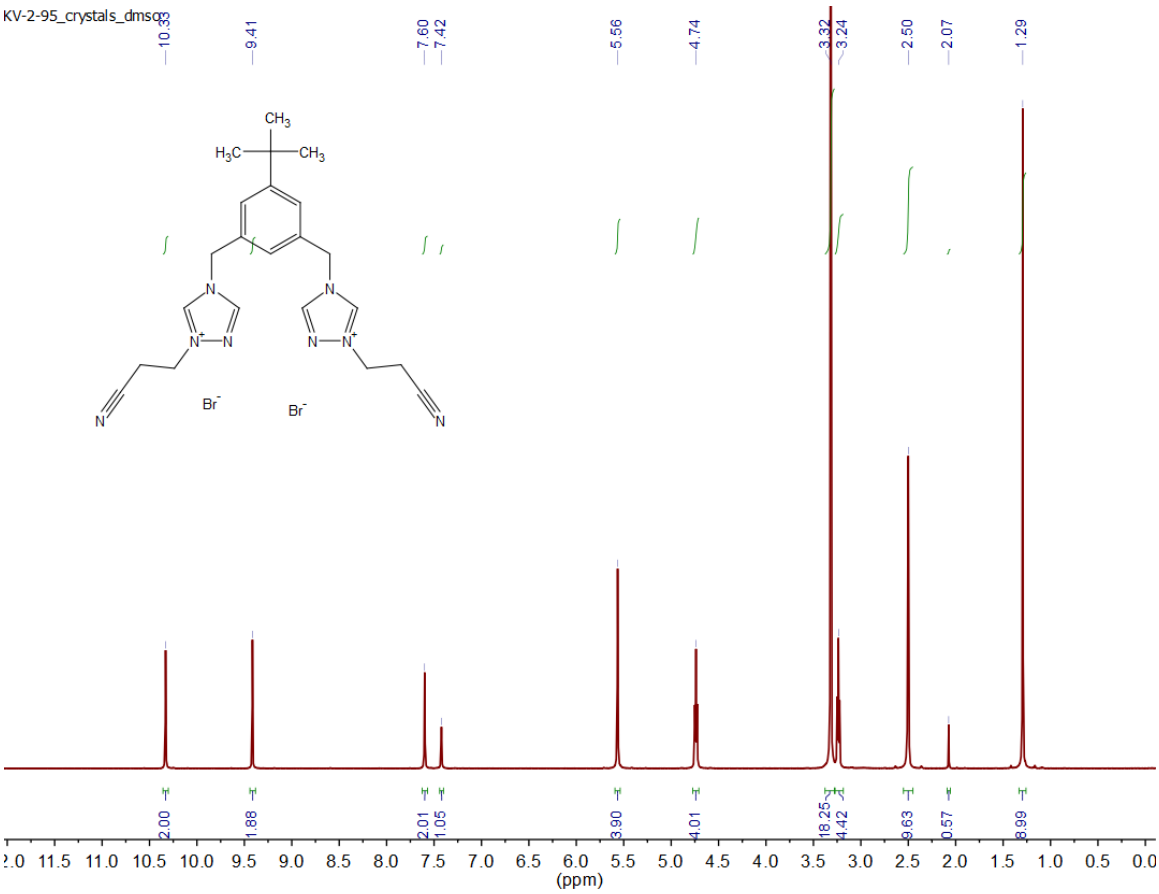

Spectra 2. 7. 1H-NMR of 2.29 in DMSO-d_6.

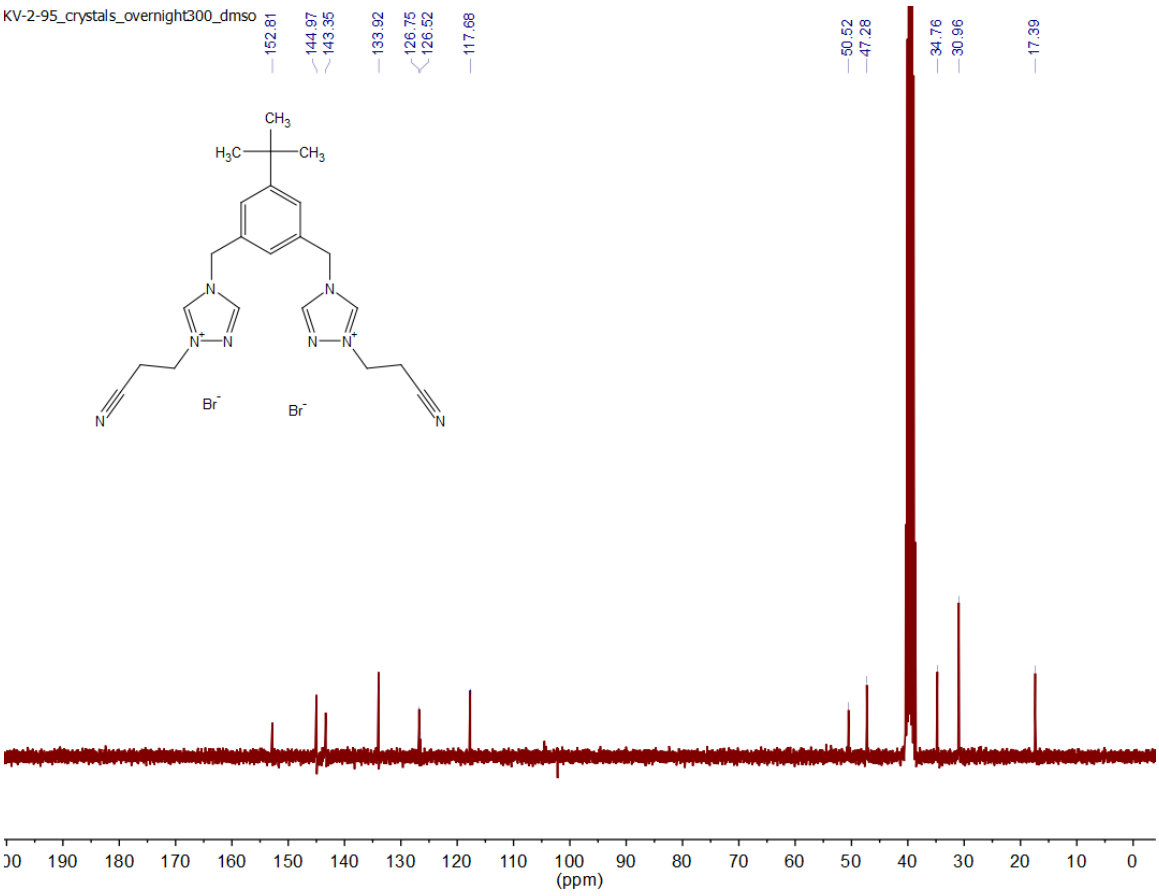

Spectra 2. 8. ^{13}C-NMR of 2.29 in DMSO-d$_6$.

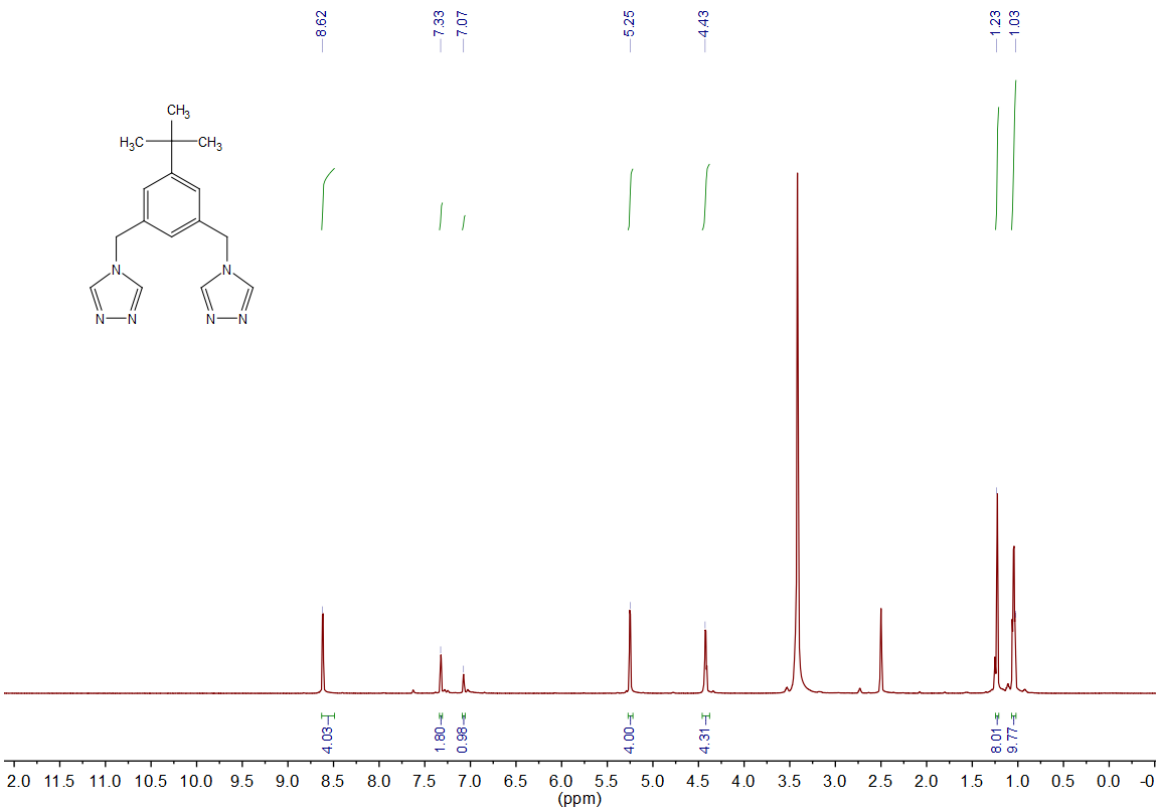

Spectra 2. 9. ^{1}H-NMR of 2.30 in DMSO-d_6.

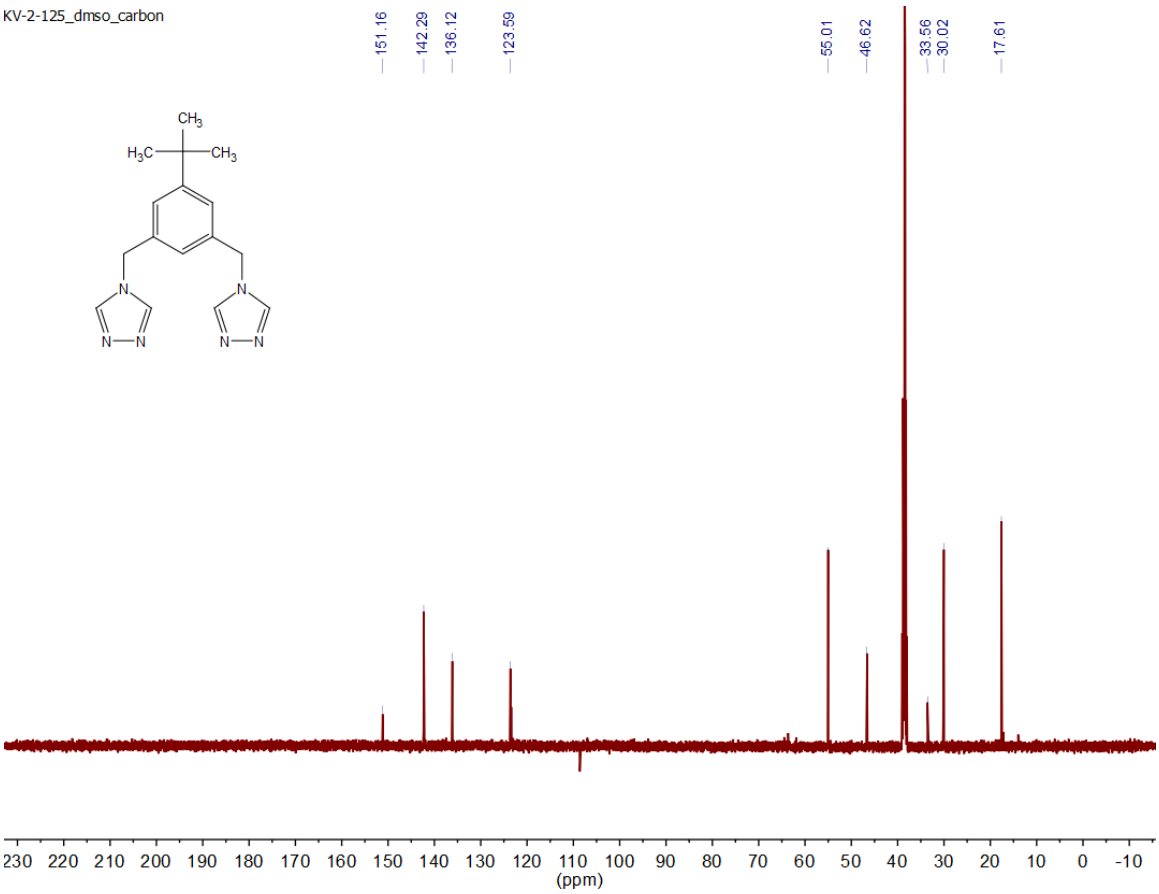

Spectra 2. 10. ^{13}C-NMR of 2.30 in DMSO-d$_6$.

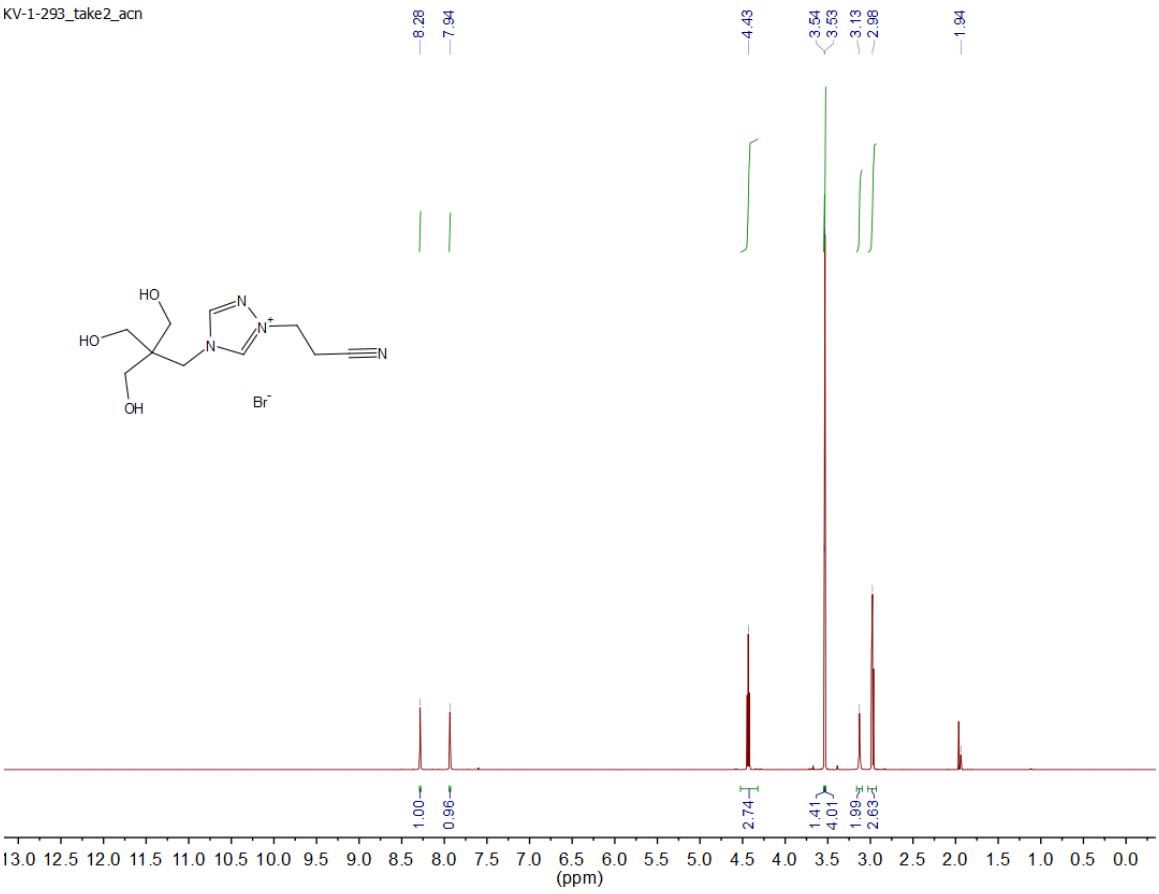

Spectra 2. 11. ^{1}H-NMR of 2.31 in CD_3CN.

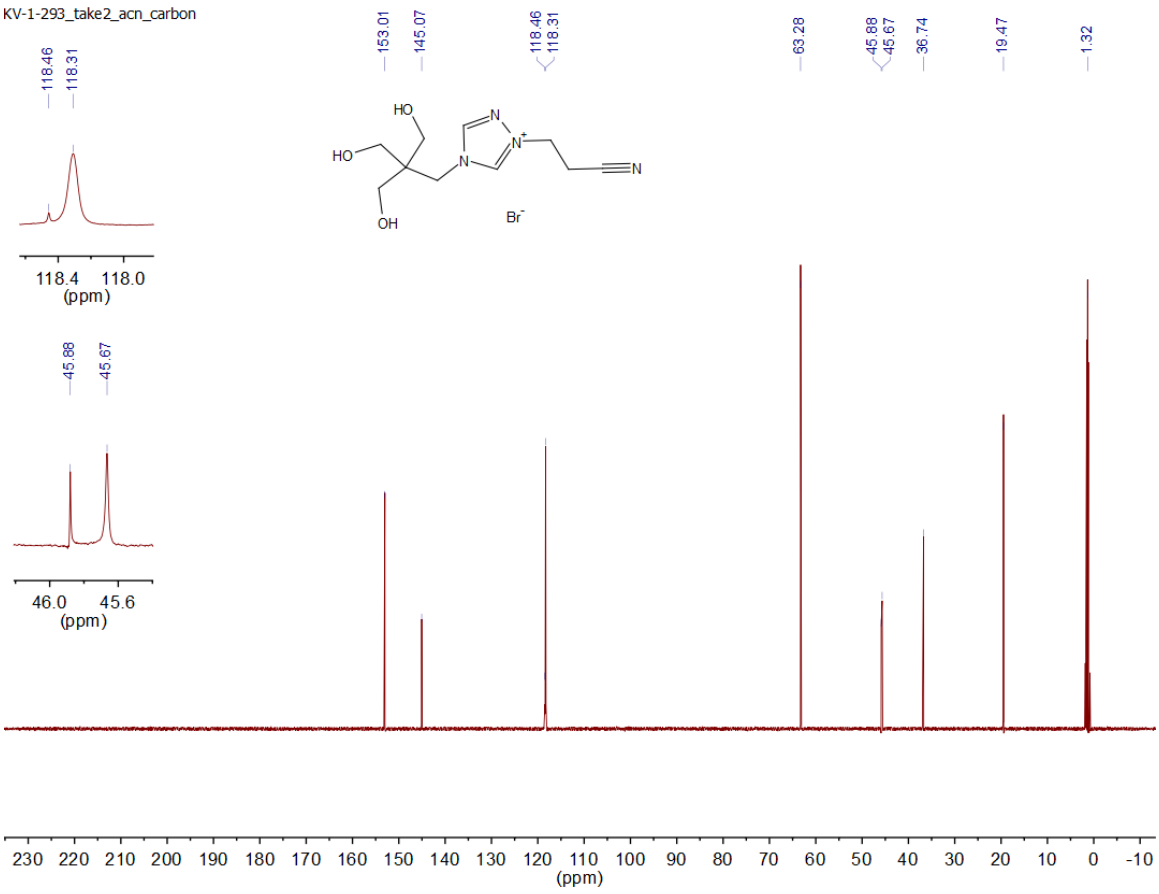

Spectra 2. 12. ^{13}C-NMR of 2.31 in CD_3CN.

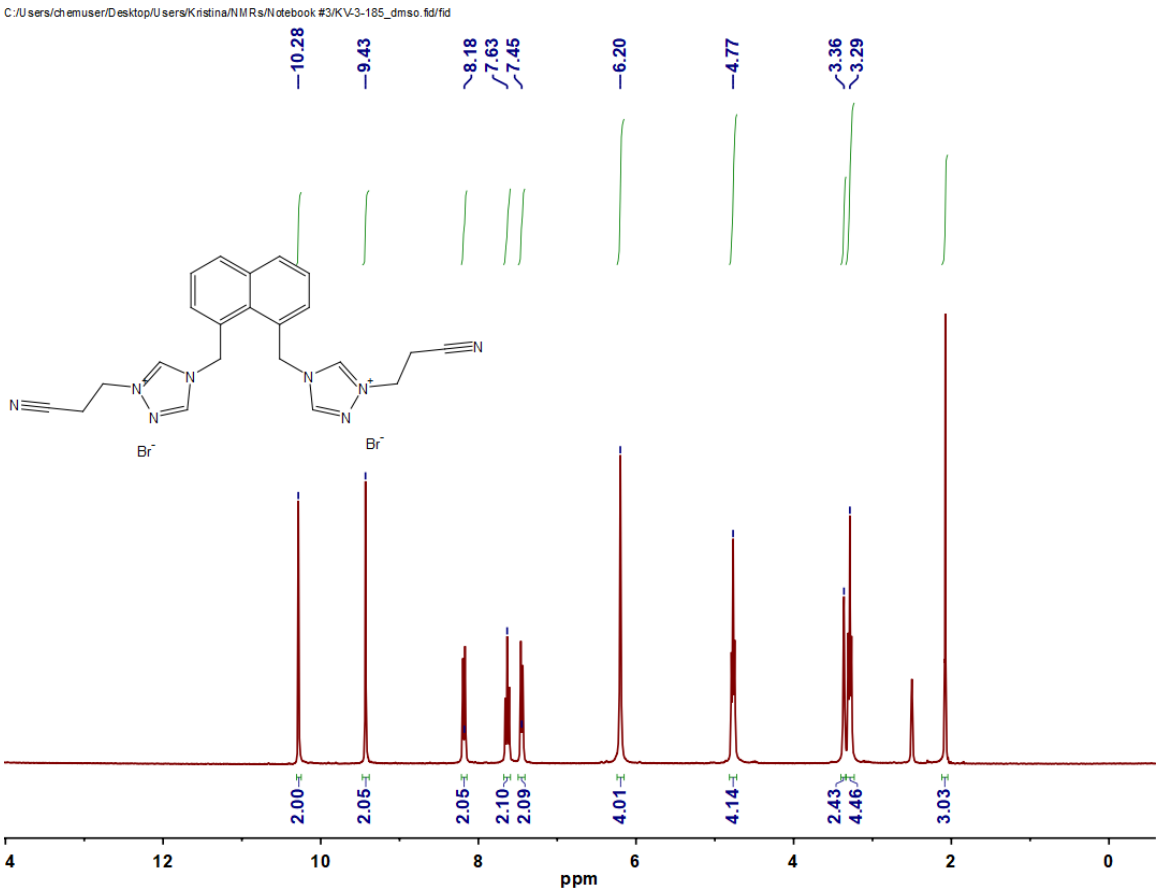

Spectra 2. 13. ^{1}H-NMR of 2.34 in DMSO-d_6.

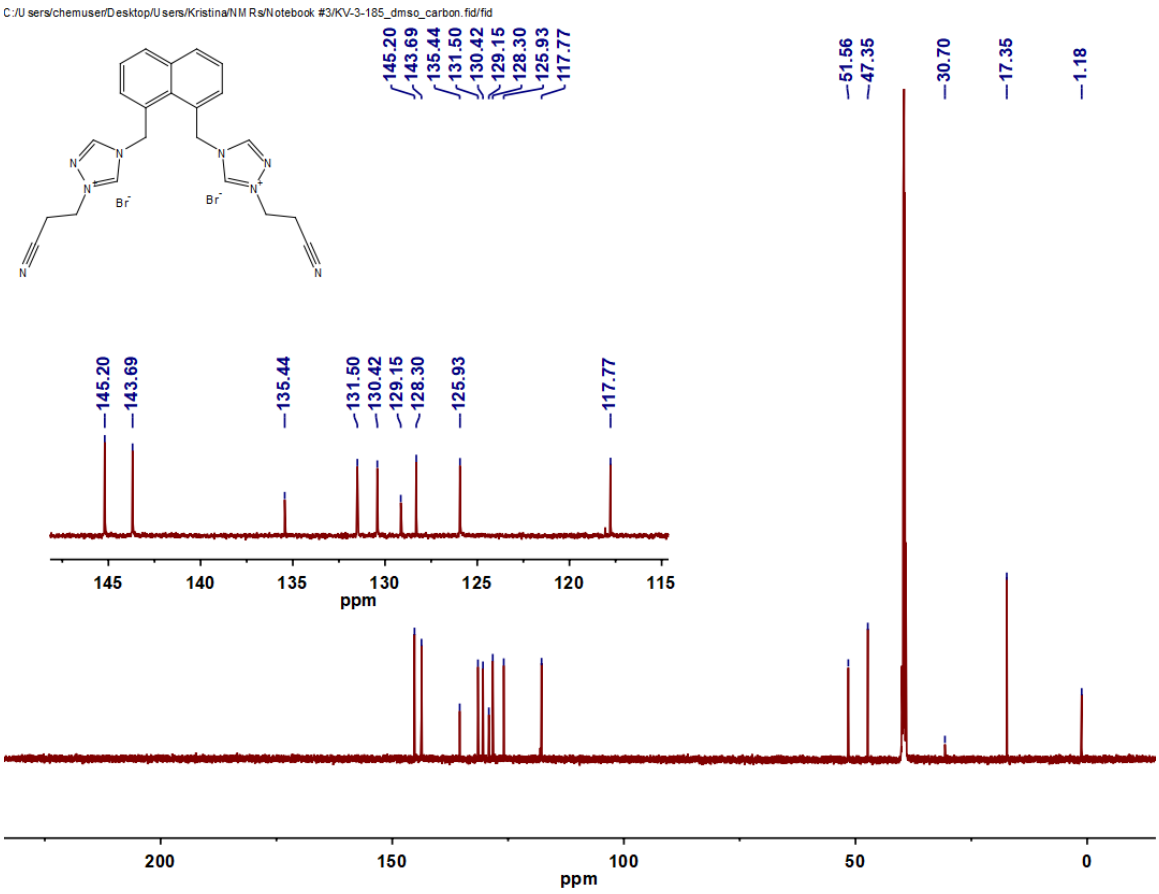

Spectra 2. 14. ^{13}C-NMR of 2.34 in DMSO-d_6.

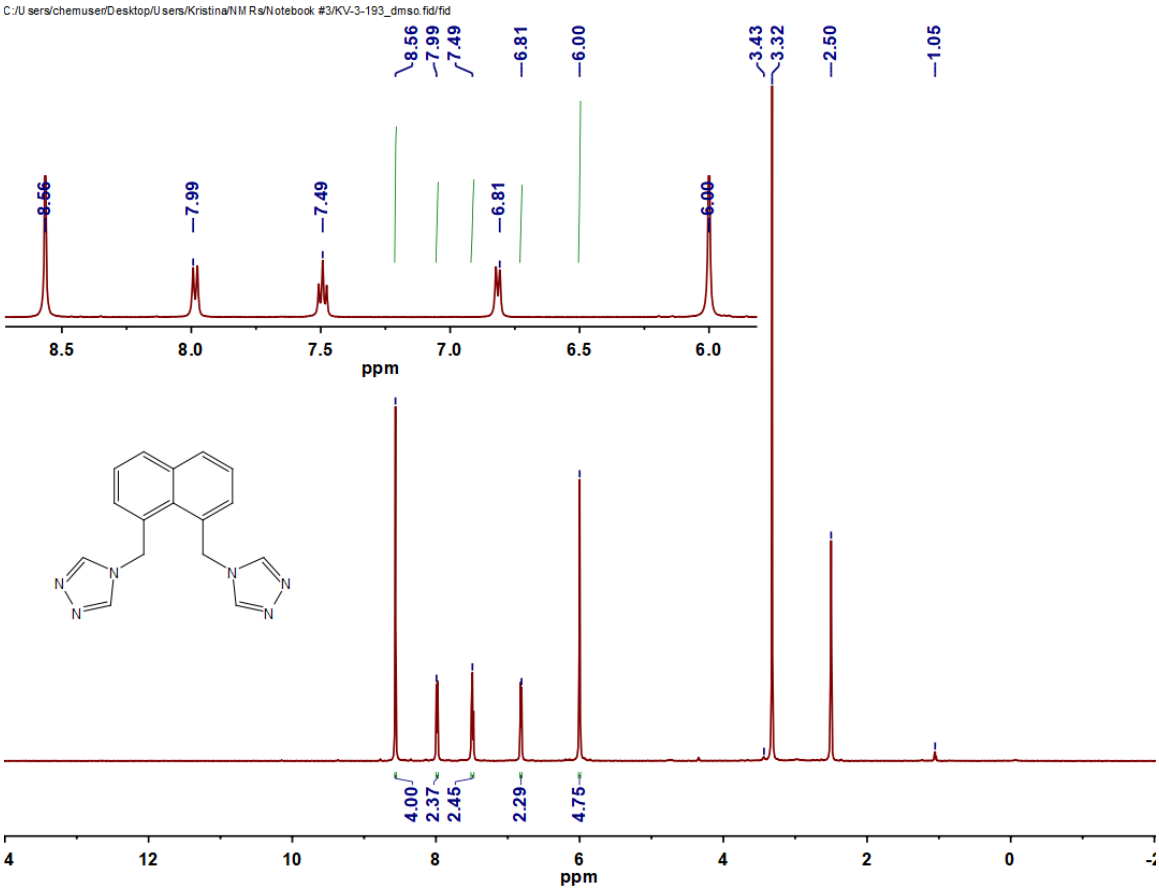

Spectra 2. 15. ^{1}H-NMR of 2.35 in DMSO-d_6.

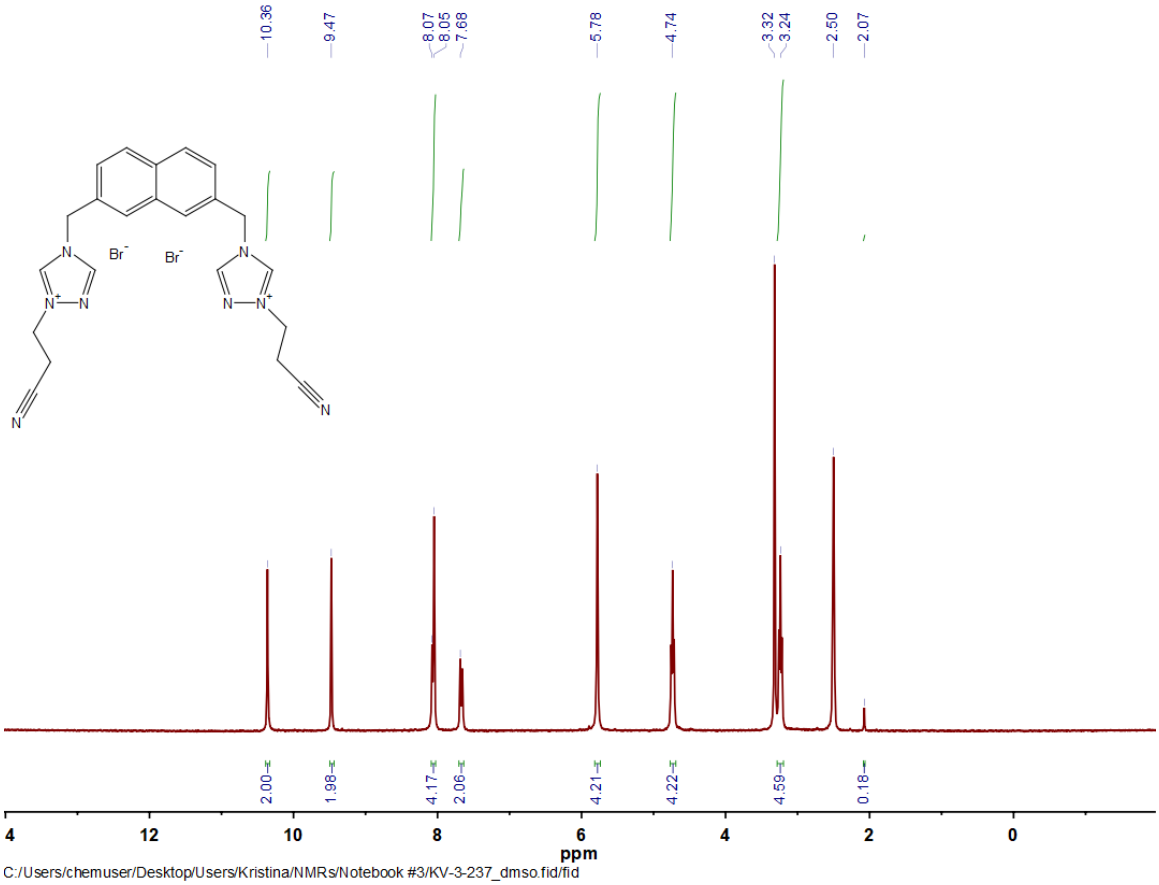

Spectra 2. 16. ^{1}H-NMR of 2.36 in DMSO-d_6.

CHAPTER 3
SYNTHESIS OF METAL-ORGANIC NANOTUBES

Biphenyl ligand was originally synthesized by Dr. Brianna Solomonson[94] and reproduced by me. All other ligands, discussed in Chapter 2, and subsequent MOFs and MONTs were synthesized by me. Dr. Xian Carroll gave assistance with single-crystal X-ray analysis and solved the structure for [Ag(1,4-bis((4H-1,2,4-triazol-4-yl)methyl)naphthalene)$(Br)_2$].

Abstract

This chapter discusses the synthesis of metal-organic nanotubes through the 2-Column Pillar approach with ligands that follow the design goals detailed in Chapter 2 which include: (1) synthesizing large pores MONTs, (2) fluorescent MONTs, (3) MONTs with limited aggregation, and (4) an isostructural set of MONTs. Ligands **2.8**, **2.30**, and **2.35** from Chapter 2, 1,4-bis((4H-1,2,4-triazol-4-yl)methyl)naphthalene from Chapter 4, and the previously reported ligand, 4,4'-bis((4H-1,2,4-triazol-4-yl)methyl)-1,1'-biphenyl, were incorporated in these solvothermal MONT reactions. While the 2-Column Pillar approach guided the synthesis for metal-organic nanotubes, only one new MONT was synthesized and characterized by single-crystal X-ray diffraction. The incorporation of an anthracene (**2.8**) and a naphthalene (**2.35**) moiety resulted in the synthesis of two and three-dimensional MOFs, while the bulky ligand **2.30** produced no identified product. Successful new MONT and MOF that were used in collaborative studies are described in later chapters.

Introduction

As discussed in Chapter 1, aggregated metal-organic nanotubes have some similar properties as three-dimensional metal-organic frameworks, especially those frameworks with one-dimensional channel-like pores (Figure 1.6).

In order for MONTs to emerge as a new material that is distinct from MOFs, it is essential for single MONTs to be synthesized. As the nanotubes are dispersed, their structures no longer have similarities to 3D MOFs and can be finally be studied as independent materials.

Metal-organic nanotubes are synthesized by solvothermal methods similarly to metal-organic frameworks. Both components, metal salt and organic ligand are dissolved in solvents and then mixed together and heated. The simplicity of solvothermal syntheses allows for a combinatorial approach to MONT chemistry that is similar to MOFs. A series of small-scale MONT reactions can be conducted to screen the correct conditions for the formation of crystalline MONTs. The frameworks synthesized in this chapter are listed in Table 3.1.

Results and Discussion

The following will discuss solvothermal reactions with selected di-1,2,4-triazole ligands that follow the four ligand design categories; (1) large pore MONTs, (2) fluorescent MONTs, (3) MONTs with limited aggregation, and (4) an isostructural set of MONTs. Single crystal X-ray structure of the resulting metal-organic frameworks will be analyzed.

Synthesis of Large Pore MONTs

The first ligand design category includes the synthesis of ligands that will form large pore MONTs. A MONT that has a larger pore will make it more feasible to image a single nanotube. Currently, most MONTs have pore sizes under or just above the detection limit (approximately 1 nm) of most transmission electron microscopes.

Table 3. 1. Ligands utilized for metal-organic framework synthesis discussed in this chapter.

Framework #	Ligand	Structural Dimension	Design Category
3.1	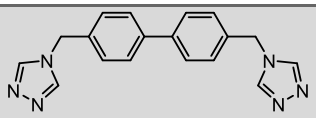 'biphenyl'	2	(1) Large Pore MONTs
NA	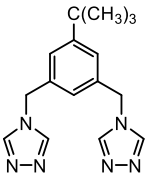 **2.30**	NA	(3) Aggregation Blocking MONTs
3.2	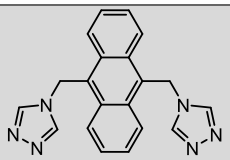 **2.8**	2 or 3	(2) Fluorescent MONTs
3.3	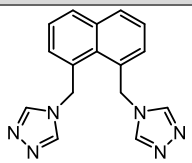 **2.35**	2	(4) Isoreticular MONTs
3.4	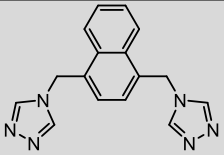 1,4-bis((4H-1,2,4-triazol-4-yl)methyl)naphthalene	1	(4) Isoreticular MONTs

The previously synthesized biphenyl ligand, 4,4'-bis((4H-1,2,4-triazol-4-yl)methyl)-1,1'-biphenyl (Figure 3.1A), incorporates a biphenyl motif in order to extend the size of the pore. This ligand was initially used for understanding the "gate" effect within two-dimensional MOFs. The "gate" effect occurs when the phenyl rings rotate between two positions; open, and closed (Figure 3.1B). The switch from opened position to the closed position is dependent on the guest molecules and creates a "breathing" effect within the MOF.[94, 103]

The initial reported structures are 2D frameworks formed from the biphenyl ligand in Figure 3.1A and metal salts of silver(I) perchlorate and copper(II) perchlorate. In efforts to synthesize a one-dimensional framework with this ligand, many small-scale reactions were screened. Screening reactions included varying the metal salt, metal to ligand ratio, concentration of total reagents, solvent, and solvent combination. Group 11 metal salts tested included copper(II) bromide, copper(II) chloride, and silver(I) nitrate with varying the metal to ligand (M:L) ratios of 1:5, 1:2, 1:1, 2:1, and 5:1. Solvent combinations of water, *n*-methyl-2-pyrrolidone, dimethylformamide, diethylformamide, dimethyl sulfoxide, and dimethylacetamide were also tested for framework formation.

The use of a smaller, less bulky anion such as a bromide and nitrate, similar to previously reported MONTs was investigated.[32] The goal was to provide a 'capping' anion that would bridge the repeating units within the framework and form favorable 1D tubes as opposed to the frameworks formed with the perchlorate anions (Figure 3.2). The perchlorate anions in the 2D framework in Figure 3.2 participates in balancing the charge of the framework, thus allowing the tetrahedral copper atoms to bind with additional triazole ligands and extending the framework.

From the screening reactions, the sample that yielded a crystalline solid (**3.1**) is from the reaction of silver(I) nitrate in, *n*-methyl-2-pyrrolidone at 85 °C as seen in Scheme 3.1. The bulk crystals grew rapidly forming microcrystalline materials that were too small to be mounted on the single-crystal X-ray diffractometer at the University of Tennessee. This sample was sent to the Advanced Light Source (ALS) at Lawrence Berkeley National Laboratory (LBML)

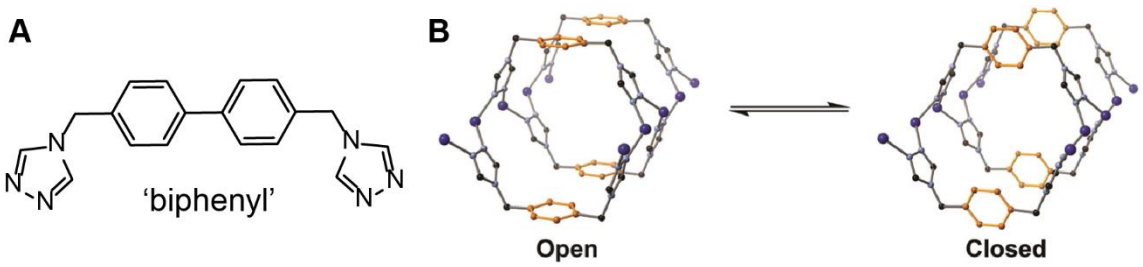

Figure 3. 1. (A) Extended width ligand, 4,4'-bis((4H-1,2,4-triazol-4-yl)methyl)-1,1'-biphenyl, previously reported by the Jenkins group. (B) Open and closed positions of the "gate" effect. This image is modified from the original reference.[94]

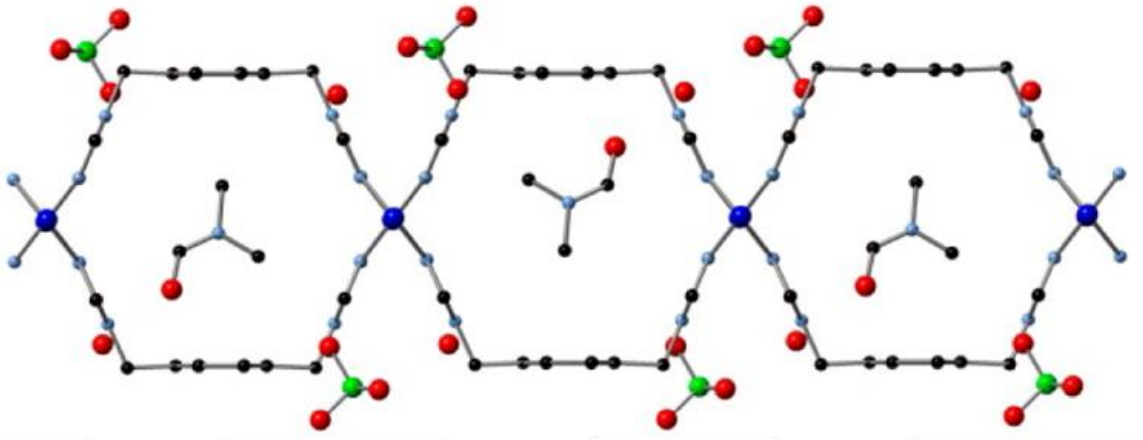

Figure 3. 2. Single crystal X-ray structure of previously reported 2D structure, [Cu(biphenyl)(ClO_4)]•DMF•H_2O. Black, light blue, dark blue, red, and green spheres represent carbon, nitrogen, copper, oxygen, and chlorine atoms respectively. Hydrogen atoms are omitted for clarity. This image is modified from the original reference.[94]

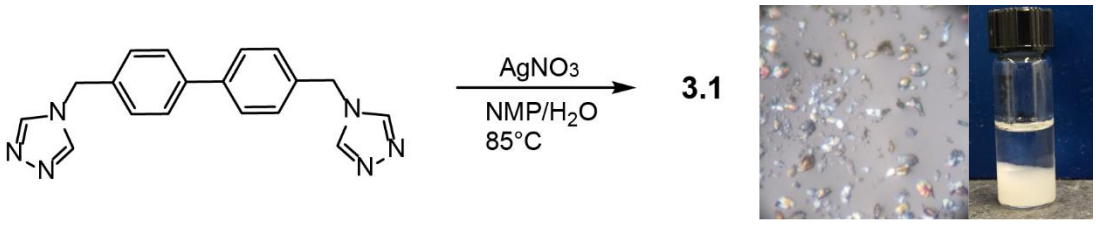

Scheme 3. 1. Synthesis of 3.1 with sliver(I) nitrate in NMP and water. The bulk solid and image of crystal under microscope.

which has the capabilities in analyzing smaller crystalline materials. The structure of **3.1** was determined to be a two-dimensional framework with tubular pores (Figure 3.3) which is isostructural to the previously reported 2D framework in Figure 3.2. Although the framework is not the desired dimensionality, the pores measure to be 15.1 Å which are indeed larger than previously synthesized MONTs.

The fused tube 2D structure of **3.1** shows water molecules within the wide tubular pores and nitrate anions on the exterior of the framework. The nitrate anions did not bridge the adjacent repeating units of the framework as seen in previously synthesized MONTs Figure 3.4A-B.[32] Figure 3.4B-C illustrates the difference in nitrate position comparing a 1D MONT and 2D MOF of similar components. The reaction conditions for the synthesis of the 1D MONT as shown in Figure 3.4A nearly identical to structure **3.1**; the only difference is the additional phenyl ring on the biphenyl ligand. It is hypothesized that the additional phenyl rings drive the aggregation of the nanotubes together due to π-π interactions, creating more space for the nitrate counterions. The 1D MONT synthesized from the *para*-xylyl ligand (Figure 3.4A) drives a similar aggregation-based reaction,[47] but in this case there is only one aromatic ring in the ligand to form π-π interactions. The nanotubes formed in this case are packed closer together. In this case, the nitrates are in close enough proximity to bridge the repeating units within the framework.

MONTs with Limited Aggregation

The second ligand design category is to synthesis ligands that will stop the aggregation of metal-organic nanotubes. To achieve this goal, ligand **2.30** was synthesized and then used in MONT screening reactions.

The goal of this ligand was to use the tert-butyl functional group to disrupt the π-π interactions of the aromatic rings within the organic ligand of adjacent MONTs in order to synthesize a singular MONT. The tert-butyl functional group proved highly effective in regard to mitigating the MONT aggregation; however, it was so effective that no MOF or MONT product was produced.

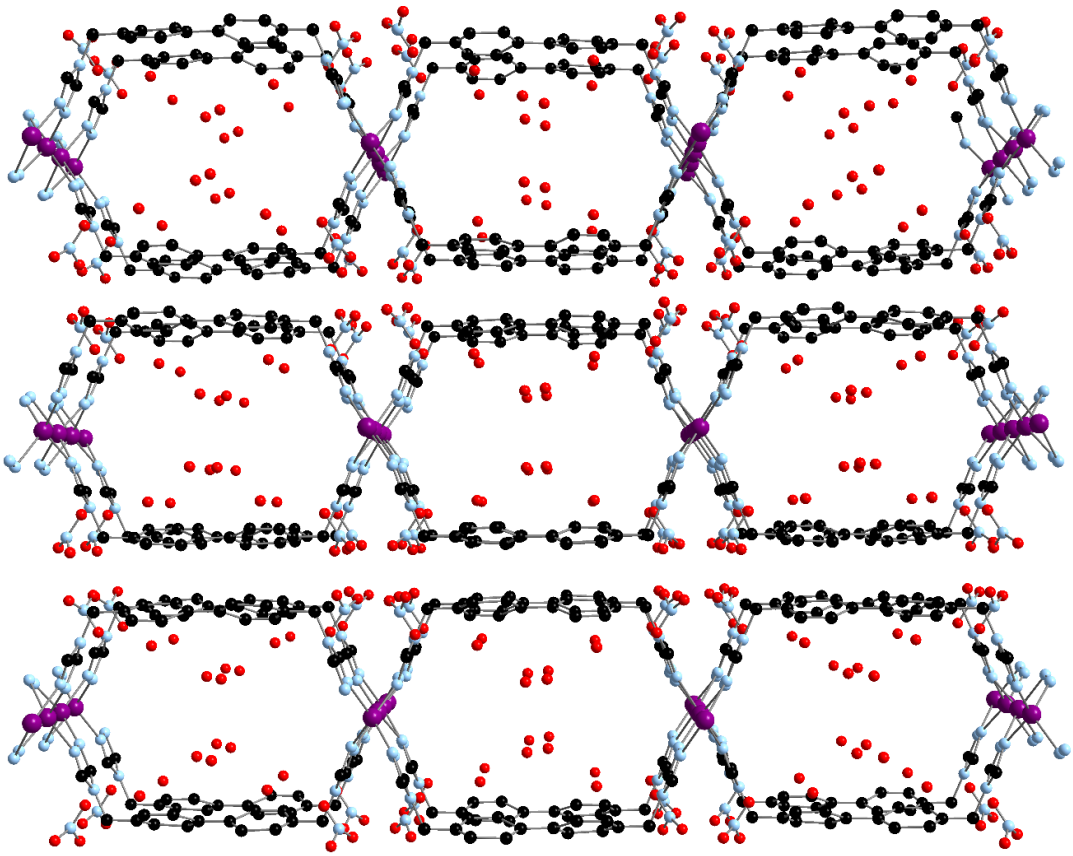

Figure 3. 3. Single crystal X-ray structure of 3.1. Black, light blue, red, purple, and brown spheres represent carbon, nitrogen, oxygen, silver, and bromine atoms respectively. Hydrogen atoms are omitted for clarity.

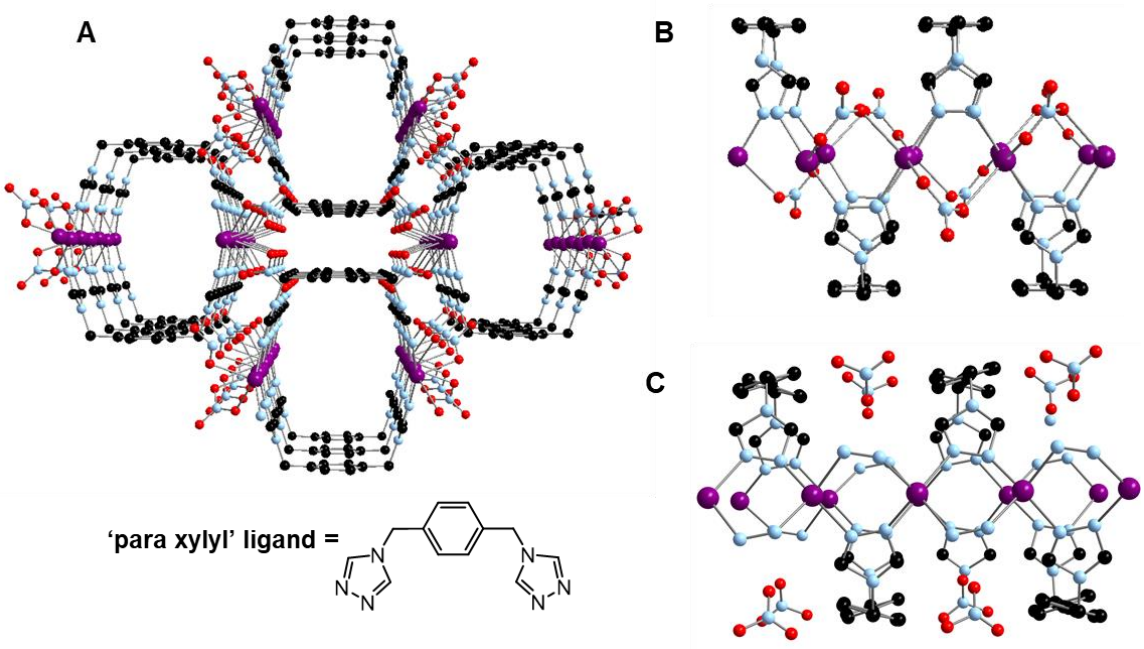

Figure 3. 4, (A) Previously reported 1D MONT structure [Ag(para-xylyl)$(NO_3)_2$]•NMP with corresponding organic linker, (B) Side view of 1D MONT illustrating the bridging nitrate.[32] (C) Side view of newly synthesized 2D MOF (structure 3.1) with non-bridging nitrate ions.

Synthesis of Spectroscopically Active MONTs

The third ligand design category includes the synthesis of spectroscopically active ligands that will form MONTs that can be studied by various fluorescence techniques. Ligand **2.8** incorporates an anthracene unit as the central moiety of the di-1,2,4-triazole ligand.

The solvothermal reaction of the anthracene based di-1,2,4-triazole ligand **2.8** and silver(I) nitrate yielded a mixture of amorphous powder and some microcrystalline material. This sample was also sent to the Advanced Light Source (ALS) at Lawrence Berkeley National Laboratory (LBML). The crystal that was mounted on the instrument was 13.9 μm x 44.3 μm x 28.9 μm, a size crystal that could not be mounted on the single-crystal X-ray diffractometer at the University of Tennessee.

The metal-organic framework obtained from the reaction depicted in Scheme 3.2 produced the structure shown in Figure 3.5. This framework is not the desired one-dimensional metal-organic nanotube. This suggests that synthesizing a ligand with bulky substituents that would occupy the potential pore of the MONT, such as the aromatic rings of **2.8**, can cause the ligand to distort and not remain in the *syn* conformation. The *anti* conformation allows for 2D or 3D structures to be formed depending on the coordination around the metal center. Thorough analysis of this structure shows extra electron density around the silver atoms; therefore, a complete description of dimensionality could not be made. This framework, however, is not a one-dimensional MONT because the geometry of the ligands around the metal center show multiple directions where the framework can repeat. Due to the limited access to the beamlines at the ALS source at LBNL and the limited crystal growth of the sample, additional characterization could not be conducted therefore a better data set was not collected. Solutions such as a SQUEEZE parameter was attempted to remove solvent from the pores, but this was unsuccessful and the disordered molecules within the framework remained. These molecules could be disordered nitrate ions or NMP solvent.

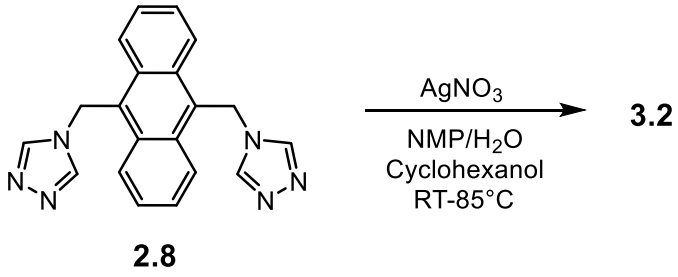

Scheme 3. 2. Synthesis of 3.2 with sliver(I) nitrate in NMP and water.

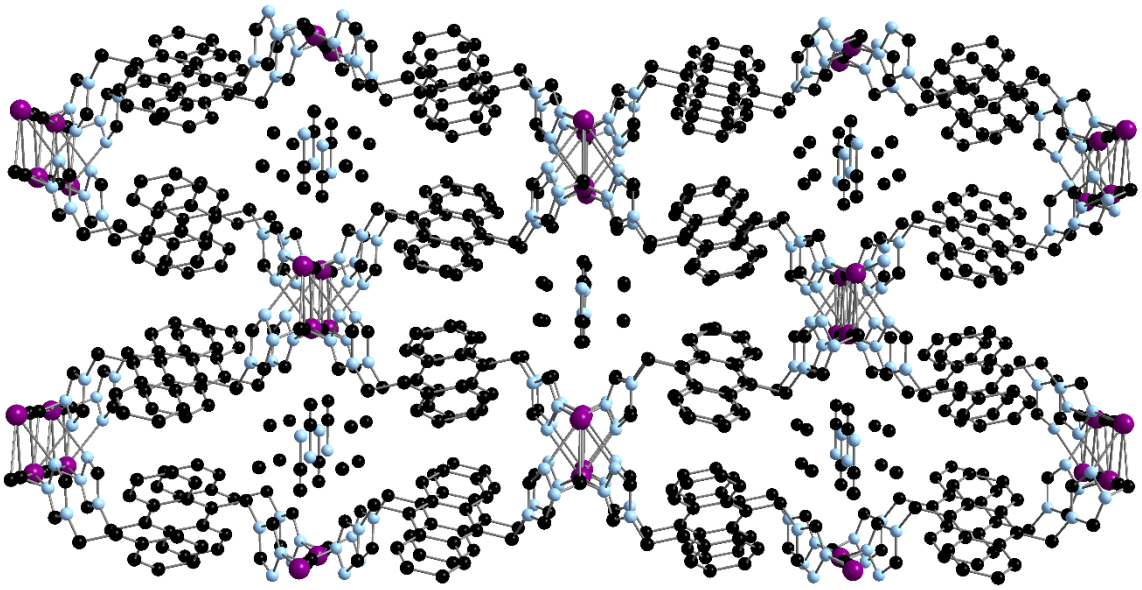

Figure 3. 5. Single crystal X-ray structure depicting framework of structure 3.2. Black, light blue, and purple spheres represent carbon, nitrogen, and silver atoms respectively.

Synthesis of Isoreticular MONTs

The last ligand design category describes the need for creating a large library of isostructural MONTs. With a set of MONT structures that are comparable, the characteristics can be analyzed as a whole, which will allow for a broader analysis that can help develop MONTs.

The isostructural series of MONTs previously synthesized in the Jenkins group (Figure 1.5) acted as a starting point to expand the catalog of metal-organic nanotubes. First, the triazole connectivity to the naphthalene ligand (Figure 1.5, Ligand 3) was changed to create a series of naphthalene based MONTs including **2.35** and 1,4-bis((4H-1,2,4-triazol-4-yl)methyl)naphthalene. Both of these ligands were reacted with silver(I) nitrate in NMP and water (Scheme 3.3). These reactions yielded vastly different single crystal X-ray structures.

Ligand **2.35** produced a two-dimensional framework as seen in Figure 3.6 with the topology similar to structure **3.1**. The framework contains narrow channel-like pores with the naphthalene moiety extending outside the framework. Adjacent two-dimensional sheets interlock the naphthalene moieties in a “zipper-like” fashion (Figure 3.7). This framework includes disordered nitrates within the narrow pores of the MOF. Additional analysis of the crystal data set proved unsuccessful towards a complete solution of the structure; however, the disorder in this structure does not change the dimensionality of the framework. This 2D framework shows the *syn* conformation ligand needs enough flexibility and distance between the ‘hinges’ to create a pore for a 1D nanotube structure. Ligand **2.35** creates a drastic angle at the ‘hinge’ which in addition to the π-π stacking of the aromatic ring drives the MONT reaction towards the 2D structure.

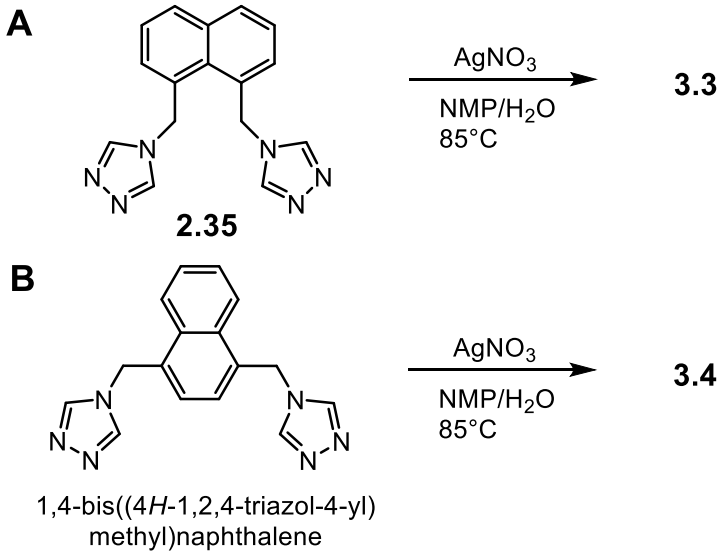

Scheme 3. 3. Synthesis of (A) structure 3.3 and (B) structure 3.4 with silver(I) nitrate in NMP and water.

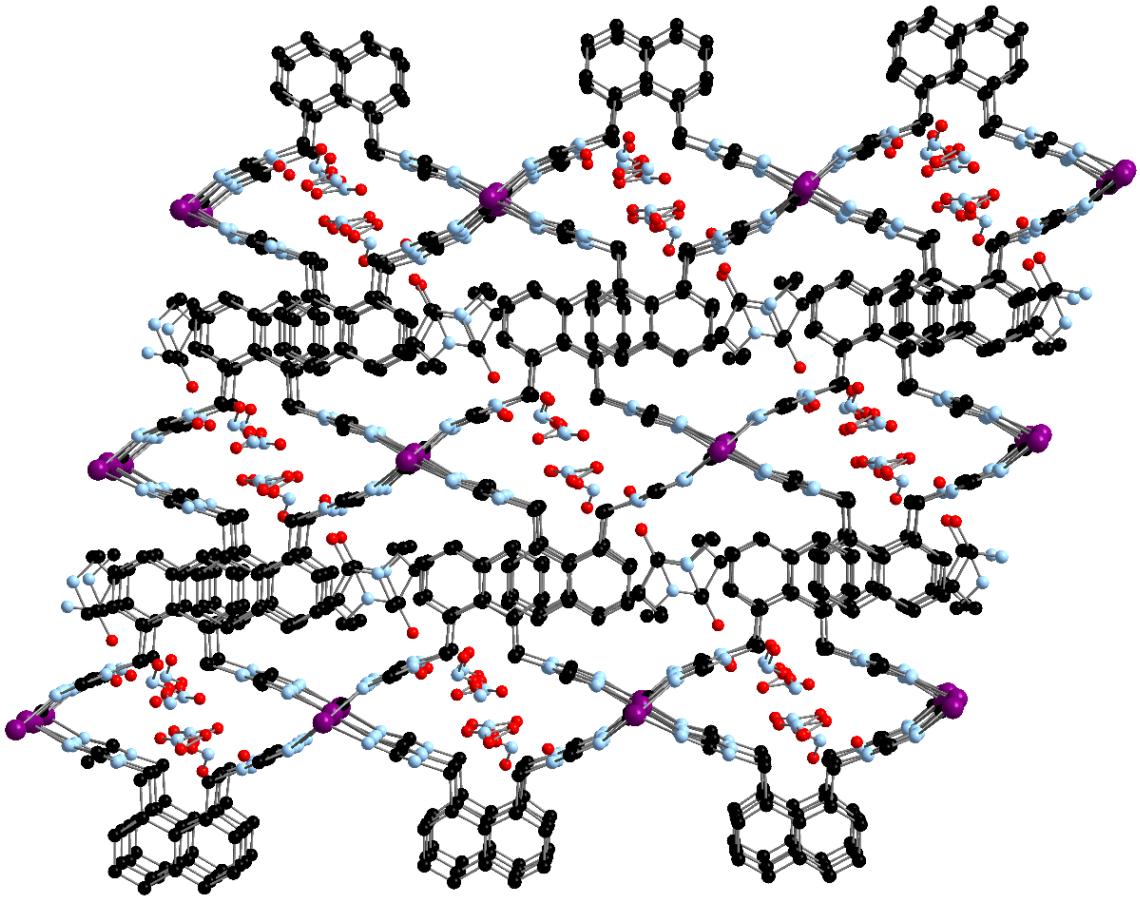

Figure 3. 6. Single crystal X-ray structure of 3.3. Black, light blue, red, and purple spheres represent carbon, nitrogen, oxygen, silver, and bromine atoms respectively. Hydrogen atoms are omitted for clarity.

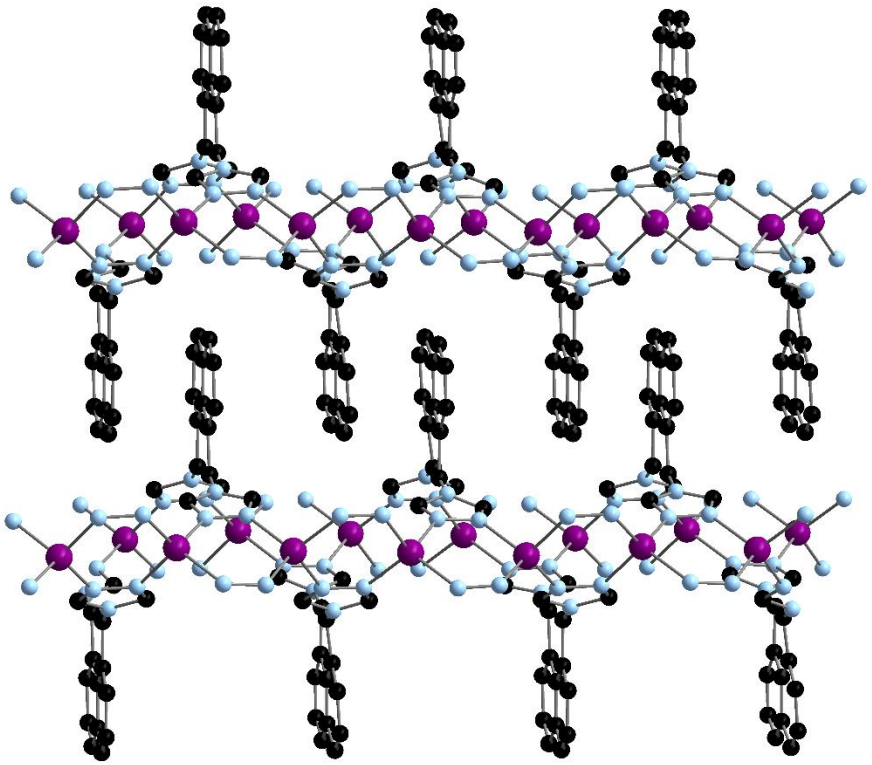

Figure 3. 7. Side view of structure 3.3 illustrating the "zipper" nature of the naphthalene moieties in the organic ligand. Black, light blue, and purple spheres represent carbon, nitrogen, silver, and bromine atoms respectively.

The last ligand used to synthesize a metal-organic nanotube is 1,4-bis((4H-1,2,4-triazol-4-yl)methyl)naphthalene. The synthesis of this ligand is detailed in Chapter 4. As seen in Scheme 3.3B, the second naphthalene ligand variation was reacted with silver nitrate in NMP and water and heated at 85 °C for three months, to produce structure **3.4**. Figure 3.8 illustrates a 1D MONT with the naphthalene ligand; however, the counter anion to the single crystal X-ray structure was solved to be a bridging bromide anion rather than the expected bridging nitrate anion. While Scheme 3.3B contains no bromine atoms, it was determined that the ligand contained a trace amount of potassium bromide impurities from the synthesis. Scheme 3.4 depicts the deprotection of the triazole moiety with potassium hydroxide. This reaction produces potassium bromide that is NMR and IR silent. Elemental analysis showed a discrepancy between the expected and actual percent abundance of carbon, hydrogen, and nitrogen which led to the determination that potassium bromide was present in the sample. It is believed that the bromides participated in an anion exchange reaction to replace the nitrates in the structure. Further solution state experiments would need to be conducted to verify this hypothesis. This anion exchange caused problems with the reproducibility of this structure.

Similar to structure **3.3**, this 1D MONT (**3.4**) creates a series of “zipper-style” π-π interactions from vertically adjacent MONTs. The naphthalene moieties extend outside the pore to create these interactions. This effect was not seen with the anthracene ligand featured in structure **3.2**. Removing the bulk of the third aromatic ring (ligand **2.8**) from the ligand successfully produced a 1D MONT. The width (i.e. pore size) of the MONT was measured to be 10.2 Å which is slightly larger than the previously synthesized MONTs in the Jenkins group.

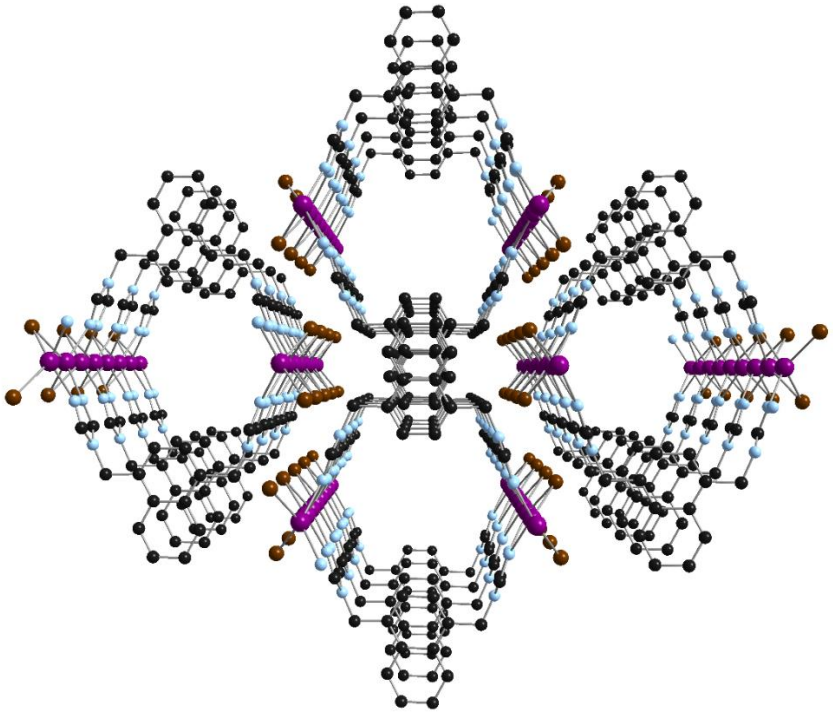

Figure 3. 8. Structure 3.4 front view. Black, light blue, purple, and brown ellipsoids (50% probability) represent carbon, nitrogen, silver, and bromine atoms respectively.

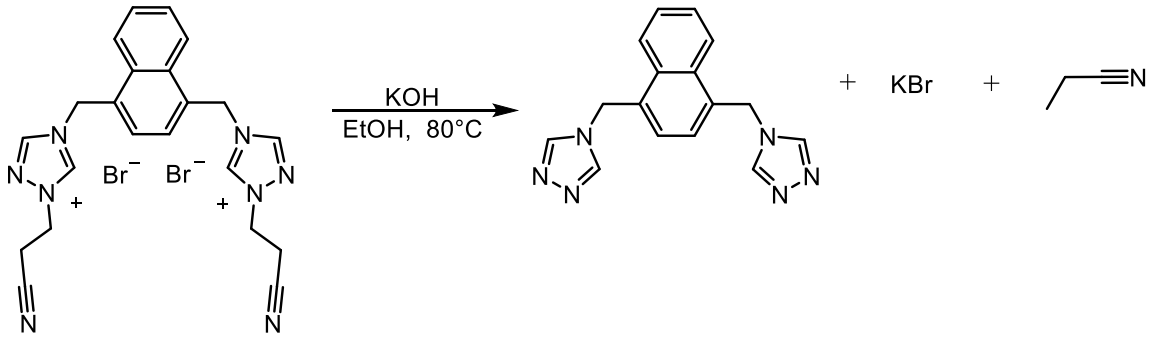

Scheme 3. 4. Deprotection synthesis of 1,4-bis((4H-1,2,4-triazol-4-yl)methyl)naphthalene ligand.

Similar to structure **3.3**, this 1D MONT (**3.4**) creates a series of "zipper-style" π-π interactions from vertically adjacent MONTs. (Figure 3.9) The naphthalene moieties extend outside the pore to create these interactions. This effect was not seen with the anthracene ligand featured in structure **3.2**. Removing the bulk of the third aromatic ring (ligand **2.8**) from the ligand successfully produced a 1D MONT. The width (i.e. pore size) of the MONT was measured to be 10.2 Å which is slightly larger than the previously synthesized MONTs in the Jenkins group.

Conclusion

In conclusion, the synthesis of metal-organic nanotubes with the proposed ligands from Chapter 2 was discussed. While methods of synthesizing MONTs have been established, this chapter shows there is still a chance of creating two or three-dimensional frameworks even via the 2-Column Pillar approach. The organic ligand in MONT reactions plays a large role in the dimensionality of the framework. 2D frameworks were formed from MONT reactions with the biphenyl ditriazole ligand and the naphthalene ligand **2.35**. A 2D or 3D framework was formed from the anthracene ditriazole ligand, **2.8**. The tert-butyl functionalized ditriazole ligand (**2.30**) produced no MONT structures. The only successful synthesis of a MONT was with the 1,4-bis((4H-1,2,4-triazol-4-yl)methyl)naphthalene ligand, yet this reaction was due to a bromide impurity and is not reproducible. While not all structures synthesized in this chapter produced the desired one-dimensional MONTs, insight towards new ligands for MONT synthesis was gathered. Organic ligands should be synthesized so that they remain in the *syn* confirmation in order to prevent 2D or 3D framework formation, and the ligands should be sterically encumbered enough to force the counter anions into bridging the repeating units of the MONT for 1D framework formation.

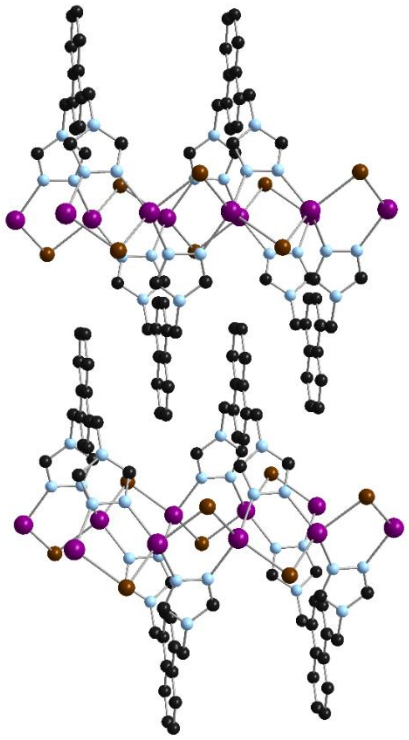

Figure 3. 9. Side view of structure 3.4, illustrating the "zipper" effect of the naphthalene moiety. Black, light blue, purple, and brown ellipsoids (50% probability) represent carbon, nitrogen, silver, and bromine atoms respectively.

Experimental

I. Synthesis of Metal-Organic Frameworks

Synthesis of Structure 3.1:

Silver(I) nitrate (6.0 mg, 0.03532 mmol) was dissolved in 1 mL DI water and heated at 85 °C for 10 minutes. The biphenyl ligand (4,4'-bis((4H-1,2,4-triazol-4-yl)methyl)-1,1'-biphenyl) (5.7 mg, 0.01802 mmol), was dissolved in 2 mL NMP and heated at 85 °C until dissolved. The hot solutions were combined in a 4 mL scintillation vial and heated at 85 °C for 24 hours to afford an off-white precipitate.

Synthesis of Structure 3.2:

Silver(I) nitrate (5.0 mg, 0.02943 mmol) was dissolved in 1 mL DI water and heated at 85 °C for 10 minutes. The anthracene ligand (**2.8**) (5.6 mg, 0.01645 mmol), was dissolved in 2 mL NMP in a 4 mL scintillation vial and heated at 85 °C until dissolved. Both metal and ligand solutions were allowed to slowly cool to room temperature. Cyclohexanol (0.5 mL) was carefully pipetted on top of the ligand solution and placed into a small beaker of dry ice until the cyclohexanol layer froze. The cooled metal solution was then carefully pipetted on top of the cyclohexanol layer. The scintillation vial with all three layers was allowed to warm to room temperature and was placed on a heating block at 85 °C for 24 hours. Yellow microcrystalline and amorphous material was formed from this reaction. Solid product was too fine to collect and isolate from the water NMP solution, thus bulk solid-state analysis was not conducted.

Synthesis of Structure 3.3:

Silver(I) nitrate (7.6 mg, 0.0465 mmol) was dissolved in 1 mL DI water and heated at 85 °C for 10 minutes. The naphthalene-based ligand (**2.35**) (4.9 mg, 0.01687

mmol), was dissolved in 2 mL NMP and heated at 85 °C until dissolved. The hot solutions were combined in a 4 mL scintillation vial, immediately forming a cloudy white precipitate. The scintillation vial was allowed to heat for 24 hours to produce a few single crystals. Bulk solid was not recovered from this reaction.

Synthesis of Structure 3.4:

Silver(I) nitrate (4.8 mg, 0.02826 mmol) was dissolved in 4 mL DI water and heated at 85 °C for 10 minutes. The naphthalene-based ligand, 1,4-bis((4H-1,2,4-triazol-4-yl)methyl)naphthalene (5.32 mg, 0.01832 mmol), was dissolved in 2 mL NMP and heated at 85 °C until dissolved. A 1 mL aliquot of the metal solution was added to the ligand solution in a 4 mL scintillation vial and heated at 85 °C for approximately 3 months. This reaction produced few single crystals on the edge of the vial. No bulk solid was recovered from this reaction.

II. X-ray Structure Determinations

Structure 3.1 crystals were grown directly from the reaction vial. A colorless plate was mounted in the 100 K cold stream provided by an Oxford Cryostream low-temperature apparatus on the head of a Bruker D8 diffractometer equipped with a PHOTON 2 CMOS detector, at beamline 12.2.1 of the Advanced Light Source (Lawrence Berkeley National Laboratory, Berkeley, CA). Data were collected with the use of synchrotron radiation (λ = 0.7288 Å).

Structure **3.2** crystals were grown directly from the reaction vial. A colorless plate was mounted in the 100 K cold stream provided by an Oxford Cryostream low-temperature apparatus on the head of a Bruker D8 diffractometer equipped with a PHOTON 2 CMOS detector, at beamline 12.2.1 of the Advanced Light Source (Lawrence Berkeley National Laboratory, Berkeley, CA). Data were collected with the use of synchrotron radiation (λ = 0.7288 Å).

Structure **3.3** crystals were grown directly from the reaction vial. A clear colorless plate crystal with dimensions of 212.3 μm x 98.5 μm x 43.6 μm was

mounted in the 100 K cold stream provided by an Oxford Cryostream low-temperature apparatus on the head of a Bruker D8 Venture diffractometer equipped with an APEXIII CCD detector, employing the use of Mo Kα radiation (λ = 0.71073 Å).

Structure **3.4** crystals were grown directly from the reaction vial. A colorless needle was mounted in the 100 K cold stream provided by an Oxford Cryostream low-temperature apparatus on the head of a Bruker SMART APEXII diffractometer equipped with an ApexII CCD detector, employing the use of Mo Kα radiation (λ = 0.71073 Å).

All data sets were reduced with Bruker SAINT and were corrected for absorption using SADABS. Structures were solved and refined using SHELXT and SHELXL-2015, respectively.

III. Selected Analytical Data for 3.1

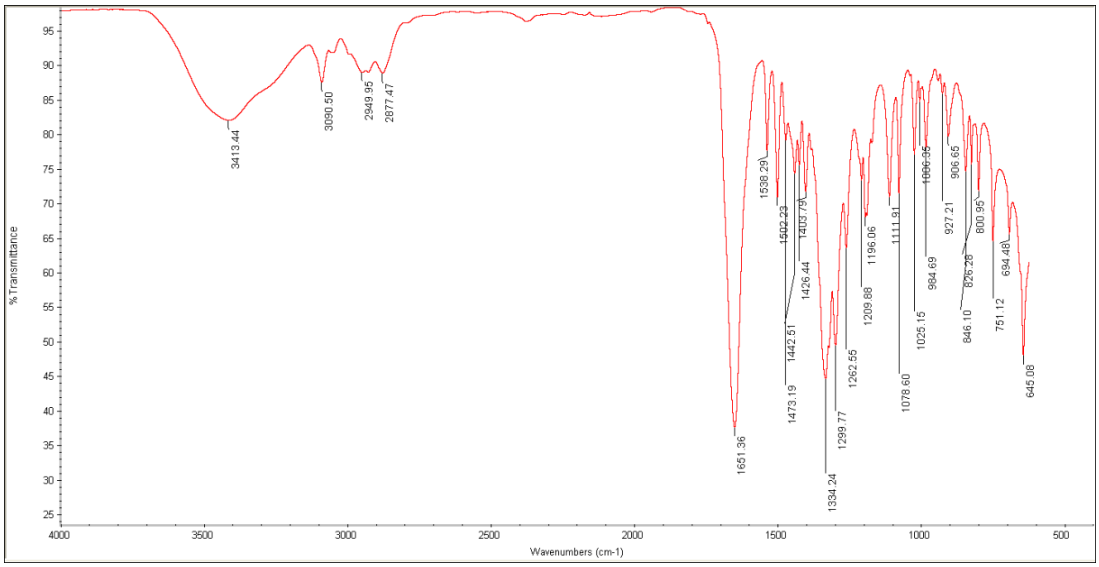

Spectra 3. 1. ATR-IR of Structure 3.1.

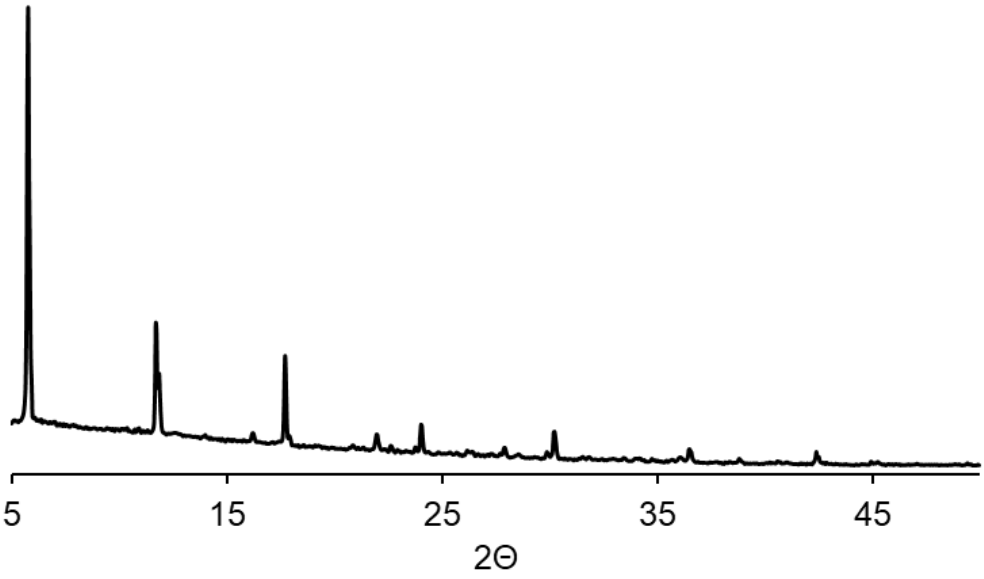

Spectra 3. 2. Experimental PXRD of Structure 3.1.

CHAPTER 4

ELUCIDATING THE GROWTH OF METAL-ORGANIC NANOTUBES COMBINING ISORETICULAR SYNTHESIS WITH LIQUID-CELL TRANSMISSION ELECTRON MICROSCOPY

A version of this chapter was originally published by Kristina M. Vailonis, Karthikeyan Gnanasekaran, Xian B. Powers, Nathan C. Gianneschi, and David M. Jenkins as:

Vailonis, K. M.; Gnanasekaran, K.; Powers, X. B.; Gianneschi, N. C.; Jenkins, D. M., Elucidating the Growth of Metal–Organic Nanotubes Combining Isoreticular Synthesis with Liquid-Cell Transmission Electron Microscopy. *Journal of the American Chemical Society* **2019,** *141* (26), 10177-10182.[70]

The work presented in this chapter was part of a collaborative project in which Dr. Karthikeyan Gnanasekaran and I shared credit for first authorship. I completed the design and synthesis of the ligand and metal-organic nanotube. Dr. Xian Powers collected single crystal X-ray diffraction structure of the MONT at the ALS source. Dr. Karthikeyan Gnanasekaran collected all microscopy data.

This work includes LCTEM videos collected by Karthikeyan Gnanasekaran and can be viewed online at the ACS Publications website (https://pubs.acs.org/doi/10.1021/jacs.9b04586).

Abstract

Metal–organic nanotubes (MONTs) are tunable porous 1D materials that are envisioned to be complementary to carbon nanotubes for anisotropic applications. To date, characterization of MONTs relies on single crystal X-ray diffraction (SCXRD) to determine structure and composition. This requires crystals on the micrometer regime, effectively rendering bulk 3D materials. By tracking the growth of a MONT as a function of time with liquid-cell transmission electron microscopy (LCTEM), TEM, and SCXRD, it was possible to ascertain that the material in the bulk phase matches the nanomaterial in terms of molecular

structure. This result allowed for the first measurements of finite bundles of MONTs on the nanometer scale. By employing *in situ* LCTEM, a time course of the formation of small bundles of MONTs could be acquired which provided mechanistic information on MONT formation which is of utility in reaction optimization and applications development.

Introduction

Dimensionality dictates properties for all materials, and metal−organic frameworks (MOFs) are no exception.[104-107] The vast majority of MOFs are 3D or 2D interconnected solids that take advantage of their rigid spaces, for applications such gas storage, liquid phase separations, or heterogeneous catalysis.[4, 108-110] Conversely, 1D MOFs, known as metal−organic nanotubes (MONTs), are still relatively unexplored.[13, 32, 111] With a high aspect ratio reminiscent of carbon nanotubes, MONTs could conceivably be designed for distinct applications, such as nanowires or nanostraws.[107,112-113] However, like MOFs, the principles of isoreticular design can be applied for MONTs in a manner that is simply impossible for other 1D materials, such as carbon or boron-nitride nanotubes.[32, 107, 112] In particular, the ability to synthesize a tube with variable height and width and a controlled, singular diameter is in stark contrast to syntheses of free carbon nanotubes, where a mixture of widths is typically formed.[114]

The key to unlocking the unique applications and properties of MONTs is the ability to form discrete tubes or small finite bundles of them (Figure 4.1). To approach small bundles, or individual MONTs (Figure 4.1A, B), it is necessary to understand their nucleation and growth, as they are built as each chemical bond is formed. Hitherto, almost all studies of MONTs focus on aggregate macroscale collections of tubes that are sufficiently large enough for single crystal X-ray diffraction (SCXRD) analysis, which is necessary to determine their structure (Figure 4.1D).[47] At this stage, the MONTs will have similar properties to classical

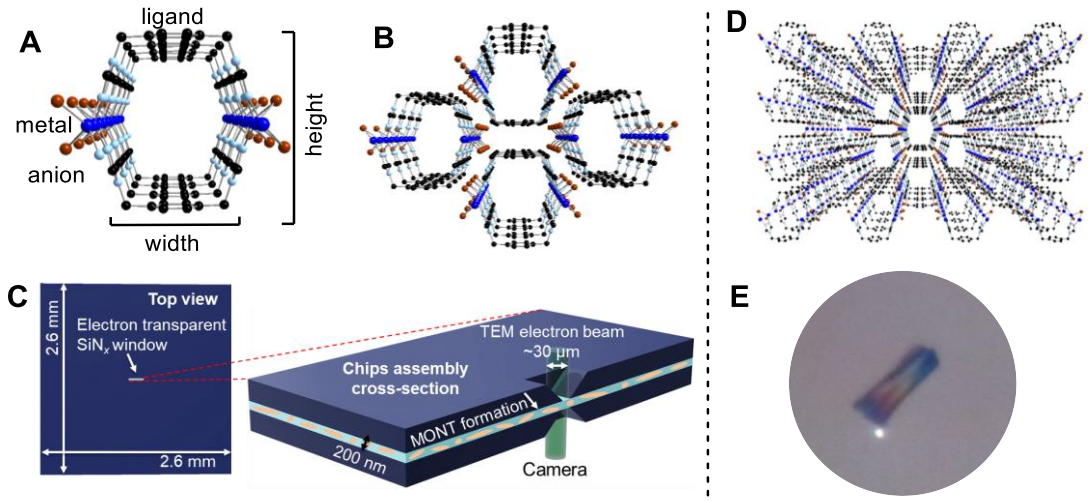

Figure 4. 1. (A) A single MONT with a two-columned pillared design. The height and width of the tubes are controlled separately (MONT shown from Reference 10). (B) Depiction of a small bundle of tubes that can be observed by LCTEM and TEM. (C) Schematic of LCTEM chip employed for MONT reactions. (D) As bundles of MONTs aggregate, they become large enough to crystallize, but approach bulk 3D materials. (E) Crystal of bulk MONT described herein ([(L1)Cu_2Br_2]).

3D MOFs as they are effectively bulk 3D materials. To succeed in evaluating individual tubes or quantifiable bundles, one must employ a combined synthetic and measurement strategy that evaluates both the bulk and the colloidal MONT.

Herein, we describe a new copper MONT studied by a combination of isoreticular synthesis with liquid-cell TEM (LCTEM) (Figure 4.1C) and classical dry state TEM to investigate the growth and morphology of these 1D materials on the colloidal scale. Two-column pillared MONTs allow for excellent isoreticular synthesis and control of MONT growth based on ligand design (Figure 4.1A).[13, 32, 59-62, 64-69, 71-74, 76-77, 82-83] By comparing measurements of the bulk MONT, including SCXRD with the colloidal MONT during its growth phase, we can ensure that the same material is being formed on the nanoscale in the confined solution cell by TEM. Liquid-cell TEM is a nascent technique with the potential to observe reactions that yield nanoscale structures.[50-51, 115-116] It has been successfully deployed in the study of the synthesis of covalent organic frameworks, and of metal−organic frameworks.[45, 52] We utilized a silicon nitride (SiNx) membrane-based liquid-cell into which organic ligands and metal salts were injected and by heating the cell, MONTs were generated.

Results and Discussion

We have developed a strategy for isoreticular synthesis of MONTs with monovalent group 11 metals.[32] These two column pillared MONTs are formed by attaching di-1,2,4- triazoles in a syn conformation.[32] Here we describe a new ligand, 1,4-bis((4H-1,2,4-triazol-4-yl)methyl)naphthalene, **L1**, that was synthesized in five steps (see Experimental). The final two steps are newly reported (Figure 4.2A). 1,4-Bis(bromomethyl)- naphthalene was reacted with 3-(1H-1,2,4-triazol-1-yl)- propanenitrile in refluxing acetonitrile to yield a white powder, compound **2**, in 97% yield.[97] This compound was deprotected with potassium hydroxide in refluxing ethanol to yield **L1** in 78% yield. Reaction of **L1**

with copper(II) bromide dihydrate in a mixture of DEF and water yielded an off-white precipitate, **[(L1)Cu_2Br_2]**, in 5 days (see Experimental).

The solid state structure determined by SCXRD showed the formation of a MONT that is isostructural to our previous reported examples, with one key difference (Figure 4.2B,C).[32] For **[(L1)Cu_2Br_2]**, the naphthyl rings have been rotated 90° and are interlocked between the tubes giving the appearance of a zipper from the π−π stacking (Figure 4.2C).[117-119] This increases the spacing between the tubes relative to previous MONTs.[32] This interlocking decreases the height of the pore to 0.8 nm (Figure 4.2B) while keeping the width the same as the phenyl variant at 1.0 nm. Single crystal X-ray diffraction gives us the exact position of the atoms in the MONT, and the interatomic distances between the heavy atoms (Cu and Br) can be verified by selected area electron diffraction (SAED) lattice spacing measurements which is critical for matching the bulk material to the small bundles of MONTs.

Next, the change in morphology of the MONT during the reaction was examined by TEM at various time points (Figure 4.3). Fibrillar-shaped structures formed at 5 min after mixing the reactants (Figure 4.3A). TEM images show that these initial structures grow over time to form larger anisotropic structures (Figure 4.3B, C, D). Sharp edges and corners indicating faceting of the anisotropic structures over time (Figure 4.3C). SAED at these corresponding time points reveals characteristic MONT diffraction. The lattice spacing of ~13 and ~10 Å represents the vertical distance between subsequent tubes and pore width, respectively (see Figure 4.2). Lattice spacing of MONT crystals were also measured from high resolution (HR) TEM images, which supports the formation of MONT immediately after the reactants mix (Figure 4.3). It is likely that at the beginning of the reaction, only the surface of the structure is crystallized with significant amount of metastable amorphous phase.[120-121]

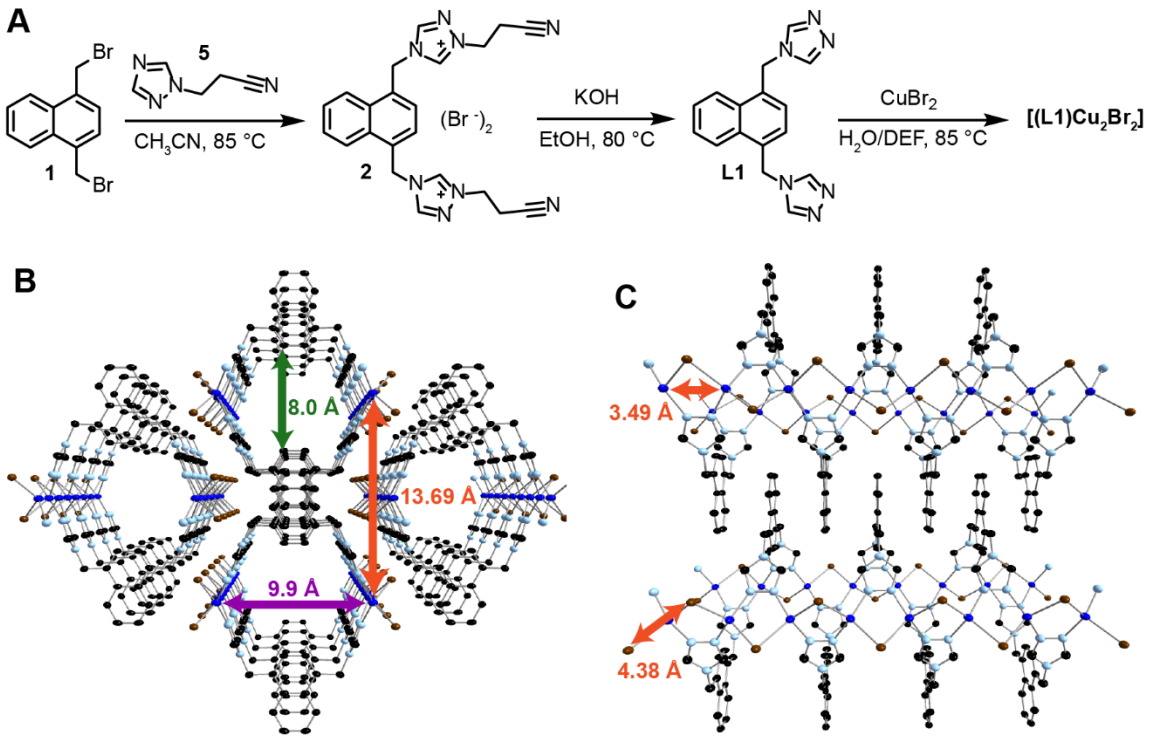

Figure 4. 2. (A) Synthesis of [(L1)Cu_2Br_2]. (B and C) Solid state structure of [(L1)Cu_2Br_2] drawn at the 50% probability level. Hydrogen atoms are omitted. Dark blue, light blue, brown, and black ellipsoids represent copper, nitrogen, bromine, and carbon atoms, respectively. (B) View down the tubes showing the pores. (C) Side-on view of two adjacent tubes, showing the "zipper" formed by π−π stacking. Key interatomic Cu···Cu and Br··· Br distances are shown.

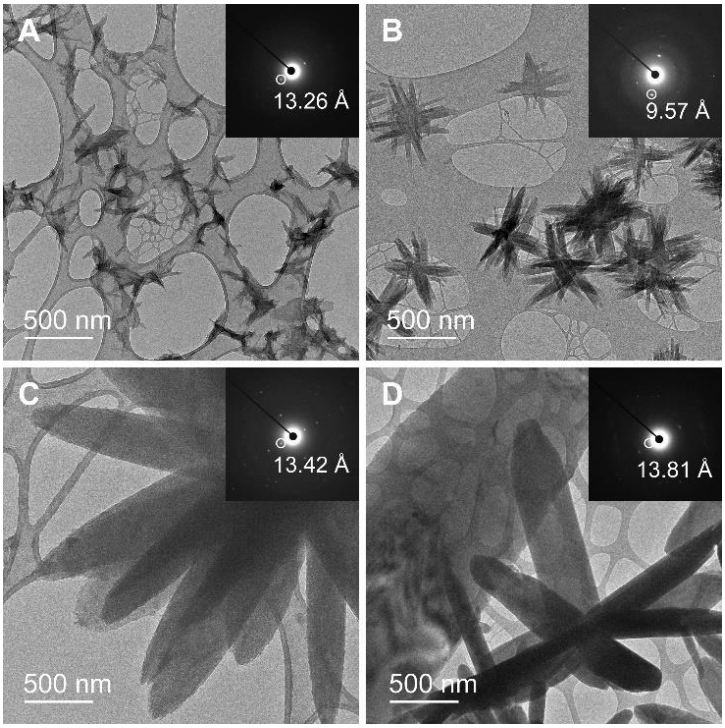

Figure 4. 3. TEM images of aliquots taken during the reaction illustrate the morphological transformation and lattice spacings of [(L1)Cu_2Br_2] over time: (A) 5 min, (B) 30 min, (C) 2 h, and (D) 24 h.

To capture the time course of MONT formation, growth was then examined by performing the reaction *in situ*, by LCTEM. Success here would lead to our ability to monitor the formation of individual MONTs or small bundles and therefore gather information related to the growth mechanism. The first step was to confirm imaging could be performed without damaging the MONT nucleation and growth by radiolysis and/or other beam induced effects.[122-124] To maximize the achievable contrast at limited electron flux, we used a beam current of 0.63 nA and an electron flux of ~0.05 e−Å−2 per second. These electron flux thresholds were determined by trial and error, confirming the safe imaging condition to be the same conditions. The very initial nucleation events were difficult to capture, with observables limited by the achievable contrast and resolution in solution at a low electron dose. However, nanocrystal growth could be observed as the reaction continued (Figure 4.4A, B, Movies 4.2, 4.3, 4.4, https://pubs.acs.org/doi/10.1021/jacs.9b04586), which led to the formation of large bundled fibril-like structures with sharp edges reminiscent of the structures observed in the bulk experiment (Figure 4.3B, C).

LCTEM chips could be pried open for analysis following the *in situ* experiments and analyzed by diffraction and energy dispersive X-ray spectroscopy (EDS) (Figure 4.4C−F). MONT crystals were observed over the entire SiNx membrane of the LCTEM chips, not only in the observed region impacted by the electron beam, which is further evidence for the formation of **[(L1)Cu_2Br_2]** within the confinement of the liquid-cell (Figures 4.4C, D and 4.26). A significant size distribution was also observed in the MONT bundles formed within the liquid-cell.

There are no apparent differences in sizes of MONT bundles formed at room and elevated temperatures (See Experimental Section, Figure 4.11). The smallest MONT crystal has a length and diameter of 300 nm × 70 nm, with the largest MONT crystal approximately 4 μm × 600 nm (See Experimental Section, Figure 4.11). The size of these MONT bundles corresponds to 10 to 100 individual tubes. SAED for one crystallite gave a diffraction spot showing lattice spacing of 13.55 and 3.62 Å (Figure 4.4E). These values are the same (within error) for the vertical distance between the MONTs (vertical Cu···Cu interatomic distance), and

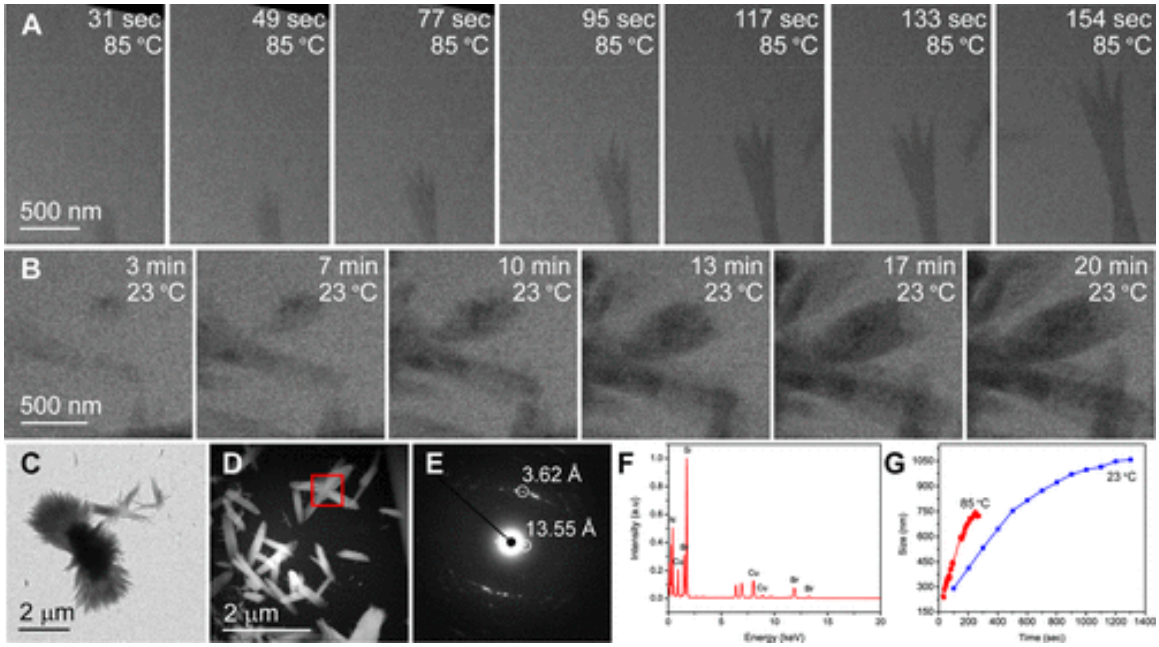

Figure 4. 4. (A and B) Snapshots of growth of MONT acquired by LCTEM. (C and D) Fully grown MONT in LCTEM environment acquired during post-mortem analysis. (E) SAED of MONT grown in LCTEM. (F) EDS spectrum of MONT grown in LCTEM. (G) Size of MONT plotted as a function of time.

the distance between each unit of the MONT longitudinally (horizontal Cu···Cu interatomic distance) (Figure 4.2). Crucially, EDS mapping from the same crystallite shows copper and bromine in proportion to the elemental composition from the bulk [(L1)Cu_2Br_2] (Figure 4.4F and See Experimental Section for Figure 4.12) demonstrating, that the same material is formed on the nanoscale as in the bulk material.

The average rate of growth of MONTs is over three times slower at room temperature (0.64 nm/sec) than at 85 °C (2.06 nm/s) (Figure 4.4G). We also examined the growth mechanism of MONTs, as defined by the Lifshitz−Slyozov−Wagner (LSW) model.[125-127] The growth evolution over time was fitted to the power law model as projected area or size, $S \alpha t^n$, where $n \geq ½$ represents the reaction-limited growth where surface specific attachment of monomers is the rate limiting step and $n < ½$ represents the diffusion-limited growth where transport of the reactants is the rate limiting step. The time dependent growth profile of **[(L1)Cu_2Br_2]** measured from its projected area reveals a growth factor following reaction-limited growth, where the power law fit yields a growth exponent $t^{½}$ for 23 and 85 °C (Figure 4.28).[125, 128] This result suggests that irrespective of the thermal energy provided to the system, MONT growth is driven by thermodynamics rather than kinetic effects. In addition, precursor ions or amorphous clusters do not react instantly, but instead seek the lowest energy face of the growing crystal, and induce anisotropic growth.[47, 116] Therefore, size distributions are not affected by the overall availability of the reactant monomers, but by localized effects within the confined LCTEM environment such as rate of nucleation, number of nucleation sites, depletion of precursor ions/amorphous clusters, surface nucleation on the SiNx membrane that controls the surface specific monomer−monomer attachment locally and hence the sizes of MONT bundles.[52, 129-131]

Conclusion

In conclusion, we have observed finite bundles of MONTs on the nanoscale, a critical step toward developing applications for these anisotropic materials that require isolation of these 1D structures. The growth of **[(L1)Cu_2Br_2]** was tracked in real time by LCTEM without electron beam damage or influence to the structures formed. The same MONT material captured over a time course measured in seconds by LCTEM could be examined by conventional single crystal X-ray diffraction, with many days required to grow a sufficiently large crystal. Two microscopy techniques were critical to matching the nanomaterial to the bulk MONT. First, the SAED measurements gave diffraction spots that were consistent with the measured distances between heavy atoms (Cu or Br) that was found in the single crystal X-ray analysis of the MONT. Second, the EDS measurements from TEM imagining confirmed the same elemental composition found in the bulk material. Our analysis shows anisotropic MONT growth is a thermodynamically driven surface-specific monomer−monomer attachment process. Future studies will focus on methods to inhibit or modulate the growth of MONTs to limit them to smaller bundles or even to individual tubes. We anticipate that reaction development of this kind, conducted in tandem with liquid phase TEM experiments, will accelerate the discovery of new MONT materials with new properties.[45, 52]

Experimental

I. General Considerations for Synthesis

Compound **5** was synthesized through a previously published procedure.[97] Compounds **1**, **3**, and **4** were synthesized following modified procedures.[132-134] The synthesis of compounds **1**-**L1** and MONT **[(L1)Cu_2Br_2]** are discussed in this section.

Naphthalene-1,4-dicarboxylic acid was purchased from Alfa Aesar and used with no further purification. Tetrahydrofuran and methylene chloride were dried on an Innovative Technologies (Newburyport, MA) Pure Solv MD-7 solvent purification system and degassed by three freeze-pump-thaw cycles, on a Schlenk line, to remove O_2 prior to use. All other reagents were purchased from commercial vendors and used with no initial purification. ^{1}H and ^{13}C NMR spectra were collected at ambient temperature on either a Varian Mercury 300 MHz, a Varian VNMRS 500 MHz, or a Varian VNMRS 600 MHz narrow-bore broadband system. ^{1}H and ^{13}C NMR chemical shifts were referenced to the residual solvent. All mass spectrometry analyses were conducted at the Mass Spectrometry Center located in the Department of Chemistry at the University of Tennessee. High resolution DART-MS were collected using a JEOL AccuTOF-D time-of-flight (TOF) Mass Spectrometer with a DART (Direct Analysis in Real Time) ionization source from JEOL USA, Inc., Peabody, MA. High resolution ESI-MS were analyzed using an electrospray ionization source set to positive mode with mass analysis performed using an Exactive Plus OrbitrapTM Mass Spectrometer (Thermo Scientific, San Jose, CA, USA). Attenuated Total Reflectance (ATR) Infrared Spectroscopy data were collected on a Thermo Scientific Nicolet iS10 with a Smart iTR accessory. Thermogravimetric analysis was collected on freshly prepared samples on a TA Instruments TGA Q50 under N_2. Elemental analysis of carbon, hydrogen, nitrogen for **[(L1)Cu_2Br_2]** was obtained from Atlantic Microlab, Inc., Norcross, GA.

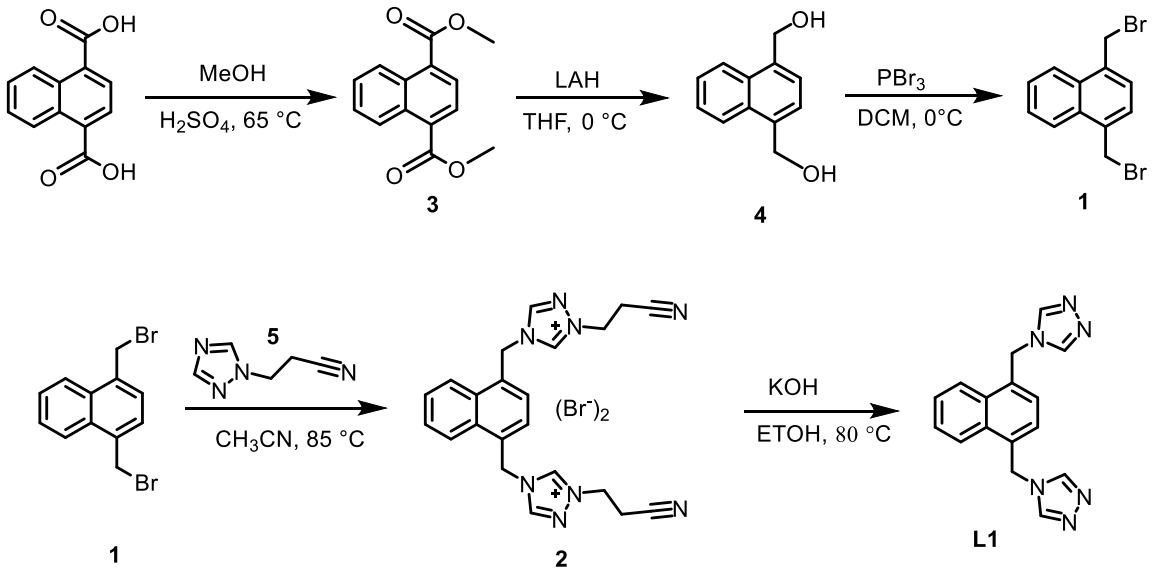

Scheme 4. 1. Synthetic Scheme for **L1**.

Synthesis of dimethyl naphthalene-1,4-dicarboxylate, 3:

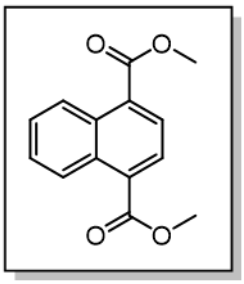

Compound **3** was synthesized by modifying the literature procedure.[133] 1,4-naphthalene dicarboxylic acid (4.999 g, 23.12 mmol) was added to a flask with 50 mL of methanol and stirred until completely dissolved. Concentrated sulfuric acid (2.5 mL) was then added to the reaction flask and the solution was refluxed overnight. The solution was cooled to room temperature, diluted with 50 mL of ethyl acetate, and washed with 10% sodium hydroxide. The organic layer was dried with magnesium sulfate then removed through rotary evaporation, and dried under high vacuum. This yielded a white solid (81.6%, 4.61 g). The spectra match literature values.[135]

DART HR MS (m/z): $[M+H]^+$: 245.08116 (found); $C_{14}H_{13}O_4$: 245.08138 (calculated).

Synthesis of naphthalene-1,4-diyldimethanol, 4:

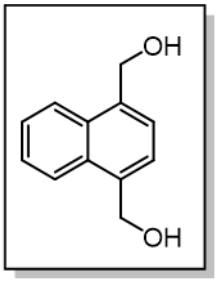

Compound **4** was synthesized by slightly modifying literature procedure with the dimethyl naphthalene-1,4-dicarboxylate analogue, **3**.[134] Compound **3** (1.0016 g, 4.1012 mmol) was weighed into a heated and dried flask and brought into a glovebox with a nitrogen atmosphere. The dicarboxylate was dissolved into 40 mL of dry tetrahydrofuran and sealed with a septum secured with copper wire. Lithium aluminum hydride (LAH) (1.7216 g, 45.365 mmol) was placed into a separate flask with 70 mL of dry tetrahydrofuran and sealed with a septum secured with a copper wire. Both flasks were carefully taken out of the glovebox and placed under nitrogen atmosphere via a Schlenk line. The flask containing the LAH was placed into an ice water bath at 0 °C. The solution of **3** was transferred dropwise into the LAH solution via syringe resulting in a green suspension. Once the transfer was complete, the reaction mixture was allowed to slowly warm up to room temperature and stir overnight. The reaction was cooled to 0 °C and then quenched by addition of approximately 7 mL 10% sodium hydroxide (w/v) followed by 7 mL water dropwise, over 40 minutes. The reaction mixture was diluted with 40 mL ethyl acetate, resulting in a yellow suspension. Quenching the reaction produced alumina which was removed by adding copious amounts of Celite to the flask and stirring for approximately 30 minutes. Additional ethyl acetate was added to facilitate stirring. The solid alumina/Celite mixture was filtered, and the filtrate was collected for isolation of the product. The organic layer

was dried over magnesium sulfate. A pale yellow solid was obtained after solvent was removed under vacuum. The crude product was recrystallized by layering hexanes over an ethyl acetate solution. This yielded a white solid which was dried under high vacuum (96.7%, 0.746 g). Additional characterization that has not been previously reported has been provided.[136]

^{1}H NMR ($CDCl_3$, 599.74 MHz): 8.17 (m, 2H), 7.59 (m, 2H), 7.51 (s, 2H), 5.16 (s, 4H), 1.69 (broad, 2H). ^{13}C NMR (DMSO-d_6, 149.94 MHz): 136.97, 130.81, 125.50, 124.21, 123.72, 61.25. IR: 3293, 2922, 1597, 1513, 1466, 1439, 1392, 1341, 1260, 1224, 1162, 1086, 1062, 1006, 985, 935, 848, 795, 775, 746, 700 cm^{-1}. DART HR MS (m/z): $[M+Na]^+$: 211.0726 (found); $C_{12}H_{12}O_2Na$: 211.0730 (calculated).

Synthesis of 1,4-bis(bromomethyl)naphthalene, 1:

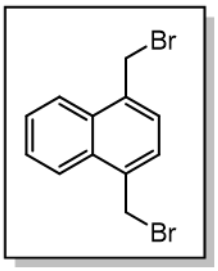

Compound **1** was synthesized by slight modification of a literature procedure with the naphthalene-1,4-diyldimethanol analogue, **4**.[132] Diol starting material, **4**, (2.237 g, 11.88 mmol) was suspended in 50 mL of dry methylene chloride in a dried and heated flask sealed with a septum secured with copper wire while under inert nitrogen atmosphere of a glovebox. Potassium tribromide (9.65 g, 35.7 mmol) was measured into a separate dried and heated flask and sealed with a septum secured with copper wire. Both flasks were carefully taken out of the glovebox and placed under nitrogen atmosphere via a Schlenk line. The flask containing the diol was placing into an ice water bath at 0 °C. The potassium tribromide was transferred via syringe dropwise into the diol solution at 0 °C. Once the transfer was complete, the reaction flask was allowed to slowly warm up to room temperature and stir for 4 hours. The resulting solution was then slowly poured into ice water (100 mL). Product was extracted with methylene chloride,

dried with magnesium sulfate, and solvent was removed through rotary evaporation and a high vacuum, yielding a white solid (82.4%, 3.07 g).

^{1}H NMR ($CDCl_3$, 599.74 MHz): 8.21 (m, 2H), 7.67 (m, 2H), 7.48 (s, 2H), 4.93 (s, 4H). ^{13}C NMR ($CDCl_3$, 125.66 MHz): 135.06, 131.73, 127.39, 127.02, 124.74, 31.37. IR: 2923, 1724, 1517, 1444, 1391, 1277, 1252, 1201, 1165, 1114, 1073, 1047, 1006, 951, 891, 846, 795, 769, 751, 697, 650 cm^{-1}. DART HR MS (m/z): $[M+H]^+$: 314.92452 (found); $C_{12}H_{11}Br_2$: 314.92074 (calculated).

Synthesis of 4,4'-(naphthalene-1,4-diylbis(methylene))bis(1-(2-cyanoethyl)-4H1,2,4-triazol-1-ium) bromide, 2:

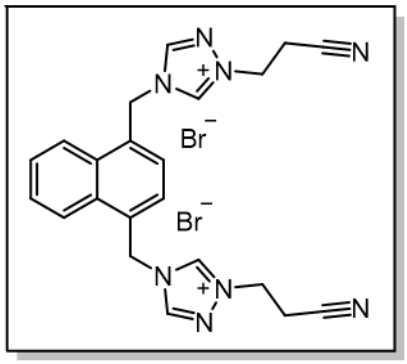

1,4-bis(bromomethyl)naphthalene (0.0792 g, 0.252 mmol), **1**, was dissolved in 10 mL of acetonitrile with 3-(1H-1,2,4-triazol-1-yl)propanenitrile (0.0642 g, 0.526 mmol), **5**, and refluxed for 3 days. The reaction mixture was cooled to room temperature. Diethyl ether was added to precipitate product which was then filtered through a fine frit, yielding a white solid (0.0924 g, 97.5%).

^{1}H NMR (DMSO-d_6, 499.74 MHz): 10.35 (s, 2H), 9.41 (s, 2H), 8.28 (m, 2H), 7.74 (m, 2H), 7.73 (s, 2H), 6.13 (s, 4H), 4.72 (t, 4H), 3.22 (t, 4H). ^{13}C NMR (DMSO-d_6, 125.66 MHz): 145.10, 143.49, 130.84, 130.81, 128.14, 127.84, 124.07, 117.65, 48.46, 47.27, 17.33. IR: 3103, 3029, 2963, 2251, 1807, 1574, 1519, 1440, 1415, 1372, 1342, 1288, 1226, 1184, 1139, 1071, 979, 923, 848, 774, 747, 627 cm^{-1}. HR ESI-MS (m/z): $[M-Br+H]^+$: 477.1136 (found); $C_{22}H_{22}BrN_8^+$: 477.1145 (calculated).

Synthesis of 1,4-bis((4H-1,2,4-triazol-4-yl)methyl)naphthalene, L1:

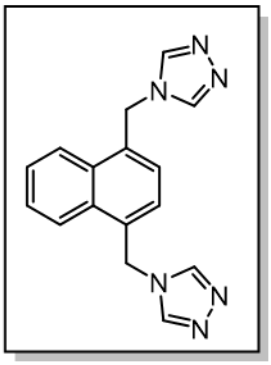

A slurry of **2** (0.3500 g, 0.6269 mmol) and potassium hydroxide (0.0986 g, 1.7573 mmol) was refluxed overnight in 15 mL of ethanol. This yielded a white solid that was collected on a fine frit (0.200 g, 78.0%).

^{1}H NMR (DMSO-d_6, 499.74 MHz): 8.61 (s, 4H), 8.23 (m, 2H), 7.66 (m, 2H), 7.32 (s, 2H), 5.80 (s, 4H). ^{13}C NMR (DMSO-d_6, 125.66 MHz): 143.40, 132.99, 130.57, 127.02, 126.01, 123.92, 45.42. IR: 3110, 1602, 1533, 1514, 1454, 1431, 1386, 1373, 1337, 1252, 12160, 1183, 1150, 1084, 1077, 1039, 994, 970, 952, 873, 819, 806, 772, 754, 745 cm^{-1}. DART HR MS (m/z): $[M+H]^+$: 291.13692 (found); $C_{16}H_{15}N_6$: 291.13582 (calculated).

Synthesis of [(L1)Cu_2Br_2]:

Copper(II) bromide dihydrate (0.0037 g, 0.0166 mmol) was dissolved in 1 mL DI water and heated at 85 °C for 10 minutes. The ligand (0.0049, 0.0169 mmol), **L1**, was dissolved in 2 mL DEF and heated at 85 °C until dissolved. The hot solutions were combined in a 4 mL scintillation vial and heated at 85 °C for 5 days to afford an off-white precipitate. The solid was washed with water and acetone to yield the pure product (0.0016 g, 33.7% yield). Single crystals of **[(L1)Cu_2Br_2]** were grown as colorless needles by combining dilute solutions of the metal (5.4 µM) and ligand (9.2 µM) at 85 °C for 5 days.

IR(neat): 3112, 3015, 2961, 1668, 1606, 1540, 1524, 1472, 1431, 1395, 1377, 1360, 1283, 1262, 1220, 1192, 1109, 1082, 1042, 1012, 985, 972, 952, 857, 825,

804, 759, 746 cm^{-1}. Anal. Calcd. For $C_8H_6N_3BrCu \cdot H_2O \cdot 0.5\ C_5H_{11}NO$: C, 35.41; H, 3.82; N, 13.76. Found: C, 35.87; H, 3.63; N, 13.29.

X-ray Structure Determinations

Ligand (**L1**) crystals were recrystallized in warm acetonitrile overnight. A colorless plate crystal was mounted in the 100 K cold stream provided by an Oxford Cryostream low-temperature apparatus on the head of a Bruker SMART APEXII diffractometer equipped with an ApexII CCD detector, employing the use of Mo K*α* radiation (λ = 0.71073 Å).

[(L1)Cu_2Br_2] crystals were grown directly from the reaction vial. A colorless plate was mounted in the 100 K cold stream provided by an Oxford Cryostream low-temperature apparatus on the head of a Bruker D8 diffractometer equipped with a PHOTON 2 CMOS detector, at beamline 12.2.1 of the Advanced Light Source (Lawrence Berkeley National Laboratory, Berkeley, CA). Data were collected with the use of synchrotron radiation (λ = 0.7288 Å).

All data sets were reduced with Bruker SAINT and were corrected for absorption using SADABS. Structures were solved and refined using SHELXT and SHELXL-2015, respectively.

Powder X-ray Experiments

Powder X-ray diffraction data were collected on the sample using a Panalytical Empyrean θ-2θ diffractometer in reflectance Bragg-Brentano geometry. Cu-Kα radiation (λ= 1.5406 Å; 1,800 W, 45 kV, 40 mA) was focused using a planar Gobel Mirror riding the K*α* line. A 0.25 mm divergence slit was used for all measurements. Diffracted radiation was detected using a PIXcel3d detector [(6° 2θ sampling width) equipped with a Ni monochromator. **[(L1)Cu_2Br_2]** sample was mounted onto a zero-background quartz plate fixed on a sample holder by dropping a suspension of the MONT powder in acetone onto the plate. The

acetone was then allowed to evaporate, leaving a thin film of **[(L1)Cu_2Br_2]** on the sample plate. The best counting statistics were achieved by using a 0.0394º 2θ step scan from 3 – 50° with an exposure time of 118.30 s per step and a revolution spin rate of 4 s.

II. Single Crystal X-ray Structures

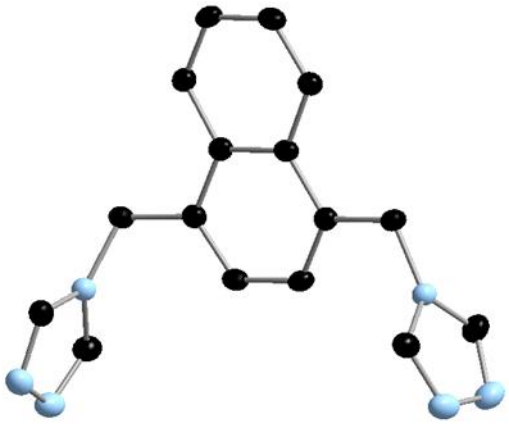

Figure 4. 5. Single Crystal X-ray structure of L1 ligand. Black, and light blue ellipsoids (50% probability) represent carbon and nitrogen atoms respectively. Hydrogen atoms have been omitted for clarity.

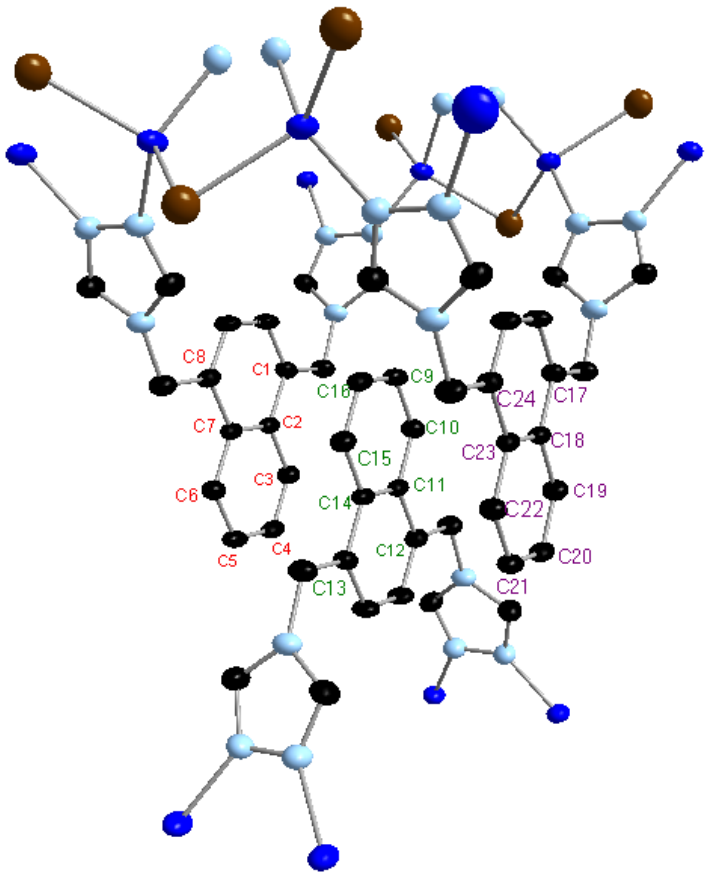

Figure 4. 6. Single Crystal X-ray structure showing the π- π distances from the alternating aromatic rings of the naphthyl of two adjacent [(L1)Cu_2Br_2]'s.

Table 4. 1. π-π distances from the alternating aromatic rings of the naphthyl of two adjacent [(L1)Cu_2Br_2]'s as shown in Figure 4.6.

Atoms	Pi-Pi Distance (Å)
C1···C9	3.5635 (4)
C2···C10	3.5582 (4)
C3···C11	3.5582 (4)
C4···C12	3.5635 (4)
C5···C13	3.5635 (4)
C6···C14	3.5582 (4)
C7···C15	3.5582 (4)
C8···C16	3.5635 (4)
C9···C17	3.5635 (4)
C10···C18	3.5582 (4)
C11···C19	3.5582 (4)
C12···C20	3.5635 (4)
C13···C21	3.5635 (4)
C14···C22	3.5582 (4)
C15···C23	3.5582 (4)
C16···C24	3.5635 (4)

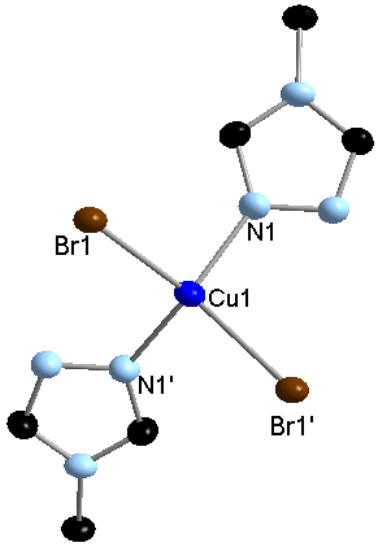

Figure 4. 7. Copper connectivity in [(L1)Cu_2Br_2].

Table 4. 2. Corresponding bond angles and bond lengths for [(L1)Cu_2Br_2].

Atoms	Bond Angle/Distance (°/Å)
Br1-Cu1-N1	98.693(2)
N1-Cu1-Br1'	102.309(3)
Br1'-Cu1-N1'	98.693(2)
N1'-Cu1-Br1	102.309(3)
N1-Cu1-N1'	137.736(2)
Br1-Cu1-Br1'	119.303(1)
Cu1-N1	1.9704(1)
Cu1-Br1	2.5402(2)
Cu1-N1'	1.9704(1)
Cu1-Br1'	2.5402(2)

III. Selected Spectra and Analytical Data for 1-5 and MONT

The corresponding spectra and analytical data for compounds **1**, **2**, **4**, **L1**, and metal-organic nanotube **[(L1)Cu_2Br_2]** are presented in this section.

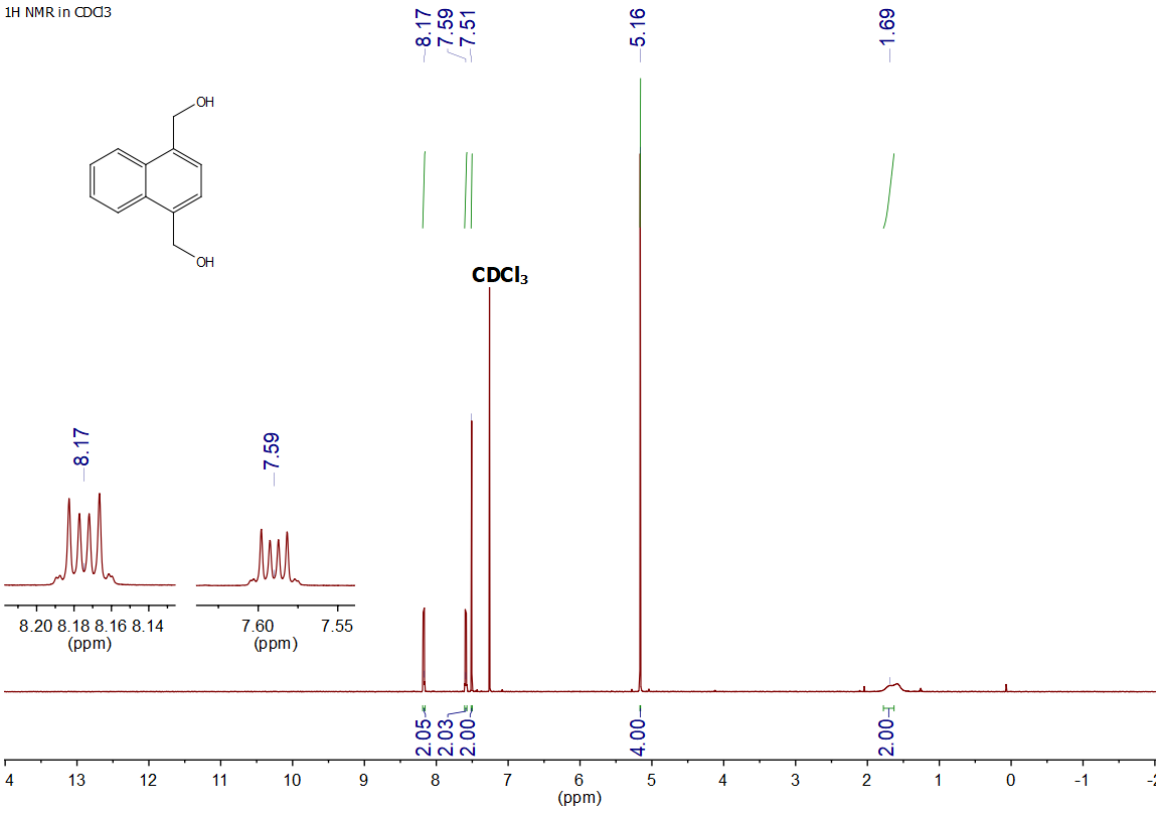

Spectra 4. 1. ^{1}H NMR of 4 in $CDCl_3$.

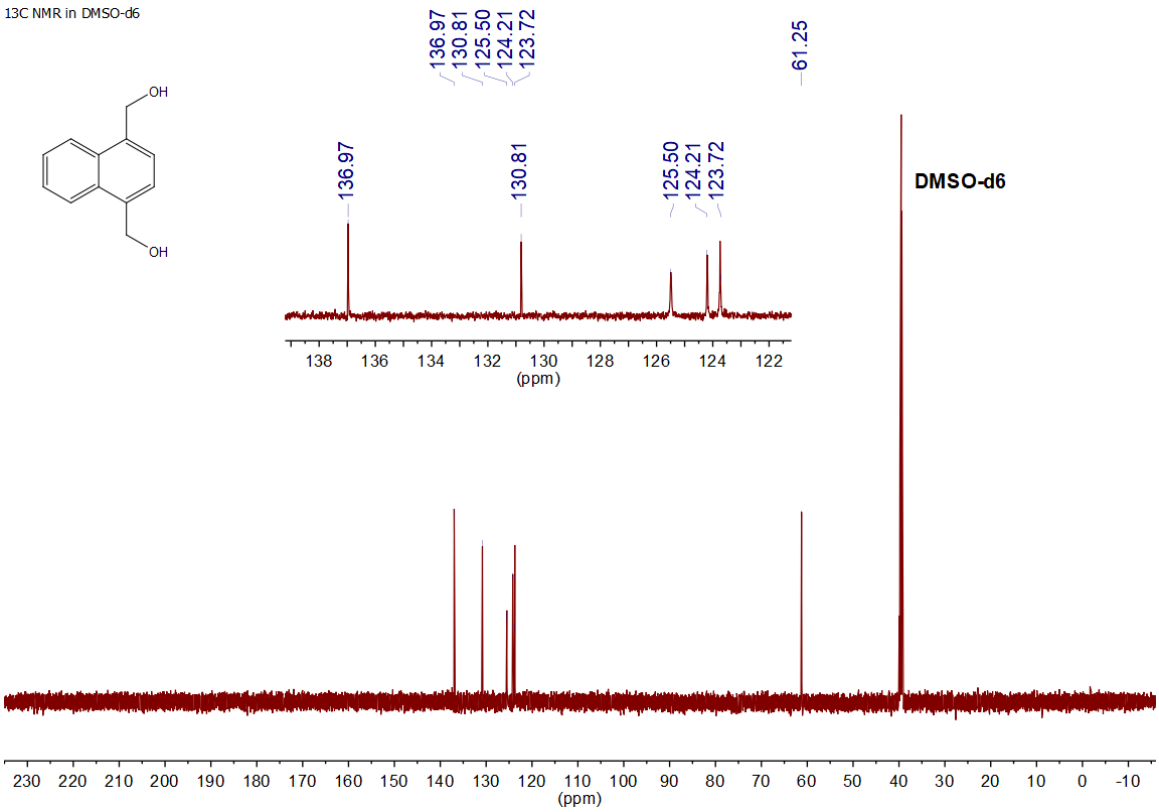

Spectra 4. 2. ^{13}C NMR of 4 in DMSO-d$_6$.

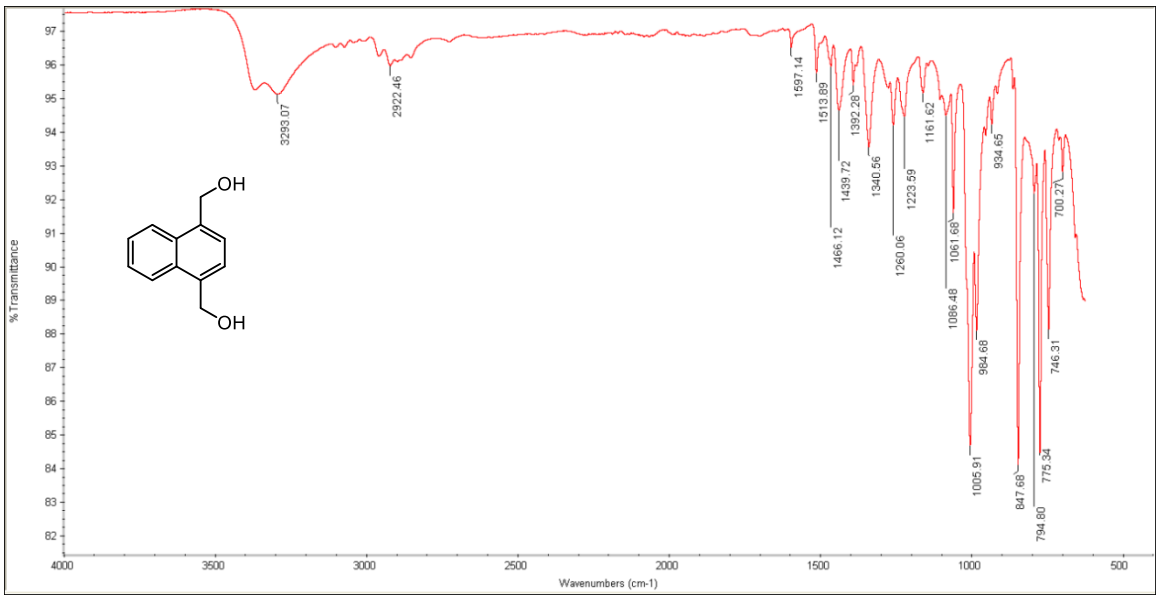

Spectra 4. 3. ATR-IR of 4.

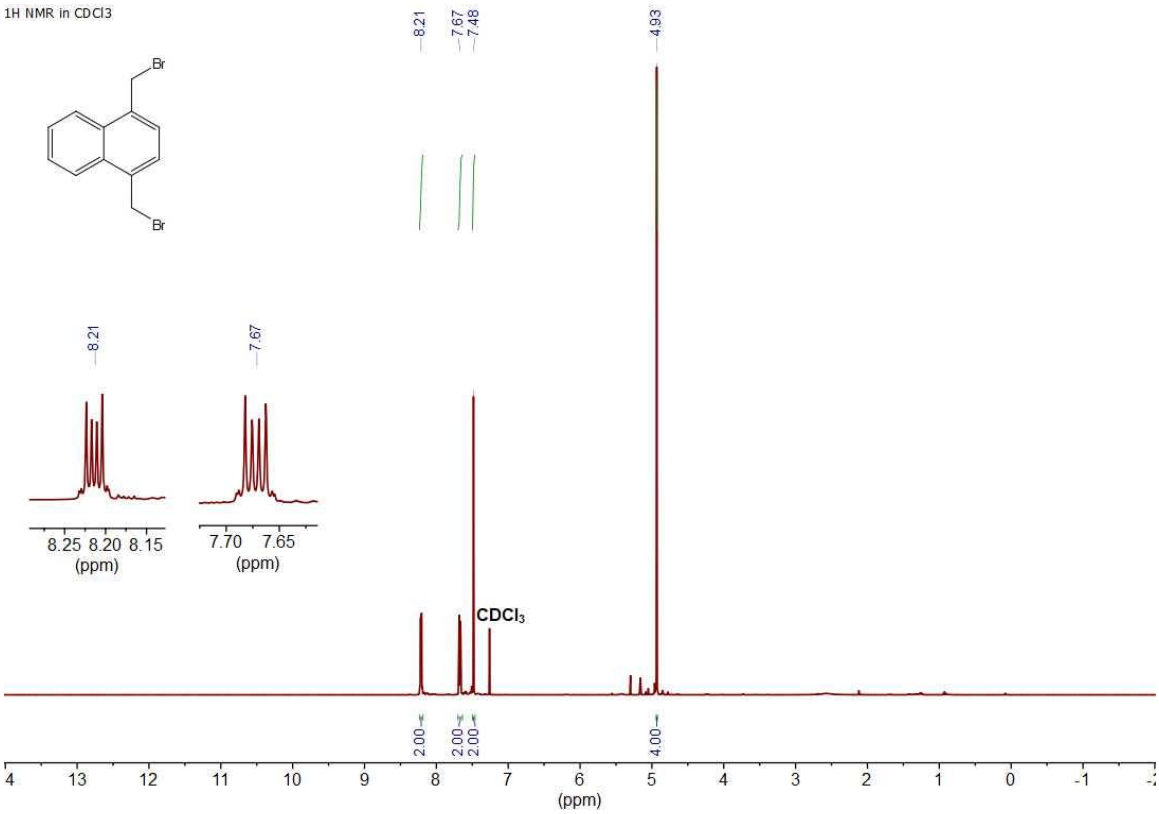

Spectra 4. 4. ^{1}H of 1 in $CDCl_3$.

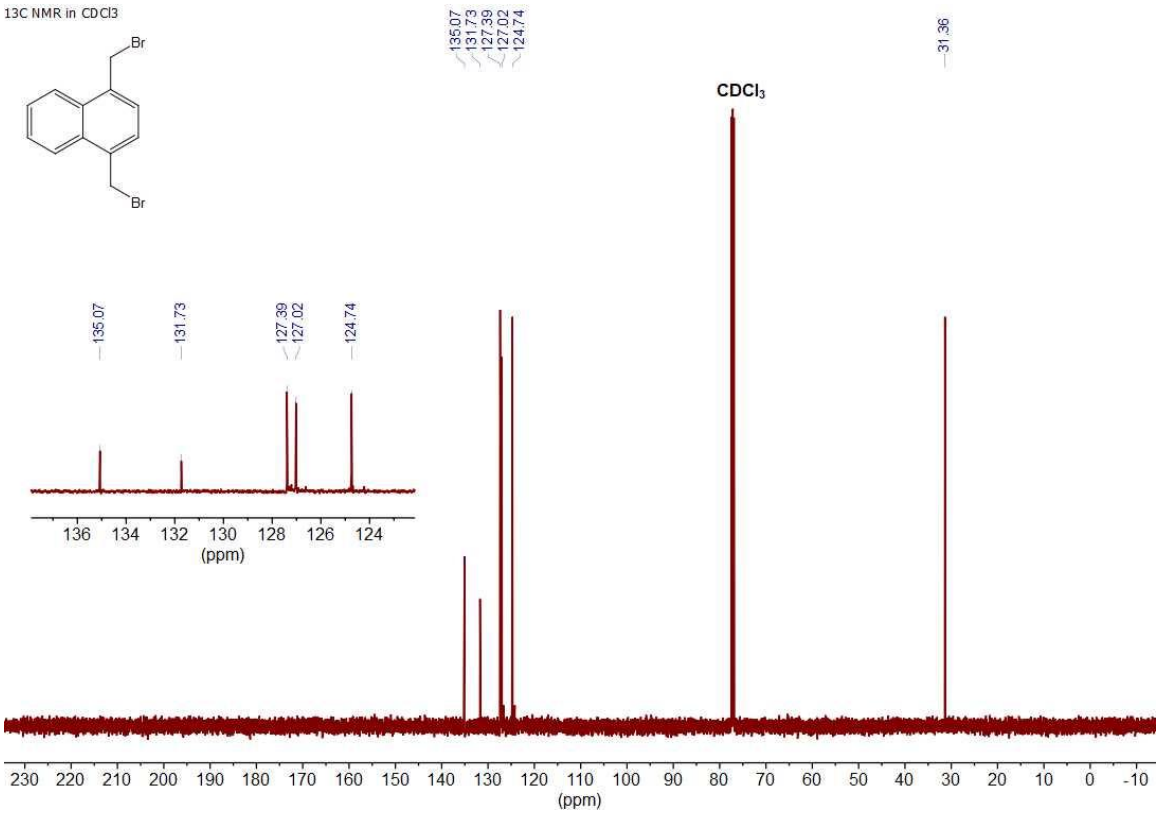

Spectra 4. 5. ^{13}C NMR of 1 in $CDCl_3$.

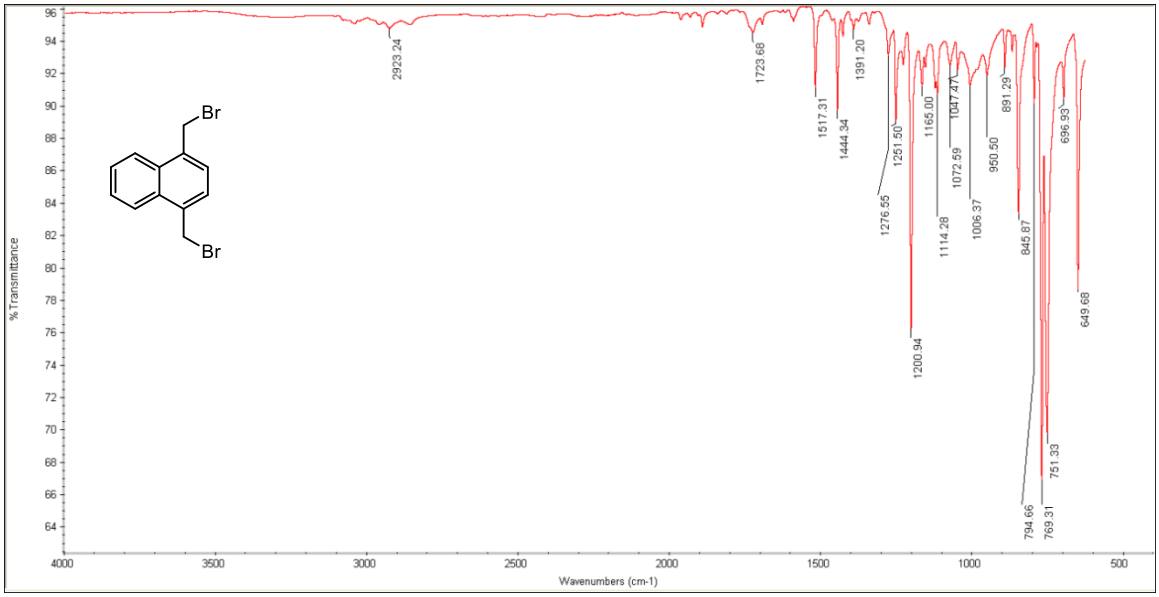

Spectra 4. 6. ATR-IR of 1.

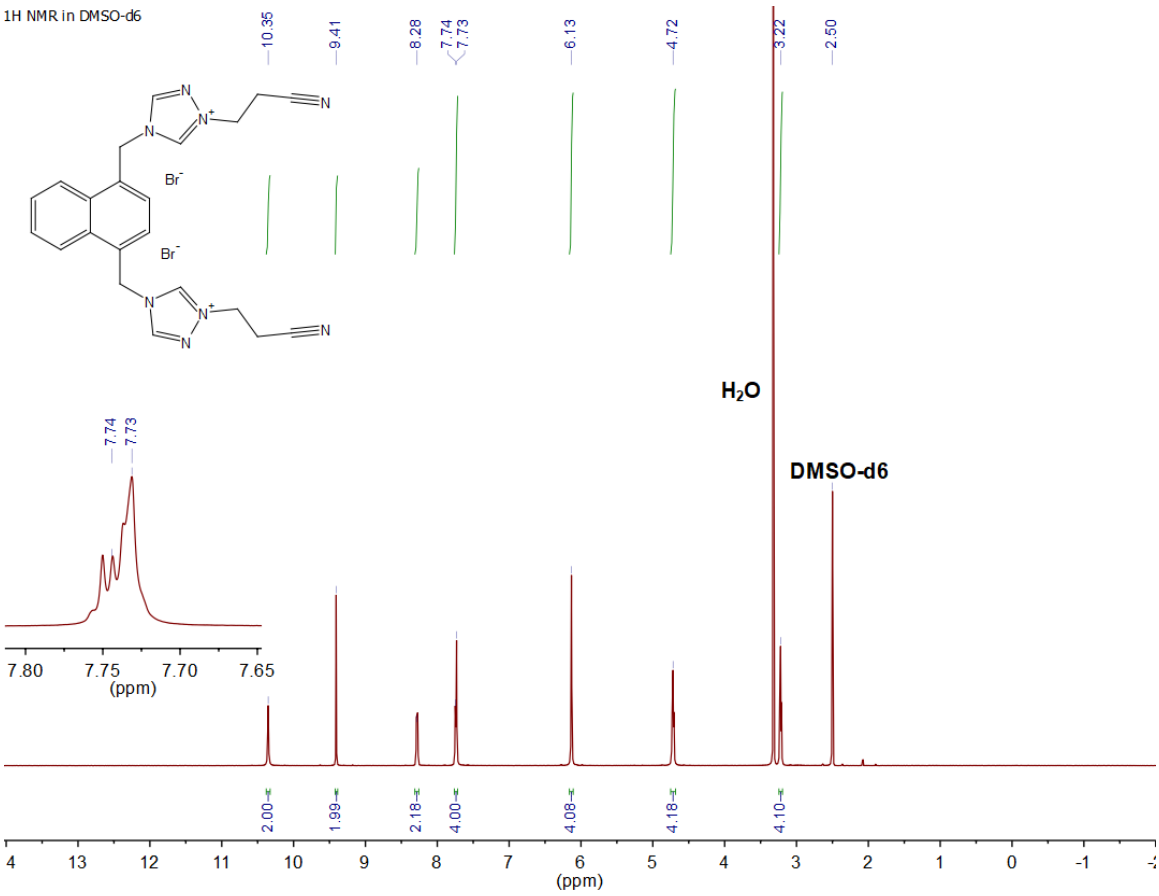

Spectra 4. 7. ^{1}H NMR of 2 in DMSO-d$_6$.

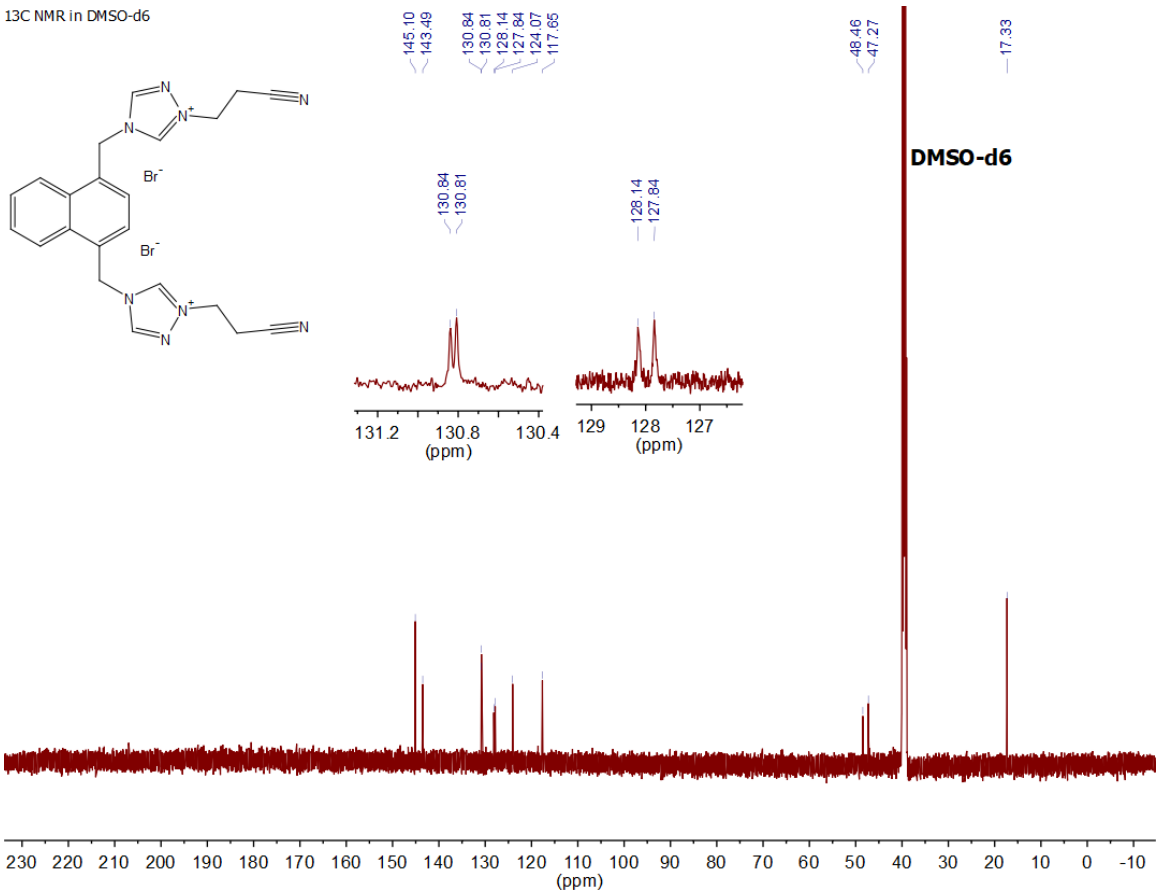

Spectra 4. 8. ^{13}C NMR of 2 in DMSO-d_6.

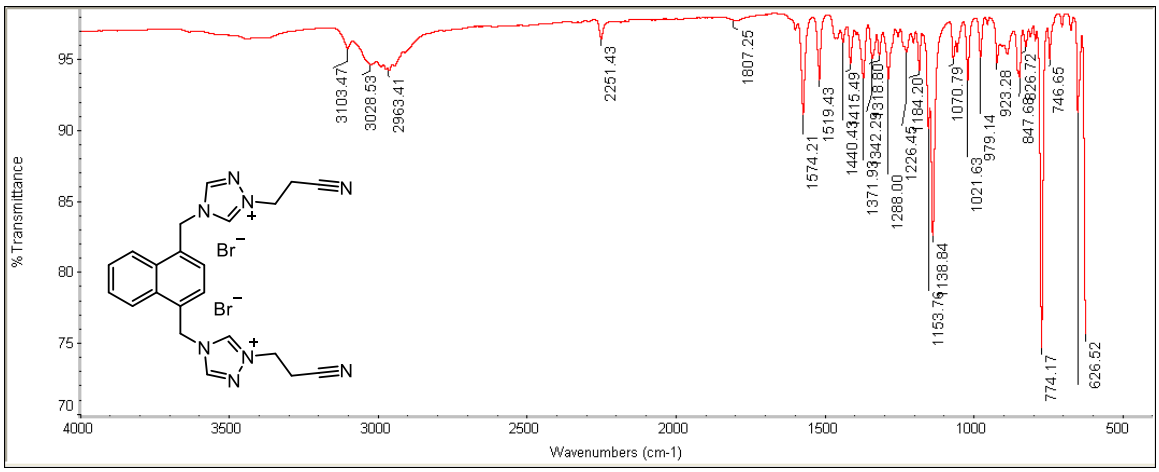

Spectra 4. 9. ATR-IR of 2.

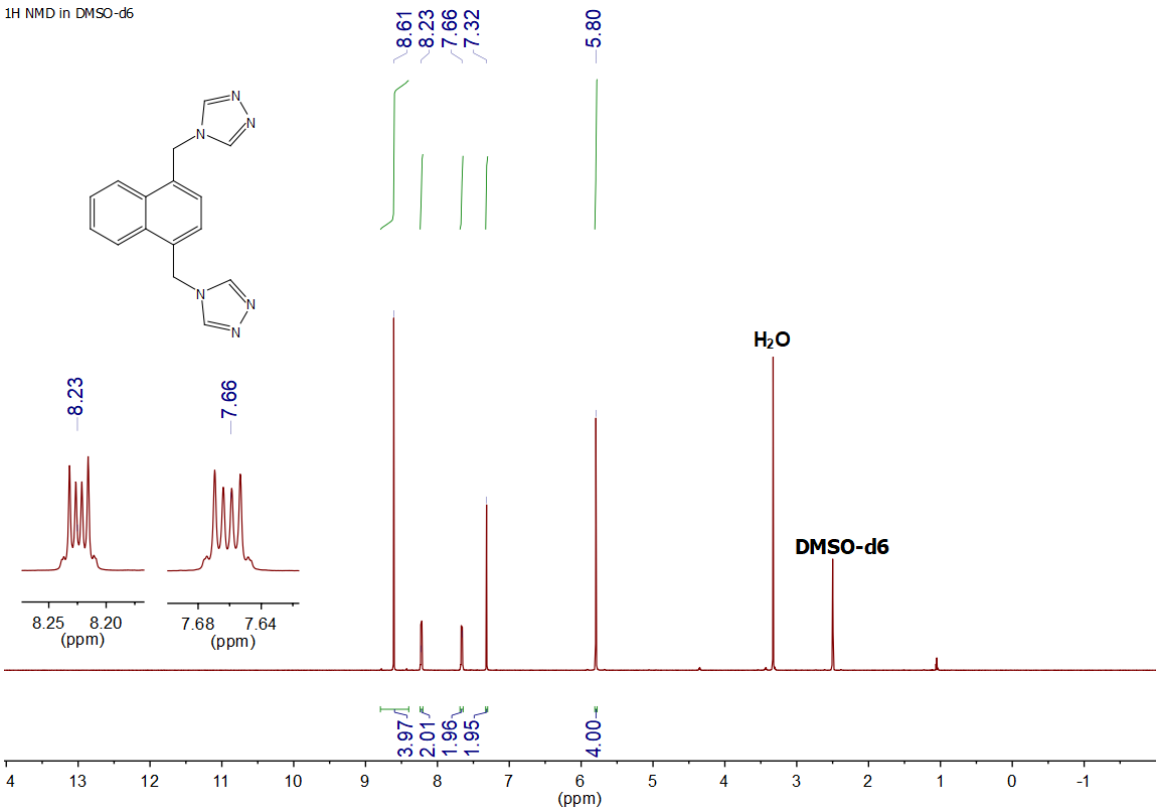

Spectra 4. 10. ^{1}H NMR of L1 in DMSO-d$_6$.

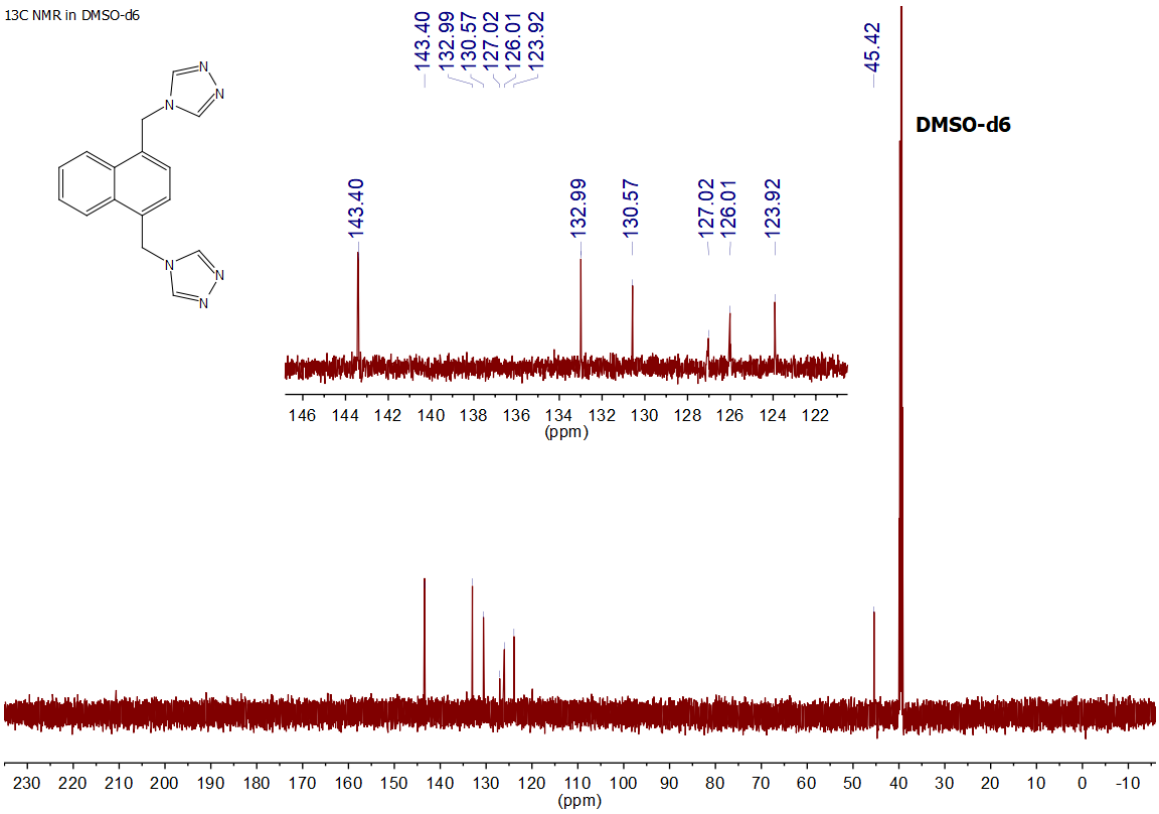

Spectra 4. 11. ^{13}C NMR of L1 in DMSO-d$_6$.

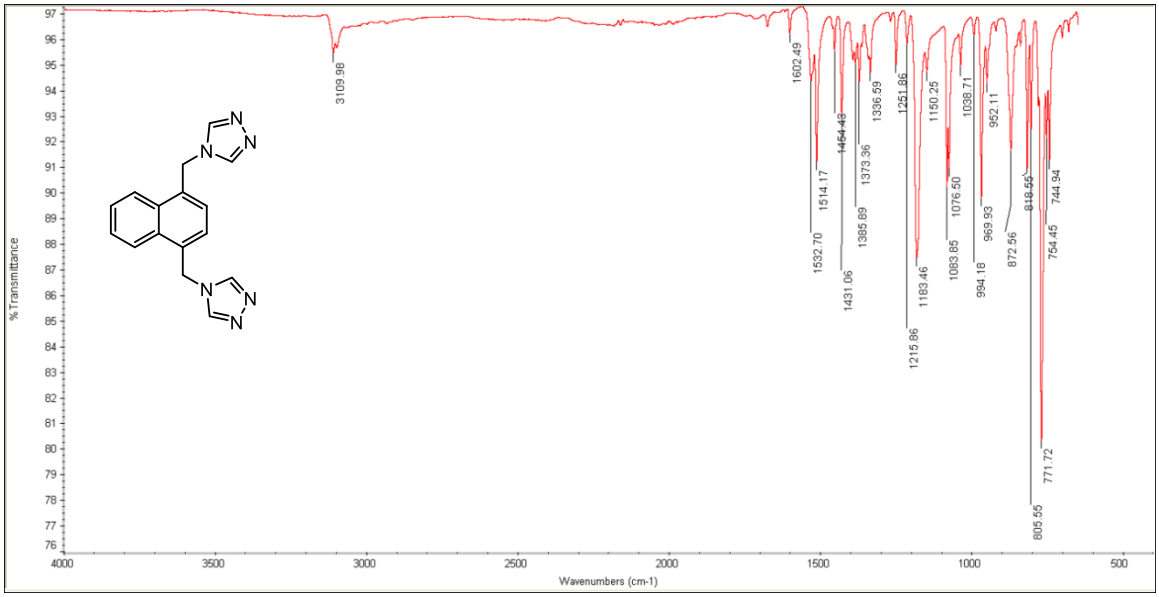

Spectra 4. 12. ATR-IR of L1.

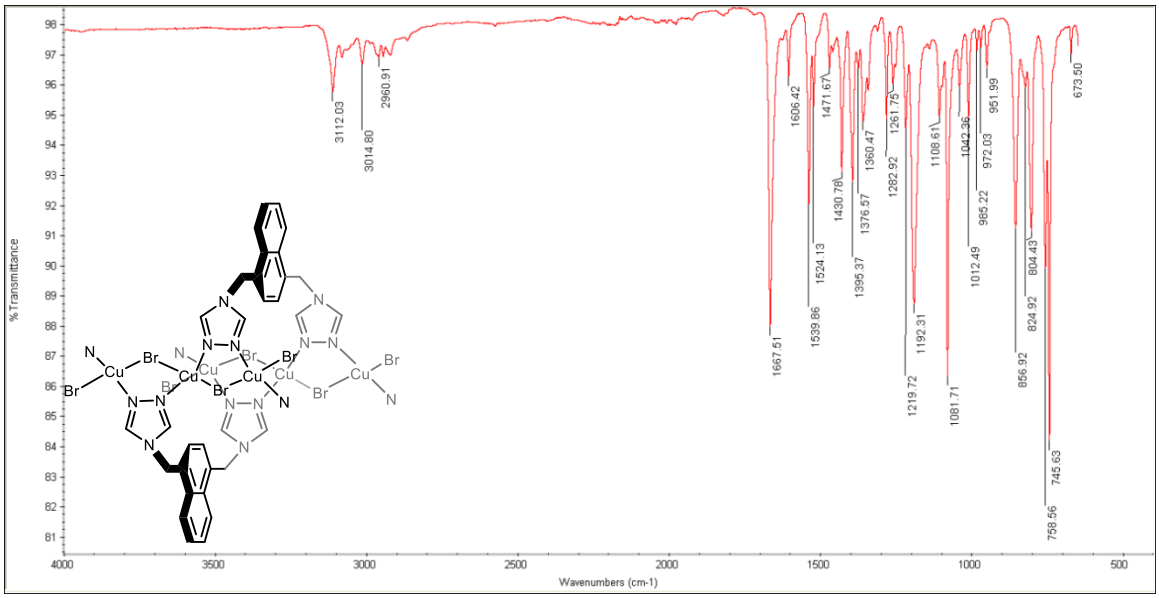

Spectra 4. 13. ATR-IR of [(L1)Cu_2Br_2].

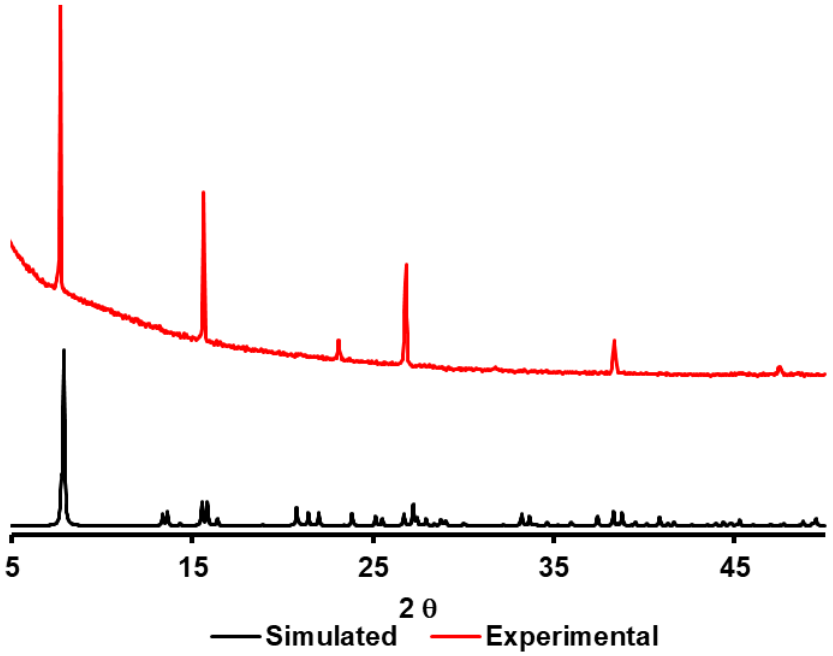

Spectra 4. 14. Simulated (black) and experimental (red) PXRD of [(L1)Cu_2Br_2].

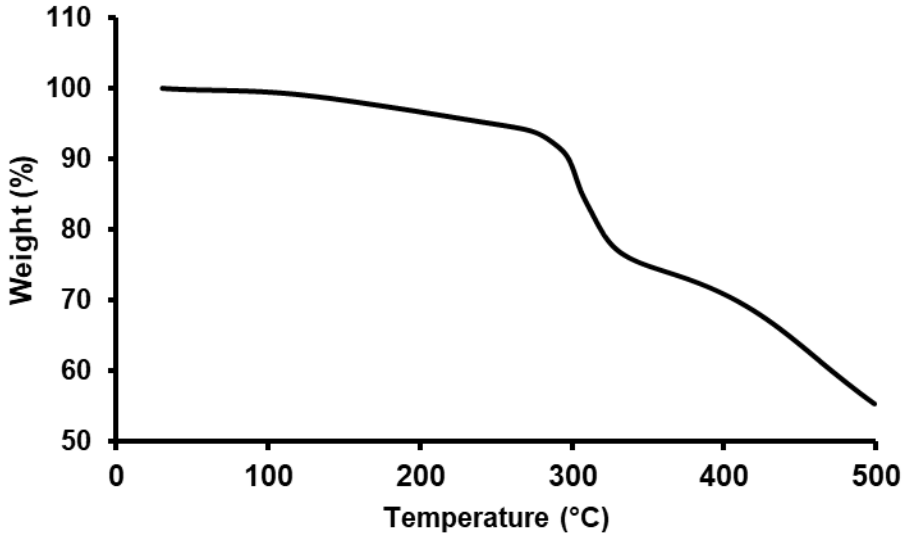

Spectra 4. 15. TGA of [(L1)Cu_2Br_2].

IV. TEM and LCTEM Imaging

TEM and LCTEM imaging was performed using a JEOL ARM300F GrandARM TEM with Gatan OneView-IS camera operated at 300 keV. Post-mortem EDS analyses were performed in HAADF-STEM mode at a camera length of 20 cm.

[(L1)Cu_2Br_2] is sensitive to the electron beam and undergoes significant beam induced transformations. However, under controlled electron dose (< 0.5 e–/Å2), and careful operation, HRTEM images of lattice spacing of MONT crystals can be acquired as shown in Figure 4.23. The spacing measured from FFT (of Figure 4.23B and 4.23D) reveals the MONT crystal along the direction and, respectively (see Figure 2 in Manuscript).

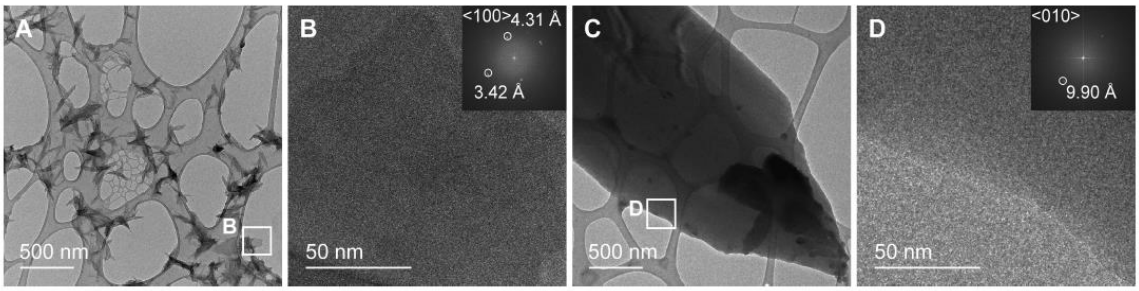

Figure 4. 8. TEM images of MONT and their corresponding FFT illustrates their lattice spacing.

For in situ liquid-cell TEM experiments, we used a Protochips Poseidon Select Heating holder (i.e. using 2 separate inlets and 1 outlet). Firstly, the liquid-cell chips (with 50 nm silicon nitride thickness) were cleaned in acetone and methanol to remove the photoresist layer. Subsequently, top and bottom chips were plasma cleaned for 5 minutes to induce hydrophilicity. Finally, the chips were assembled in the tip of the holder, and leak checked to prevent breakage of the column vacuum during the experiment. After inserting the holder into the column of the microscope, $CuBr_2$ in DI water and **L1** in DEF were allowed to flow through the inlets separately using a syringe pump at the rate of 1 µl/min. After approximately 20 min, we observed the wetting of the liquid-cell. Once, the wetting of the chips was observed, they were heated to 85 °C using a Protochips temperature controller at the rate of 1 °C/sec. During heating the chips were not exposed to the electron beam. Once the temperature reached 85 °C, the movies of growth events were captured using screen recorder software (Camtasia Studio 7 Recorder screen capture software – TechSmith Corporation, USA). Before starting movie capture, the wetted liquid cell was exposed to the electron beam for approximately 2-3 min. Note: All the TEM alignments, beam settings, dose settings, and calibrations were carried-out prior to the liquid-cell experiments using a standard gold nanoparticles or diffraction grating waffle TEM sample.

We also performed the growth experiments at room temperature, with minimum exposure of the electron beam. Precisely, reactant monomers were flowed in and allowed to mix, nucleate and grow in the pumping station (outside the microscope). After confirming the mixing of reactants, the liquid-cell holder was transferred to the column of the microscope and several time lapse images were acquired at various time points.

V. LCTEM—Dose Analysis

The effect of the electron beam, and its interactions with the reactant molecules cannot be avoided.[45, 122] Hence, to prevent and minimize the effect of

the electron beam during in situ growth experiments, we performed several trial and error experiments at various electron flux conditions. At an electron flux of ~1 e–Å–2s–1 (with beam current of 1.52 nA), de-wetting of the chips was predominant upon irradiating with the electron beam. Immediately after the electron beam exposure, the reactant mixture receded away from the viewing area (exposed area). And, further exposure results in the nucleation of residual metal precursors onto the SiNx membrane (Figure 4.24). By reducing the electron flux to 0.36 e–Å–2s–1 (with beam current of 0.63 nA), de-wetting of the liquid-cell was prevented, and we do not observe any apparent beam induced transformation, or damage. Nevertheless, upon heating the reactants to 85 °C, we did not observe the formation of MONTs in the viewing area. MONTs were formed in other regions that were not exposed to the electron beam (Movie 4.2, https://pubs.acs.org/doi/10.1021/jacs.9b04586, Figure 4.25). Upon irradiating these growing MONTs, beam induced transformations and damage can be observed after certain cumulative electron flux. Initially, MONT growth was observed. As the cumulative electron flux exceeds ~11 e–Å–2, the MONTs shrink and disappear. After the cumulative electron flux of ~20 e–Å–2, we observed the formation of smaller structures from the dissolved MONT. By further increase in electron flux (at ~27 e–Å–2 of cumulative electron flux), we observed the complete destruction of MONT material, resulting in the formation of secondary products (Movie 4.1, https://pubs.acs.org/doi/10.1021/jacs.9b04586). For the room temperature experiments, we used an electron flux of 0.15 e–Å–2 and time lapse images were acquired for every 100 sec with an exposure of 1 sec.

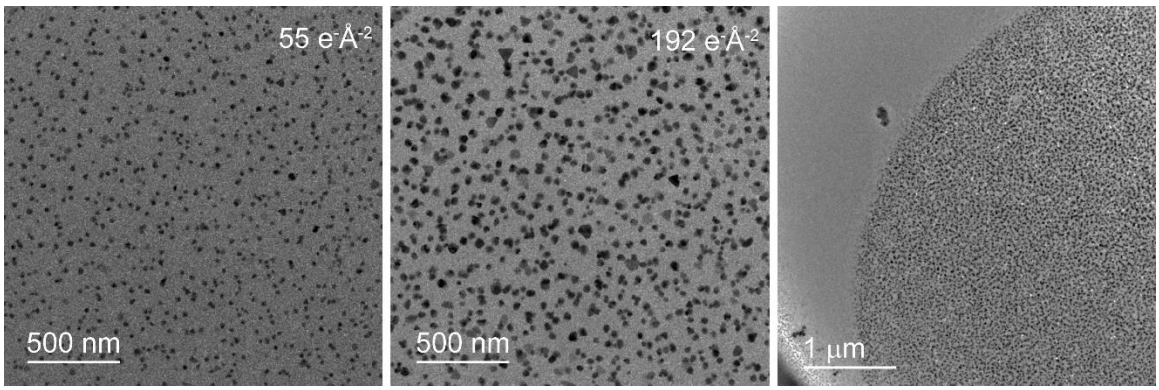

Figure 4. 9. Snapshots of de-wetted LCTEM chip illustrates the formation of metal nanoparticles from the residual metal precursors after prolonged exposure at high flux.

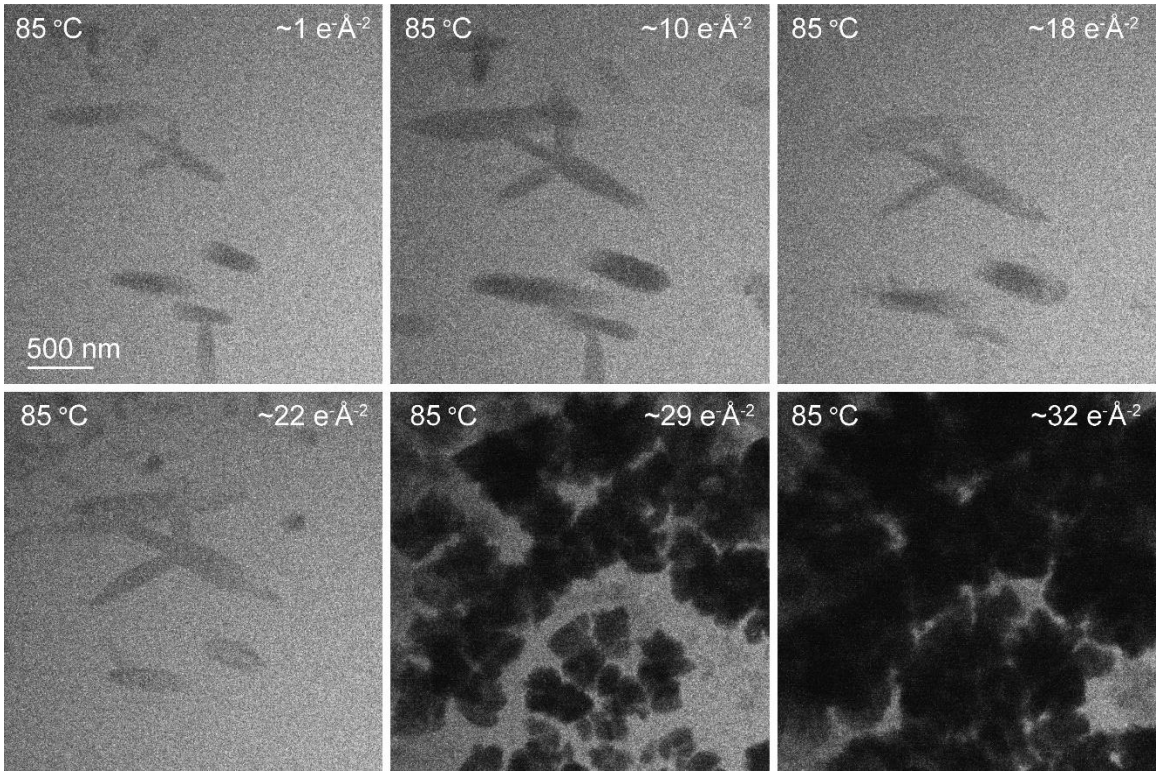

Figure 4. 10. Snapshots of growth of [(L1)Cu_2Br_2] MONT and subsequent beam induced transformation/damage (snapshots from Movie 4.2, https://pubs.acs.org/doi/10.1021/jacs.9b04586**).**

VI. LCTEM—Post-mortem Analyses

Post-mortem analyses were performed after the in-situ TEM experiments. The liquid-cell chips were opened carefully and washed gently with pure water to remove the excess reactants and solvent mixture. The chips were then placed on a standard TEM holder and analyzed by EDS and diffraction.

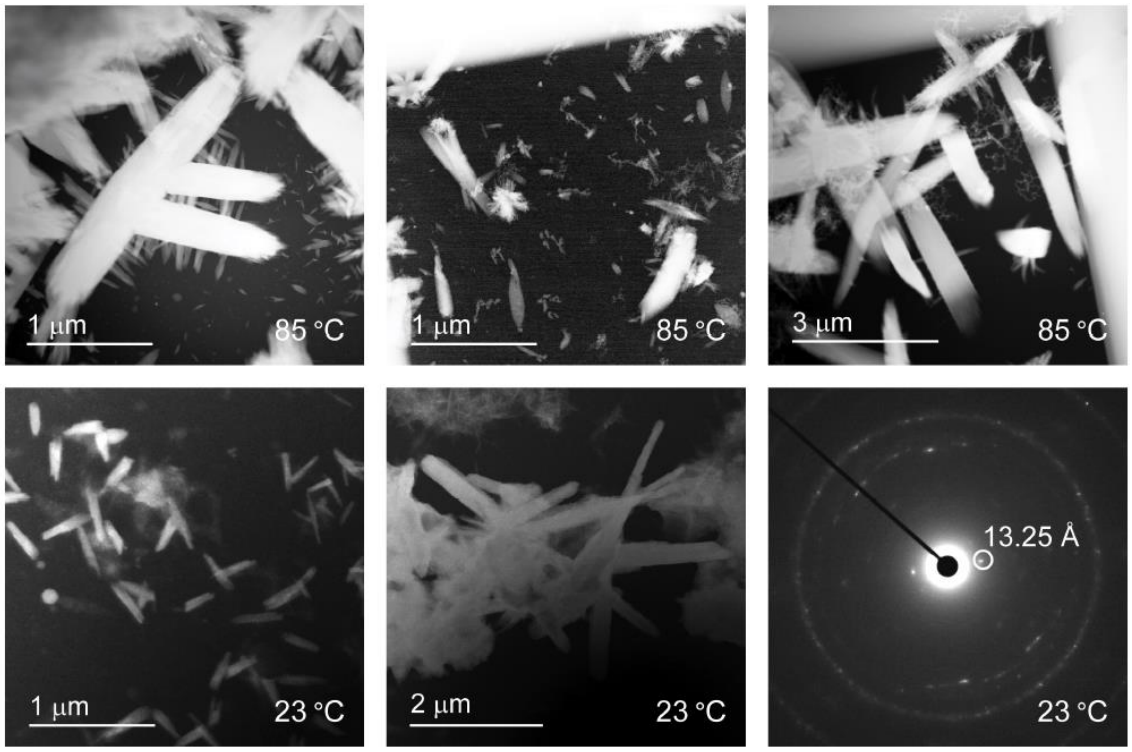

Figure 4. 11. HAAD-STEM images and SAED of MONT grown within the liquid-cell.

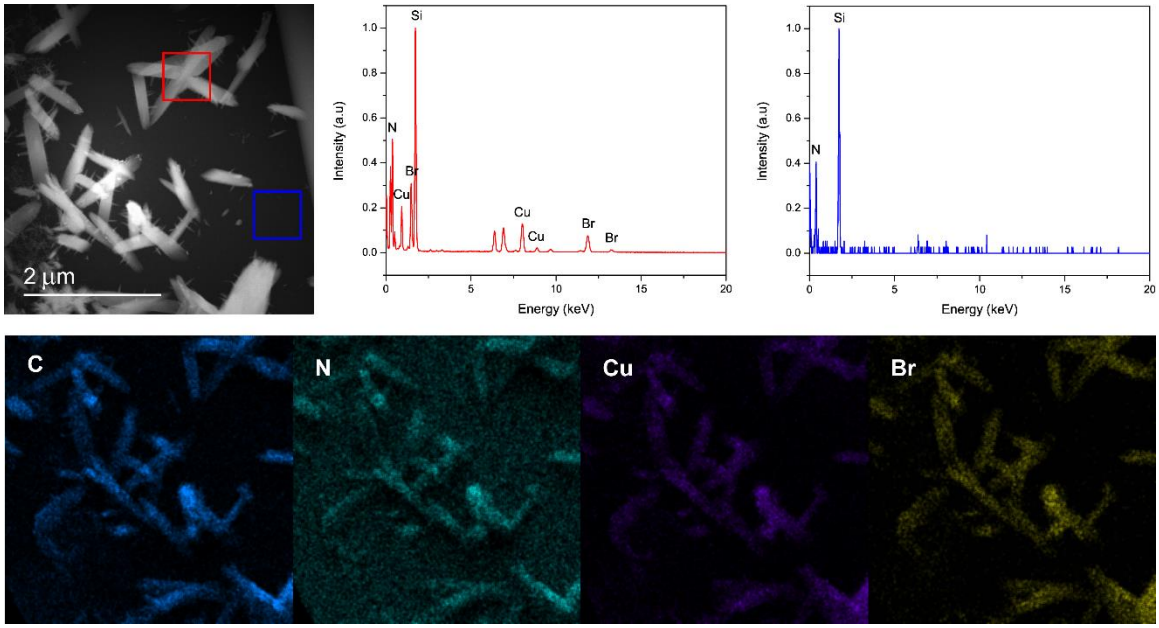

Figure 4. 12. EDS analysis of MONT grown at 85 °C – HAADF-STEM image EDS spectrum and corresponding elemental mapping illustrates the formation of micron sized MONTs within the liquid-cell. Note: In addition to light elements, Cu, Br, strong Si signal originates from the SiN membrane of the LCTEM window. The peaks between 5 and 7.5 keV represent Fe and Co from the TEM holder.

VII. Kinetic Measurements from LCTEM Data

Growth exponents of MONTs were measured by fitting the size vs. time data to power law: y = axt + c, where y is the normalized area measured by image analysis (see Image Analysis, Section VII), x is the time (in sec), c is the uncertainty in the data, t is the growth exponent which reveals whether the growth process is predominately diffusion limited (when t < ½) or surface-reaction limited (when t ≥ ½) as proposed by Lifshitz−Slyozov−Wagner (LSW) model.[125-127] Power law fit to our data yields a = 0.1, t = ½, c = –0.48 with R2 = 0.98 for elevated temperature measurements; a = 0.04, t = ½, c = – 0.48 with R2 = 0.99 for room temperature measurements.

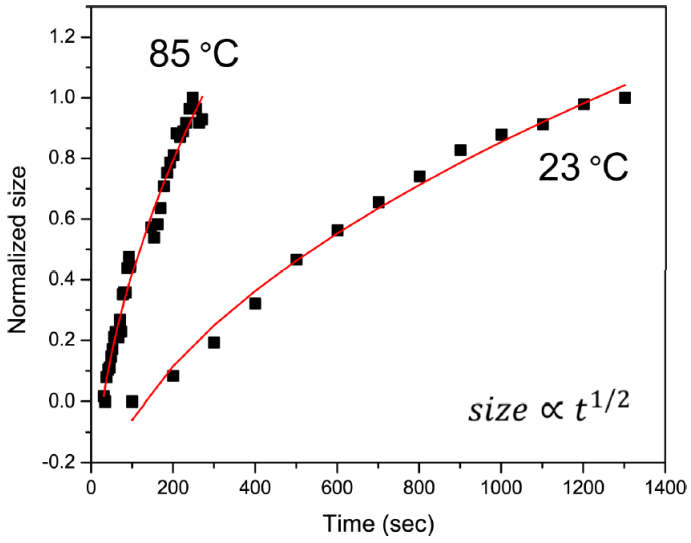

Figure 4. 13. Power law fitting to the kinetic data measured from LCTEM data.

VIII. Image Analysis

To quantify the growth parameters of MONTs, the acquired time series were segmented frame-by-frame. Firstly, the acquired time series was median filtered (2x2x5 elliptical) to remove salt and pepper noise (Figure 4.29). Followed by Gaussian filtered with sigma of 50 or more, and the background was subtracted (Figure 4.29B). The data was 'Otsu' thresholded to generate binary images where MONTs were set as 1 and rest as 0 (Figure 4.29C). To further remove the noise, data was dilated (2 px elliptical) and objects smaller than 100 nm2 in area were removed (Figure 4.29D). Then, the area was quantified for each frame.

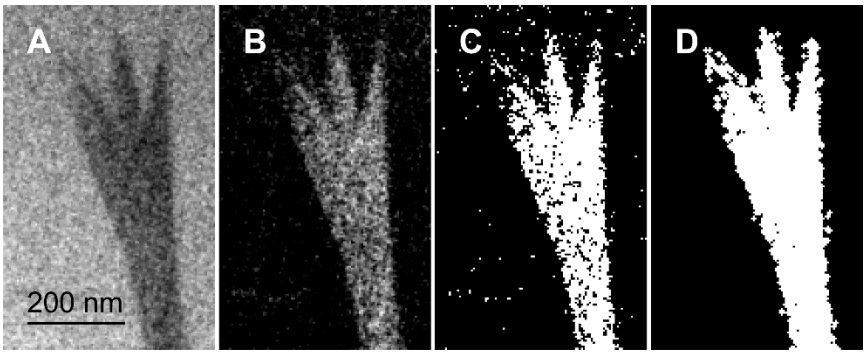

Figure 4. 14. Illustration of image analysis carried-out to obtain size of [(L1)Cu_2Br_2] as a function of time.

CHAPTER 5

MECHANISTIC INSIGHTS ON NUCLEATION AND GROWTH OF METAL-ORGANIC NANOTUBES VIA LIQUID-CELL TRANSMISSION ELECTRON MICROSCOPY

A version of this chapter is in preparation for publication by Karthikeyan Gnanasekaran, Kristina M. Vailonis, David M. Jenkins, and Nathan C. Gianneschi.

The work presented in this chapter was part of a collaborative project. The synthesis of all organic ligands were reproduced by myself and the LCTEM experiments were conducted by Dr. Karthikeyan Gnanasekaran.

Abstract

Metal-organic nanotubes (MONTs) are highly ordered one-dimensional crystalline porous frameworks. Despite being one-dimensional, virtually all studies of MONTs rely on characterization of the bulk crystalline material (micron-sized) by single crystal X-ray diffraction. However, for MONTs to achieve their raison d'être as tunable one-dimensional materials, individual tubes or small finite bundles of tubes must be synthesized and characterized. Therefore, to directly observe their formation under a variety of reaction conditions in solution, we employed liquid-cell transmission electron microscopy (LCTEM) which allows the MONT formation to be monitored in real time. Notably, changing the metal-to-ligand ratio in the reaction, not only leads to different nucleation and growth mechanisms of the MONTs but also diverse morphologies of the nanoscale material. Despite these diverse morphologies at the nanometer regime, each MONT eventually grows to a similar needle phase in the bulk materials. These LCTEM measurements demonstrate the importance of MONTs morphology on the nanoscale for potential applications and suggests that LCTEM is a critical tool for monitoring reactions on nanomaterials more generally.

Introduction

Metal–organic nanotubes (MONTs) are highly ordered one-dimensional crystalline frameworks composed of metal ions connected together via coordination bonds of organic ligands that repeat in one direction.[13, 32, 111, 137-138] Their porous and tubular architectures, with substantial specific surface areas, make them potential candidates for several applications including: gas storage, sensing, separations, and as hosts for small molecules, such as organic conductors.[139-140] Like their more widespread three dimensional cousin, metal-organic frameworks (MOFs), the principles of isoreticular design can be leveraged to control the size and porosity of the MONTs. However, understanding their atomic structure is predicated on successful single crystal X-ray diffraction of the bulk material, which eliminates many of their intrinsic advantages.

Despite the value in improved understanding of MONTs on the nanoscale regime, either as individual tubes or small finite bundles of them, very few studies have been conducted.[47, 67, 141] Methods for monitoring the progress of MONT reactions in solution in real time are desirable if they can be coupled with detailed characterization of the purified material. For organic compounds the this is already possible with *in situ* NMR and *in situ* IR.[142-143] Time lapse transmission electron microscopy (TEM) images of bulk experiments aliquoted onto TEM grids at defined timepoints can be used to monitor the morphological changes and different morphologies at of each different reaction condition as it progresses.[70] As an additional complication, the nanoscale morphology of the MONTs cannot by directly deduced from the bulk mixture as seen in SCXRD. For comparison, protein solutions and colloidal systems have been reported that undergo phase separation at the nanoscale and leading to complex assembly of intermediate phases.[129, 131, 144-145]

Liquid-cell transmission electron microscopy (LCTEM) has shown potential for monitoring morphological changes during reactions and self-assembly of nanomaterials *in situ*.[115, 131] LCTEM allows testing of reactions on a minute-by-minute basis, beginning at the very first instance of the appearance of nanoscale seeds. To date, LCTEM has predominately been used to study the nucleation and growth of metal nanoparticles,[116, 128, 146-153] with very limited studies addressing the nucleation, growth behavior of highly beam sensitive and low contrast organic or hybird materials.[50-51, 154-155] Recent exceptions include studies on porous materials including metal-organic frameworks,[52] covalent organic frameworks (COFs),[45] and a recently reported copper-based MONT where 1D growth was observed in the liquid phase.[70]

In this chapter, we explore the growth and nanoscale morphology of two MONTs over a range of reaction conditions by varying metal and ligand ratios during the reaction as well as the temperature. We conducted studies by direct observation and propose growth mechanisms using LCTEM of isoreticular copper and silver MONTs with a ditriazole ligand. These studies demonstrate that the process of forming the same bulk material can proceed through multiple mechanisms depending on the reaction conditions.[32]

Results and Discussion

Electron Dose Measurements

LCTEM measurements present significant challenges and limitations because of liquid-cell confinement, liquid thicknesses, small observable reaction volumes (in contrast to bulk experiments), and electron beam interactions with reactants and solvent.[116, 151-152, 154, 156] To capture the formation of initial primary

particles, we performed LCTEM experiments in flow mode at an elevated temperature (85 °C) or at room temperature using a Protochips Poseidon Select Heating holder with two separate inlets and one outlet for solution flow control. In this geometry, a metal ion solution and an organic ligand solution are made to mix immediately prior to entering the SiN_x window allowing the beginning of the reaction to be captured.[52, 70, 154, 157-158]

These studies require the prevention of metal nanoparticle formation by reducing and minimizing the effect of the electron beam induced growth or destruction of the MONTs. Kinetic modelling, empirical observation, and control experiments have shown that the electron beam can induce metal nanoparticle nucleation from solutions of metal salts by reduction, with their size increasing monotonically with time through monomer addition.[116, 122] Previous research has shown that the rate of nucleation increases as a function of electron flux, with a cumulative electron flux of 50 to 100 $e^{-}Å^{-2}$ necessary to initiate the nucleation of metal nanoparticles from metal salts.[116] Hence, the first step was to confirm imaging could be performed without inhibiting or damaging MONT formation by radiolysis or other beam induced effects.[122-124] Therefore, we first determined the imaging and electron flux thresholds to confirm safe imaging conditions to be less than 70 $e^{-}Å^{-2}$ in terms of cumulative electron flux at a rate of 0.1 to 0.2 $e^{-}Å^{-2}$ per second (Figures 5.9, 5.10).[70]

Observation of MONT Growth

To understand the nucleation and growth mechanisms of metal-organic nanotubes, analysis of the immediate solution phase reaction was studied by LCTEM. Two metal-organic nanotubes such as **Ag-MONT** and **Cu-MONT** which were previously characterized in the bulk phase were chosen for this study. Single crystal X-ray diffraction of both MONTs previously confirmed the nanotubular structure and give key intermetallic distances for comparison with LCTEM. **Ag-**

MONT and **Cu-MONT** are isostructural MONTs and were synthesized with the same di-triazole ligand, 4,4′-(1,4-(xylene)diyl)bis(1,2,4-triazole) (**L1**). This ligand adopts a *syn* conformation to form the 2-pillared motif about the metal ion. Altering the metal salt and concentration of reactants will also allow for understanding their role in the growth and nucleation mechanisms of MONTs (Figure 5.1).

Ag-MONT Growth

The first reaction that was attempted in the LCTEM was of the **Ag-MONT** and included an equivalent ratio of metal to ligand (1:1 $AgNO_3$:**L1** ratio) at 85 °C (i.e. **Ag-MONT, Reaction 1**, Figure 5.1). The silver nitrate and **L1** reagents were first introduced into the liquid cell (Figure 5.2) and formed heterogeneous particles with broad size distributions from 50 nm to 200 nm after approximately 30 seconds. These broad structures are in contrast to MONT crystals that typically form highly anisotropic morphologies (Figure 5.2A, Movie 5.1).[32, 47, 70] To capture morphological evolution at extended time scales for **Reaction 1**, the growth was captured by imaging the sample every 30 seconds to limit overall electron beam exposure. The stroboscopic imaging at 30 second pulses revealed the growth of small **Ag-MONT** nanotubes (< 200 nm in length) in the presence of the initially formed larger faceted particles (Figure 5.2B, Movie 5.2). After 10 minutes, fully grown rod- and sheet-like structures along with the initial faceted particles were observed (Figure 5.2C, Movie 5.3). Because of the stroboscopic imaging, the appearance of the individual rods was instantaneous, and the MONT growth was not able to be observed in real time.

Post-mortem analysis of the materials formed in the liquid cell following the LCTEM experiment revealed the presence of large sheet-like structures with significant length-to-width ratios (10 μm by 2 μm) and large faceted particles. A selected area electron diffraction (SAED) pattern of the faceted particles exhibit distinct diffraction spots of 3.77 Å that are not representative of MONT crystals (Figures 5.2D, 5.12). By contrast, a diffraction spot at 12.37 Å with uniform

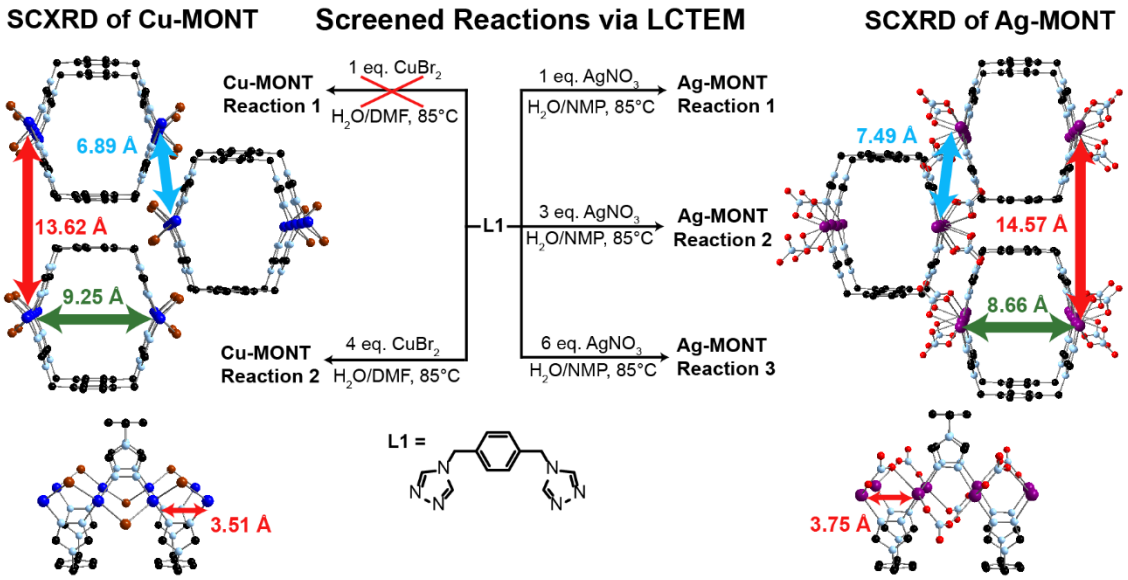

Figure 5. 1. Crystal structures and reaction conditions for the preparation of Ag-MONT and Cu-MONT evaluated by LCTEM herein. Single crystal X-ray diffraction structures were obtained from the bulk scale synthesis of the respective MONTs, and analyzed on micron sized crystals. Key intermetallic distances are shown.[32, 47] Black, light blue, red, purple, dark blue, and brown spheres represent carbon, nitrogen, oxygen, silver, copper, and bromine atoms respectively. Hydrogen atoms are omitted for clarity.

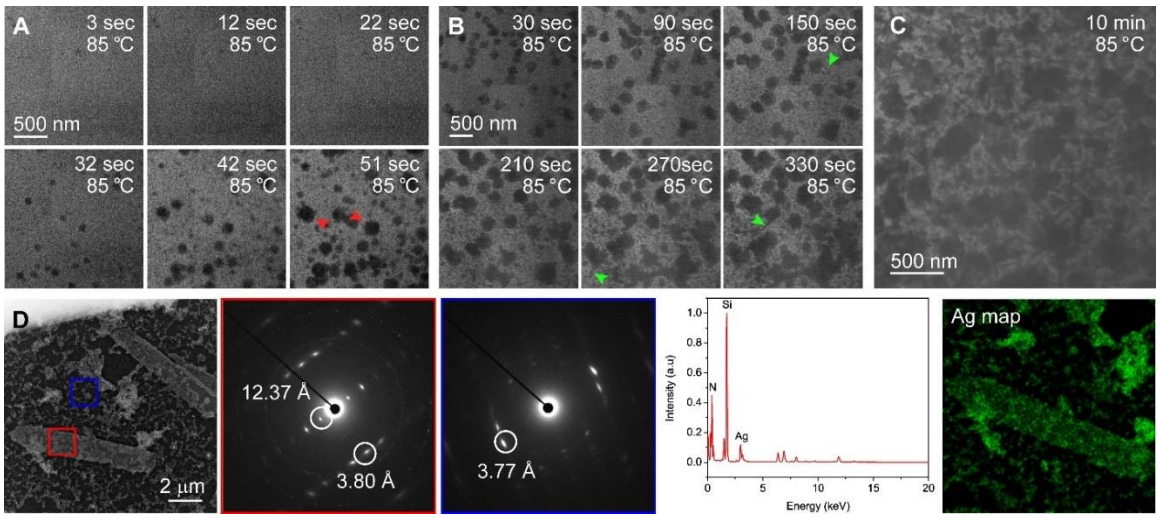

Figure 5. 2. LCTEM analysis of Ag-MONT, Reaction 1. (A) Snapshots of growth of initial metastable faceted nanoparticles (red arrows); (B) Snapshots of growth of small nanotubes on the surface of the faceted nanoparticles (green arrows); (C) Snapshots of fully grown metastable morphologies and anisotropic morphologies within liquid-cell; (D) Post-mortem analyses – HAADF-STEM image of Ag-MONT prepared under these reactions conditions, corresponding SAED pattern, EDS spectrum and Ag map.

distribution of Ag (shown by EDS map) was obtained from the large sheet-like morphologies. This revealed the formation of large-scale crystallites (Figure 5.2D). Depending on the orientation of the crystal, we obtained diffraction data between ~7 Å to ~14 Å that represent the MONT pore dimensions and the distances between MONT tubes (shown in Figure 5.1). Additional key intermetallic distances for Ag-MONT can be seen in the Experimental Section VI, Figure 5.11. This data suggests the faceted particles are not metal-organic nanotubes due to the lack of long-range diffraction data. The faceted particles may be aggregated clusters of silver nitrate and triazole ligands formed from π−π stacking of the aromatic rings of the triazole ligand. Addition testing may be required to make a final determination. Therefore, we propose, at present, that these initial particles, are a kinetic metastable phase.[47, 150]

By increasing the silver nitrate concentration and changing the $AgNO_3$:**L1** ratio to 3:1 (i.e. **Ag-MONT, Reaction 2**), the supersaturation of reactant monomers was tuned (Figure 5.3). More importantly, it was observed that the initially formed metastable particles that were seen in **Reaction 1** served as reservoirs of monomers or possible sites for heterogeneous nucleation for anisotropic particle growth. Movie 5.4 shows the formation of these metastable particles which form and then grow into anisotropic MONT structures and further suggests the composition of the metastable particles are silver nitrate and **L1** aggregations. This nucleation is similar to classical zeolite nucleation described by the secondary building unit (SBU) model (Figure 5.3A, Movie 5.4).[47, 159-161] Not all MONT bundles in the reaction medium grew by this heterogeneous nucleation mechanism, as the formation of elongated sheet- and rod-like structures were observed to form directly from solution (Figure 5.3B, Movie 5.5).

In contrast to the previous two reactions, by adding additional excess $AgNO_3$ to the reaction (i.e. 6:1 $AgNO_3$:**L1** ratio, **Ag-MONT**, **Reaction 3**) only **Ag-MONT** primary particles were observed when the reactants were mixed (Figure

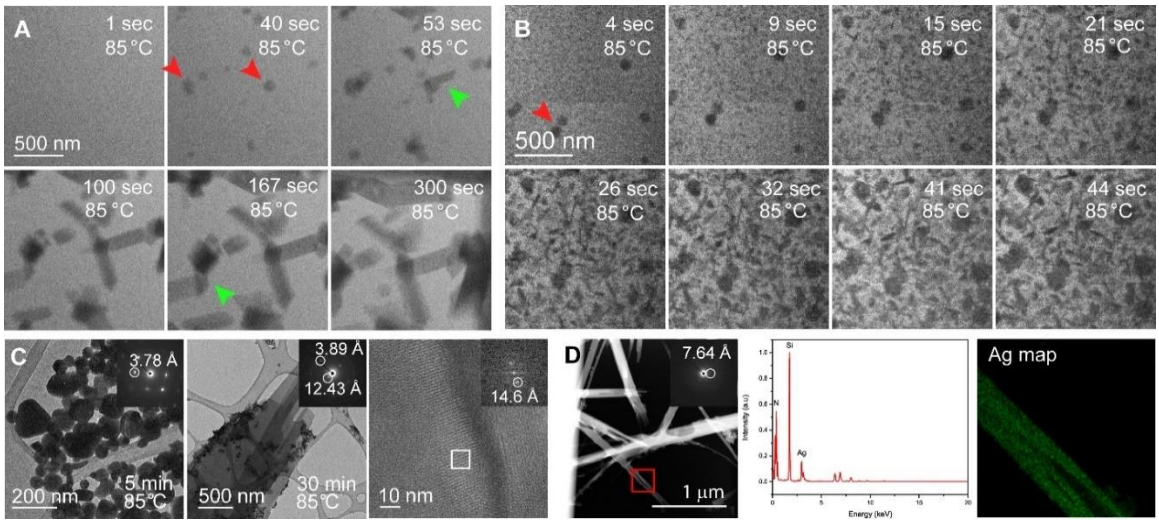

Figure 5. 3. LCTEM analysis of Ag-MONT, Reaction 2. (A and B) Snapshots of growth of metastable (red arrow) and anisotropic morphologies of Ag-MONT (green arrow) within liquid-cell; (C) TEM, SAED, and HRTEM of MONT nanotube bundles grown in bulk synthesis conditions;[32, 47] (D) Post-mortem analyses – HAADF-STEM image of Ag-MONT prepared under these reactions conditions, corresponding SAED pattern, EDS spectrum and Ag map.

5.4A, Movie 5.6). In this case, the size of initially formed particles were smaller than in previous experiments at 20-50 nm in diameter (Figures 5.2, 5.3). The anisotropic growth of the MONT primary particles (up to 1 μm in length) was observed and matched the morphology observed in bulk experiments under the same reaction conditions (Figure 5.4B-C). Formation of **Ag-MONT** bundles were confirmed by the post-mortem analysis with distinct SAED diffraction spots corresponding to Ag···Ag distances within the **Ag-MONT** (Figures 5.4D, 5.11, 5.14).

The length of the individual metal-organic nanotubes was measured over time from the LCTEM data. Figure 5.4E shows the length growth of five **Ag-MONT** structures during the reaction. These structures are denoted by the corresponding colored arrows in Figure 5.4A. The analysis of the anisotropic growth of the **Ag-MONTs** revealed the nanotubes grew via two mechanisms. One mechanism was observed directly as the continuous growth of individual nanotubes where monomers of metal salts and ligands attached to the ends of the growing tubes. The second mechanism progressed by the coalescence of two or more smaller **Ag-MONT** particles (Figures 5.4F, 5.15, Movie 5.7). It is well accepted that MOFs and MOF-like particles predominately grow through the addition of smaller MOF clusters (~1 nm) in solution, but not through coalescence as seen in the second mechanism.[52, 120, 162] However, the heterogeneous nucleation and 1D growth of **Ag-MONTs** suggested the assembly of metal-organic nanotubes took place over several stages. (See Experimental, Section XI).

Ag-MONT Growth Mechanisms

Classical nucleation theory (CNT) explains the rate of nucleation $J_n = A \exp(-B\alpha^3/\sigma^2)$, where A is the pre-factor depends on kinetic considerations, B depends on temperature and volume, α is the interfacial energy and σ is the supersaturation of the solution. The step speed (i.e. rate of the growth of crystal) increases linearly with time and leads to non-linear change in area and/or volume

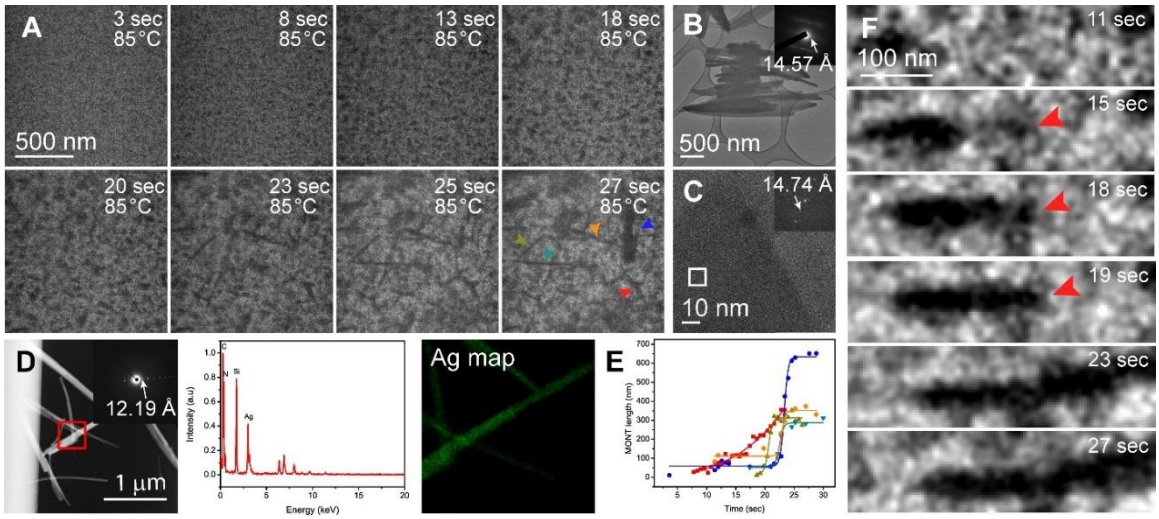

Figure 5. 4. LCTEM analysis of Ag-MONT, Reaction 3. (A) Snapshots of growth of Ag-MONT within liquid-cell; (B and C) TEM image of fully-grown Ag-MONT in bulk synthesis and corresponding SAED pattern and FFT; (D) Post-mortem analyses – HAADF-STEM image of MONT bundles grown within the liquid-cell, and corresponding SAED pattern, EDS spectrum, and silver map; (E) Length evolution of individual Ag-MONT bundles plotted as a function of time; (F) Magnified snapshots of a Ag-MONT bundle that illustrates the coalescence of primary particles.

of the MONT crystal growth.[163] An inherent assumption in the above discussion is that the pathway of nucleation goes directly from the solution to the formation of MONT nuclei with ordered crystalline structures identical to that of the eventual bulk MONT crystal. The formation of kinetic metastable particles (in **Reaction 1** and **2**), and coalescence events in **Reaction 3** contradicts the classical growth pathways and instead suggests multiple nucleation and growth pathways within the same reaction. Similar observations were made for MOF-5, and $CaCO_3$.[131, 164] I Increasing the concentration of $AgNO_3$ from **Reaction 1** to **Reaction 3** causes the growth of MONT morphologies changes from non-linear to linear behavior with time. This change indicates a gradual deviation from classical pathways upon increasing the concentration of $AgNO_3$ (Figure 5.5A). This deviation suggests that at low to moderate concentration of $AgNO_3$ as in **Reaction 1** and **Reaction 2**, there exists a localized competing behavior for the formation of thermodynamically stable MONT crystals by classical pathway as well as the kinetic (metastable) product within the same reaction that was controlled by the local availability and depletion of reactant monomers ($AgNO_3$ and **L1**), MONT precursor ions, and amorphous clusters.[129-131] Upon increasing the concentration of $AgNO_3$ to a large excess such as in **Reaction 3**, the growth behavior changes to a linear behavior and increases in area with time which reveals the growth cannot be driven predominately by monomer attachment, but by coalescence and aggregation of particles.[163] Due to the secondary attachment of particles at later time scales, the average size of the **Ag-MONT** particle also increases drastically in **Reaction 3** (Figure 5.5B).

Mean crystal growth rate of MONTs from solution was also measured by Lifshitz−Slyozov−Wagner (LSW) model for Ostwald ripening.[125-127] The projected sizes, $\langle S \rangle$, evolved over time, t, were fitted to the power law model as $\langle S \rangle \alpha t^n$, where $n \geq ½$ representing reaction-limited growth; i.e., surface specific attachment of monomers being the rate limiting step. For $n < ½$ represents diffusion-limited growth wherein, transport of the reactants is the rate limiting step (See

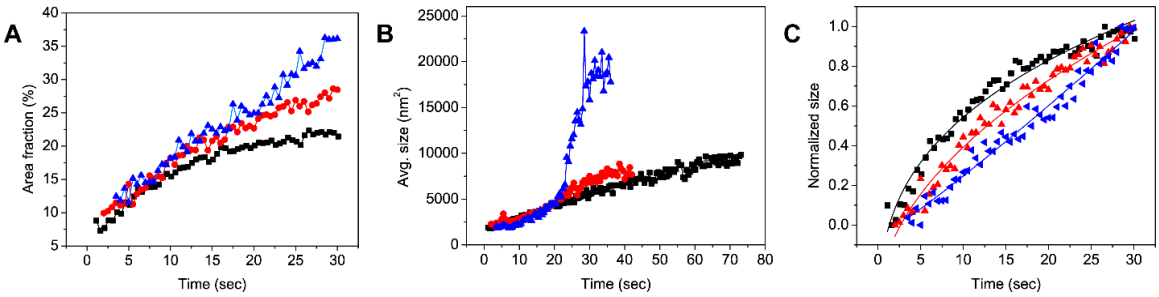

Figure 5. 5. Ag-MONT bundles growth parameters measured from LCTEM data. (A) Increase in area fraction of MONT growth plotted as a function of time; (B) Increase in average size of MONT particles plotted as a function of time; (C) Normalized size of MONT growth and their corresponding power fit plotted as a function of time. In all above data black curve represents growth of metastable particles in Reaction 1; red curve represents growth of anisotropic MONT crystals directly from solution in Reaction 2; blue curve represents anisotropic MONT crystal growth observed by coalescence in Reaction 3.

Experimental, Section XI).[125, 150] The exponent measured from the growth profile of the metastable morphologies in the beginning of the reaction yielded n = ⅓ (Figure 5.5C), revealing the growth of these initial particles was controlled by the diffusion of reactants ($AgNO_3$ or **L1**) or precursor ions (clusters of $AgNO_3$ and **L1**).[125] However, the time dependent growth of elongated sheet-like and rod-like MONT morphologies directly from the solution phase (Figure 5.5C) measured from LCTEM data revealed a reaction-limited growth as the power law fit yielded a growth exponent of n = ½. This power law fit is commonly observed in other MOF and MOF-like materials (Figure 5.5C).[45, 52, 70] A linear growth profile, secondary aggregation, and coalescence observed in **Reaction 3** clearly contradicts the LSW model for Ostwald ripening as the power law fit yielded a growth exponent n = 1.11.[52, 125-127, 165]

Based on the above results, the complexity of the free-energy landscape on **Ag-MONT** growth can be accessed. When less supersaturated reactant monomers mix (as in the beginning of the **Reaction 1** and **Reaction 2**), the interfacial surface energy of precursor ions and their density fluctuations create unstable amorphous clusters that lead to a metastable phase as the free energy cost for the transformation of MONT nuclei is significantly higher. As reactant monomers continue to flow into the reaction cell, steady state supersaturation was achieved. Thus the metastable phase could lower the energy barrier and enhance the anisotropic MONT crystal nucleation from the metastable phase which lead to heterogeneous nucleation.[144, 166-167] When highly supersaturated reactant mix (as in **Reaction 3**), precursor ions and ligands produce initial particles by monomer attachment, and once a certain length scale was achieved, oriented attachment and coalescence of ensemble particles occurred predominately that led to anisotropic MONT crystals. Along with these indirect pathways, local variation in the availability and depletion of reactant precursors, and local variation in supersaturation also facilitates classical growth mechanisms within the same

reaction. A schematic illustration of the **Ag-MONT** growth from the three reactions is described in Figure 5.6.

In addition to the bulk characterization of **Ag-MONT** by single crystal X-ray diffraction,[32] this MONT was previously characterized through the complementary solution phase measurements, small angle X-ray scattering (SAXS).[47] A **Ag-MONT** reaction with a 5:1 $AgNO_3$:**L1** ratio was analyzed by *ex-situ* SAXS to obtain information of the reaction kinetics. Time resolved SAXS interpreted by the Gualtieri model indicated the nucleation of the **Ag-MONT** grew through an autocatalytic reaction where initial aggregates form and then grow in a preferred direction until the reagents were consumed. This SAXS analysis supports the preferential aggregation leading to micron-sized anisotropic MONT crystals as seen in the LCTEM of this study.

These combined results on growth pathways over the three reactions are critical for developing future MONT applications since nanoscale bundles of tubes are the required particle size for MONTs to take advantage of their inherent anisotropy. In this case, adding additional silver nitrate as metal source, with respect to ligand concentration, forms only the desired MONT with no additional metastable phases even at the beginning of the reaction. *Thus, the reaction can be stopped at different lengths of time to yield different sized MONTs, with no additional phases which is crucial for the integration and application of metal-organic nanotubes.*

Cu-MONT Growth

A second **L1** based MONT was investigated by changing the metal salt to copper(II) bromide for comparison to the silver based MONT (Figure 5.7).[32] *In situ* experiments were performed with copper(II) bromide as the metal salt with $CuBr_2$:**L1** ratios of 1:1 and 4:1. At the ratio of 1:1 $CuBr_2$:**L1** (**Cu-MONT, Reaction 1**), no structure formations were observed over extended periods of time. At a 4:1

$CuBr_2$:**L1** ratio (**Cu-MONT, Reaction 2**), **Cu-MONT** nanocrystal growth was observed after approximately 30 seconds, which lead to large elongated sheet-like structures as also observed in bulk experiments (Figures 5.7A-B, Movie 5.8). The growth of these MONTs were limited to < 1 μm. However, an increase in contrast suggested they thickened with time (Figure 5.7C). Post-mortem analysis of the **Cu-MONT** crystals included an EDS spectrum with copper and bromine composition and corresponding elemental mapping showing uniform distribution of carbon, nitrogen, copper, and bromine (Figure 5.20). Unlike **Ag-MONT**, intermediate phases, coalescence events, and kinetic products were not observed; instead, continuous transformation of precursor ions into a crystalline phase was observed suggesting the classical growth mechanism (Figure 5.7D, 5.21). This mechanism is qualitatively consistent with the previous copper MONT that we studied with LCTEM.[163]

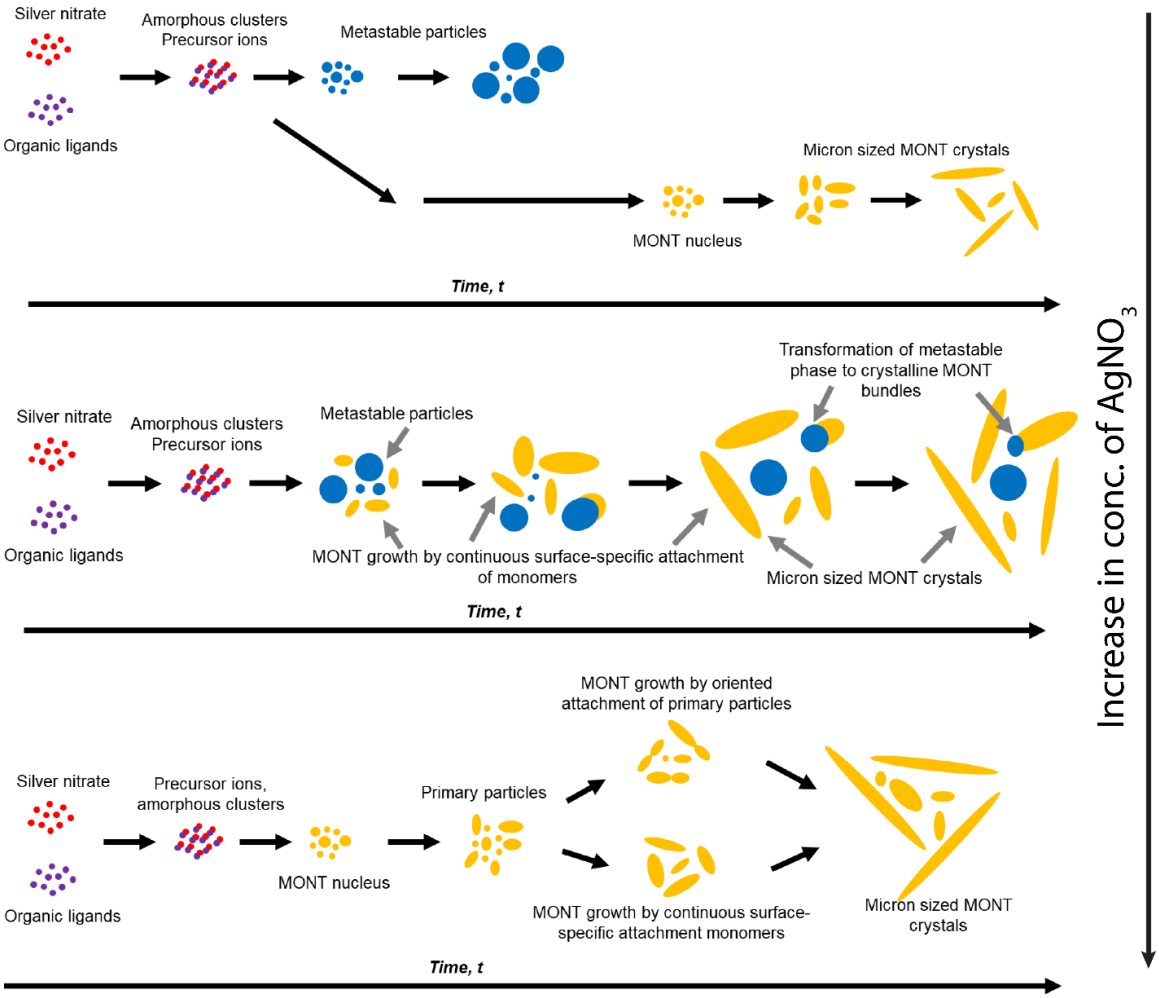

Figure 5. 6. Schematic illustration of Ag-MONT growth observed by LCTEM in Reactions 1, 2, and 3. Key structures: silver nitrate (red circles), organic ligand (purple circles), precursor ions (red and purple overlapping circles), metastable particles (blue circles), MONT nuclei (yellow circles), and MONTs (yellow ovals).

$CuBr_2$:**L1** ratio (**Cu-MONT, Reaction 2**), **Cu-MONT** nanocrystal growth was observed after approximately 30 seconds, which lead to large elongated sheet-like structures as also observed in bulk experiments (Figures 5.7A-B, Movie 5.8). The growth of these MONTs were limited to < 1 μm. However, an increase in contrast suggested they thickened with time (Figure 5.7C). Post-mortem analysis of the **Cu-MONT** crystals included an EDS spectrum with copper and bromine composition and corresponding elemental mapping showing uniform distribution of carbon, nitrogen, copper, and bromine (See Experimental Section, Figure 5.20). Unlike **Ag-MONT**, intermediate phases, coalescence events, and kinetic products were not observed; instead, continuous transformation of precursor ions into a crystalline phase was observed suggesting the classical growth mechanism (Figure 5.7D, See Experimental Section for Figure 5.21). This mechanism is qualitatively consistent with the previous copper MONT that we studied with LCTEM.[163]

Conclusion

In summary, we have demonstrated that changing the reaction conditions lead to different reactions on the nanoscale in the formation of bulk MONTs. Depending on the ratio of the reactant molecules, the nucleation of the precursor ions is skewed either to monomer-based or particle-based pathways. For example, by increasing the concentration of $AgNO_3$, MONT growth shifts from classical pathways to non-classical pathways. At low $AgNO_3$ concentration, there exists a competition for the formation of thermodynamically stable MONT crystals and kinetically driven amorphous metastable morphologies. This interplay of thermodynamic and kinetic effects is controlled by the local availability and depletion of reactant monomers, precursor ions, and amorphous clusters.[129-131] Here the surface energy minimization is attained by the aggregation and short-range clustering of precursor ions that do not form MONT crystals immediately. Instead we observe a faceted metastable phase that serves as a reservoir for

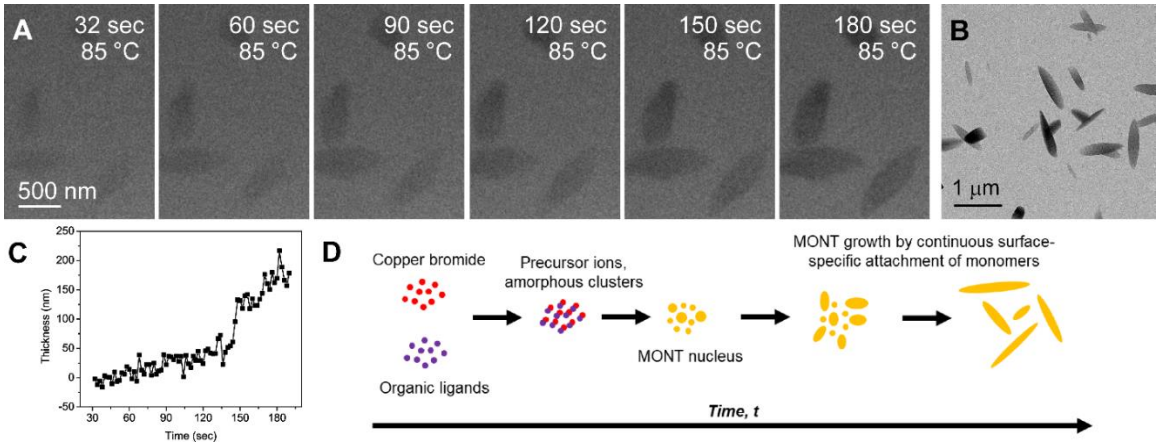

Figure 5. 7. LCTEM analysis of Cu-MONT, Reaction 2. (A) Snapshots of growth of Cu-MONT within liquid-cell; (B) TEM image of fully-grown Cu-MONT in bulk synthesis; (C) Increase in thickness of MONT plotted as a function of time; (D) Schematic illustration of Cu-MONT grown mechanism within LCTEM environment. Key structures: copper bromide (red circles), organic ligand (purple circles), precursor ions (red and purple overlapping circles), MONT nuclei (yellow circles), and MONTs (yellow ovals).

MONT crystal growth. Critically, adding more silver favors the formation of only nanorods that are identified as metal-organic nanotubes. This observation is critical in developing applications since only MONTs that are smaller than 1 μm in diameter will be employed for anisotropic applications. By changing the metal salt to copper bromide, the free-energy barrier is significantly skewed toward the classical pathway. That is, it involves only a continuous transformation of the supersaturated solution into the crystalline MONT phase. In addition to these physical insights specific to MONT nucleation and growth mechanisms, we have shown that LCTEM has significant potential as a tool for reaction development. Insights like this are of utility in subsequent bulk solution phase tuning of reaction conditions, where understanding reaction progression through specific intermediates and self-assembly mechanisms are important.

Experimental

I. TEM and Liquid-Cell TEM (LCTEM) Imaging

TEM and LCTEM imaging was performed using a JEOL ARM300F GrandARM TEM with Gatan OneView-IS camera operated at 300 kV. Post-mortem EDS analyses were performed in HAADF-STEM mode at a camera length of 20 cm. We used a Protochips Poseidon Select Heating holder for the *in situ* experiments. Firstly, the liquid-cell chips (with 50 nm silicon nitride thickness) were cleaned in acetone and methanol to remove the photoresist layer. Subsequently, top and bottom chips were plasma cleaned for 5 minutes to induce hydrophilicity. The chips were assembled in the tip of the holder, and leak checked to prevent any leak or breakage of the column vacuum during the experiment. After inserting the liquid-cell holder into the column of the microscope, reactants were flowed through the inlets separately using a syringe pump at the rate of 1 μL/min (Figure 5.8B). After approximately 20 min, we observed the wetting of the liquid-cell. BF-

TEM images were acquired before and after the flow of the reactants for the liquid thickness measurements. Once the wetting of the chips was observed, they were heated to 85 °C using a Protochips temperature controller at the rate of 1 °C/sec. During heating, the chips were not exposed to the electron beam. Once the temperature reached 85 °C, the movies of growth events were captured using screen recorder software (Camtasia Studio 7 Recorder screen capture software – TechSmith Corporation, USA). Note: All the TEM alignments, beam settings, dose settings, and calibrations were carried-out prior to the liquid-cell experiments using a standard gold nanoparticles or diffraction grating waffle TEM sample.

Movie 5.1: **Ag-MONT**, **Reaction 1**
Movie 5.2: **Ag-MONT**, **Reaction 1**
Movie 5.3: **Ag-MONT, Reaction 1**
Movie 5.4: **Ag-MONT**, **Reaction 2**
Movie 5.5: **Ag-MONT**, **Reaction 2**
Movie 5.6: **Ag-MONT**, **Reaction 3**
Movie 5.7: **Ag-MONT**, **Reaction 3**, Coalescence of primary particles
Movie 5.8: **Cu-MONT**, **Reaction 2**
Movie 5.9: Structural damage of MONT from excess electron flux

II. Schematics of Liquid-Cell TEM (LCTEM) Assembled Chips and Holder

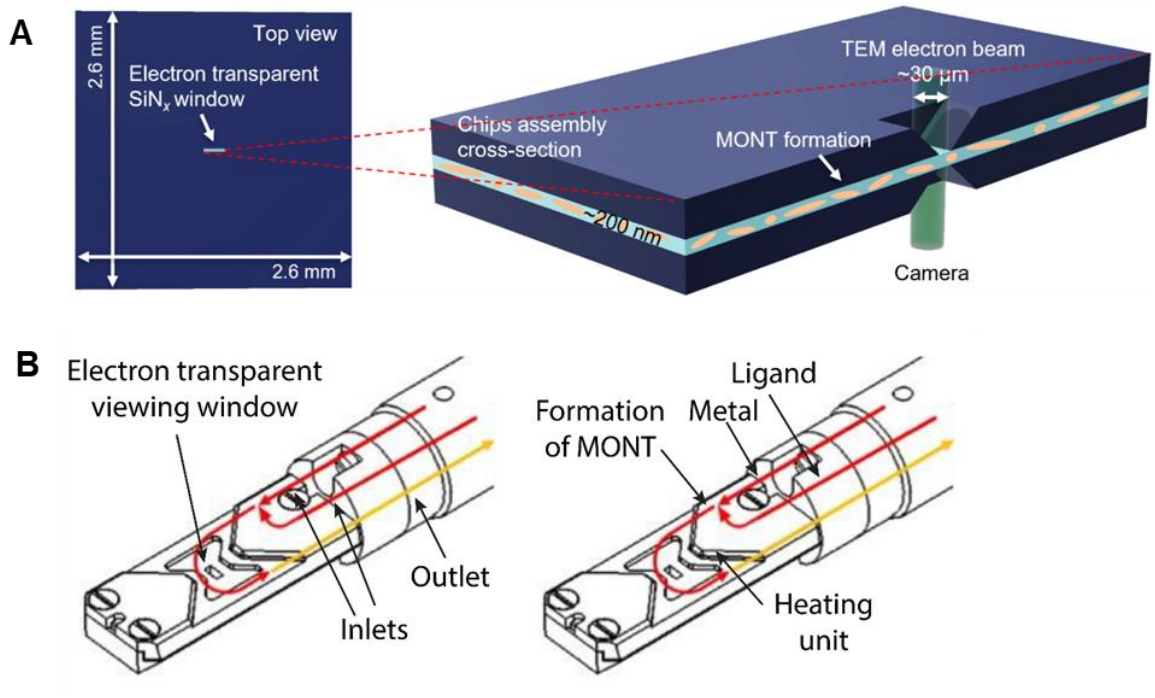

Figure 5. 8. (A) Schematic illustration of LCTEM chips employed for MONT reactions. (B) Schematic illustration of flow of reactants in Protochips Poseidon Select™ Liquid-cell TEM holder.

III. LCTEM Electron Flux Measurements

The effect of the electron beam and its interactions with the reactant molecules cannot be avoided.[45, 122] Hence, to prevent and minimize the effect of the electron beam during *in situ* growth experiments, we performed several trial and error experiments at various electron flux conditions. At an electron flux of ~1 $e^{-}Å^{-2}s^{-1}$ (with beam current of 1.52 nA), de-wetting of the chips was predominant upon irradiating with the electron beam. Immediately after the electron beam exposure, the reactant mixture receded away from the viewing area (exposed

area). And, further exposure results in the nucleation of residual metal precursors onto the SiN_x membrane (Figure 5.8A). By reducing the electron flux to 0.36 $e^{-}Å^{-2}s^{-1}$ (with beam current of 0.63 nA), de-wetting of the liquid-cell was prevented. Upon heating the reactants to 85 °C, we allowed the MONT to form and grow. Followed by, we irradiated the fully-grown MONT with electron beam and measured the cumulative electron flux. We observed beam induced transformation and structural damage of MONT as the cumulative flux exceeds 70 $e^{-}Å^{-2}$ (See Figure 5.10, Movie 5.9). Hence, we further reduced the electron flux to 0.1 $e^{-}Å^{-2}s^{-1}$ or 0.2 $e^{-}Å^{-2}s^{-1}$ as such the cumulative flux did not exceed 70 $e^{-}Å^{-2}$. Further details and in-depth analyses were presented in our prior publication – *Vailonis et al.*[70]

IV. LCTEM- Electron Flux Analysis

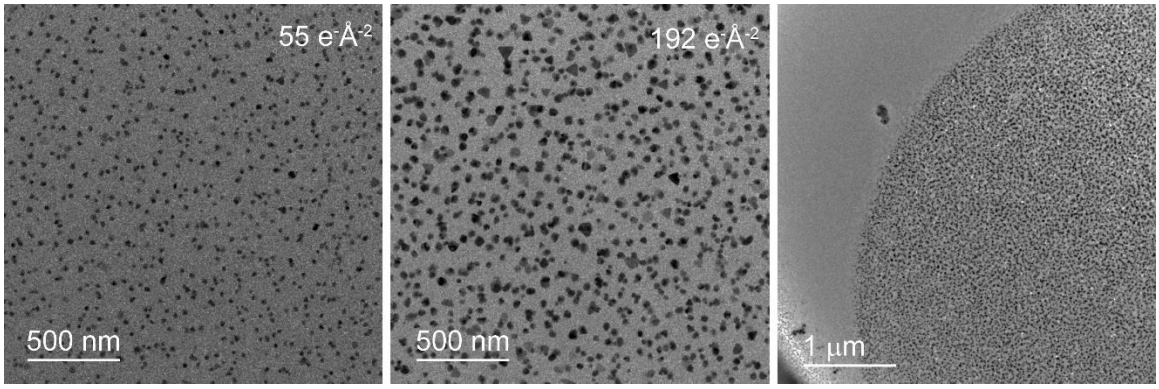

Figure 5. 9. Snapshots of de-wetted LCTEM chip illustrates the formation of Ag nanoparticles from the residual metal precursors after prolonged exposure at high flux.

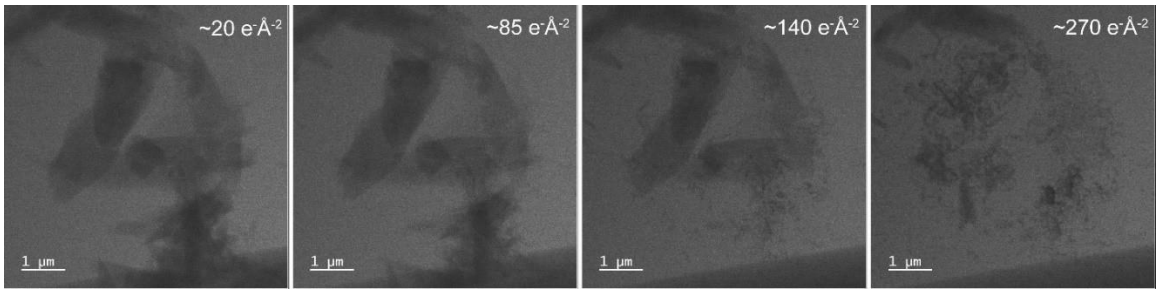

Figure 5. 10. Snapshots of disintegration of MONT bundles due to the prolonged exposure to the electron beam (see Movie 5.9).

V. Sample Preparation for In Situ Experiments.

Ag-MONT, Reaction 1: 10 mg of **L1** dispersed in 3 mL of NMP, and 10 mg of $AgNO_3$ dispersed in 3 mL of deionized water was prepared separately. **Ag-MONT, Reaction 2**: 10 mg of **L1** dispersed in 3 mL of NMP, and 30 mg of $AgNO_3$ dispersed in 3 mL of deionized water was prepared separately. **Ag-MONT, Reaction 3**: 10 mg of **L1** dispersed in 3 mL of NMP, and 60 mg of $AgNO_3$ dispersed in 3 mL of deionized water was prepared separately. **Cu-MONT, Reaction 1**: 10 mg of **L1** dispersed in 3 mL of DMF, and 10 mg of $CuBr_2$ dispersed in 3 mL of deionized water was prepared separately. **Cu-MONT, Reaction 2**: 10 mg of **L1** dispersed in 3 mL of DMF, and 40 mg of $CuBr_2$ dispersed in 3 mL of deionized water was prepared separately. All the reactants were dispersed by ultrasonication for 3 minutes.

VI. Single-Crystal Structures

The synthesis and single-crystal X-ray structures of **Ag-MONT** and **Cu-MONT** have been previously reported.[32]

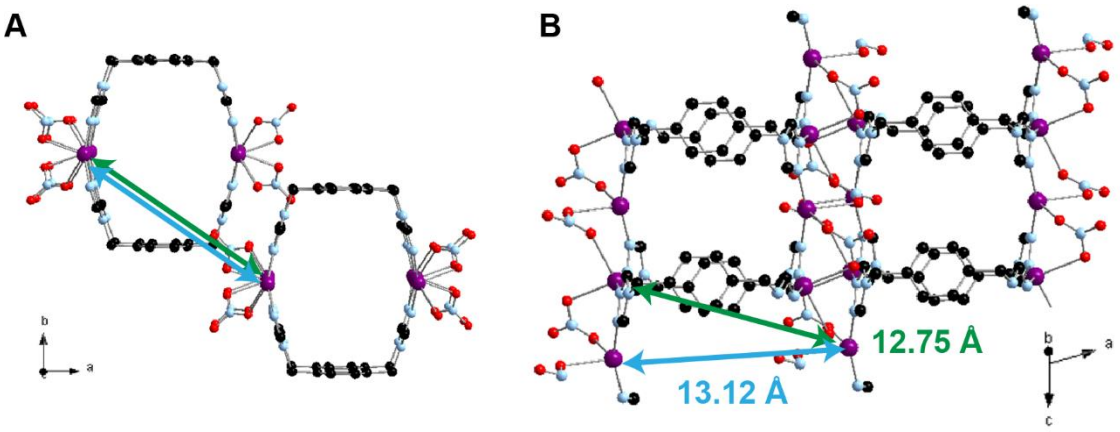

Figure 5. 11. Additional key intermetallic distances of Ag-MONT. (A) Front view, and (B) top view. Black, light blue, red, and purple spheres represent carbon, nitrogen, oxygen, and silver atoms respectively. Hydrogen atoms are omitted for clarity.

VII. Post-mortem analysis of Ag-MONT, Reaction 1

Post-mortem analyses were performed after the *in situ* experiments. The liquid-cell chips were opened carefully and washed gently with pure water to remove the excess reactants and solvent mixture. Followed by, the chips were placed on the standard TEM holder and analyzed by EDS and diffraction.

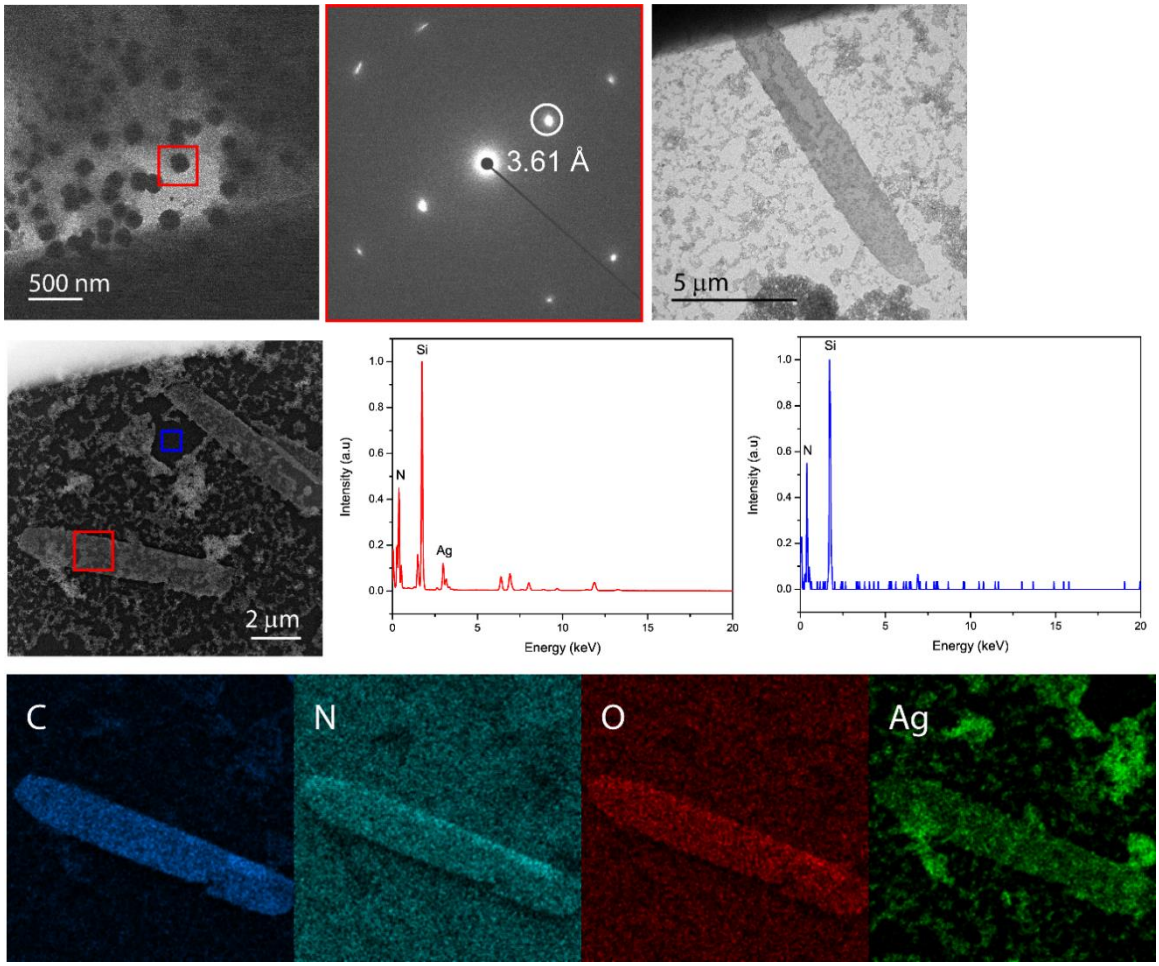

Figure 5. 12. Post-mortem analysis of Ag-MONT, Reaction 1. TEM images, SAED pattern, HAADF-STEM image, EDS spectrum and corresponding elemental mapping illustrates the faceted particles and elongated sheet-like Ag-MONT bundles within the liquid-cell. Note: In addition to light elements and Ag, strong Si signal represents the inevitable SiN_x membrane of the LCTEM window. The peaks between 5 and 7.5 keV represents the Fe and Co signal arises from the TEM holder. We also observed the same peaks at different experiments using the same holder.

VIII. Post-mortem Analysis of Ag-MONT, Reaction 2

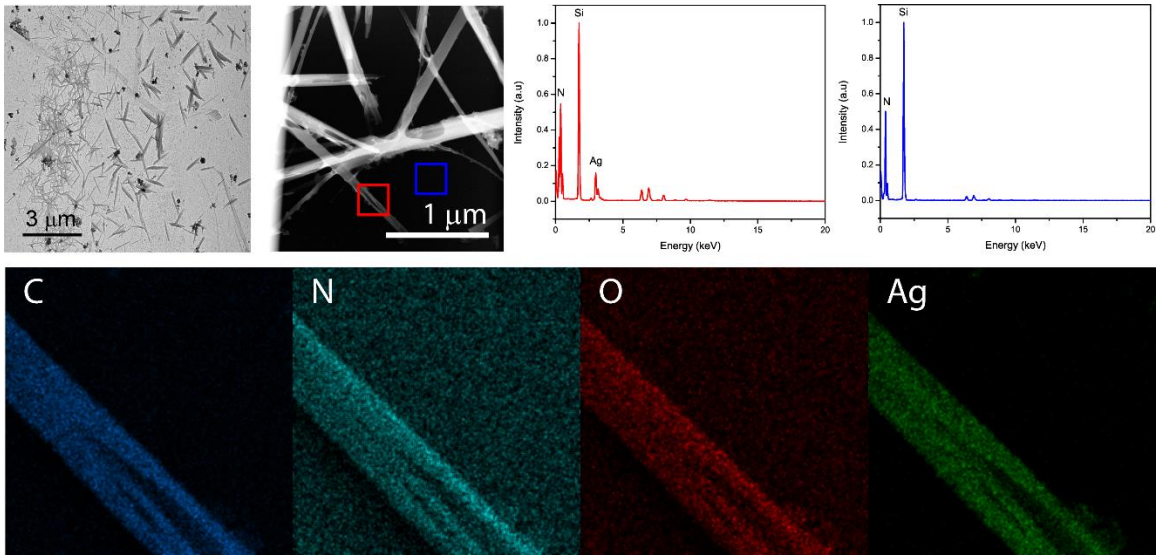

Figure 5. 13. Post-mortem analysis of Ag-MONT growth in Reaction 2. TEM image, HAADF-STEM image, EDS spectrum and corresponding elemental mapping illustrates the formation of micron sized MONT bundles within the liquid-cell.

IX. LCTEM post-mortem Analysis of Ag-MONT, Reaction 3

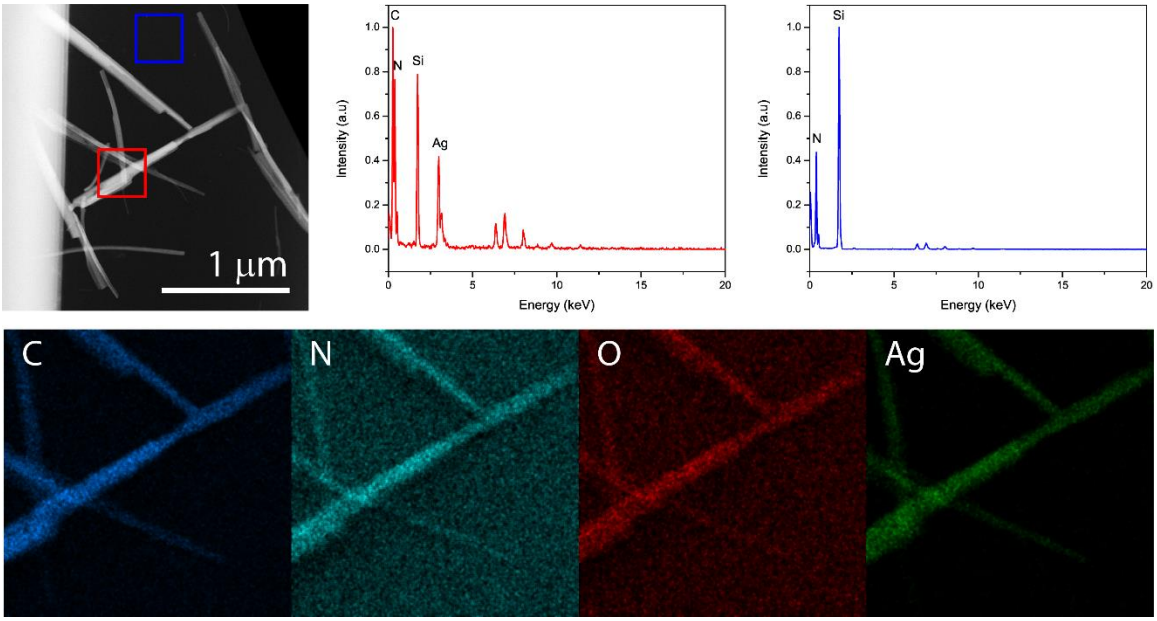

Figure 5. 14. Post-mortem analysis of Ag-MONT growth in Reaction 3. HAADF-STEM image, EDS spectrum and corresponding elemental mapping illustrates the formation of micron sized MONTs within the liquid-cell.

X. Coalescence of Primary Particles

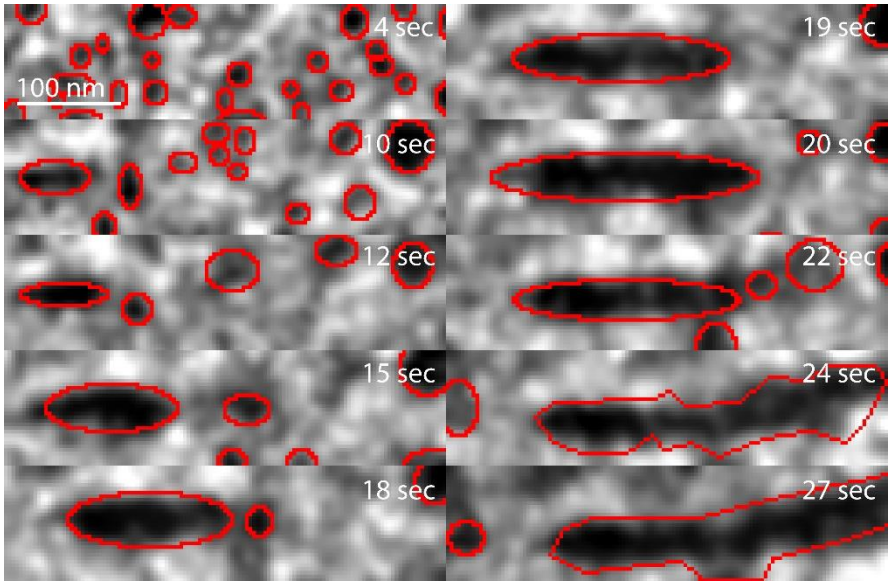

Figure 5. 15. Magnified snapshots of Movie 5.7 illustrate the coalescence of primary particles from elongated rod-like morphologies.

XI. TEM and EDS Analysis of Ag-MONT, Reaction 3

In the bulk experiments, immediately after mixing the reactants, the solution turns turbid which suggests the immediate formation of initial primary particles or MONT nanocrystals directly from solution. For the development of long-range order of crystals, leading to the fully crystalline phase, the reaction was continued for 24 hours. The structure formation, morphological transformation, and crystallinity were analyzed by TEM at intermediate time points. Immediately after the reactants mix, inhomogeneous strands (Figure 5.16a) of structures were formed. These primitive strands were transformed to sheet like structures with sharp edges and corners that indicating the faceting with increase in time (Figure 5.16b). We observed the thickness of these sheet-like structures increases with

reaction time and they also seem to bend (Figure 5.16c). It is known that in order to reduce the surface tension between several layers of growing sheets, the sheets could bend or roll and takes tubular morphology.[31] The length (long axis) of the structures also increased (Figure 5.16d) by continuing the reaction to 24 hours. This increase in length of the MONT suggests the heterogeneous nucleation of crystals takes place on the existing crystals. The reaction was continued for 48 hours to examine the change in morphology; however, no significant difference in morphology was observed. Selected area electron diffraction (SAED) at various time points also illustrates the increase in relative crystallinity over time. It is likely that at the beginning of the reaction, only the surface of the particle is crystallized with significant amount of metastable phase.[121] MONTs are very sensitive to the electron beam and undergo significant beam induced transformations. Hence, under controlled electron flux (<0.5 $e^{-}/Å^{2}$), and careful operation, HRTEM images of lattice spacing of MONT crystals were acquired (Figure 5.16e and Figure 5.16g). The measured lattice spacings from FFT (inset – Figure 5.16e and Figure 5.16g) corresponds to 101 plane and 011 plane, respectively. We also observe some long-range grain boundaries (Figure 5.17), which represents the discontinued 1D growth of MONTs, suggesting that the assembly of MONT morphology took place at several stages. This supports the LCTEM observations, that relatively isotropic primary particles were formed immediately after mixing the reactants, which then grow in a preferred orientation and forms rod-like or sheet-like structures. These anisotropic structures would further aggregate to forms secondary structures which results in mismatch and discontinued lattice structure. In addition, EDS analysis on **Ag-MONT** illustrates the uniform distribution of silver centers, triazoles and nitrate anions (Figure 5.18).

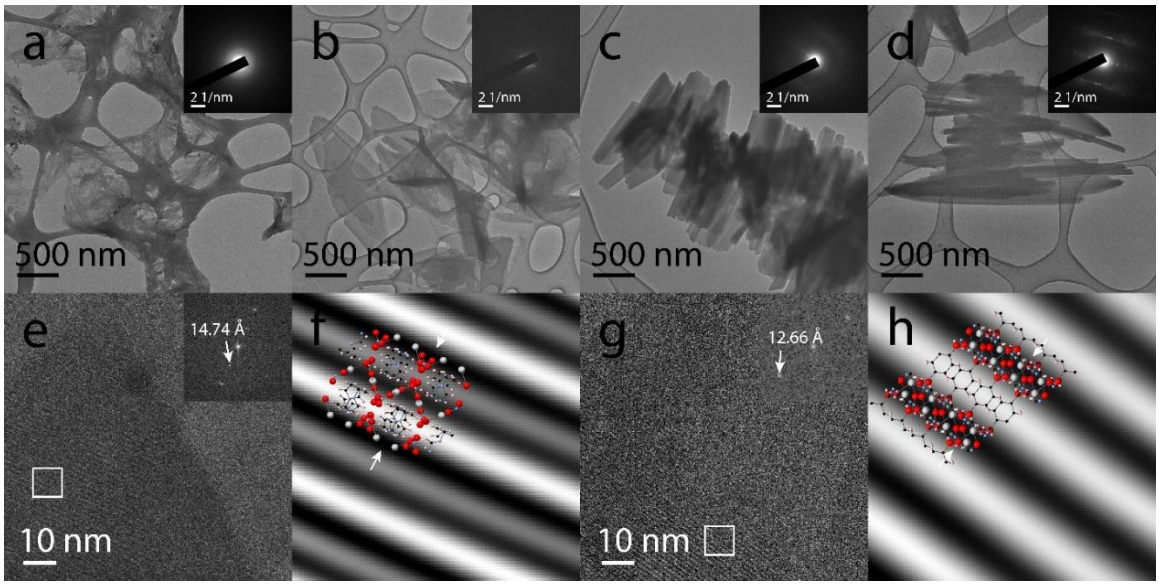

Figure 5. 16. Morphological transformation of Ag-MONT as observed by TEM. (a) 5 min), (b) ~30 min, (c) ~2 hours, (d) ~ 24 hours, (e and f) HRTEM image, corresponding FFT and iFFT illustrating assembly of MONT bundles in 101 plane, (g and h) HRTEM image, corresponding FFT and iFFT illustrating the assembly of MONT bundles in 011 plane.

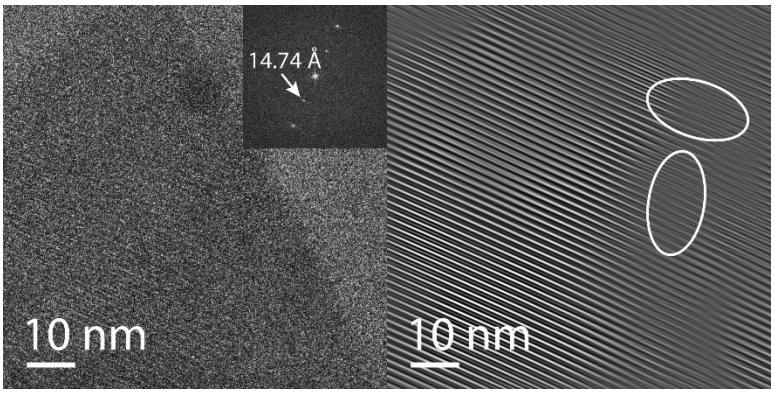

Figure 5. 17. HRTEM image illustrating the grain boundaries of Ag-MONT.

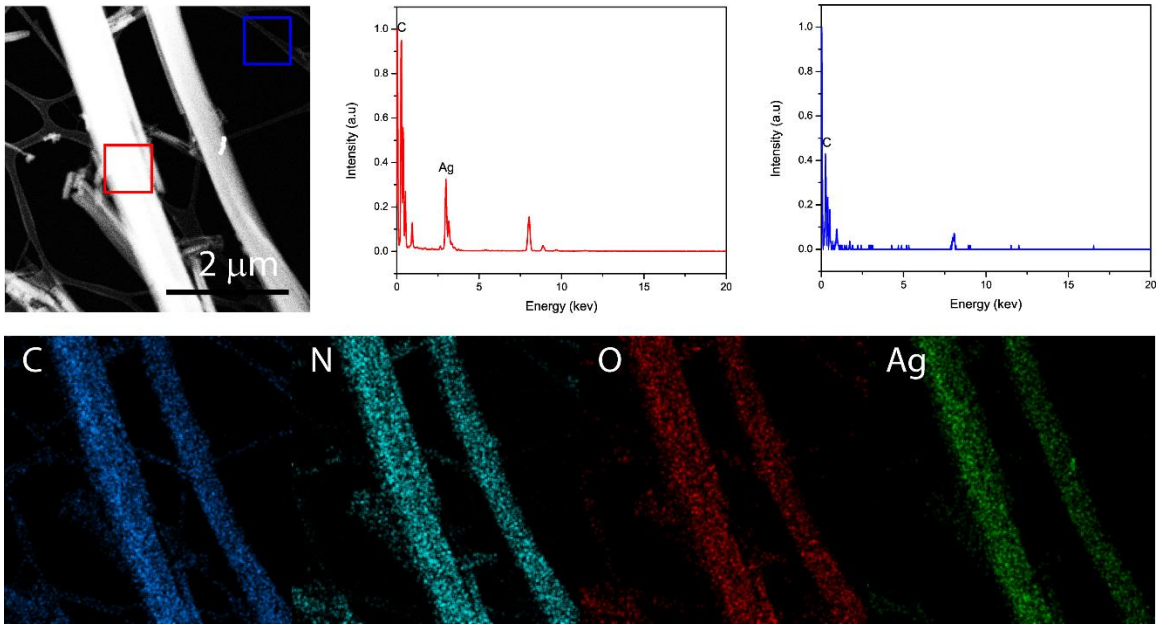

Figure 5. 18. HAADF-STEM image, EDS spectrum and corresponding elemental mapping illustrates the formation of Ag-MONT in Reaction 3 conditions.

XII. Image Analysis to Segment MONT Bundles

To quantify the growth parameters of MONT bundles, the acquired time series were segmented frame-by-frame (Figure 5.19A). First, the acquired time series was median filtered (2x2x5 elliptical) to remove salt and pepper noise. Followed by Gaussian filtered with sigma of 50 or more, and the background was subtracted (Figure 5.19B). The data was *'Otsu'* thresholded to generate binary images where MONTs were set as 1 and rest as 0 (Figure 5.19C). To further remove the noise, objects smaller than 100 nm^2 in area were removed (Figure 5.19D). Then, the area was quantified for each frame.

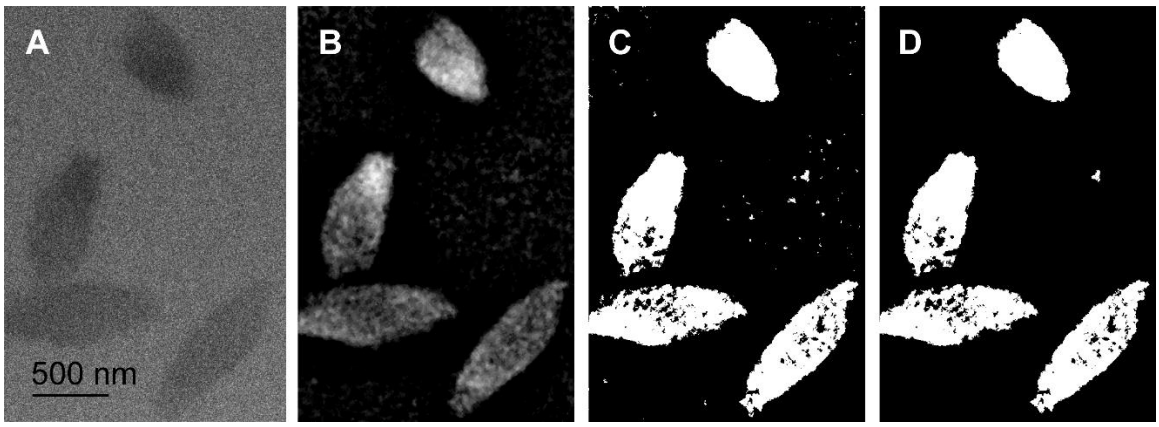

Figure 5. 19. Illustration of image analysis performed to obtain size of growing MONT bundles as a function of time.

XIII. MONT Bundles- Growth Measurements from LCTEM Data

Growth exponents of MONTs were measured by fitting the size vs. time data to the power law: $y = ax^t$,+ c where *y* is the normalized area measured by image analysis, *x* is the time (in sec), c is the uncertainty in the data, t is the growth exponent which reveals whether the growth process is predominately diffusion limited (when t < ½) or surface-reaction limited (when t ≥ ½) as proposed by Lifshitz−Slyozov−Wagner (LSW) model.[125-127]

Ag-MONT, **Reaction 1**: a = 0.52, t = ⅓, c = –0.57 with $R^2 = 0.97$

Ag-MONT, R**eaction 2**: a = 0.26, t = ½, c = –0.42 with $R^2 = 0.98$

Ag-MONT, **Reaction 3**: a = 0.02, t = 1.11, c = –0.06 with $R^2 = 0.97$

Cu-MONT, **Reaction 2**: a = 0.12, t = ½, c = –0.65 with $R^2 = 0.95$

XIV. LCTEM Post-mortem Analysis of Cu-MONT Bundles, Reaction 2

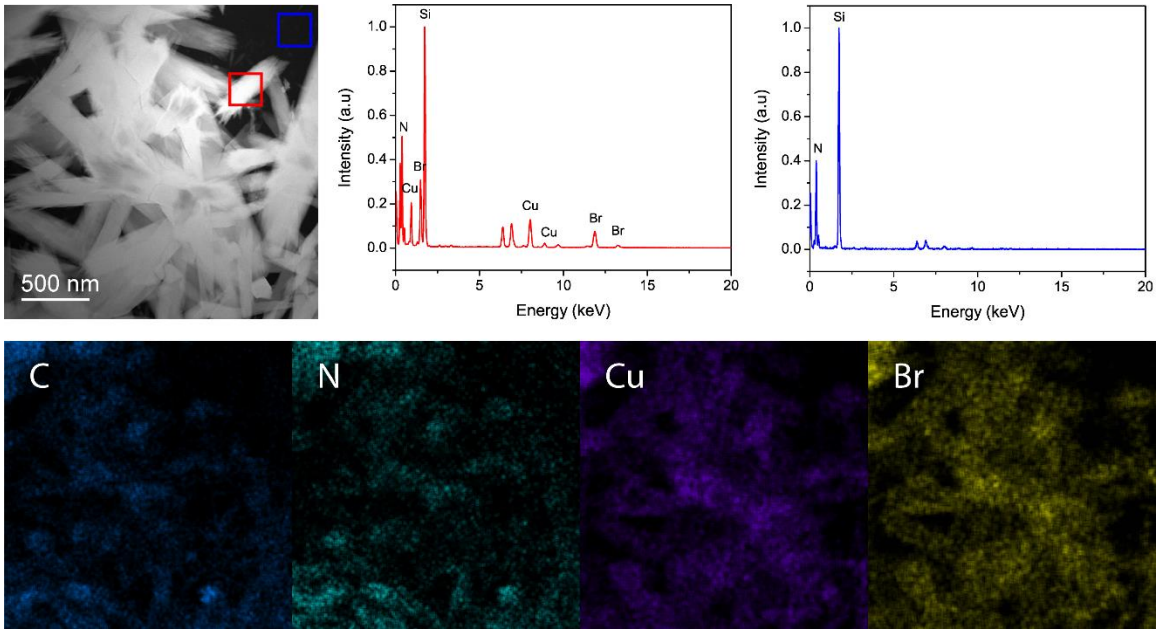

Figure 5. 20. Post-mortem analysis of Cu-MONT growth, Reaction 2. HAADF-STEM image, EDS spectrum and corresponding elemental mapping illustrates the formation of micron sized MONTs within the liquid-cell.

XV. Cu-MONT Bundles Growth Measurement from LCTEM Data

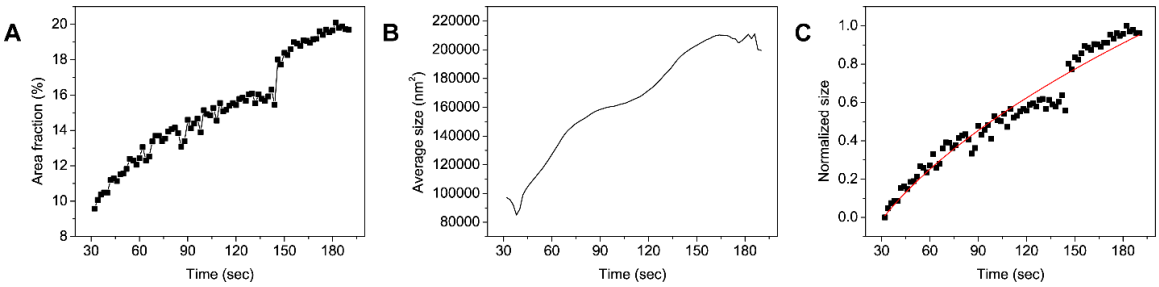

Figure 5. 21. Cu-MONT bundles growth measurements from LCTEM data. (A) Increase in area fraction of MONT growth plotted as a function of time; (B) Increase in average size of MONT particles plotted as a function of time; (C) Normalized size of MONT growth and their corresponding power fit plotted as a function of time.

XVI. Room Temperature Analysis

In situ LCTEM experiments were also performed at room temperature. Reactants were flowed into the liquid-cell holder and allowed to mix, nucleate, within the liquid cell, without initially imaging. After mixing of reactants, the liquid-cell holder was transferred to the column of the microscope and several time lapse images were acquired at various times. Using this method, the formation and existence of initial metastable phases could not be imaged. This was mainly limited by the time interval between static images (Figure 5.22). Nevertheless, MONT growth could be observed, and the morphologies found were similar to those observed during elevated temperature experiments, with the exception of their formation at a reduced growth rate (Figure 5.22). The MONT bundles were also larger in size than those formed at elevated temperature. This suggests a decrease

in nucleation rate and a preference for larger particle growth by monomer attachment rather than non-classical pathways.

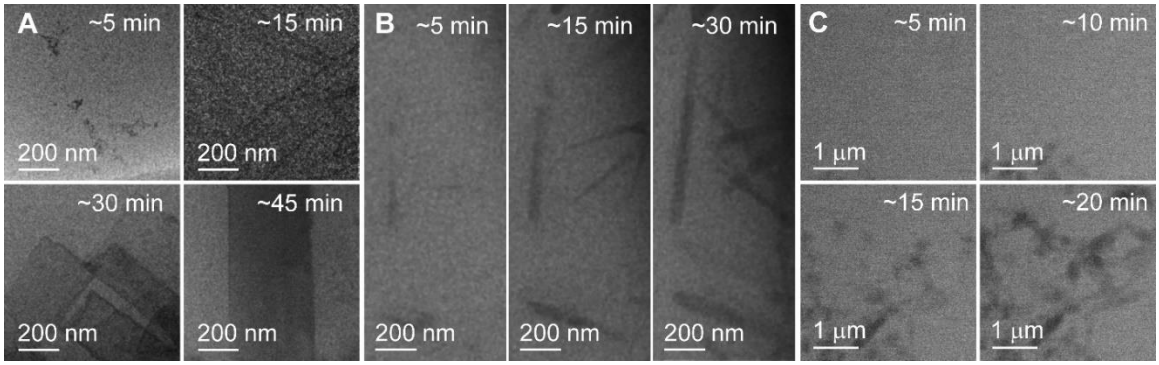

Figure 5. 22. Time lapse TEM images of room temperature growth experiments of Ag-MONT and Cu-MONT crystals at various reaction conditions. (A) 3:1 $AgNO_3$:ligand ratio; (B) 6:1 $AgNO_3$:ligand ratio; (C) 4:1 $CuBr_2$:ligand ratio.

CHAPTER 6

ASSEMBLY OF METAL-ORGANIC NANOSTRUCTURES FROM MIXED LIGANDS: A SMALL-ANGLE NEUTRON SCATTERING STUDY

A version of this chapter is in preparation by Umesh Shrestha, Kristina M. Vailonis, David M. Jenkins, and Mark Dadmun.

The work presented in this chapter was part of a collaborative project with the Dadmun group. Ligand **L1**, and MONT **[Cu(L1)(Br)$_2$]** were previously synthesized by Dr. Christopher Murdock.[32] I designed and synthesized ligand **L2**, and coordination polymer **[Cu(L2)(Br)$_2$]**. Dr. Umesh Shrestha conducted the SANS experiments and data analysis on the mixed ligand reactions.

Abstract

Metal-organic nanotubes (MONTs) are the one-dimensional analogue of metal-organic frameworks. When MONTs are aggregated together to form bulk solids (on the μm scale), their properties are hypothesized to be similar to bulk 3D MOFs. It is expected that once MONTs are dispersed, new and unique properties can be studied. To achieve this, an understanding of MONTs on the nanoscale must be accomplished. This includes the initial colloidal phase reactions. Small angle neutron scattering can be used to study these nanoscale structures. Currently, only reactions with one type of MONT product have be analyzed. In this manuscript, we examine how small changes in ligand architecture can lead to dramatic differences in material and measure these changes with small angle neutron scattering (SANS).

Introduction

Metal-organic nanotubes (MONTs) are the one-dimensional versions of metal-organic frameworks (MOFs). The key to unlocking the unique applications and properties of MONTs is the ability to form discrete tubes or finite bundles of

them. To approach the small bundles, or even individual MONTs, it is necessary to understand their nucleation and growth since these materials are built one chemical bond at a time, analogously to polymers.

Therefore, it is necessary to study MONTs on the nanometer regime as they are constructed and to develop tools that can determine the type of material being formed during the chemical reaction. *In situ* characterization techniques such as small-angle X-ray or neutron scattering (SAXS/SANS)[47] and liquid-cell transmission electron microscopy (LCTEM)[70] have been employed for these purposes. However, to date, all examples of these measurements have looked at reactions with one type of MONT product.[168] Mixed ligand and metal MONT reactions have not been investigated. Nor have different structures been compared simultaneously. Through blending multiple ligands into a MONT reaction, multiple distinct structures may be formed which would be previously impossible. This process may also allow for built-in defect sites in a manner that is not possible with other 1D materials such as carbon nanotubes.

Since the synthesis of an isoreticular series of metal-organic nanotubes previously conducted by our group,[32] we have investigated preparing non-aggregated MONTS. Creating a method to isolate individual tubes or at the very least, small quantifiable bundles of them would allow for their unique anisotropic structure to be studied and ultimately utilization in nanomaterials.

Previously, the Jenkins group has synthesized 1D MONTs from the reaction of 1,3-bis((4H-1,2,4-triazol-4-yl)methyl)benzene ligand (**L1**) with metal salts.[32] They have also shown that the addition of a small methyl group on the same ligand interferes with assembly of the MONTs and resulted in the formation of a 2D sheet MOF, rather than the 1D MONT. A methyl group incorporated in L1 gives 4,4'-((5-methyl-1,3-phenylene)bis(methylene))bis(4H-1,2,4-triazole), (**L2**) ligand, which reacts with the metal salt to form a zig-zag 2D sheet. It somewhat surprising and that the addition of the small methyl group to the ligand drives the assembly process to a 2D structure, but this result provides a conduit for a critical study that examines the competition of the 1D and 2D assembly processes. By examining

the assembly of metal organic assemblies that are formed from a mixture of **L1** and **L2** ligands, the relative influence of each on the assembly growth can be elucidated. **L1** is designated as the meta ligand, while **L2** is termed the methyl meta ligand.

Therefore, in this study, small angle neutron scattering is used to monitor the formation of metal organic assemblies that consist of mixtures of the **L2** and **L1** ligand to elucidate the impact of each ligand on the formation of ultimate 1D or 2D structure. The result from SANS study showed that formation of a metal organic assembly occurs immediately as the metal salt and ligand are mixed, with similar initial structures for all **L1** and **L2** concentrations. Increased reaction time showed a variation in structure formation that was dependent on **L2** loading, with a larger deviation in structure from the MONT only exhibited at larger **L2** loadings. The formation of the pure 2D sheet (**L2**) was much faster compared to that of the pure MONT (**L1**), yet for most **L1**/**L2** ratios, the formation of the 1D MONT appeared to dominate the assembly process.

Materials and Sample Preparation

Samples for the small angle neutron scattering study were prepared by mixing solutions of the metal salt and ligand dissolved in deuterated solvents. Deuterium oxide (D_2O) and deuterated dimethyl formamide (d_7-DMF) were purchased from Cambridge Isotope Laboratories, Inc. and used as received. The metal salt was dissolved in 1 mL D_2O and **L1** and **L2** ligands were dissolved in 2mL of d_7-DMF. (See Experimental section for detailed information regarding amount of ligand and metal salt used for the study) The ligands were dissolved using a vortex spinner and heating the solution to 85 °C. After completely dissolving both ligand and metal salt, both solutions were heated at 85 °C for a few minutes. The metal solution was then mixed with the ligand solution and shaken carefully. The mixture solutions were immediately syringed into banjo cells to

complete the scattering experiments. Formation of the metal organic assemblies for mixtures of **L1** and **L2** of 0, 10, 40, 60, and 100% **L2** were monitored for reaction times that ranged from 2 to 15 hours. Preliminary small angle X-ray scattering studies showed that the reaction of the 100% **L2** sample was completed in about 8 hours, so this sample was examined for a maximum of 8.5 hours of reaction time.

The SANS experiments were performed at two neutron facilities, on the general-purpose SANS (CG GP-SANS) at HFIR, Oak Ridge National Laboratory (ORNL) and on the NG-7 SANS at NCNR, National Institute of Standards and Technology (NIST). Sample to detector distances were varied to cover *q* ranges from ~ 0.0039$Å^{-1}$ to 0.57$Å^{-1}$. *q* is momentum transfer vector and characterized by $q = 4\pi \sin\theta/\lambda$, where θ is the scattering angle of the neutron beam and λ is the neutron wavelength. The raw data from HFIR is reduced using the SPICE SANS data reduction package whereas the NCNR SANS reduction package was used to reduce the data from the NG-7 SANS. Scattering from background, empty cell and mixed solvents with the same composition as the sample were accounted for in the data reduction.

Experimental data from the SANS experiments are fitted using the SasView program. The structure of the MONT formed from the meta **L1** ligand as determined from previous studies.[32] The neutron scattering length density of the meta MONT and the mixed solvent (calculated according to the ratio of two solvents) were calculated and used as starting parameters to fit the scattering data. From each scattering curve, the slope of the log I vs log q plot was measured in the low *q* region to provide insight into the dimensionality of the formed nanostructure and guide in the choice of the model to fit the data. From these results, it is clear that the structure of the assemblies on the length scale of 10-100 nm is two dimensional throughout the formation process, and thus the data were fit to three two-dimensional models: lamellar, elliptical cylinder and parallelepiped.

All the samples reasonably fit to the lamellae, elliptical cylinder and parallelepiped form factors, which is not surprising as they are all similar geometrically. In all cases, the background was allowed to fit according to the

scattering from the high *q* and the scale factor is fixed to the volume fraction of solutes in solution. All three models provided similar results for the thickness and change in length. However, close inspection of the various models showed subtle differences, and it was found that the elliptical cylinder model provided the most robust fits and consistent results, and thus was chosen to fit the scattering curves to provide quantitative information on the structural changes to the forming metal organic nanostructures with reaction time and ligand composition.

Results and Discussion

Previous studies have shown that the reaction of **L1** in dimethylformamide and copper(II) bromide dihydrate in water under solvothermal conditions produced the MONT, **[Cu_2Br_2(L1)]•DMF**, as illustrated in Scheme 6.1A.[32] The driving force of the MONT formation is the intertubular π- π stacking from the organic linkers within the MONT. To more fully understand the relationship between ligand structure and geometry of the formed metal organic assembly, an identical solvothermal synthesis was completed utilizing a ligand with a methyl group to the meta position on the 1,3-bis((4H-1,2,4-triazol-4-yl)methyl)benzene ligand (**L1**) to form ligand **L2**. Our hypothesis was to add additional steric bulk to the ligand in order to break up the π- π stacking and inhibit the aggregation of the MONTs. Adding larger R-groups to the meta position on the 1,3-bis((4H-1,2,4-triazol-4-yl)methyl)benzene ligand (**L1**) that we previously synthesized achieves this goal. A methyl R-group was chosen as a moderately sized R-group. This methyl functionalized ligand, 4,4'-((5-methyl-1,3-phenylene)bis(methylene))bis(4H-1,2,4-triazole), (**L2**) can be prepared in three steps (See Experimental Section, Scheme 6.2). The key step is refluxing 1,3-bis(bromomethyl)-5-methylbenzene in acetonitrile with 3-(1H-1,2,4-triazol-1-yl)propanenitrile by the method of Horváth to yield a white powder, 4,4'-((5-methyl-1,3-phenylene)bis(methylene))bis(1-(2-cyanoethyl)-4H-1,2,4-triazol-1-ium) dibromide, in 83.6 % yield.

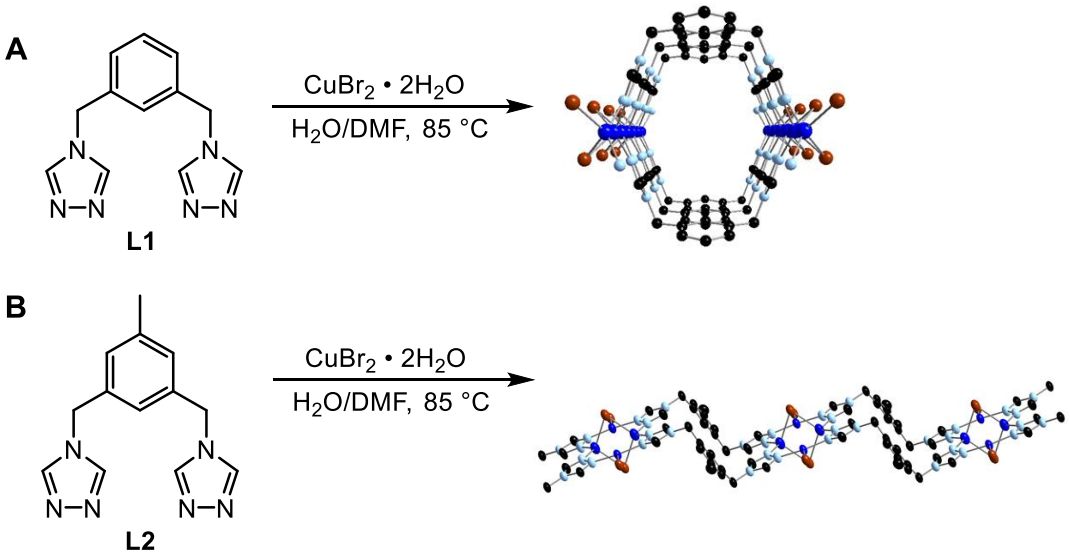

Scheme 6. 1. Synthesis of (A) MONT, $[Cu_2Br_2(L1)]$•DMF (B) double-stranded coordination polymer $[Cu_2Br_2(L2)]$.

4,4'-((5-methyl-1,3-phenylene)bis(methylene))bis(1-(2-cyanoethyl)-4H-1,2,4-triazol-1-ium) dibromide was then deprotected with potassium hydroxide in refluxing ethanol to yield **L2**, 4,4'-((5-methyl-1,3-phenylene)bis(methylene))bis(4H-1,2,4-triazole), in 63.1 % yield (See Experimental Section, Scheme 6.2).

A previously reported MONT, **[Cu_2Br_2(L1)]•DMF**, was synthesized with **L1** and copper(II) dihydrate under solvothermal conditions in dimethylformamide and water as seen in Scheme 6.1A. To synthesize a MONT with **L2**, the ligand was subjected to analogous conditions as the previously reported MONT synthesis.[32] This reaction yielded a white crystalline solid. However, single crystal X-ray diffraction (SCXRD) analysis of the solid revealed that instead of creating a new isostructural MONT, we had synthesized a double stranded coordination polymer with **L2** (Scheme 6.1B).

This double-stranded coordination polymer **[Cu_2Br_2(L2)]** exhibits two unique copper atoms, both in a 1+ oxidation state (Figure 6.1B). Cu_1 occupies a T-shaped geometry bound to one bromide and two nitrogens from two separate **L2** ligands. Cu_2 occupies a tetrahedral geometry bound to two bromides and two nitrogens from two separate **L2** ligands. This polymer packs in a zig-zag fashion and creates void spaces similar to a 2D MOF (See Experimental Section for Figures 6.9-6.11).

Given that the mere introduction of a methyl group to the **L1** ligand shifts the geometry of the molecular organic assembly from a 1D MONT to a double stranded coordination polymer, we sought to understand the assembly of metal organic structures that form from a *mixture* of the two similar ligands, **L1** and **L2**. To understand the formation process, we turned to small angle neutron scattering as a method to monitor the formation of the MONT and/or 2D sheets *in situ* during the reaction. Small-angle neutron scattering (SANS) is effective for studying the nanostructure of materials in solution including polymers and MOFs.[47] To study the blending systematically, we evaluated the time evolution of the formation of the MONT and the double-stranded coordination polymer with SANS from the reaction of pure **L1** and **L2**, respectively. After that, similar experiments to monitor the

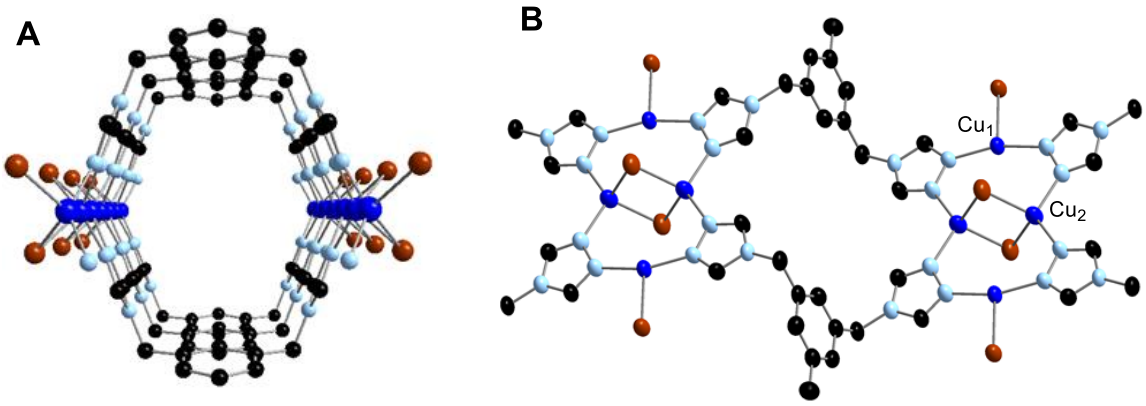

Figure 6. 1. (A) 1D MONT, $[Cu_2Br_2(L1)]$•DMF (B) double-stranded coordination polymer, $[Cu_2Br_2(L2)]$. Black, light blue, dark blue, and brown ellipsoids (50% probability) represent carbon, nitrogen, copper, and bromine atoms respectively.

growth of metal organic structures formed from the reaction of copper(II) dihydrate and mixtures of **L1** and **L2** in water were completed. The loading of **L2** ligand in these reactions was 0, 10, 40, 60, or 100% **L2**.

Figure 6.2 shows an example set of SANS scattering curves, in this case for the reaction of the pure **L1** ligand and the copper(II) bromide dihydrate as a function of reaction time. This data provides structural information over a *q* range of ~ 0.004Å^{-1} to 0.35Å^{-1}, which corresponds to monitoring the growth of the structures over length scales that range from ~20 to 1500 Å. Qualitative analysis of the scattering curves shows that the slope of the scattering curves at the lowest q values does not change with time, indicating that the shape if the scattering object is fairly constant, though its size changes with reaction time.

The slope at the low *q* region is approximately -2 for all reaction times indicating the formation of two-dimensional structures. The increase in scattering at higher q indicates that the size of the metal organic structure grows with time on length scales that are *ca.* below 300 Å (i.e., q > .02 Å^{-1}) Moreover, fitting the data to a specific structural model provides a pathway to quantify the geometry and extent of this growth. Careful analysis shows that the scattering data for all reaction times is well fitted using the elliptical cylinder model, a two-dimensional sheet like structure. Similar representations of the SANS data collected for all samples are provided in the Experimental Section, where Figure 6.13 shows the data for the 90% **L1** sample, Figure 6.15 documents the 60% **L1** sample, Figure 6.16 presents the scattering of the 40% **L1** sample and Figure 6.17 shows the scattering of the pure **L2** sample.

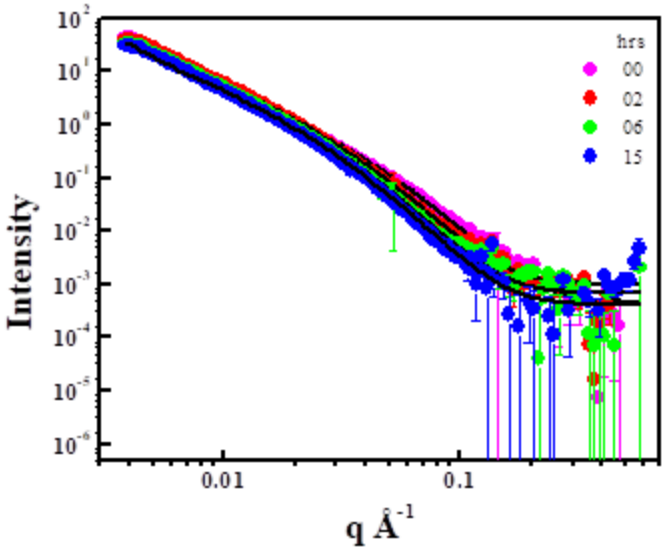

Figure 6. 2. SANS scattering curves for the pure L1 ligand and metal salt at indicated reaction time, where symbol is for experimental data and solid line is fit using elliptical cylinder model.

Quantitative analysis of the changes to the size and shape of the metal organic structures as a function of ligand composition and reaction time is possible from the fits of the scattering data to the elliptical cylinder model. The elliptical cylinder can best be pictured as a thin rectangular solid with an elliptical cross section, as shown in Figure 6.3. The parameters that emerge from the analysis include the lengths of the major (R_m) and minor (R_s) axes of the cross-section and the length (L) of the cylinder, as well as the volume fraction of the formed metal organic structure. For instance, Figure 6.4 shows the change in the thickness (minor axis, R_s) of the elliptical cylinder as a function of reaction time for all of the ligand mixtures, while Figure 6.5 shows the same information for time evolution during the reaction of the cross sectional width of the elliptical cylinder (major axis, R_m). Figure 6.6 shows the growth of the length of the metal organic structures as a function of reaction time for each ligand mixture.

Inspection of these plots provides interesting insight into the growth of the two-dimensional metal organic nanostructure. The thickness of the structure formed at the beginning of the reaction of pure **L1** is ~8 Å which is similar to the thickness of the meta MONT as determined from a previous study.[32, 47] Similarly, the thickness of the structure formed by the reaction of pure **L2** is about 10 Å. As the reaction proceeds, the thickness of the two-dimensional structure essentially doubles for the **L1** sample, while the thickness increases by a factor of 3 for the **L2** structure. Examination of Figure 6.5 shows similar trends for the growth of the width of the elliptical cylinder with reaction time – the width of the nanostructure is about ~200 Å at the beginning of the reaction for both the pure **L1** and pure **L2** reaction mixtures. However, the width grows quickly to ~ 1400 Å (~7x original size) for the **L2** methyl ligand sample, but only extends to approximately 400 Å (~ 2x original size) for the **L1** meta ligand. Thus, it appears that the reaction of the methyl ligand, **L2**, in the 2D MOF formation is faster than the inclusion of the meta ligand **L1** in the MONT.

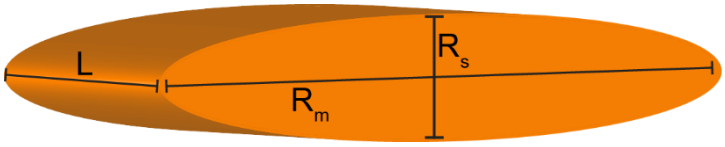

Figure 6. 3. Diagram of elliptical cylinder.

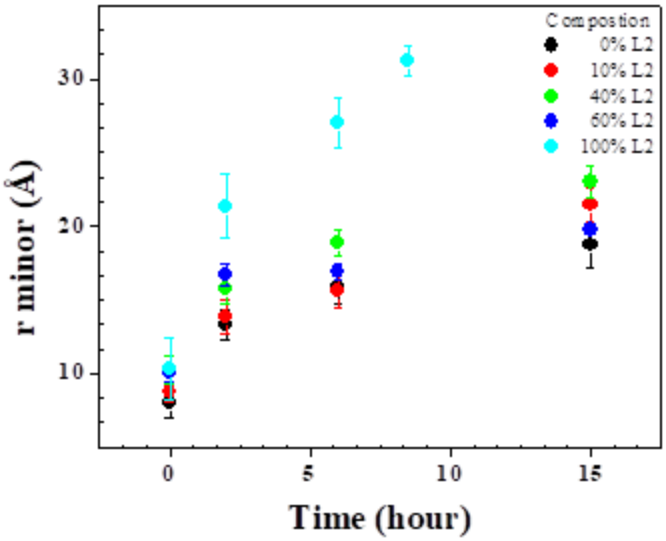

Figure 6. 4. Change in thickness of the nanoscale metal organic structure as a function of reaction time for all ligand compositions.

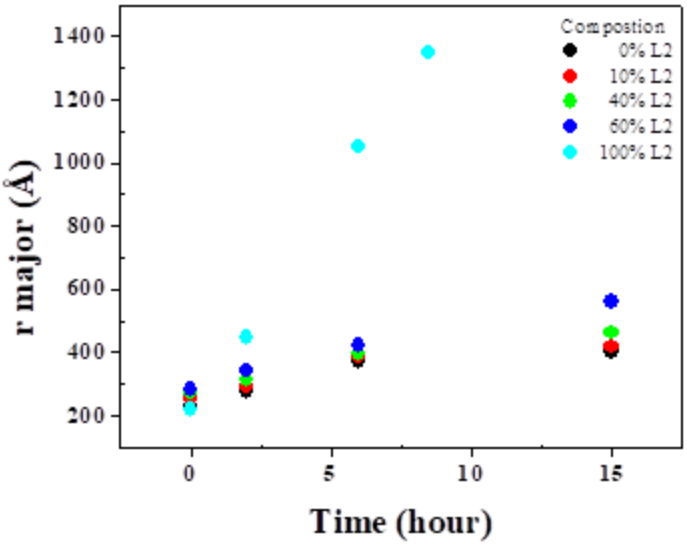

Figure 6. 5. Change in width of the 2-dimensional nanoscale metal organic structure as a function of reaction time for all ligand compositions.

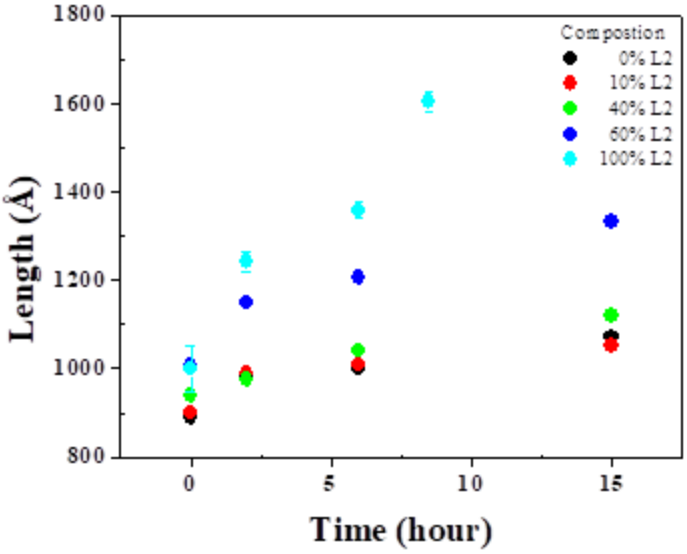

Figure 6. 6. Change in length of structure for all composition as a function of reaction time.

Moreover, in both Figures 6.4 and 6.5, the behavior of the mixed ligand samples mimics the growth behavior of the pure **L1** ligand, more than it does the growth of the structure formed by the pure **L2** ligand sample. With the addition of 10, 40 or 60% **L2** ligand, the thickness only grows from 9-10 Å to 20-22 Å, approximately doubling, while the same ligand compositions results in the growth of the width of the 2-dimensional nanostructure from *ca.* 250-300 Å to 400-500 Å as the reaction proceeds. Clearly, in the mixed ligand reaction, the presence of the **L1** meta ligand inhibits the growth of the cross-section of the metal organic structure that appears to occur much more quickly in the pure **L2** sample. This is true even when the **L1** ligand is the minor phase, i.e. for the 60% **L2** sample.

This relationship does not appear to hold true for the growth of the length of the two-dimensional metal organic structure. Figure 6.6 shows that the reaction of pure meta ligand **L1** causes the length to increase by about 20% (~900 Å to 1100 Å), while the pure **L2** methyl ligand reaction grows the length of the two-dimensional MOF by 60% (from 1000Å to 1600 Å). It is interesting that the change in the growth of the metal organic nanostructure length appears to be much more dependent on the composition of the ligand mixture than the thickness or width (Figures 6.4 and 6.5). Figure 6.6 clearly shows that the addition of the **L2** ligand to the reaction mixture increases the growth along the length of the elliptical cylinder for all compositions, where the growth rate of the 60% **L2** sample is nearly proportional to the **L2** loading.

Figures 6.4-6.6 clearly show that the growth of the metal organic nanostructure occurs primarily along the length and the width of the nanostructure, with very little change in the thickness. Therefore, these growths in structure can also be followed by inspection of Figure 6.7, which plots the change in the width and length of the elliptical cylinder as a function of reaction time for each ligand composition on the same plot. Inspection of this plot verifies that the pure **L2** sample grows along the width and length faces of the elliptical cylinder, but much more quickly along the width. The growth along the width occurs so quickly that the final structure of the pure **L2** methyl ligand nanostructure evolves to form a

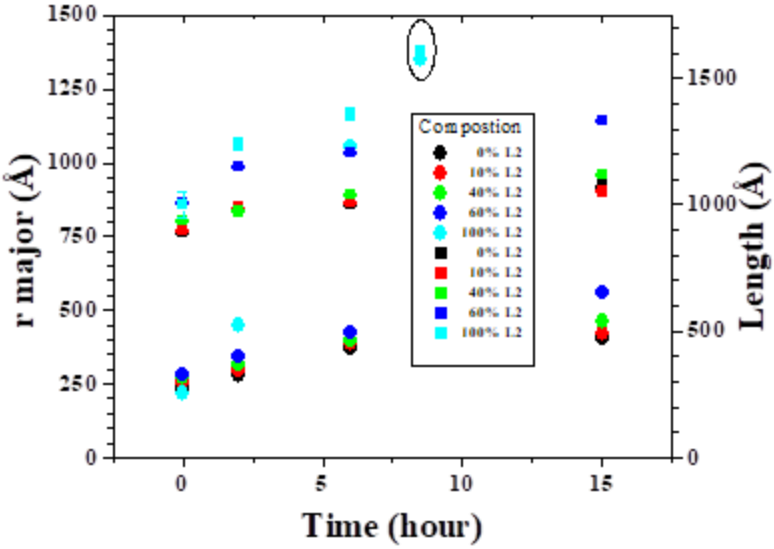

Figure 6. 7. Change in the length (squares) and width (circles) as a function of reaction time for all ligand compositions.

square (length ~ width), while all other ligand compositions form rectangular cross-sections (length >> width).

Finally, Figure 6.8 shows the overall growth in the volume of the metal organic nanostructure as a function of the ligand composition for all reaction times. Inspection of this figure shows that the volume of the metal organic nanostructure increases with % **L2** methyl ligand for all reaction times, but combining this insight with the previous figures shows that most of the growth occurs on the faces of the two-dimensional nanostructure.

The results presented above show that as soon as the ligands are mixed with the metal salt, a reaction occurs that form two-dimensional metal organic nanostructures. These initially formed structures are of similar size regardless of the composition of the ligand composition, indicating that the mixture of the two different types of ligands form similar structure in the initial reaction. As the reaction proceeds the metal organic nanostructure grows in all dimensions, but primarily along the width, which doubles. The growth process for the metal organic nanostructures changes very little when 10%, 40% and 60% of the methyl ligand (**L2**) is added to the **L1** meta ligand, even though the growth process of the pure **L2** ligand sample is much faster. We interpret this to indicate that the presence of the **L1** ligand controls the growth of the metal organic nanostructure, slowing the growth process regardless of loading of **L2**.

Recalling that the pure **L2** methyl ligand forms a sheet like structure and that the pure **L1** meta ligand forms a nanotube, it appears that the formation of the nanotube motif is dominant in the growth of the metal organic nanostructure from the mixed ligands. The idea of a competition between the growth of the sheets and tubes also leads to the question of whether the formed nanostructures contain both methyl (**L2**) and meta (**L1**) ligands or if sheets and tubes are formed separately. Unfortunately, the data do not unequivocally answer this question, but does provide some clues. First, there is no indication of a mixture of structures, suggesting that the metal organic nanostructures that are formed for all ligand compositions have the same geometry. Second, the size of the initial structures

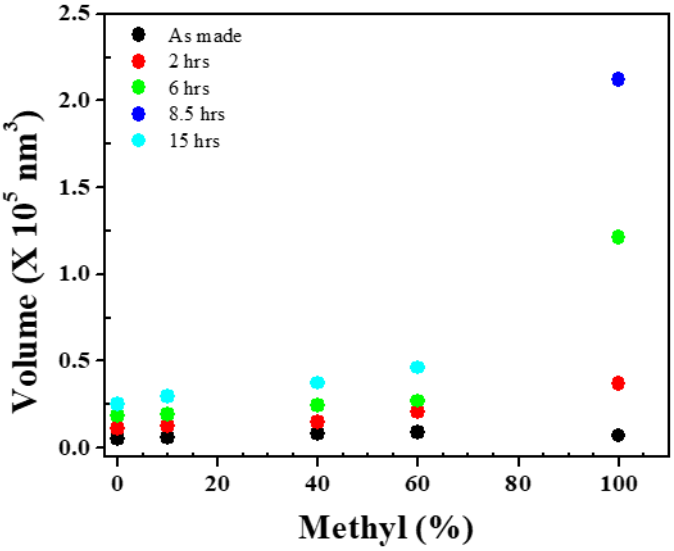

Figure 6. 8. Change in volume of structure formed with composition.

formed in the reaction is very similar for all ligand composition. Both of these observations are consistent with the metal organic structures formed containing both ligands. Third, the absolute scattering intensities of the structures formed from all ligand compositions are very similar, which indicates that the *number* of metal organic nanostructures that are formed do not change with ligand composition. This is also consistent with the inclusion of both ligands in the growing 2-dimensional structures, as one would expect a decrease in the number of formed metal organic nanostructures with an increase in the loading of a ligand that is excluded from the formed structure.

Conclusion

The solvothermal reaction of the **L1** meta ligand with copper(II) dihydrate forms a one-dimensional metal organic nanotube, while the same reaction of copper(II) dihydrate with the **L2** methyl ligand forms a two-dimensional MOF. This research program explores the formation process of copper(II) dihydrate with mixtures of the **L1** and **L2** ligands at a range of compositions from pure **L1** to pure **L2**. Small angle neutron scattering provides insight into the nanoscale structure that form during the reactions, and interpretation of the observed scattering curves elucidates the growth and geometry of the metal organic nanostructure that are formed in these reactions. Regardless of ligand concentration, anisotropic two-dimensional sheet like nanostructures are formed immediately after mixing the organic ligand mixture with the metal salt solution. These two-dimensional structures grow with reaction time, primarily along the width, and to a lesser extent along the length with reaction time. Interestingly the rate of growth is very similar for the pure **L1** ligand sample and the three mixture of **L1** and **L2** ligands (10%, 40% and 60% **L2**). The growth of the metal organic sheets formed from the pure **L2** methyl sample occurs much more quickly than samples that contain **L1** meta ligand at any loading. We interpret this to indicate that the presence of the **L1** meta

ligands inhibits the growth of the **L2** sheets, driving the reaction to include both **L1** and **L2** ligands. Additionally, careful analysis of the absolute intensity scattering data as well as the similarity of the geometry of all ligand compositions suggests that the formed nanostructure incorporate both the **L1** and **L2** ligand, though more careful contrast variation neutron experiments are needed to verify this interpretation.

Experimental

I. General Considerations for Synthesis

Compound **1**, 1,3-bis(bromomethyl)-5-methylbenzene, was synthesized as previously reported by Lu(R) from 5-methylisophthalic acid, which was purchased from Fischer Scientific and used with no further purification. Compound **2**, 1,2,4-triazole-1-propanenitrile, was synthesized as previously reported by Horváth. (R) Synthesis of **L1** and **[(L1)Cu_2Br_2]·DMF** was previously reported by Jenkins. (R) All other reagents were purchased from commercial vendors and used with no additional purification.

^{1}H and ^{13}C NMR spectra were collected at ambient temperature on either a Varian Mercury 300 MHz, a Varian VNMRS 500 MHz, or a Varian VNMRS 600 MHz narrow-bore broadband system. ^{1}H and ^{13}C NMR chemical shifts were referenced to the residual solvent. All mass spectrometry analyses were conducted at the Mass Spectrometry Center located in the Department of Chemistry at the University of Tennessee. High resolution ESI-MS were analyzed using an electrospray ionization source in the positive mode of detection, with mass analysis performed by an Exactive Plus Orbitrap^{TM} Mass Spectrometer (Thermo Scientific, San Jose, CA, USA). Attenuated Total Reflectance (ATR) infrared spectroscopy data were collected on a Thermo Scientific Nicolet iS10 with a Smart iTR accessory. Thermogravimetric analysis was collected on freshly

prepared samples on a TA Instruments TGA Q50, under N_2. Elemental analysis of carbon, hydrogen, nitrogen for **[(L2)Cu$_2$Br$_2$]** was obtained from Atlantic Microlab, Inc., Norcross, GA.

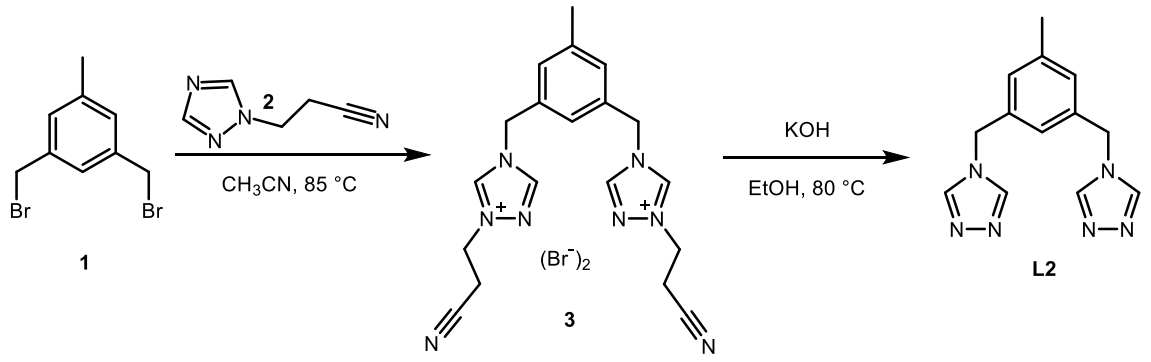

Scheme 6. 2. Synthetic scheme for L2.

Synthesis of 4,4'-((5-methyl-1,3-phenylene)bis(methylene))bis(1-(2-cyanoethyl)-4H-1,2,4-triazol-1-ium) dibromide, 3:

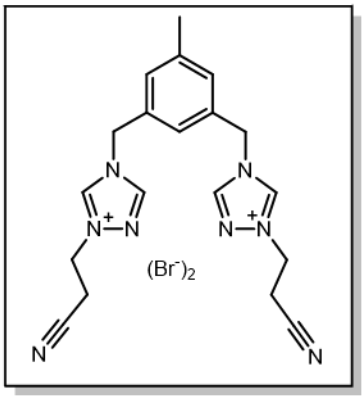

1,3-bis(bromomethyl)-5-methylbenzene **(1)** (0.2189 g, 0.7874 mmol) was added to a round bottom flask with 1,2,4-triazole-1-propanenitrile **(2)** (0.3063 g, 2.507 mmol) in 200 mL of acetonitrile. The reaction was heated to reflux at 85 °C for 24 hours, after which a white solid precipitated. The reaction mixture was then cooled to room temperature. Diethyl ether was added to the reaction flask to initiate additional precipitate formation. The crude

solid was then filtered through a medium frit and washed with acetonitrile (3 x 30 mL) and dried under reduced pressure to yield the pure product (0.239 g, 83.6% yield).

^{1}H NMR (DMSO-d_6, 499.74 MHz): 10.30 (s, 2H), 9.38 (s, 2H), 7.41 (s, 1H), 7.34 (s, 2H), 5.54 (s, 4H), 4.73 (t, 4H), 3.23 (t, 4H), 2.33 (s, 3H). ^{13}C NMR (DMSO-d_6, 125.66 MHz): 144.93, 143.41, 139.39, 134.10, 130.05, 126.54, 117.70, 50.22, 47.26, 20.80, 17.33. IR: 3103, 3050, 3026, 2975, 2912, 2253, 1843, 1743, 1605, 1577, 1522, 1469, 1436, 1414, 1383, 1366, 1341, 1314, 1280, 1256, 1225, 1205, 1180, 1136, 1064, 1048, 1021, 980, 955, 931, 917, 895, 877, 828, 757, 665 cm^{-1}. HR ESI-MS (m/z): $[M-Br]^+$: 441.1144 (found); $C_{19}H_{22}BrN_8^+$: 441.1145 (calculated).

Synthesis of 4,4'-((5-methyl-1,3-phenylene)bis(methylene))bis(4H-1,2,4-triazole), L2:

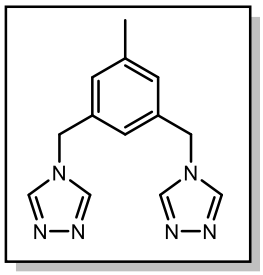

In a 100 mL round bottom flask, potassium hydroxide (0.4982 g, 8.881 mmol) and compound **3** (1.3391 g, 2.565 mmol) were suspended in 50 mL of ethanol and refluxed at 78 °C for 48 hours. Minimal amounts of water (20 mL) was added to the reaction flask and the solution was extracted with a 1:1 chloroform:ethanol solution (6 x 10 mL). This was done to separate the ligand from the potassium bromide side product. The organic layer was dried with magnesium sulfate, filtered, and subsequently evaporated under reduced pressure. The resulting white solid was dried under reduced pressure to yield a crude product (0.593 g, 63.1%). Further purification was achieved by Soxhlet extraction with methylene chloride to remove excess salt impurities.

^{1}H NMR (DMSO-d_6, 499.74 MHz): 8.57 (s, 4H), 7.06 (s, 1H) 7.05 (s, 2H), 5.22 (s, 4H), 2.26 (s, 3H). ^{13}C NMR (DMSO-d_6, 125.66 MHz): 143.22, 138.85, 137.23, 127.95, 124.16, 47.29, 20.82. IR: 3102, 3023, 2949, 2918, 2870, 2851, 1672, 1608, 1530, 1451, 1378, 1349, 1329, 1283, 1263, 1184, 1172, 1108, 1072, 1038, 973, 951, 919, 867, 744, 668, 637 cm^{-1}. HR ESI-MS (m/z): $[M+H]^+$: 255.1351 (found); $C_{13}H_{15}N_6^+$: 255.1353 (calculated).

Synthesis of Coordination Polymer, [(L2)Cu_2Br_2]:

Copper(II) bromide dihydrate (0.0382 g, 0.1710 mmol) was dissolved in 0.5 mL of deionized water and **L2** (0.0191 g, 0.0751 mmol) was dissolved in 1 mL of dimethylformamide. The two solutions were heated independently at 85 °C for 10 minutes in an aluminum heating block. The hot copper solution was added to the hot ligand solution, immediately forming a blue gel. After heating for 5 days at 85 °C, a white solid formed, which was isolated and washed with water and acetone to yield the pure product (3.8 mg, 9.35% yield).

IR: 3409, 3070, 2931, 2865, 1650, 1542, 1496, 1439, 1413, 1389, 1255, 1228, 1190, 1175, 1099, 1080, 1063, 1015, 845, 744, 661, 637 cm^{-1}. Anal. Calcd. For $C_{13}H_{14}Br_2Cu_2N_6$: C, 28.85; H,2.61; N, 15.53. Found: C, 29.87; H, 2.97; N, 15.47.

X-ray Structure Determination

L2 crystals were grown in hot acetonitrile overnight and **[(L2)Cu_2Br_2]** crystals were grown directly from the reaction vial. A clear colorless plate crystal of each compound was mounted in the 100 K cold stream provided by an Oxford Cryostream low-temperature apparatus on the head of a Bruker SMART APEXII diffractometer equipped with an ApexII CCD detector, employing the use of Mo Kα radiation (λ = 0.71073 Å). Data set was reduced with Bruker SAINT and was

corrected for absorption using SADABS. Structures were solved and refined using SHELXT.

Powder X-ray Experiments

Powder X-ray diffraction data were collected on the sample using a Panalytical Empyrean θ-2θ diffractometer in reflectance Bragg-Brentano geometry. Cu-Kα radiation (λ= 1.5406 Å; 1,800 W, 45 kV, 40 mA) was focused using a planar Gobel Mirror riding the K*α* line. A 0.25 mm divergence slit was used for all measurements. Diffracted radiation was detected using a PIXcel3d detector [(6° 2θ sampling width) equipped with a Ni monochromator. **[(L2)Cu_2Br_2]** sample was mounted onto a zero-background quartz plate fixed on a sample holder. The best counting statistics were achieved by using a 0.0394° 2θ step scan from 3 – 50° with an exposure time of 118.30 s per step and a revolution spin rate of 4 s.

II. Single Crystal X-ray Structures

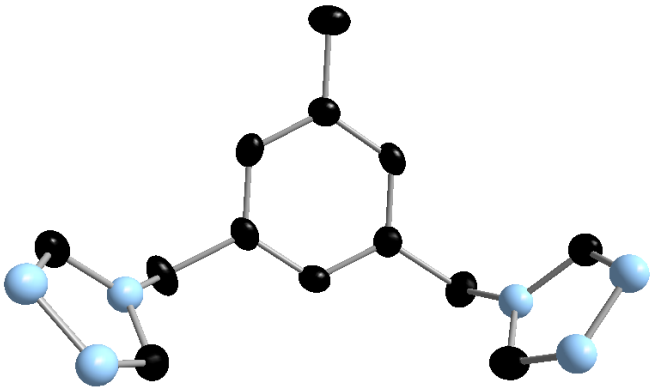

Figure 6. 9. Single Crystal X-ray structure of L2, Black and light blue ellipsoids (50% probability) represent carbon and nitrogen atoms respectively. Hydrogen atoms have been omitted for clarity.

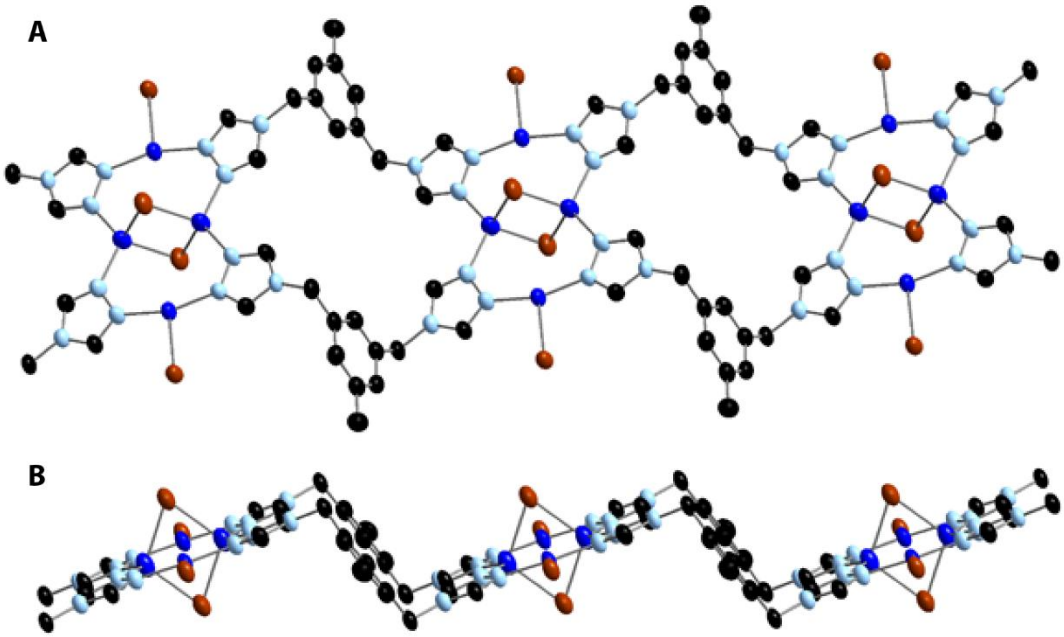

Figure 6. 10. Single Crystal X-ray structure of [(L2)Cu_2Br_2], (A) top view, and (B) side view. Black, light blue, dark blue, and brown ellipsoids (50% probability) represent carbon, nitrogen, copper, and bromine atoms respectively. Hydrogen atoms have been omitted for clarity.

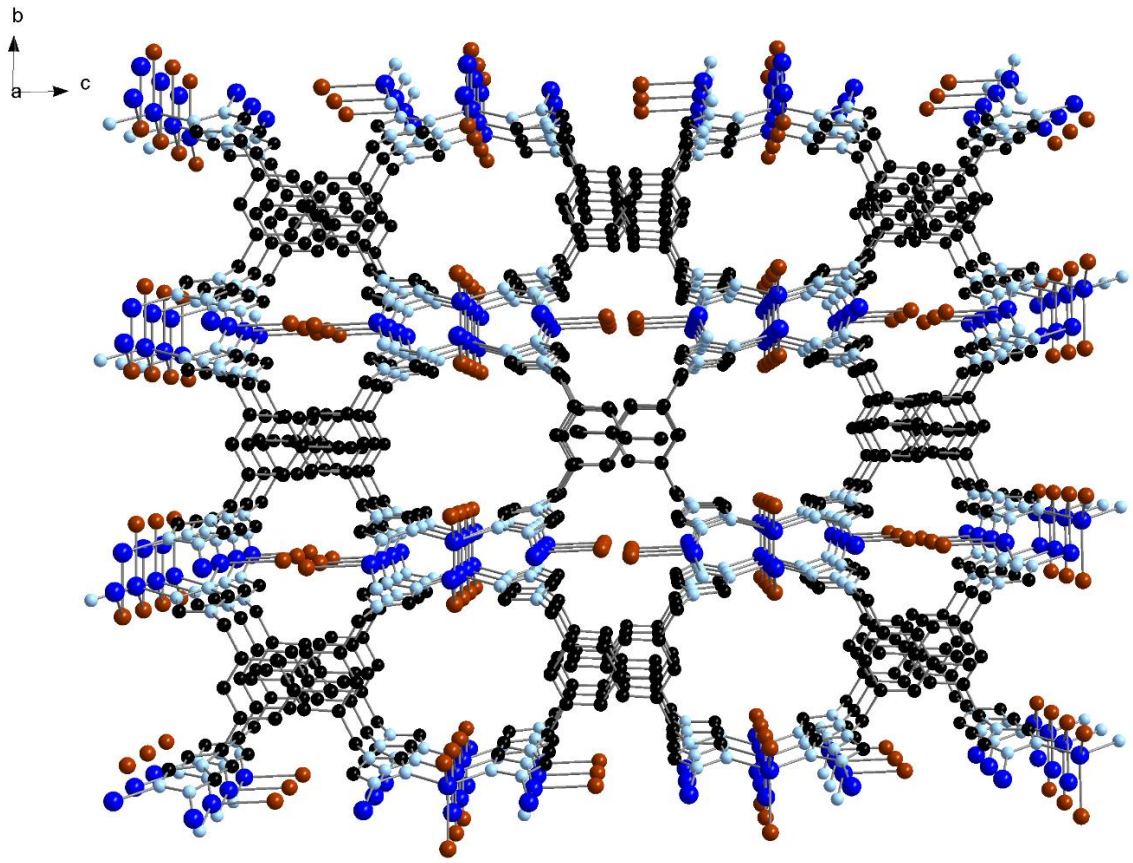

Figure 6. 11. Packing structure from single crystal X-ray structure of [(L2)Cu_2Br_2]. Black, light blue, dark blue, and brown ellipsoids (50% probability) represent carbon, nitrogen, copper, and bromine atoms respectively. Hydrogen atoms have been omitted for clarity.

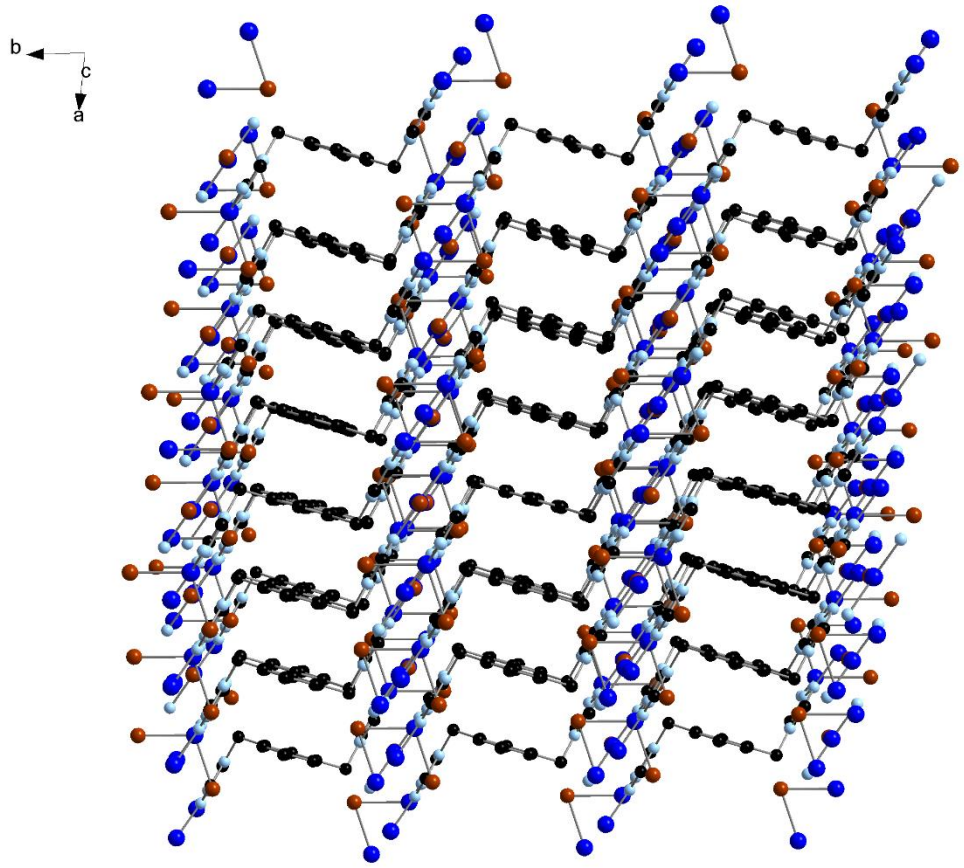

Figure 6. 12. Packing structure from single crystal X-ray structure of [(L2)Cu_2Br_2]. Black, light blue, dark blue, and brown ellipsoids (50% probability) represent carbon, nitrogen, copper, and bromine atoms respectively. Hydrogen atoms have been omitted for clarity.

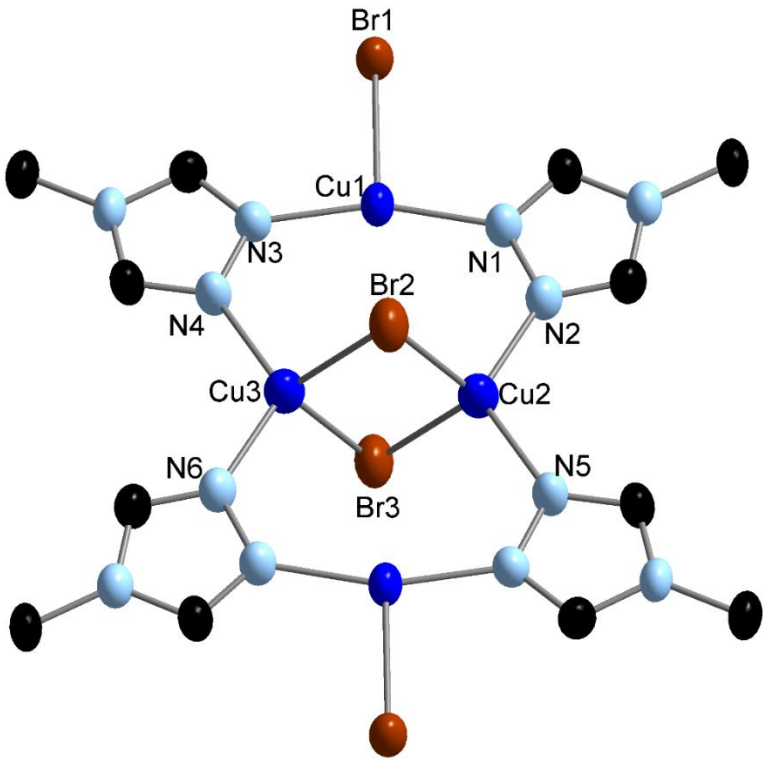

Figure 6. 13. Copper connectivity for [(L2)Cu_2Br_2].

Table 6. 1. Corresponding bond distances and angles for [(L2)Cu_2Br_2].

Atoms	Bond Angle (°)	Atoms	Bond Distance (Å)
Br1-Cu1-N1	100.046(4)	**Cu1-Br1**	2.5567(2)
N1-Cu1-N3	160.449(6)	**Cu1-N1**	1.9424(2)
N3-Cu1-Br1	99.503(3)	**Cu1-N3**	1.9237(2)
Cu1-N1-N2	125.877(6)	**N1-N2**	1.3649(1)
Cu1-N3-N4	126.128(6)	**N3-N4**	1.3712(1)
N2-Cu2-Br2	106.081(4)	**Cu2-N2**	2.0033(2)
Br2-Cu2-Br3	108.179(5)	**Cu2-N5**	2.0094(2)
Br3-Cu2-N5	108.572(4)	**Cu2-Br3**	2.4973(2)
N5-Cu2-N2	117.433(4)	**Cu2-Br2**	2.5092(2)
Br2-Cu2-Br3	108.179(5)	**Cu3-N4**	2.0094(2)
Cu3-Br2-Cu2	71.821(4)	**Cu3-N6**	2.0033(2)
Cu3-Br3-Cu2	71.821(4)	**Cu3-Br2**	2.5092(2)
Br2-Cu3-Br3	108.179(5)	**Cu3-Br3**	2.4973(2)
Br3-Cu3-N6	106.081(4)		
N6-Cu3-N4	117.433(4)		
N4-Cu3-Br2	108.572(4)		

III. Selected Spectra and Analytical Data for 1-5 and MONT

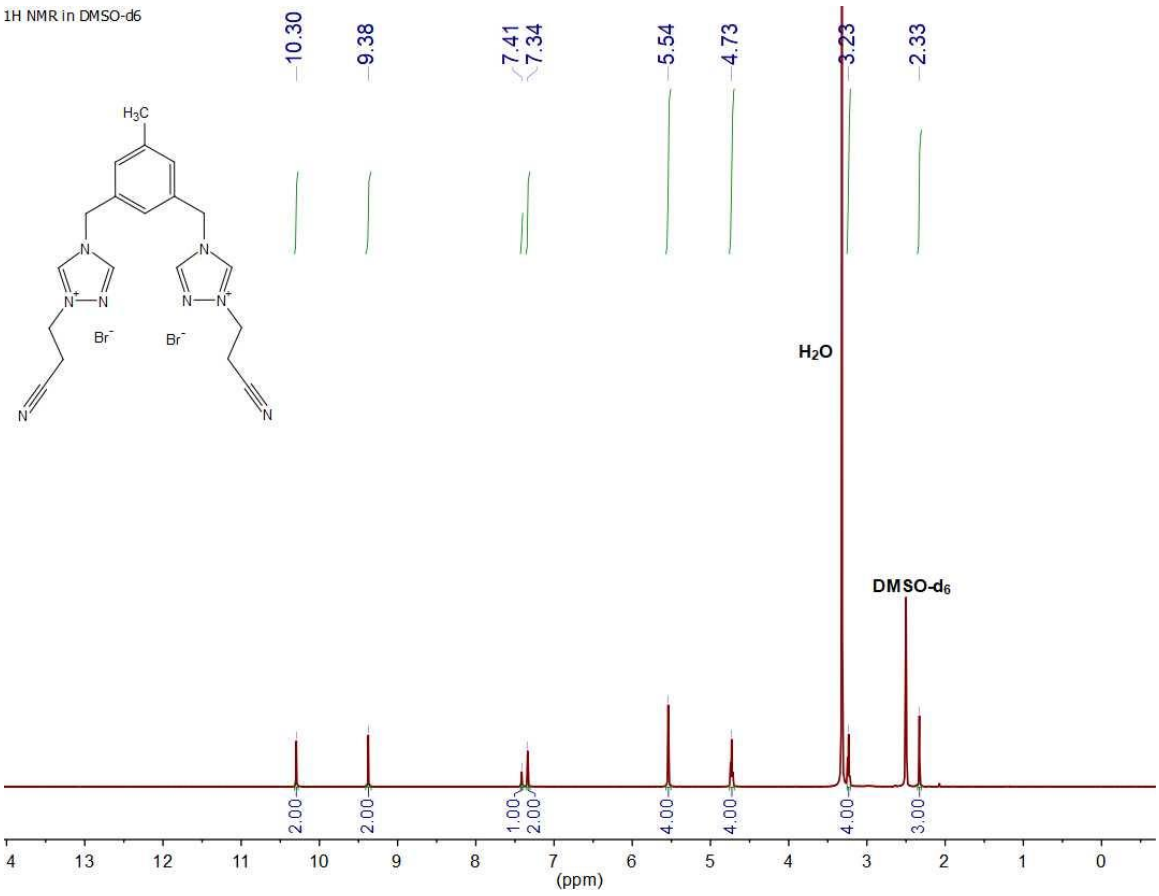

Spectra 6. 1. ^{1}H NMR of 3 in DMSO-d$_6$.

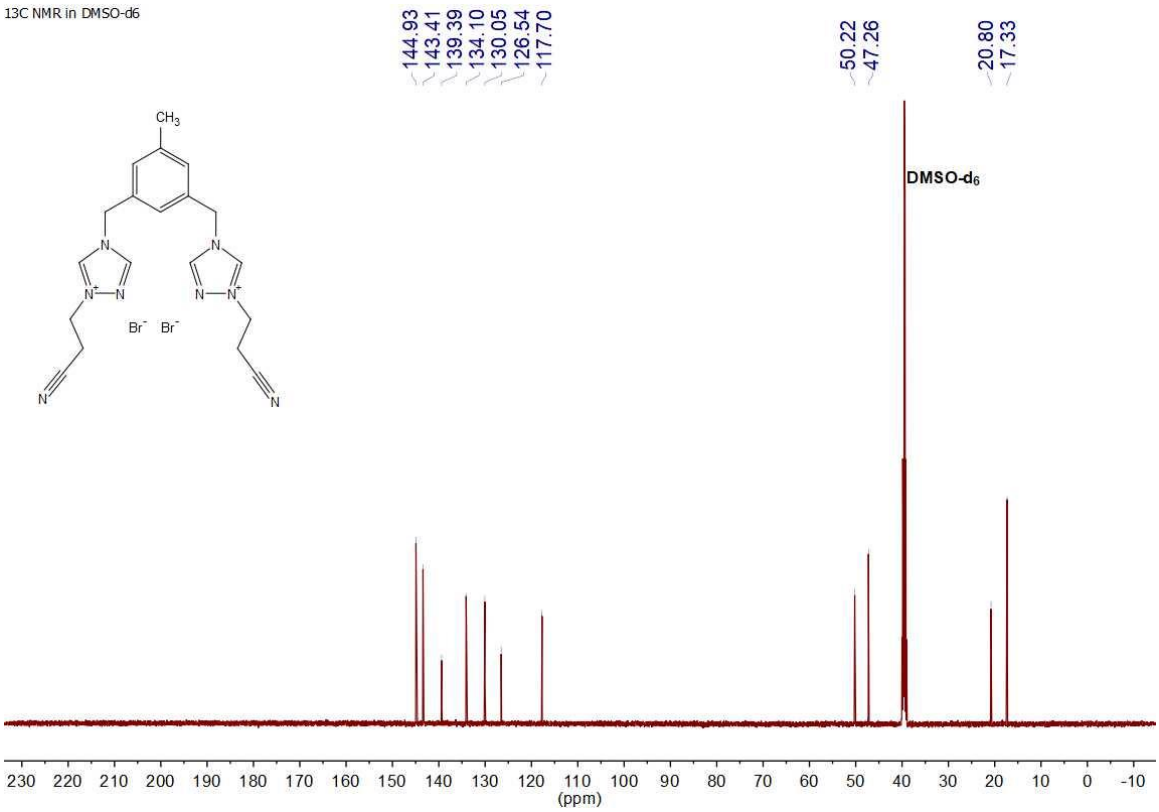

Spectra 6. 2. ^{13}C NMR of 3 in DMSO-d$_6$.

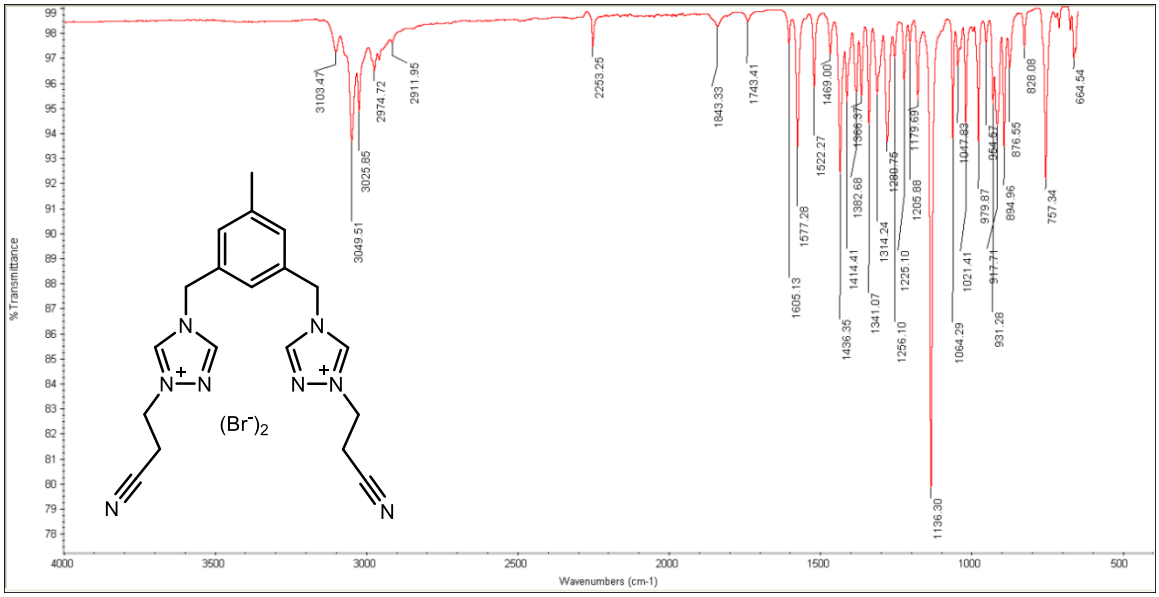

Spectra 6. 3. ATR-IR of 3.

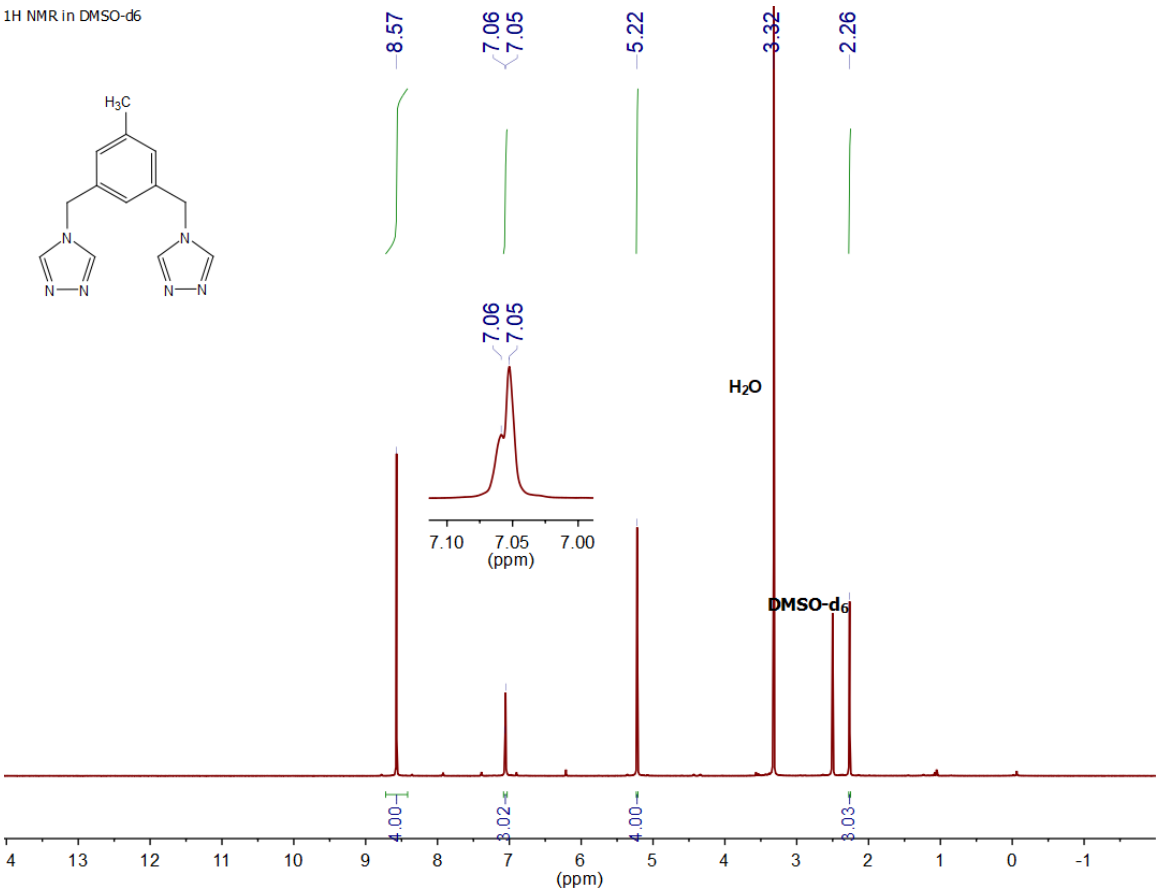

Spectra 6. 4 ^{1}H NMR of L2 in DMSO-d$_6$.

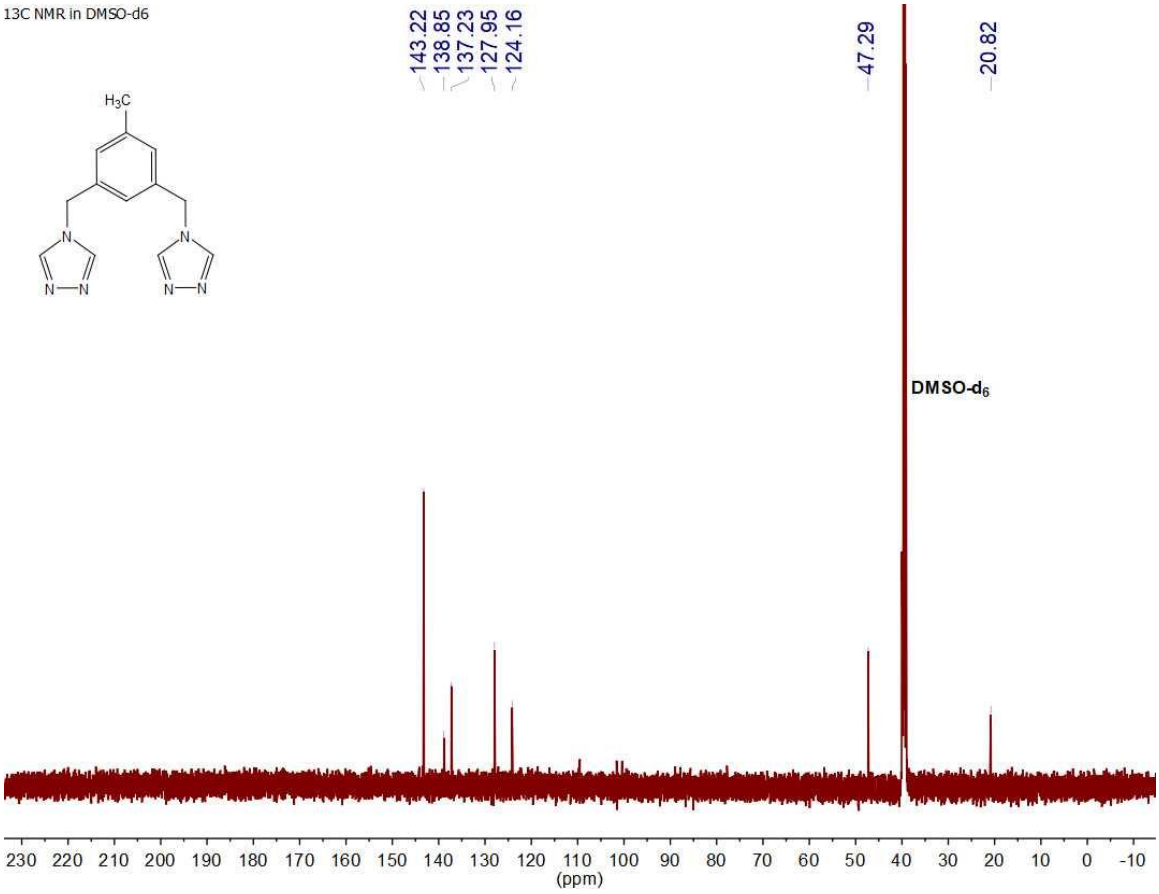

Spectra 6. 5. ^{13}C NMR of L2 in DMSO-d_6.

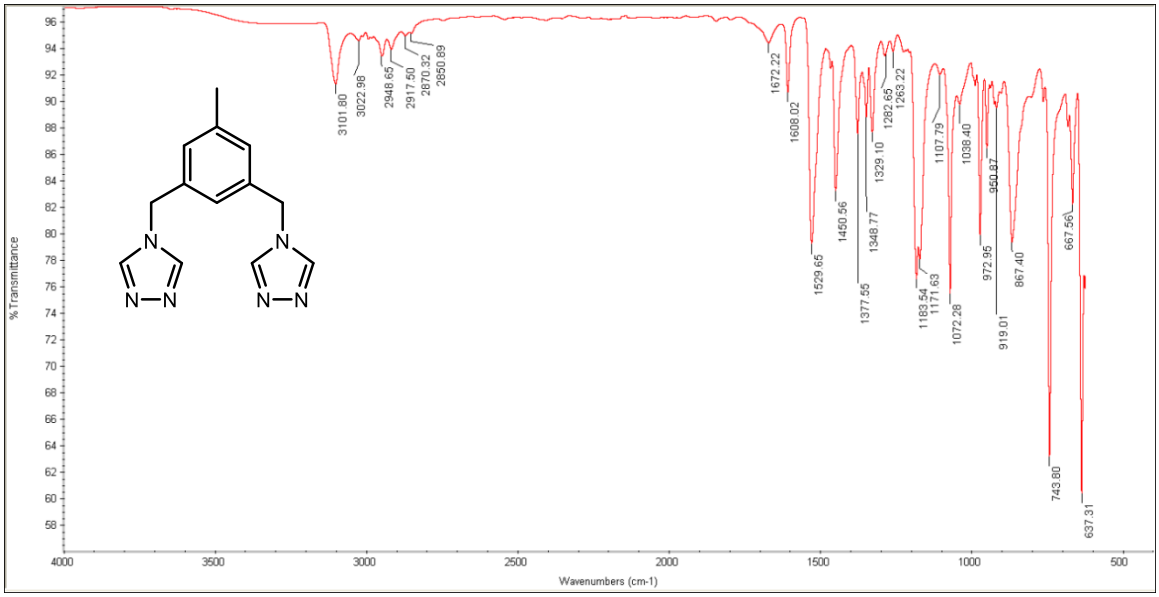

Spectra 6. 6. ATR-IR of L2.

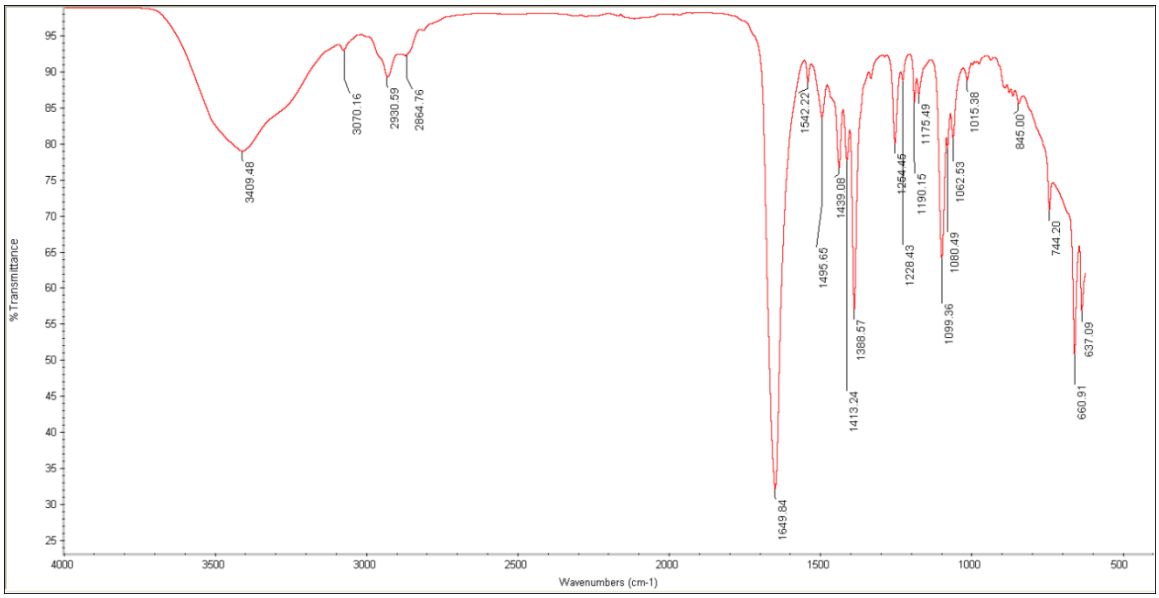

Spectra 6. 7. ATR-IR of [(L2)Cu_2Br_2].

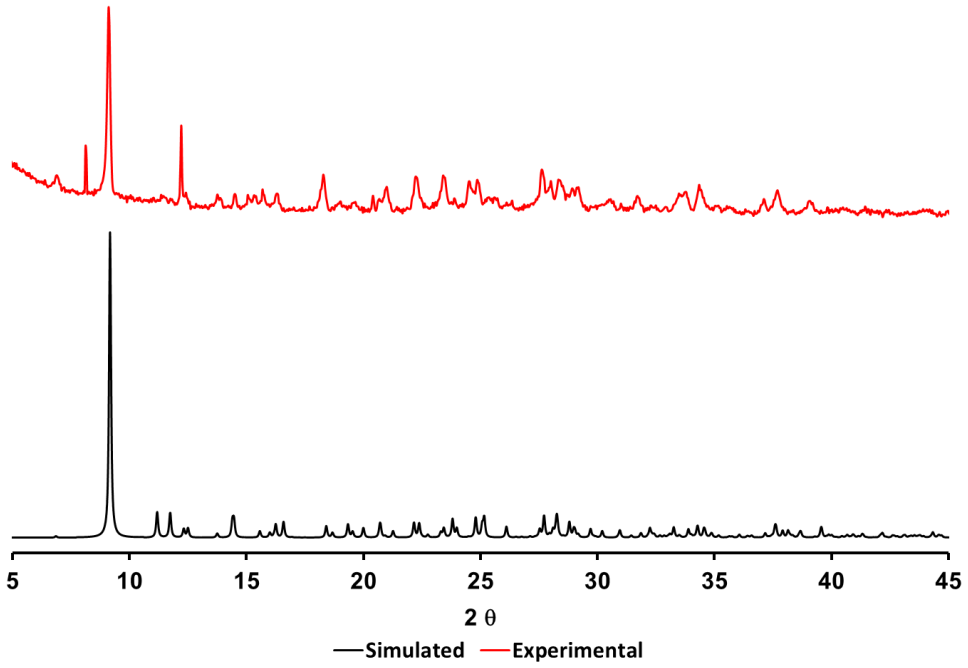

Spectra 6. 8. Simulated (black) and experimental (red) PXRD of [(L2)Cu_2Br_2].

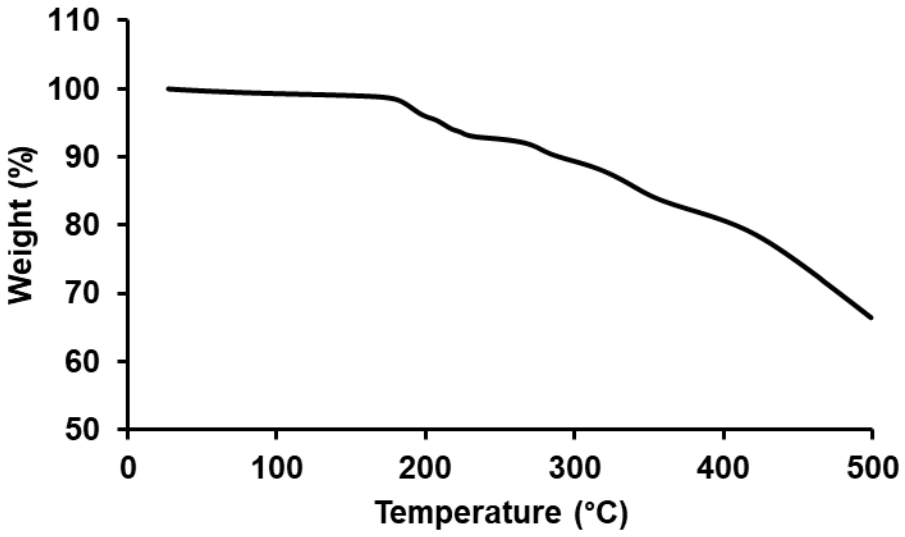

Spectra 6. 9. TGA of [(L2)Cu_2Br_2].

IV. Small Angle Neutron Scattering Experiments

A set of mixed ligand MOFs were synthesized by varying the amount of the methylated **L2** ligand into the **[(L1)Cu_2Br_2] · DMF** framework. The **L2** ligand was incorporated at 10%, 40%, and 60% by weight through identical synthesis.

Synthesis of 10% L2 Mixed Ligand Materials for SAXS/SANS:

Copper(II) bromide dihydrate (0.0164 g, 0.07343 mmol) dissolved in 1 mL of deionized water and placed into a 4 mL scintillation vial. **L1** (0.0078 g, 0.0325 mmol) and **L2** (0.0013 g, 0.0051 mmol) were weighed out and placed in separate 4 mL scintillation vials. Each set of ligands were dissolved in 1 mL DMF. The vials sonicated for several minutes, until the ligand dissolved in DMF. The ligand precursor solutions were mixed and then added to the metal precursor solution. The resulting reaction vial was heated at 85 °C. These conditions were used for both SAXS and SANS experiments.

Synthesis of 40% L2 Mixed Ligand Materials for SAXS/SANS:

Copper(II) bromide dihydrate (0.0166 g, 0.07432 mmol) dissolved in 1 mL of deionized water and placed into a 4 mL scintillation vial. **L1** (0.0054 g, 0.0225 mmol) and **L2** (0.0038 g, 0.0149 mmol) were weighed out and placed in separate 4 mL scintillation vials. Each set of ligands were dissolved in 1 mL DMF. The vials sonicated for several minutes, until the ligand dissolved in DMF. The ligand precursor solutions were mixed and then added to the metal precursor solution. The resulting reaction vial was heated at 85 °C. These conditions were used for both SAXS and SANS experiments.

Synthesis of 60% L2 Mixed Ligand Materials for SAXS/SANS:

Copper(II) bromide dihydrate (0.0167 g, 0.07477 mmol) dissolved in 1 mL of deionized water and placed into a 4 mL scintillation vial. **L1** (0.0036 g, 0.0150 mmol) and **L2** (0.0058 g, 0.0228 mmol) were weighed out and placed in separate 4 mL scintillation vials. Each set of ligands were dissolved in 1 mL DMF. The vials sonicated for several minutes, until the ligand dissolved in DMF. The ligand precursor solutions were mixed and then added to the metal precursor solution. The resulting reaction vial was heated at 85 °C. These conditions were used for both SAXS and SANS experiments.

Synthesis of Coordination Polymer, [(L2)Cu_2Br_2], for SAXS/SANS:

The coordination polymer was synthesized by modifying the reported procedure (See Experimental). This was done by diluting each of the reported precursor solutions to half of their original concentration. Copper(II) bromide dihydrate (0.0382 g, 0.1710 mmol) was dissolved in 1 mL of deionized water and **L2** (0.0191 g, 0.0751 mmol) was dissolved in 2 mL of dimethylformamide.

Synthesis of Metal-Organic Nanotube, [(L1)Cu_2Br_2] · DMF, for SAXS/SANS:

The MONT was synthesized by modifying the previously reported procedure.[32] This was done by diluting each of the reported precursor solutions to half of their original concentration. Copper(II) bromide dihydrate (0.0185 g, 0.0828 mmol) was dissolved in 1 mL of deionized water and **L1** (0.0097 g, 0.0381 mmol) was dissolved in 2 mL of dimethylformamide.

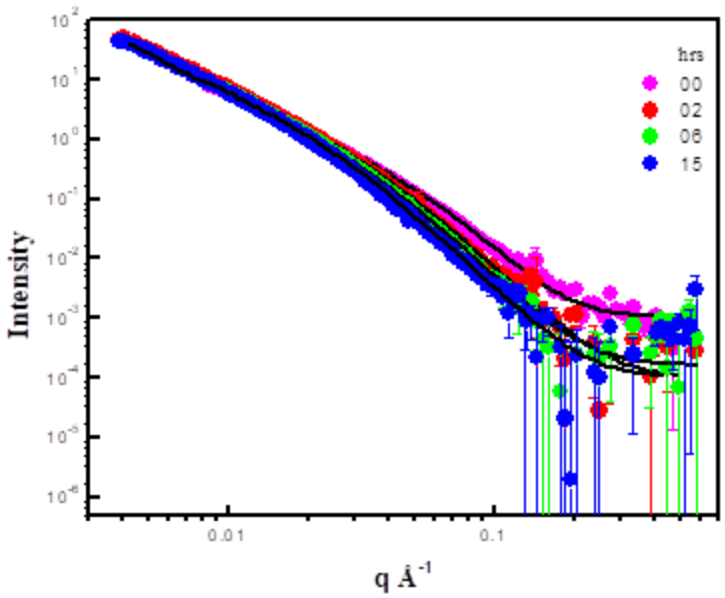

Figure 6. 14. SANS scattering curves for the composition with 10% L2 ligand and metal salt at indicated reaction time, where symbol is for experimental data and solid line is fit using elliptical cylinder model.

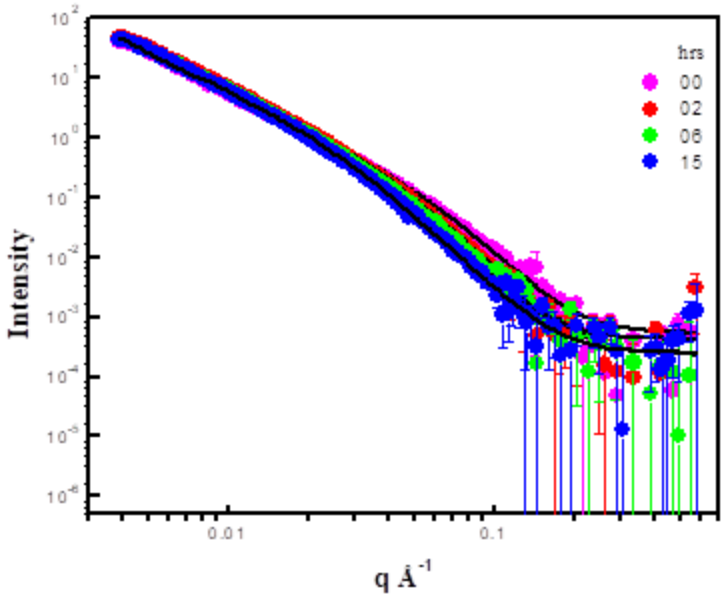

Figure 6. 15. SANS scattering curves for the composition with 40% L2 ligand and metal salt at indicated reaction time, where symbol is for experimental data and solid line is fit using elliptical cylinder model.

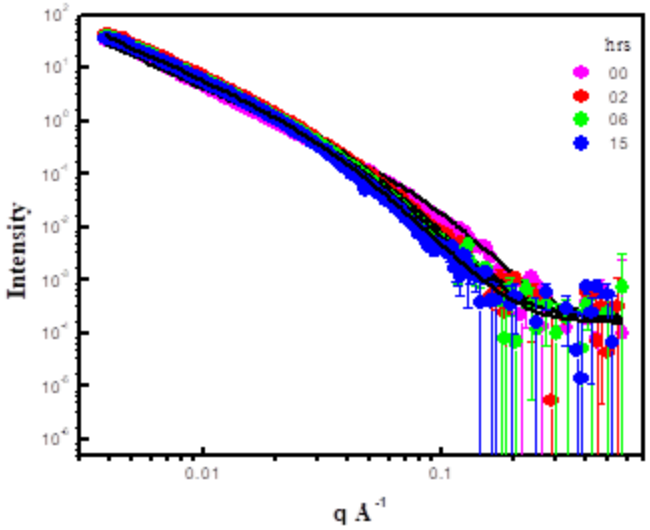

Figure 6. 16. SANS scattering curves for the composition with 60% L2 ligand and metal salt at indicated reaction time. Symbol is for experimental data and solid line is fit.

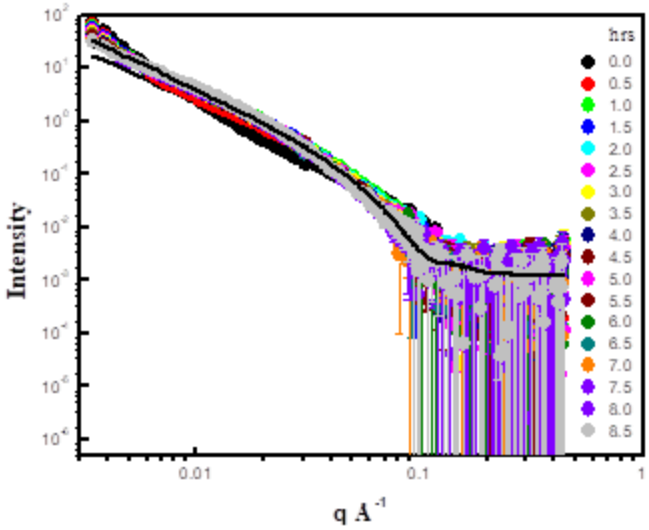

Figure 6. 17. SANS scattering curves for the composition with 100% L2 ligand and metal salt at indicated reaction time. Symbol is for experimental data and solid line is fit.

CHAPTER 7
CONCLUSION

Metal-organic nanotubes are the one-dimensional variant of the class of materials known as metal-organic frameworks. The structure of MONTs are composed of organic ligands that bind with metal salts to form tubular frameworks with pores ranging from 3 Å to 33 Å. All literature examples of metal-organic nanotubes are synthesized and characterized by bulk analyses such as PXRD, SCXRD, SSNMR and IR. This is problematic because as MONTs pack together, their structures resemble 3D MOFs. The packed nanotubes create an array of tubular pores similar to 3D MOFs, effectively making MONTs redundant. In order to study the unique properties of metal-organic nanotubes and highlight their potential as anisotropic materials, packing and aggregation of the tubes must be reduced. As a result, crystalline materials or microcrystalline materials on the micron or mm scale are not desired products.

For metal-organic nanotubes to truly become a new unique class of materials, it is essential to understand the fundamental chemistry of MONTs at the nanoscale. To do so, it is critical to study their growth and formation mechanisms since MONTs are formed one chemical bond at a time. This dissertation takes the first steps towards this goal through new synthesis of ligands designed to reduce aggregation and through collaborative work with experts on transmission electron microscopy and small-angle X-ray and neutron scattering.

First, di-1,2,4-triazole ligands were designed based off the overall goal to synthesize and then image discrete or colloidal MONTs. This goal was separated into four sub-categories including synthesizing (1) large pore MONTs, (2) fluorescent MONTs, (3) MONTs that do not aggregate together, and (4) an isostructural series of MONTs. A ligand from each of the design categories was incorporated in new MONT syntheses; however, only one new MONT was synthesized with the remaining reactions forming 2D or 3D frameworks. These results suggest two lessons. First, the dimensionality of the framework greatly relies on the structure of the organic ligand. Second, our predictive power for knowing when MONTs will be formed is in its infancy.

A collaboration with Dr. Nathan Gianneschi's group at Northwestern University was created to study the metal-organic nanotubes at the nanoscale by using liquid-cell transmission electron microscopy (LCTEM). The growth of a copper-based metal-organic nanotube (**[(L1)Cu_2Br_2]**) was tracked in real time by liquid-cell transmission electron microscopy. The formation of finite bundles of this MONT were observed and diffraction analyses from the LCTEM of this framework were found to match the distances between the heavy atoms within the single-crystal X-ray structure from the bulk material. This study allowed for TEM to be highlighted as a tool for monitoring reactions and a way to obtain mechanistic information. The growth mechanism of the formation of this MONT was determined to be a thermodynamically driven surface-specific monomer–monomer attachment process.

A follow-up study with the Gianneschi group was able to analyze the growth mechanisms of two additional metal-organic nanotubes and compared multiple reaction conditions. In this case, the metal to ligand ratios for both MONT reactions were varied, and the resulting products were analyzed by LCTEM. The ratio of the reactant molecules changed the nucleation pathway of the precursor ions between monomer-based or particle-based pathways. Furthermore, increasing the silver(I) nitrate concentration favored the formation of metal-organic nanotubes with few other metastable products. These insights are critical for developing MONTs in the nanoscale since we want to avoid the formation of byproducts on the nanometer regime. This study has shown that LCTEM has significant potential as a tool for reaction development of MONTs.

A collaboration with Dr. Mark Dadmun's group at The University of Tennessee was created to study MONTs through small-angle neutron and X-ray scattering. A solvothermal reaction of the *meta*-xylyl ditriazole ligand with copper(II) bromide forms a 1D MONT. This ligand was modified with a methyl functional group in an effort to mitigate the aggregation of MONTs through steric blocking. This ligand does not form the expected metal-organic nanotube, but instead formed a double-stranded coordination polymer. Small-angle neutron and

X-ray scattering was used to study the formation of both structures as well as reactions with mixtures of both ligands. Small angle neutron scattering provided insight into the nanoscale structures that form during the reactions and determined that regardless of ligand concentration, anisotropic 2-dimensional sheet-like nanostructures are formed immediately after mixing the organic ligand mixture with the metal salt solution. The presence of the meta ligands inhibits the growth of the 2D coordination polymer sheets, driving the reaction to include both di-triazole ligands.

The studies detailed in this dissertation are just the beginning for metal-organic nanotubes. There is still much more to be understood about this class of materials. The future of MONT chemistry relies on the ability to study these materials at the nanoscale and only once this fundamental chemistry is achieved can applications be found for these nanomaterials. By studying how MONTs form in solution prior to the bulk aggregation, new ligands and reaction conditions can be made to tailor the desired MONT product. New organic ligands should be synthesized so that they remain in the *syn* confirmation to prevent 2D or 3D framework formation. Ligands should also be sterically encumbered enough to force the counter anions into bridging the repeating units of the MONT for 1D framework formation. With these directions in mind, it appears that MONTs can be a tunable anisotropic material in a similar manner to MOFs.

REFERENCES

1. Yaghi, O. M.; Li, H., Hydrothermal Synthesis of a Metal-Organic Framework Containing Large Rectangular Channels. *Journal of the American Chemical Society* **1995,** *117*, 10401-10402.
2. Li, H.; Eddaoudi, M.; O'Keeffe, M.; Yaghi, O. M., Design and synthesis of an exceptionally stable and highly porous metal-organic framework. *Nature* **1999,** *402*, 276-279.
3. Li, B.; Wen, H.-M.; Zhou, W.; Chen, B., Porous Metal–Organic Frameworks for Gas Storage and Separation: What, How, and Why? *The Journal of Physical Chemistry Letters* **2014,** *5*, 3468-3479.
4. Li, J.-R.; Ma, Y.; McCarthy, M. C.; Sculley, J.; Yu, J.; Jeong, H.-K.; Balbuena, P. B.; Zhou, H.-C., Carbon dioxide capture-related gas adsorption and separation in metal-organic frameworks. *Coordination Chemistry Reviews* **2011,** *255*, 1791-1823.
5. Herm, Z. R.; Bloch, E. D.; Long, J. R., Hydrocarbon Separations in Metal–Organic Frameworks. *Chemistry of Materials* **2014,** *26*, 323-338.
6. Wang, Q.; Astruc, D., State of the Art and Prospects in Metal–Organic Framework (MOF)-Based and MOF-Derived Nanocatalysis. *Chemical Reviews* **2019**.
7. Kreno, L. E.; Leong, K.; Farha, O. K.; Allendorf, M.; Van Duyne, R. P.; Hupp, J. T., Metal–Organic Framework Materials as Chemical Sensors. *Chemical Reviews* **2012,** *112*, 1105-1125.
8. Furukawa, H.; Cordova, K. E.; O'Keeffe, M.; Yaghi, O. M., The Chemistry and Applications of Metal-Organic Frameworks. *Science* **2013,** *341*, 1230444.
9. Almeida Paz, F. A.; Klinowski, J.; Vilela, S. M. F.; Tomé, J. P. C.; Cavaleiro, J. A. S.; Rocha, J., Ligand design for functional metal–organic frameworks. *Chemical Society Reviews* **2012,** *41*, 1088-1110.
10. Yaghi, O. M.; O'Keeffe, M.; Ockwig, N. W.; Chae, H. K.; Eddaoudi, M.; Kim, J., Reticular synthesis and the design of new materials. *Nature* **2003,** *423*, 705-714.
11. Xu, G.; Peng, Y.; Hu, Z.; Yuan, D.; Donnadieu, B.; Zhao, D.; Cheng, H., A 2D metal–organic framework composed of a bi-functional ligand with ultra-micropores for post-combustion CO2 capture. *RSC Advances* **2015,** *5*, 47384-47389.
12. Fang, C.; Liu, Q.-K.; Ma, J.-P.; Dong, Y.-B., Independent 1D Nanosized Metal–Organic Tube: Anion Exchange, Separation, and Anion-Responsive Luminescence. *Inorganic Chemistry* **2012,** *51*, 3923-3925.
13. Otsubo, K.; Wakabayashi, Y.; Ohara, J.; Yamamoto, S.; Matsuzaki, H.; Okamoto, H.; Nitta, K.; Uruga, T.; Kitagawa, H., Bottom-up realization of a porous metal–organic nanotubular assembly. *Nature Materials* **2011,** *10*, 291.
14. Ahmad Alshammari, Z. J. a. K. E. C., Metal Organic Frameworks as Emerging Photocatalysts, Semiconductor Photocatalysis - Materials, Mechanisms and Applications. Cao, W., Ed. IntechOpen: August 24, 2016.

https://www.intechopen.com/books/semiconductor-photocatalysis-materials-mechanisms-and-applications/metal-organic-frameworks-as-emerging-photocatalysts.
15. Playskool Tinker Toy 200-piece Plastic Construction Set. https://www.amazon.com/Tinker-Toy-200-piece-Plastic-Construction/dp/B000231G30.
16. Iijima, S., Helical microtubules of graphitic carbon. *Nature* **1991,** *354*, 56-58.
17. Kaye, S. S.; Dailly, A.; Yaghi, O. M.; Long, J. R., Impact of Preparation and Handling on the Hydrogen Storage Properties of Zn4O(1,4-benzenedicarboxylate)3 (MOF-5). *Journal of the American Chemical Society* **2007,** *129*, 14176-14177.
18. Rao, R.; Pint, C. L.; Islam, A. E.; Weatherup, R. S.; Hofmann, S.; Meshot, E. R.; Wu, F.; Zhou, C.; Dee, N.; Amama, P. B.; Carpena-Nuñez, J.; Shi, W.; Plata, D. L.; Penev, E. S.; Yakobson, B. I.; Balbuena, P. B.; Bichara, C.; Futaba, D. N.; Noda, S.; Shin, H.; Kim, K. S.; Simard, B.; Mirri, F.; Pasquali, M.; Fornasiero, F.; Kauppinen, E. I.; Arnold, M.; Cola, B. A.; Nikolaev, P.; Arepalli, S.; Cheng, H.-M.; Zakharov, D. N.; Stach, E. A.; Zhang, J.; Wei, F.; Terrones, M.; Geohegan, D. B.; Maruyama, B.; Maruyama, S.; Li, Y.; Adams, W. W.; Hart, A. J., Carbon Nanotubes and Related Nanomaterials: Critical Advances and Challenges for Synthesis toward Mainstream Commercial Applications. *ACS Nano* **2018,** *12*, 11756-11784.
19. Wei, X.; Luo, T., Effects of Electrostatic Interaction and Chirality on the Friction Coefficient of Water Flow Inside Single-Walled Carbon Nanotubes and Boron Nitride Nanotubes. *The Journal of Physical Chemistry C* **2018,** *122*, 5131-5140.
20. Golberg, D.; Bando, Y.; Huang, Y.; Terao, T.; Mitome, M.; Tang, C.; Zhi, C., Boron Nitride Nanotubes and Nanosheets. *ACS Nano* **2010,** *4*, 2979-2993.
21. Geng, J.; Kim, K.; Zhang, J.; Escalada, A.; Tunuguntla, R.; Comolli, L. R.; Allen, F. I.; Shnyrova, A. V.; Cho, K. R.; Munoz, D.; Wang, Y. M.; Grigoropoulos, C. P.; Ajo-Franklin, C. M.; Frolov, V. A.; Noy, A., Stochastic transport through carbon nanotubes in lipid bilayers and live cell membranes. *Nature* **2014,** *514*, 612.
22. Yu, W. J.; Lee, S. Y.; Chae, S. H.; Perello, D.; Han, G. H.; Yun, M.; Lee, Y. H., Small Hysteresis Nanocarbon-Based Integrated Circuits on Flexible and Transparent Plastic Substrate. *Nano Letters* **2011,** *11*, 1344-1350.
23. Hills, G.; Lau, C.; Wright, A.; Fuller, S.; Bishop, M. D.; Srimani, T.; Kanhaiya, P.; Ho, R.; Amer, A.; Stein, Y.; Murphy, D.; Arvind; Chandrakasan, A.; Shulaker, M. M., Modern microprocessor built from complementary carbon nanotube transistors. *Nature* **2019,** *572*, 595-602.
24. Scott, C. D.; Arepalli, S.; Nikolaev, P.; Smalley, R. E., Growth mechanisms for single-wall carbon nanotubes in a laser-ablation process. *Applied Physics A* **2001,** *72*, 573-580.

25. Arora, N.; Sharma, N. N., Arc discharge synthesis of carbon nanotubes: Comprehensive review. *Diamond and Related Materials* **2014,** *50*, 135-150.
26. Esconjauregui, S.; Fouquet, M.; Bayer, B. C.; Ducati, C.; Smajda, R.; Hofmann, S.; Robertson, J., Growth of Ultrahigh Density Vertically Aligned Carbon Nanotube Forests for Interconnects. *ACS Nano* **2010,** *4*, 7431-7436.
27. Kim, J. H.; Pham, T. V.; Hwang, J. H.; Kim, C. S.; Kim, M. J., Boron nitride nanotubes: synthesis and applications. *Nano Convergence* **2018,** *5*, 17.
28. Lu, W.; Wei, Z.; Gu, Z.-Y.; Liu, T.-F.; Park, J.; Park, J.; Tian, J.; Zhang, M.; Zhang, Q.; Gentle Iii, T.; Bosch, M.; Zhou, H.-C., Tuning the structure and function of metal–organic frameworks via linker design. *Chemical Society Reviews* **2014,** *43*, 5561-5593.
29. Charlier, J. C., Defects in Carbon Nanotubes. *Accounts of Chemical Research* **2002,** *35*, 1063-1069.
30. Jia, J.-G.; Zheng, L.-M., Metal-organic nanotubes: Designs, structures and functions. *Coordination Chemistry Reviews* **2020,** *403*, 213083.
31. Wu, G.; Bai, J.; Jiang, Y.; Li, G.; Huang, J.; Li, Y.; Anson, C. E.; Powell, A. K.; Qiu, S., Rolling Up the Sheet: Constructing Metal–Organic Lamellae and Nanotubes from a [{Mn3(propanediolato)2}(dicyanamide)2]n Honeycomb Skeleton. *Journal of the American Chemical Society* **2013,** *135*, 18276-18279.
32. Murdock, C. R.; Jenkins, D. M., Isostructural Synthesis of Porous Metal–Organic Nanotubes. *Journal of the American Chemical Society* **2014,** *136*, 10983-10988.
33. Zhou, Z.; He, C.; Xiu, J.; Yang, L.; Duan, C., Metal–Organic Polymers Containing Discrete Single-Walled Nanotube as a Heterogeneous Catalyst for the Cycloaddition of Carbon Dioxide to Epoxides. *Journal of the American Chemical Society* **2015,** *137*, 15066-15069.
34. Tseng, T.-W.; Luo, T.-T.; Lu, K.-H., Impeller-like dodecameric water clusters in metal–organic nanotubes. *CrystEngComm* **2014,** *16*, 5516-5519.
35. Lucier, B. E. G.; Chen, S.; Huang, Y., Characterization of Metal–Organic Frameworks: Unlocking the Potential of Solid-State NMR. *Accounts of Chemical Research* **2018,** *51*, 319-330.
36. Howarth, A. J.; Peters, A. W.; Vermeulen, N. A.; Wang, T. C.; Hupp, J. T.; Farha, O. K., Best Practices for the Synthesis, Activation, and Characterization of Metal–Organic Frameworks. *Chemistry of Materials* **2017,** *29*, 26-39.
37. Yakovenko, A. A.; Wei, Z.; Wriedt, M.; Li, J.-R.; Halder, G. J.; Zhou, H.-C., Study of Guest Molecules in Metal–Organic Frameworks by Powder X-ray Diffraction: Analysis of Difference Envelope Density. *Crystal Growth & Design* **2014,** *14*, 5397-5407.
38. Lee, S.; Bürgi, H.-B.; Alshmimri, S. A.; Yaghi, O. M., Impact of Disordered Guest–Framework Interactions on the Crystallography of Metal–Organic

Frameworks. *Journal of the American Chemical Society* **2018,** *140*, 8958-8964.
39. Zheng, J.; Barpaga, D.; Gutiérrez, O. Y.; Browning, N. D.; Mehdi, B. L.; Farha, O. K.; Lercher, J. A.; McGrail, B. P.; Motkuri, R. K., Exceptional Fluorocarbon Uptake with Mesoporous Metal–Organic Frameworks for Adsorption-Based Cooling Systems. *ACS Applied Energy Materials* **2018,** *1*, 5853-5858.
40. Whitby, R. L. D., Chemical Control of Graphene Architecture: Tailoring Shape and Properties. *ACS Nano* **2014,** *8*, 9733-9754.
41. Wang, Y.; Mao, J.; Meng, X.; Yu, L.; Deng, D.; Bao, X., Catalysis with Two-Dimensional Materials Confining Single Atoms: Concept, Design, and Applications. *Chemical Reviews* **2019,** *119*, 1806-1854.
42. Bloch, E. D.; Murray, L. J.; Queen, W. L.; Chavan, S.; Maximoff, S. N.; Bigi, J. P.; Krishna, R.; Peterson, V. K.; Grandjean, F.; Long, G. J.; Smit, B.; Bordiga, S.; Brown, C. M.; Long, J. R., Selective Binding of O2 over N2 in a Redox–Active Metal–Organic Framework with Open Iron(II) Coordination Sites. *Journal of the American Chemical Society* **2011,** *133*, 14814-14822.
43. Bolze, J.; Peng, B.; Dingenouts, N.; Panine, P.; Narayanan, T.; Ballauff, M., Formation and Growth of Amorphous Colloidal CaCO3 Precursor Particles as Detected by Time-Resolved SAXS. *Langmuir* **2002,** *18*, 8364-8369.
44. Li, T.; Senesi, A. J.; Lee, B., Small Angle X-ray Scattering for Nanoparticle Research. *Chemical Reviews* **2016,** *116*, 11128-11180.
45. Smith, B. J.; Parent, L. R.; Overholts, A. C.; Beaucage, P. A.; Bisbey, R. P.; Chavez, A. D.; Hwang, N.; Park, C.; Evans, A. M.; Gianneschi, N. C.; Dichtel, W. R., Colloidal Covalent Organic Frameworks. *ACS Central Science* **2017,** *3*, 58-65.
46. Müller, C. B.; Loman, A.; Richtering, W.; Enderlein, J., Dual-Focus Fluorescence Correlation Spectroscopy of Colloidal Solutions: Influence of Particle Size. *The Journal of Physical Chemistry B* **2008,** *112*, 8236-8240.
47. Etampawala, T.; Mull, D. L.; Keum, J. K.; Jenkins, D. M.; Dadmun, M., Insights into the Morphology and Kinetics of Growth of Silver Metal–Organic Nanotubes. *Crystal Growth & Design* **2016,** *16*, 1395-1403.
48. Ramachandramoorthy, R.; Bernal, R.; Espinosa, H. D., Pushing the Envelope of In Situ Transmission Electron Microscopy. *ACS Nano* **2015,** *9*, 4675-4685.
49. Ngo, T.; Yang, H., Toward Ending the Guessing Game: Study of the Formation of Nanostructures Using In Situ Liquid Transmission Electron Microscopy. *The Journal of Physical Chemistry Letters* **2015,** *6*, 5051-5061.
50. Parent, L. R.; Bakalis, E.; Ramírez-Hernández, A.; Kammeyer, J. K.; Park, C.; de Pablo, J.; Zerbetto, F.; Patterson, J. P.; Gianneschi, N. C., Directly Observing Micelle Fusion and Growth in Solution by Liquid-Cell Transmission Electron Microscopy. *Journal of the American Chemical Society* **2017,** *139*, 17140-17151.

51. Touve, M. A.; Figg, C. A.; Wright, D. B.; Park, C.; Cantlon, J.; Sumerlin, B. S.; Gianneschi, N. C., Polymerization-Induced Self-Assembly of Micelles Observed by Liquid Cell Transmission Electron Microscopy. *ACS Central Science* **2018,** *4*, 543-547.
52. Patterson, J. P.; Abellan, P.; Denny, M. S.; Park, C.; Browning, N. D.; Cohen, S. M.; Evans, J. E.; Gianneschi, N. C., Observing the Growth of Metal–Organic Frameworks by in Situ Liquid Cell Transmission Electron Microscopy. *Journal of the American Chemical Society* **2015,** *137*, 7322-7328.
53. Cherukuri, T. K.; Tsyboulski, D. A.; Weisman, R. B., Length- and Defect-Dependent Fluorescence Efficiencies of Individual Single-Walled Carbon Nanotubes. *ACS Nano* **2012,** *6*, 843-850.
54. Jameson, D. M.; Ross, J. A., Fluorescence Polarization/Anisotropy in Diagnostics and Imaging. *Chemical Reviews* **2010,** *110*, 2685-2708.
55. Hazani, M.; Naaman, R.; Hennrich, F.; Kappes, M. M., Confocal Fluorescence Imaging of DNA-Functionalized Carbon Nanotubes. *Nano Letters* **2003,** *3*, 153-155.
56. Hintz, H.; Wuttke, S., Postsynthetic modification of an amino-tagged MOF using peptide coupling reagents: a comparative study. *Chemical Communications* **2014,** *50*, 11472-11475.
57. Fluch, U.; McCarthy, B. D.; Ott, S., Post synthetic exchange enables orthogonal click chemistry in a metal organic framework. *Dalton Transactions* **2019,** *48*, 45-49.
58. Orrit, M.; Bernard, J., Single pentacene molecules detected by fluorescence excitation in a p-terphenyl crystal. *Physical Review Letters* **1990,** *65*, 2716-2719.
59. Ju, P.; Jiang, L.; Lu, T.-B., An unprecedented dynamic porous metal–organic framework assembled from fivefold interlocked closed nanotubes with selective gas adsorption behaviors. *Chemical Communications* **2013,** *49*, 1820-1822.
60. Su, C.-Y.; Smith, M. D.; zur Loye, H.-C., Columnar Supramolecular Architecture Self-Assembled from S4-Symmetric Coordination Nanotubes Encapsulating Neutral Guest Molecules. *Angewandte Chemie International Edition* **2003,** *42*, 4085-4089.
61. Xu, Y.; Yuan, D.; Wu, B.; Han, L.; Wu, M.; Jiang, F.; Hong, M., 1D Tube, 2D Layer, and 3D Framework Derived from a New Series of Metal(II)−5-Aminodiacetic Isophthalate Coordination Polymers. *Crystal Growth & Design* **2006,** *6*, 1168-1174.
62. Thuéry, P., A Highly Adjustable Coordination System: Nanotubular and Molecular Cage Species in Uranyl Ion Complexes with Kemp's Triacid. *Crystal Growth & Design* **2014,** *14*, 901-904.
63. Fei, Z.; Zhao, D.; Geldbach, T. J.; Scopelliti, R.; Dyson, P. J.; Antonijevic, S.; Bodenhausen, G., A Synthetic Zwitterionic Water Channel: Characterization in the Solid State by X-ray Crystallography and NMR

Spectroscopy. *Angewandte Chemie International Edition* **2005,** *44*, 5720-5725.
64. Yamaguchi, T.; Tashiro, S.; Tominaga, M.; Kawano, M.; Ozeki, T.; Fujita, M., A 3.5-nm Coordination Nanotube. *Journal of the American Chemical Society* **2004,** *126*, 10818-10819.
65. Bu, F.; Xiao, S.-J., A 4-connected anionic metal–organic nanotube constructed from indium isophthalate. *CrystEngComm* **2010,** *12*, 3385-3387.
66. Ren, S.-B.; Yang, X.-L.; Zhang, J.; Li, Y.-Z.; Zheng, Y.-X.; Du, H.-B.; You, X.-Z., An infinite photoluminescent coordination nanotube [CuSCN(L)][middle dot](DMF)0.5. *CrystEngComm* **2009,** *11*, 246-248.
67. Panda, T.; Kundu, T.; Banerjee, R., Self-assembled one dimensional functionalized metal–organic nanotubes (MONTs) for proton conduction. *Chemical Communications* **2012,** *48*, 5464-5466.
68. Xia, J.; Shi, W.; Chen, X.-Y.; Wang, H.-S.; Cheng, P.; Liao, D.-Z.; Yan, S.-P., A CNT-like coordination tube with cyano-bridges. *Dalton Transactions* **2007**, 2373-2375.
69. Ding, B.; Guo, C.; Liu, S. X.; Cheng, Y.; Wu, X. X.; Su, X. M.; Liu, Y. Y.; Li, Y., A unique multi-functional cationic luminescent metal–organic nanotube for highly sensitive detection of dichromate and selective high capacity adsorption of Congo red. *RSC Advances* **2016,** *6*, 33888-33900.
70. Vailonis, K. M.; Gnanasekaran, K.; Powers, X. B.; Gianneschi, N. C.; Jenkins, D. M., Elucidating the Growth of Metal–Organic Nanotubes Combining Isoreticular Synthesis with Liquid-Cell Transmission Electron Microscopy. *Journal of the American Chemical Society* **2019,** *141*, 10177-10182.
71. Dai, F.; He, H.; Sun, D., Polymorphism in High-Crystalline-Stability Metal−Organic Nanotubes. *Inorganic Chemistry* **2009,** *48*, 4613-4615.
72. Bataille, T.; Costantino, F.; Lorenzo-Luis, P.; Midollini, S.; Orlandini, A., A new copper(II) tubelike metal–organic framework constructed from P,P′-diphenylmethylenediphosphinic acid and 4,4′-bipyridine: Synthesis, structure, and thermal behavior. *Inorganica Chimica Acta* **2008,** *361*, 9-15.
73. Wei, Y.; Sun, D.; Yuan, D.; Liu, Y.; Zhao, Y.; Li, X.; Wang, S.; Dou, J.; Wang, X.; Hao, A.; Sun, D., Pb(ii) metal-organic nanotubes based on cyclodextrins: biphasic synthesis, structures and properties. *Chemical Science* **2012,** *3*, 2282-2287.
74. Wang, X.-L.; Qin, C.; Wang, E.-B.; Li, Y.-G.; Su, Z.-M.; Xu, L.; Carlucci, L., Entangled Coordination Networks with Inherent Features of Polycatenation, Polythreading, and Polyknotting. *Angewandte Chemie International Edition* **2005,** *44*, 5824-5827.
75. Xue, H.; Cao, J.; Zhao, L.; Hao, H.; Hong, M., Conformation-Driven Self-Assembly: From a 1D Metal–Organic Polymer to an Infinite Double Nanotube. *ACS Omega* **2019,** *4*, 10755-10760.

76. Adarsh, N. N.; Dîrtu, M. M.; Naik, A. D.; Léonard, A. F.; Campagnol, N.; Robeyns, K.; Snauwaert, J.; Fransaer, J.; Su, B. L.; Garcia, Y., Single-Walled Metal–Organic Nanotube Built from a Simple Synthon. *Chemistry – A European Journal* **2015,** *21*, 4300-4307.
77. Luo, T.-T.; Wu, H.-C.; Jao, Y.-C.; Huang, S.-M.; Tseng, T.-W.; Wen, Y.-S.; Lee, G.-H.; Peng, S.-M.; Lu, K.-L., Self-Assembled Arrays of Single-Walled Metal–Organic Nanotubes. *Angewandte Chemie International Edition* **2009,** *48*, 9461-9464.
78. Jin, J.-C.; Wang, Y.-Y.; Liu, P.; Liu, R.-T.; Ren, C.; Shi, Q.-Z., An Unusual Independent 1D Metal−Organic Nanotube with Mesohelical Structure and 1D → 2D Interdigitation. *Crystal Growth & Design* **2010,** *10*, 2029-2032.
79. Kim, J. G.; Noh, T. H.; Cho, Y.; Park, J. K.; Jung, O.-S., A triple-function nanotube as a reactant reservoir, reaction platform, and byproduct scavenger for photo-cyclopropanation. *Chemical Communications* **2016,** *52*, 2545-2548.
80. Orr, G. W.; Barbour, L. J.; Atwood, J. L., Controlling Molecular Self-Organization: Formation of Nanometer-Scale Spheres and Tubules. *Science* **1999,** *285*, 1049.
81. Cui, Y.; Lee, S. J.; Lin, W., Interlocked Chiral Nanotubes Assembled from Quintuple Helices. *Journal of the American Chemical Society* **2003,** *125*, 6014-6015.
82. Zhou, Y.; Yao, S.; Ma, Y.; Li, G.; Huo, Q.; Liu, Y., An anionic single-walled metal–organic nanotube with an armchair (3,3) topology as an extremely smart adsorbent for the effective and selective adsorption of cationic carcinogenic dyes. *Chemical Communications* **2018,** *54*, 3006-3009.
83. Zhang, G.-L.; Zhou, L.-P.; Yuan, D.-Q.; Sun, Q.-F., Bottom-Up Construction of Mesoporous Nanotubes from 78-Component Self-Assembled Nanobarrels. *Angewandte Chemie International Edition* **2015,** *54*, 9844-9848.
84. Kong, G.-Q.; Ou, S.; Zou, C.; Wu, C.-D., Assembly and Post-Modification of a Metal–Organic Nanotube for Highly Efficient Catalysis. *Journal of the American Chemical Society* **2012,** *134*, 19851-19857.
85. Eddaoudi, M.; Kim, J.; Rosi, N.; Vodak, D.; Wachter, J.; Keeffe, M.; Yaghi, O. M., Systematic Design of Pore Size and Functionality in Isoreticular MOFs and Their Application in Methane Storage. *Science* **2002,** *295*, 469.
86. Bheemireddy, S. R.; Ubaldo, P. C.; Rose, P. W.; Finke, A. D.; Zhuang, J.; Wang, L.; Plunkett, K. N., Stabilizing Pentacene By Cyclopentannulation. *Angewandte Chemie International Edition* **2015,** *54*, 15762-15766.
87. Zhou, L.-P.; Sun, Q.-F., A self-assembled Pd2L4 cage that selectively encapsulates nitrate. *Chemical Communications* **2015,** *51*, 16767-16770.
88. Iyengar, B. S.; Dorr, R. T.; Alberts, D. S.; Sólyom, A. M.; Krutzsch, M.; Remers, W. A., 1,4-Disubstituted Anthracene Antitumor Agents. *Journal of Medicinal Chemistry* **1997,** *40*, 3734-3738.

89. Celis-Salazar, P. J.; Epley, C. C.; Ahrenholtz, S. R.; Maza, W. A.; Usov, P. M.; Morris, A. J., Proton-Coupled Electron Transport in Anthraquinone-Based Zirconium Metal–Organic Frameworks. *Inorganic Chemistry* **2017,** *56*, 13741-13747.
90. Elbs, K., Contribution of Knowledge of Homologs of Anthracene and Anthraquinone. *Journal für praktische Chemie* **1890,** *41*, 7-32.
91. Gundermann, K.-D.; Röker, K.-D., Konstitution und Chemilumineszenz, VII. Chemilumineszierende Paracyclophane, II: Intramolekular sensibilisierte Chemilumineszenz. *Justus Liebigs Annalen der Chemie* **1976,** *1976*, 140-152.
92. Boyle, M. M.; Gassensmith, J. J.; Whalley, A. C.; Forgan, R. S.; Smaldone, R. A.; Hartlieb, K. J.; Blackburn, A. K.; Sauvage, J.-P.; Stoddart, J. F., Stereochemistry of Molecular Figures-of-Eight. *Chemistry – A European Journal* **2012,** *18*, 10312-10323.
93. Murai, K.; Fukushima, S.; Nakamura, A.; Shimura, M.; Fujioka, H., C3-Symmetric chiral trisimidazoline: the role of a third imidazoline and its application to the nitro Michael reaction and the α-amination of β-ketoesters. *Tetrahedron* **2011,** *67*, 4862-4868.
94. Hughes, B. C.; Murdock, C. R.; Jenkins, D. M., Isoreticular synthesis of 2D MOFs with rotating aryl rings. *Inorganic Chemistry Frontiers* **2015,** *2*, 1001-1005.
95. Norio Miyaura, Y. Y. Reagent for Organic Synthesis Reaction Containing Organic Triol Borate Salt. US 8,207,337 B2, 2012.
96. Gong, Y.; Zhou, Y.; Qin, J.; Li, J.; Cao, R., Synthesis, crystal structure and photoluminescence of 2,6-dimethylanthracene and its pseudo-triptycene derivatives. *Journal of Molecular Structure* **2010,** *963*, 76-81.
97. Horváth, A., Michael Adducts in the Regioselective Synthesis of N-Substituted Azoles. *Synthesis* **1995,** *1995*, 1183-1189.
98. Zang, Y.; Aoki, T.; Liu, L.; Abe, Y.; Kakihana, Y.; Teraguchi, M.; Kaneko, T., Pseudo helix-sense-selective polymerisation of achiral substituted acetylenes. *Chemical Communications* **2012,** *48*, 4761-4763.
99. Sander, F.; Peterle, T.; Ballav, N.; Wrochem, F. v.; Zharnikov, M.; Mayor, M., Loops versus Stems: Benzylic Sulfide Oligomers Forming Carpet Type Monolayers. *The Journal of Physical Chemistry C* **2010,** *114*, 4118-4125.
100. Chung, C. Y.-S.; Li, S. P.-Y.; Lo, K. K.-W.; Yam, V. W.-W., Synthesis and Electrochemical, Photophysical, and Self-Assembly Studies on Water-Soluble pH-Responsive Alkynylplatinum(II) Terpyridine Complexes. *Inorganic Chemistry* **2016,** *55*, 4650-4663.
101. Tokimizu, Y.; Wieteck, M.; Rudolph, M.; Oishi, S.; Fujii, N.; Hashmi, A. S. K.; Ohno, H., Dual Gold Catalysis: A Novel Synthesis of Bicyclic and Tricyclic Pyrroles from N-Propargyl Ynamides. *Organic Letters* **2015,** *17*, 604-607.
102. Taher, E. S.; Guest, P.; Benton, A.; Ma, X.; Banwell, M. G.; Willis, A. C.; Seiser, T.; Newton, T. W.; Hutzler, J., The Synthesis of Certain

Phomentrioloxin A Analogues and Their Evaluation as Herbicidal Agents. *The Journal of Organic Chemistry* **2017,** *82*, 211-233.
103. Murdock, C. R.; McNutt, N. W.; Keffer, D. J.; Jenkins, D. M., Rotating Phenyl Rings as a Guest-Dependent Switch in Two-Dimensional Metal–Organic Frameworks. *Journal of the American Chemical Society* **2014,** *136*, 671-678.
104. Zhou, H.-C.; Long, J. R.; Yaghi, O. M., Introduction to Metal–Organic Frameworks. *Chemical Reviews* **2012,** *112*, 673-674.
105. Morris, R. E.; Brammer, L., Coordination change, lability and hemilability in metal–organic frameworks. *Chemical Society Reviews* **2017,** *46*, 5444-5462.
106. Falcao, E. H. L.; Wudl, F., Carbon allotropes: beyond graphite and diamond. *Journal of Chemical Technology & Biotechnology* **2007,** *82*, 524-531.
107. Baughman, R. H.; Zakhidov, A. A.; de Heer, W. A., Carbon Nanotubes--the Route Toward Applications. *Science* **2002,** *297*, 787-792.
108. Furukawa, H.; Cordova, K. E.; O'Keeffe, M.; Yaghi, O. M., The Chemistry and Applications of Metal-Organic Frameworks. *Science* **2013,** *341*.
109. Kuppler, R. J.; Timmons, D. J.; Fang, Q.-R.; Li, J.-R.; Makal, T. A.; Young, M. D.; Yuan, D.; Zhao, D.; Zhuang, W.; Zhou, H.-C., Potential applications of metal-organic frameworks. *Coordination Chemistry Reviews* **2009,** *253*, 3042-3066.
110. Yuan, S.; Chen, Y.-P.; Qin, J.-S.; Lu, W.; Zou, L.; Zhang, Q.; Wang, X.; Sun, X.; Zhou, H.-C., Linker Installation: Engineering Pore Environment with Precisely Placed Functionalities in Zirconium MOFs. *Journal of the American Chemical Society* **2016,** *138*, 8912-8919.
111. Unruh, D. K.; Gojdas, K.; Libo, A.; Forbes, T. Z., Development of Metal–Organic Nanotubes Exhibiting Low-Temperature, Reversible Exchange of Confined "Ice Channels". *Journal of the American Chemical Society* **2013,** *135*, 7398-7401.
112. Dresselhaus, M. S.; Lin, Y. M.; Rabin, O.; Jorio, A.; Souza Filho, A. G.; Pimenta, M. A.; Saito, R.; Samsonidze, G.; Dresselhaus, G., Nanowires and nanotubes. *Materials Science and Engineering: C* **2003,** *23*, 129-140.
113. Eatemadi, A.; Daraee, H.; Karimkhanloo, H.; Kouhi, M.; Zarghami, N.; Akbarzadeh, A.; Abasi, M.; Hanifehpour, Y.; Joo, S. W., Carbon nanotubes: properties, synthesis, purification, and medical applications. *Nanoscale Research Letters* **2014,** *9*, 393.
114. Sun, Y.-P.; Fu, K.; Lin, Y.; Huang, W., Functionalized Carbon Nanotubes: Properties and Applications. *Accounts of Chemical Research* **2002,** *35*, 1096-1104.
115. Ross, F. M.; Wang, C.; de Jonge, N., Transmission electron microscopy of specimens and processes in liquids. *MRS Bulletin* **2016,** *41*, 791-803.
116. Woehl, T. J.; Evans, J. E.; Arslan, I.; Ristenpart, W. D.; Browning, N. D., Direct in Situ Determination of the Mechanisms Controlling Nanoparticle Nucleation and Growth. *ACS Nano* **2012,** *6*, 8599-8610.

117. Murdock, C. R.; Hughes, B. C.; Lu, Z.; Jenkins, D. M., Approaches for synthesizing breathing MOFs by exploiting dimensional rigidity. *Coordination Chemistry Reviews* **2014,** *258-259*, 119-136.
118. Gupta, M.; Kottilil, D.; Tomar, K.; Lu, S.; Vijayan, C.; Ji, W.; Bharadwaj, P. K., Two-Photon Absorption and Fluorescence in Micrometer-Sized Single Crystals of a Rhodamine B Coordinated Metal-Organic Framework. *ACS Appl. Nano Mater.* **2018,** *1*, 5408-5413.
119. Katsoulidis, A. P.; Antypov, D.; Whitehead, G. F. S.; Carrington, E. J.; Adams, D. J.; Berry, N. G.; Darling, G. R.; Dyer, M. S.; Rosseinsky, M. J., Chemical control of structure and guest uptake by a conformationally mobile porous material. *Nature (London, U. K.)* **2019,** *565*, 213-217.
120. Cravillon, J.; Schröder, C. A.; Nayuk, R.; Gummel, J.; Huber, K.; Wiebcke, M., Fast Nucleation and Growth of ZIF-8 Nanocrystals Monitored by Time-Resolved In Situ Small-Angle and Wide-Angle X-Ray Scattering. *Angewandte Chemie International Edition* **2011,** *50*, 8067-8071.
121. Feng, X.; Carreon, M. A., Kinetics of transformation on ZIF-67 crystals. *Journal of Crystal Growth* **2015,** *418*, 158-162.
122. Woehl, T. J.; Abellan, P., Defining the radiation chemistry during liquid cell electron microscopy to enable visualization of nanomaterial growth and degradation dynamics. *Journal of Microscopy* **2017,** *265*, 135-147.
123. Moser, T. H.; Mehta, H.; Park, C.; Kelly, R. T.; Shokuhfar, T.; Evans, J. E., The role of electron irradiation history in liquid cell transmission electron microscopy. *Science Advances* **2018,** *4*, eaaq1202.
124. Woehl, T. J.; Jungjohann, K. L.; Evans, J. E.; Arslan, I.; Ristenpart, W. D.; Browning, N. D., Experimental procedures to mitigate electron beam induced artifacts during in situ fluid imaging of nanomaterials. *Ultramicroscopy* **2013,** *127*, 53-63.
125. Viswanatha, R. S., D.D., Growth of Nanocrystals in Solution. In *Nanomaterials Chemistry*, 2007; pp 139-170.
126. Lifshitz, I. M.; Slyozov, V. V., The kinetics of precipitation from supersaturated solid solutions. *Journal of Physics and Chemistry of Solids* **1961,** *19*, 35-50.
127. Wagner, C., Theory of precipitate change by redissolution. *Z. Elektrochem* **1961,** *65*, 581-591.
128. Liu, Y.; Tai, K.; Dillon, S. J., Growth Kinetics and Morphological Evolution of ZnO Precipitated from Solution. *Chemistry of Materials* **2013,** *25*, 2927-2933.
129. De Yoreo, J. J.; Gilbert, P. U. P. A.; Sommerdijk, N. A. J. M.; Penn, R. L.; Whitelam, S.; Joester, D.; Zhang, H.; Rimer, J. D.; Navrotsky, A.; Banfield, J. F.; Wallace, A. F.; Michel, F. M.; Meldrum, F. C.; Cölfen, H.; Dove, P. M., Crystallization by particle attachment in synthetic, biogenic, and geologic environments. *Science* **2015,** *349*, aaa6760.

130. Cölfen, H.; Mann, S., Higher-Order Organization by Mesoscale Self-Assembly and Transformation of Hybrid Nanostructures. *Angewandte Chemie International Edition* **2003,** *42*, 2350-2365.
131. Nielsen, M. H.; Aloni, S.; De Yoreo, J. J., In situ TEM imaging of CaCO3 nucleation reveals coexistence of direct and indirect pathways. *Science* **2014,** *345*, 1158.
132. Kang, M. T.; Meng, M.; Tan, Y. N.; Cheng, T.; Liu, C. Y., Tuning the Electronic Coupling and Electron Transfer in Mo2 Donor–Acceptor Systems by Variation of the Bridge Conformation. *Chemistry – A European Journal* **2016,** *22*, 3115-3126.
133. Cohen, F. T. V., H.-W.; Ly, C.; Flygare, J. A. Pyrrolidine Inhibitors of IAP. 2006.
134. Jiang, X.-F.; Hu, J.-H.; Tong, J.; Yu, S.-Y., Coexistence of molecular Pd6 triangle and Pd8 square self-assembled from naphthyl-dipyrazole with di-palladium motifs. *Inorganic Chemistry Communications* **2013,** *36*, 232-235.
135. Serum, E. M.; Selvakumar, S.; Zimmermann, N.; Sibi, M. P., Valorization of 2,5-furandicarboxylic acid. Diels–Alder reactions with benzyne. *Green Chemistry* **2018,** *20*, 1448-1454.
136. Johnson R. A. S.; Herman, W. Phosphonic Acid Derivatives Useful as Anti-inflammatory agents. 1993.
137. Zou, L.; Hou, C.-C.; Liu, Z.; Pang, H.; Xu, Q., Superlong Single-Crystal Metal–Organic Framework Nanotubes. *Journal of the American Chemical Society* **2018,** *140*, 15393-15401.
138. Arbulu, R. C.; Jiang, Y.-B.; Peterson, E. J.; Qin, Y., Metal–Organic Framework (MOF) Nanorods, Nanotubes, and Nanowires. *Angewandte Chemie International Edition* **2018,** *57*, 5813-5817.
139. Li, Q.-L.; Li, Q.; Guo, S.-F.; Li, D.; Wo, R.; Zhao, R.-S.; Jiang, W., Composite Material that Comprised Metal–Organic Nanotubes and a Sponge as a High-Performance Adsorbent for the Extraction of Pharmaceuticals and Personal Care Products from Environmental Water Samples. *Chemistry – An Asian Journal* **2019,** *14*, 1487-1495.
140. Davis, M. E., Ordered porous materials for emerging applications. *Nature* **2002,** *417*, 813-821.
141. Aerts, A.; Kirschhock, C. E. A.; Martens, J. A., Methods for in situ spectroscopic probing of the synthesis of a zeolite. *Chemical Society Reviews* **2010,** *39*, 4626-4642.
142. Bhattacharyya, R.; Key, B.; Chen, H.; Best, A. S.; Hollenkamp, A. F.; Grey, C. P., In situ NMR observation of the formation of metallic lithium microstructures in lithium batteries. *Nature Materials* **2010,** *9*, 504-510.
143. Kehrle, J.; Kaiser, S.; Purkait, T. K.; Winnacker, M.; Helbich, T.; Vagin, S.; Veinot, J. G. C.; Rieger, B., In situ IR-spectroscopy as a tool for monitoring the radical hydrosilylation process on silicon nanocrystal surfaces. *Nanoscale* **2017,** *9*, 8489-8495.

144. Savage, J. R.; Dinsmore, A. D., Experimental Evidence for Two-Step Nucleation in Colloidal Crystallization. *Physical Review Letters* **2009,** *102*, 198302.
145. Vekilov, P. G., Two-step mechanism for the nucleation of crystals from solution. *Journal of Crystal Growth* **2005,** *275*, 65-76.
146. Abellan, P.; Moser, T. H.; Lucas, I. T.; Grate, J. W.; Evans, J. E.; Browning, N. D., The formation of cerium(iii) hydroxide nanoparticles by a radiation mediated increase in local pH. *RSC Advances* **2017,** *7*, 3831-3837.
147. Liao, H.-G.; Cui, L.; Whitelam, S.; Zheng, H., Real-Time Imaging of Pt3Fe Nanorod Growth in Solution. *Science* **2012,** *336*, 1011.
148. Asoro, M. A.; Kovar, D.; Ferreira, P. J., In situ Transmission Electron Microscopy Observations of Sublimation in Silver Nanoparticles. *ACS Nano* **2013,** *7*, 7844-7852.
149. Yu, L.; Han, R.; Sang, X.; Liu, J.; Thomas, M. P.; Hudak, B. M.; Patel, A.; Page, K.; Guiton, B. S., Shell-Induced Ostwald Ripening: Simultaneous Structure, Composition, and Morphology Transformations during the Creation of Hollow Iron Oxide Nanocapsules. *ACS Nano* **2018,** *12*, 9051-9059.
150. Zhang, Y.; Keller, D.; Rossell, M. D.; Erni, R., Formation of Au Nanoparticles in Liquid Cell Transmission Electron Microscopy: From a Systematic Study to Engineered Nanostructures. *Chemistry of Materials* **2017,** *29*, 10518-10525.
151. Evans, J. E.; Jungjohann, K. L.; Browning, N. D.; Arslan, I., Controlled Growth of Nanoparticles from Solution with In Situ Liquid Transmission Electron Microscopy. *Nano Letters* **2011,** *11*, 2809-2813.
152. Parent, L. R.; Bakalis, E.; Proetto, M.; Li, Y.; Park, C.; Zerbetto, F.; Gianneschi, N. C., Tackling the Challenges of Dynamic Experiments Using Liquid-Cell Transmission Electron Microscopy. *Accounts of Chemical Research* **2018,** *51*, 3-11.
153. Zhu, C.; Liang, S.; Song, E.; Zhou, Y.; Wang, W.; Shan, F.; Shi, Y.; Hao, C.; Yin, K.; Zhang, T.; Liu, J.; Zheng, H.; Sun, L., In-situ liquid cell transmission electron microscopy investigation on oriented attachment of gold nanoparticles. *Nature Communications* **2018,** *9*, 421.
154. Proetto, M. T.; Rush, A. M.; Chien, M.-P.; Abellan Baeza, P.; Patterson, J. P.; Thompson, M. P.; Olson, N. H.; Moore, C. E.; Rheingold, A. L.; Andolina, C.; Millstone, J.; Howell, S. B.; Browning, N. D.; Evans, J. E.; Gianneschi, N. C., Dynamics of Soft Nanomaterials Captured by Transmission Electron Microscopy in Liquid Water. *Journal of the American Chemical Society* **2014,** *136*, 1162-1165.
155. Ianiro, A.; Wu, H.; van Rijt, M. M. J.; Vena, M. P.; Keizer, A. D. A.; Esteves, A. C. C.; Tuinier, R.; Friedrich, H.; Sommerdijk, N. A. J. M.; Patterson, J. P., Liquid–liquid phase separation during amphiphilic self-assembly. *Nature Chemistry* **2019,** *11*, 320-328.

156. Kunnas, P.; Rzadkiewicz, S.; Moradi, M.-A.; Patterson, J.; Sommerdijk, N.; de Jonge, N., Challenges in Observing the Formation of Colloidal, Self-Assembled Monolayers with In Situ Electron Microscopy in Liquid. *Microscopy and Microanalysis* **2019,** *25*, 55-56.
157. Williamson, M. J.; Tromp, R. M.; Vereecken, P. M.; Hull, R.; Ross, F. M., Dynamic microscopy of nanoscale cluster growth at the solid–liquid interface. *Nature Materials* **2003,** *2*, 532-536.
158. de Jonge, N.; Ross, F. M., Electron microscopy of specimens in liquid. *Nature Nanotechnology* **2011,** *6*, 695-704.
159. Rimer, J. D.; Tsapatsis, M., Nucleation of open framework materials: Navigating the voids. *MRS Bulletin* **2016,** *41*, 393-398.
160. Cundy, C. S.; Cox, P. A., The hydrothermal synthesis of zeolites: Precursors, intermediates and reaction mechanism. *Microporous and Mesoporous Materials* **2005,** *82*, 1-78.
161. Férey, G., Building Units Design and Scale Chemistry. *Journal of Solid State Chemistry* **2000,** *152*, 37-48.
162. Saha, S.; Springer, S.; Schweinefuß, M. E.; Pontoni, D.; Wiebcke, M.; Huber, K., Insight into Fast Nucleation and Growth of Zeolitic Imidazolate Framework-71 by In Situ Time-Resolved Light and X-ray Scattering Experiments. *Crystal Growth & Design* **2016,** *16*, 2002-2010.
163. De Yoreo, J. J.; Vekilov, P. G., Principles of Crystal Nucleation and Growth. *Reviews in Mineralogy and Geochemistry* **2003,** *54*, 57-93.
164. Li, M.; Dincă, M., On the Mechanism of MOF-5 Formation under Cathodic Bias. *Chemistry of Materials* **2015,** *27*, 3203-3206.
165. Woehl, T. J.; Park, C.; Evans, J. E.; Arslan, I.; Ristenpart, W. D.; Browning, N. D., Direct Observation of Aggregative Nanoparticle Growth: Kinetic Modeling of the Size Distribution and Growth Rate. *Nano Letters* **2014,** *14*, 373-378.
166. Galkin, O.; Chen, K.; Nagel, R. L.; Hirsch, R. E.; Vekilov, P. G., Liquid–liquid separation in solutions of normal and sickle cell hemoglobin. *Proceedings of the National Academy of Sciences* **2002,** *99*, 8479.
167. Chung, S.; Shin, S.-H.; Bertozzi, C. R.; De Yoreo, J. J., Self-catalyzed growth of S layers via an amorphous-to-crystalline transition limited by folding kinetics. *Proceedings of the National Academy of Sciences* **2010,** *107*, 16536.
168. Tsao, C.-S.; Yu, M.-S.; Chung, T.-Y.; Wu, H.-C.; Wang, C.-Y.; Chang, K.-S.; Chen, H.-L., Characterization of Pore Structure in Metal−Organic Framework by Small-Angle X-ray Scattering. *Journal of the American Chemical Society* **2007,** *129*, 15997-16004.
169. Szuromi, P., Glimpsing growing nanotubes. *Science* **2019,** *365*, 246.

VITA

Kristina Marie Vailonis was born in Hartford, Connecticut to Maria and Joe Vailonis. She attended Rocky Hill High School where she was captain of the Color Guard in the Rocky Hill Royal Blues Marching Band, and member of both National Honor Society and National Art Honor Society.

She then attended Stonehill College in Easton, Massachusetts. During her time as an undergraduate student she worked as tutor for general chemistry and as an astronomy teaching assistant, where she had the privilege to work in the campus observatory. Kristina participated in undergraduate research at Stonehill College during the semester with Dr. Leon Tilley and two NSF-REU programs; the first with Dr. Al Schwab at Appalachian State University in Boone, North Carolina and then with Dr. Ted Burkey at the University of Memphis in Memphis, Tennessee. She presented research from both REU programs at national ACS conferences, and won the ACS Excellence in Undergraduate Polymer Research Award. In her last year of undergraduate studies, she co-taught a student-lead 1-credit elective entitled “Chemistry of the Cupcake” where students were actively engaged in investigating the chemistry behind food. This class allowed her to share her two passions; science and baking. Kristina graduated with a Bachelor of Science degree in Chemistry and minor in Physics in the spring of 2014.

In August of 2014, Kristina entered the Chemistry department at The University of Tennessee and soon joined Dr. David Jenkins’ research group. During her time at UTK she worked as a teaching assistant for many classes from general chemistry to inorganic chemistry. She attended and presented her research at two national ACS meetings. Her collaborative research with Dr. Nathan Gianneschi at Northwestern University was published in the *Journal of American Chemical Society* and was even highlighted in the July 2019 edition of *Science* magazine.[169]